Interior and Exterior Shaping of Organic Molecular Dyes for Optoelectronic Applications

Dissertation

Takuya Okabe

2018

Laboratory for Photofunctional Organic Chemistry
Graduate School of Materials Science
Nara Institute of Science and Technology

Table of Contents

Abbreviations

AFM: Atomic force microscopy

ATR: Attenuated total reflection

BHJ: Bulk-heterojunction

CCD: Charge-coupled device

CN-PPV: Poly[5-(2-ethylhexyloxy)-2-methoxycyanoterephthalyliden]

CT: Charge-transfer

CuPc: Cu(II) phthalocyanine

CV: Cyclic voltammetry

D−A: Donor–acceptor

DCTB: *Trans*-2-[3-(4-*tert*-Butylphenyl)-2-methyl-2-propenylidene]

DFT: Density functional theory

DMF: *N*,*N*-Dimethylformamide

DMSO: Dimethyl sulfoxide

DPP: Diketopyrrolopyrrole

DPV: Differential pulse voltammetry

DTS(PTTh$_2$)$_2$: 4,4′-[4,4-Bis(2-ethylhexyl)-4H-silolo[3,2-*b*:4,5-*b*′]dithiophene-2,6-diyl]bis[7-(5′-hexyl-[2,2′-bithiophen]-5-yl)-[1,2,5]thiadiazolo[3,4-*c*]pyridine], 5,5′-bis{[4-(7-hexylthiophen-2-yl)thiophen-2-yl]-[1,2,5]thiadiazolo[3,4-*c*]pyridine}-3,3′-di-2-ethylhexylsilylene-2,2′-bithiophene

$E^{1/2}$: Half-wave potential

$E_{g,\,opt}$: Optical energy gap

EQE: External quantum efficiency

Equiv: Equivalence

ESI: Electrospray ionization

FF: Fill factor

GIWAXD: Grazing-incident wide-angle X-ray diffractometry

GPC: Gel permeation chromatography

HOMO: Highest occupied molecular orbital

HRMS: High-resolution mass spectroscopy

I_{ph}/I_{dark}: Photo-to-dark-current ratio

I_{SD}: Source–drain current

I–V: Current–Voltage

ITIC: 3,9-Bis(2-methylene-(3-(1,1-dicyanomethylene)-indanone))-5,5,11,11-tetrakis(4-hexylphenyl)-dithieno[2,3-*d*:2′,3′-*d*′]-s-indaceno[1,2-*b*:5,6-*b*′]dithiophene

ITO: Indium–tin oxide

J_{SC}: Short-circuit current density

J–V: Current density−voltage

L_D: Exciton diffusion length

LUMO: Lowest unoccupied molecular orbital

μ_h: Charge-carrier hole-mobility

μ_e: Charge-carrier electron-mobility

MALDI: Matrix-assisted laser desorption/ionization

MEH-PPV: Poly [2-methoxy-5-(ethylhexyloxy)-1,4-phenylene vinylene]

NBS: *N*-Bromosuccinimide

NIR: Near-infrared

NIS: *N*-Iodosuccinimide

NMR: Nuclear magnetic resonance

OEG: Oligo(ethylene glycol)

OFETs: Organic field-effect transistors

OLEDs: Organic light-emitting diodes

OPTs: Organic phototransistors

OSCs: Organic solar cells

P3HT: Poly(3-hexylthiophene)

PBDTTPD-HT: Poly[benzo(1,2-*b*:4,5-*b*′)dithio-phene–thieno(3,4-*c*)pyrrole-4,6-dione]

PCE: Power conversion efficiency

$PC_{61}BM$: [6,6]-Phenyl-C_{61}-butyric acid methyl ester

$PC_{71}BM$: [6,6]-Phenyl-C_{71}-butyric acid methyl ester

PCPDTBT: Poly[2,6-(4,4-bis-(2-ethylhexyl)-4H-cyclopenta [2,1-*b*;3,4-*b*′]dithiophene)-*alt*-4,7(2,1,3-benzothiadiazole)]

PDI: Perylene diimide

PEDOT:PSS: Poly(3,4-ethylenedioxy thiophene):poly(4-styrenesulfonate)

PHJ: Planar-heterojunction

PV: Perylene tetracarboxylic dye

SCLC: Space-charge-limited current

TBAF: Tetrabutylammonium fluoride

TFA: Trifluoroacetic acid

TGA: Thermogravimetric analysis

THF: Tetrahydrofuran

TLC: Thin-layer chromatography

TMEDA: *N*,*N*,*N*',*N*'-Tetramethylethylenediamine

TMS: Tetramethylsilane

TOF: Time of flight

UV: Ultraviolet

V_G: Gate voltage

Vis: Visible

V_{th}: Threshold voltage

V_{SD}: Source–Drain voltage

V_{OC}: Open-circuit voltage

XRD: X-ray diffraction

Chapter 1

General Introduction

This chapter provides a general introduction to organic optoelectronics with a special focus on the solar cell and phototransistor technologies. In addition, this chapter defines the aims of this work and overviews the contents of the following chapters.

1-1. Organic Optoelectronic Devices

Organic optoelectronic devices are optical-to-electrical or electrical-to-optical converters based on organic semiconductors with a conjugated π-electron system. These devices can be highly flexible and lightweight, and thus are expected to be used in a wide vaiety of applications including those hard to access for the currently dominant silicon-besed devices. In addition, the rich backgrounds of organic chemistry and molecular simulation make it possible to precisely tune the molecular structure of organic semiconductors in order to render optimal properties for each specific application by design. Indeed, researchers have successfully developed several different types of organic devices including organic solar cells (OSCs) for energy harvesting,[1–2] organic light-emitting diodes (OLEDs) for illumination and display applications[3] and organic phototransistors (OPTs) for photosensing.[4]

The development of organic optoelectronic technology has already reached to the stage in which several companies have started or come close to commercialization of devices.[5] At the same time, there are still many problems and unknowns associated with such devices before they find wide use in society. The following sections overview the current status of OSC and OPT technologies which are the two main targets of this dissertaion research.

1-2. Organic Solar Cells

1-2-1. Introduction to the Solar Cell Technology

Global energy consumption is predicted to increase from 540×10^{18} J per year in 2010 to approximately 750×10^{18} J per year by 2030. The exhaustible fossil fuel (430×10^{18} J per year) accounts for ca. 80% of current energy supply.[6] Reducing of demand for fossil fuels can help to improve the global energy outlook and the environmental issues, and it is important to focus on alternative energy resources for meeting future global energy needs. Solar energy is the best alternative renewable energy source because the sun continuously irradiates the earth

with a huge available energy of 1470 × 10^{18} J per year which is much larger compared with other renewable energies such as wind (195 × 10^{18} J per year) and biomass (156 × 10^{18} J per year) as shown in Figure 1-1. Currently, the solar cells based on silicon, copper–indium–Selenide, cadmium–telluride are commercialized. In 2015, the solar cell market continued its global expansion, with a 20% growth bringing the market to 50 × 10^{9} W compared with the market in 2014 (40 × 10^{9} W).[7] In addition, the proportion of the solar power in the total energy supply significantly increased from 0.05% in 2010 to 0.45% in 2015. Thus, the photovoltaics is a power-generation method which can be expected to grow as a large energy source. However, the required device properties are different depending on the environment in which the solar cell is installed. For example, Si-based solar cells show a low power conversion efficiency (PCE) at a low irradiation intensity. Therefore, various types of solar cells are required to fit the needs of different environments.

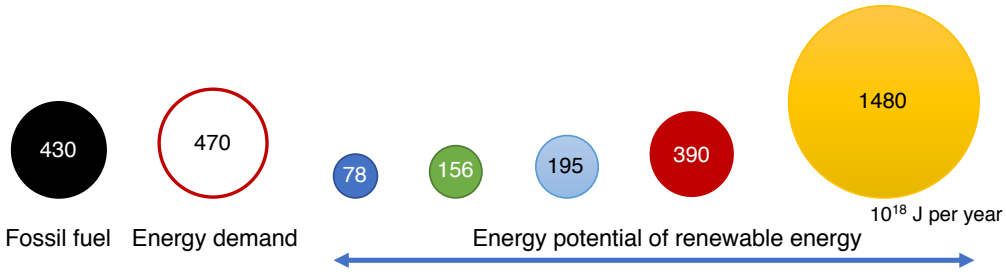

Energy	Utilizable energy potential / 10^{18} J per year
Solar radiation	1480
Geothermal	390
Wind	195
Biomass	156
Hydro/tide power	78
	Energy demand and supply / 10^{18} J per year
Global energy demand	470
Exhaustible fossil fuel	430 (accounting for 80% of total)

Figure 1-1. World's primary energy resources. Solar energy dwarfs all other energy resources whether they are non-renewable or renewable.[6]

1-2-2. Characteristics and Operating Principles of Organic Solar Cells

The active layer of OSCs is typically as thin as 100–300 nm. Thus, OSCs can be extremely flexible and lightweight, although these aspects are highly dependent on the materials used in other parts of the device and the module design. It is also expected for OSCs that low-cost manufacturing of large-area devices would be possible with solution-processable organic semiconductors by employing already well-established printing technologies. Another characteristics of OSCs is the high efficiengy under low-intensity light from, for example, a room lamp.[8] These characteristics allow the OSC to be a promising power source for small electronic appliances and wearable sensors, or for the on-site generation at buildings and houses.

The photon-to-electricity conversion in OSCs involves the following four elementary steps (Figure 1-2). Note that the organic photovoltaic active layer is usually a mixture of electron-donor (p-type) and electron-acceptor (n-type) semiconductors that are capable of transporting holes and electrons, respectively, as major charge carriers.

In the first step, either the p-type or n-type material absorbs the photons from sunlight to generate strongly bound hole–electron pairs called excitons (step ①). Since the generation of excitons depends on the number of absorbed photons, desirable materials are those able to absorb a wide range of solar spectrum with high absorption coefficients.

The second step involves diffusion of the excitons to the interface between p- and n-type materials (p–n interface) (step ②). It is preferable to form domains of each mateial with a radius of exciton diffusion distance (typically 5 to 20 nm in organic semiconductors) in the active layer. Larger-sized domains cause the quenching of excitons before reaching the p–n interface.[9]

The third step is the genaration of cherge carriers (i.e., holes and electrons) through charge transfer and charge separation at the p–n interface (step ③). Empirically, the energetic driving

force required for the charge transfer is represented by the energy difference between the lowest unoccupied molecular orbitals (LUMOs) of p- and n-type materials or that between the highest occupied molecular orbitals (HOMOs). It has been widely accepted that an energy difference of ca. 0.3 eV is minimally required to effect the generation of charge carriers.[10] It is also worth noting that the energy difference between the HOMO of p-type material and the LUMO of n-type material correlates very well with the open-circuit voltage (V_{OC}) of OSC.

Finally, the dissociated free holes and electrons are transported through the p- and n-type materials to anode and cathode electrodes, respectively (step ④). High and balanced mobilities of the both charge carriers are required for facilitating this step, which largely depend on the degree and directionality of intermolecular π–π stacking. In order to achieve a high PCE, all the four steps should proceed with high efficiency.

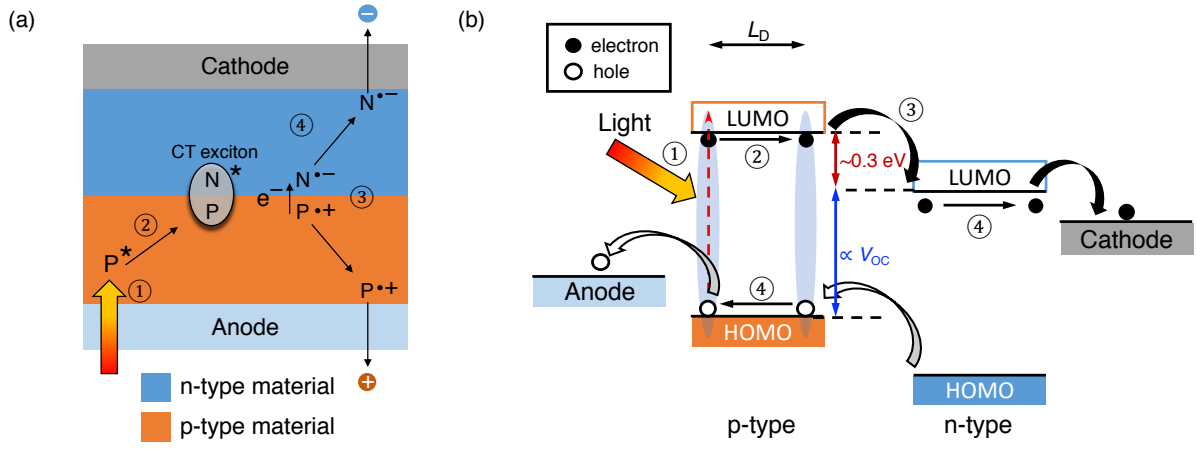

Figure 1-2. (a) Elementary processes of bilayer heterojunction OSCs. (b) Typical HOMO–LUMO energy diagram of OSCs.

1-2-3. Development and Current Status of Organic Solar Cells

This section describes the development of OSCs focusing on materials for the active layer, and then present issues of them. In 1986, Tang reported prototype OSC with bilayer structure, a planar-heterojunction (PHJ) device, consisted of Cu(II) phthalocyanine (CuPc) as a p-type material and perylene tetracarboxylic dye (PV) as an n-type material by vacuum deposition as shown in Figure 1-3a.[11] Since organic semiconductors generally have a low dielectric constant of 2–4, organic excitons have a strong coulomb-binding energy of a hole–electron pair (0.5–1 eV).[12] In this case, generated CT excitons reduced a binding energy and promoted charge separation at the p–n interface. Consequently, a PCE of PHJ device significantly increased from single-component OSCs to be 1%. After Tang's report, researchers developed materials for OSCs with suitable properties: phase separation between p- and n-type materials, light-absorption capacity, and charge transport.

In 1995, Halls et al. and Yu et al. reported solution processable BHJ devices based on MEH-PPV as a p-type polymer and CN-PPV as an n-type polymer as shown in Figure 1-3b.[13–14] The blend films showed nanometer-scale phase separation between p- and n-type polymers, which was favorable for exciton diffusion and dissociation. Those devices exhibited a PCE of 0.9% which is 20 times higher than in a single-component device with MEH-PPV and 100 times higher than in a CN-PPV device.

Fullerene was known as superior n-type materials because of the high electron affinity. However, it has a low solubility in common solvents. In 1995, Yu et al. demonstrated a BHJ device based on p-type MEH-PPH and a soluble fullerene derivative, [6,6]-phenyl-C_{61}-butyric acid methyl ester ($PC_{61}BM$), as an n-type material developed by Hummelen et al. (Figure 1-3c).[15–16] This device exhibited a PCE of 1.5% because of suitable exciton diffusion and dissociation in the the polymer:$PC_{61}BM$ blend.

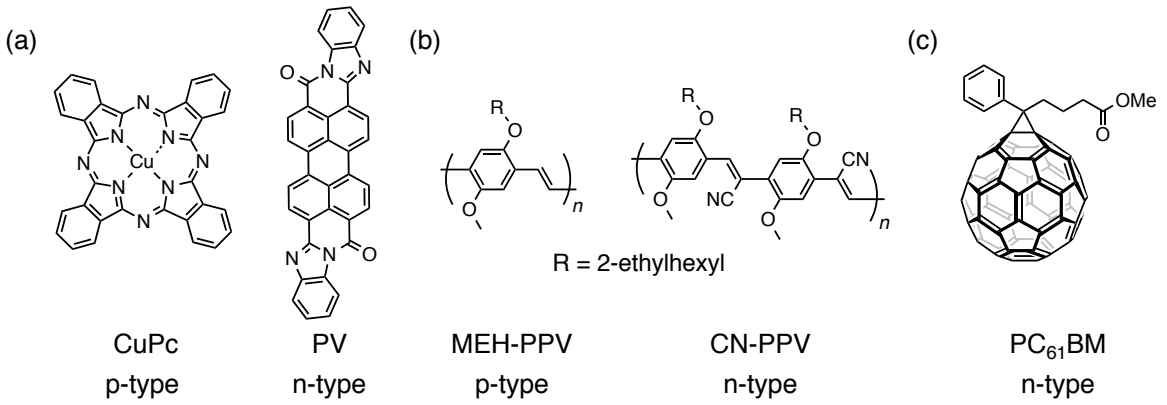

Figure 1-3. Molecular structures of OSC materials: (a) CuPc and PV, (b) PPV-based polymers and (c) $PC_{61}BM$.

In 2002, Schilinsky et al. reported a BHJ device combined poly(3-hexylthiophene) (P3HT) as alternative p-type material to the PPV-base polymer with $PC_{61}BM$ (Figure 1-4a). This device achieved a higher PCE of 2.8% than PPV-based OSCs.[17] In this system, many researchers have investigated an optimized phase separation between P3HT and $PC_{61}BM$ using post-annealing techniques. The most-used annealing method is the simple thermal annealing of active layers after spin-coating. An as-cast blend film showed too mixed to form efficient carrier paths. Thermal annealing induced the P3HT and $PC_{61}BM$ domain sizes to be increased up to optimized values corresponding to the exciton diffusion lengths in each material (3 nm and 30 nm, respectively). In 2005, Li et al. achieved a PCE of 4.5% with the thermal annealing at 110 °C for 10 min.[18]

Although P3HT was one of the most widely used p-type material in OSCs with $PC_{61}BM$, some novel p-type polymers have been developed as replacements for P3HT. Their narrower band-gaps absorb more light and lower HOMO levels increase the V_{OC} of the device compared with the P3HT system. In 2006, Mühlbacher et al. reported a narrow band-gap polymer, PCPDTBT, based on an electron-donor unit and an electron-acceptor unit into a π-conjugates (Figure 1-4b). It showed long-wavelength absorption due to intramolecular charge transfer. PCPDTBT-based BHJ device with [6,6]-phenyl-C_{71}-butyric acid methyl ester ($PC_{71}BM$) achieved a PCE of 3.5%.[19]

In the small molecule-based OSCs, Sun et al. reported that an OSC based on DTS($PTTh_2$)$_2$ as a p-type small molecule and $PC_{71}BM$ as an n-type material recorded a PCE of 6.7% which is higher than previous small molecular OSC (2–5.2%) in 2011.[20] DTS($PTTh_2$)$_2$ was based on acceptor–donor–acceptor (A–D–A)-type structure as shown in Figure 1-4c, leading to strong intramolecular charge transfer and narrow band gap. The mechanism is a similar strategy to narrow band-gap polymers. Such OSC applications of D–A material have been supported by detailed molecular design based on computational chemistry to control the frontier-orbital energies, and synthesis techniques using cross-coupling reactions which could combine a number of π-building blocks.[19–23]

As described earlier, the fullerene derivatives are known as superior n-type materials because of the high electron affinity, good electron mobility, and provision of suitable morphology. However, they have a poor absorption intensity in the visible to near-infrared (NIR) region. In order to overcome this absorption problem of fullerene derivatives, several non-fullerene n-type materials have been reported. For instance, in 2015, Lin et al. reported an A–D–A-based n-type material, ITIC, which was designed by the narrow band-gap strategy and restriction of a large aggregation using bulky substituents as shown in Figure 1-4d.[24] BHJ device based on PBDTTPD-HT as a p-type polymer and ITIC as an n-type material demonstrated a higher PCE of 10.2 % than that of $PC_{71}BM$-based OSC (PCE = 7.3%) because of controlled phase-separation and well-matched energy levels between PBDTTPD-HT and ITIC.

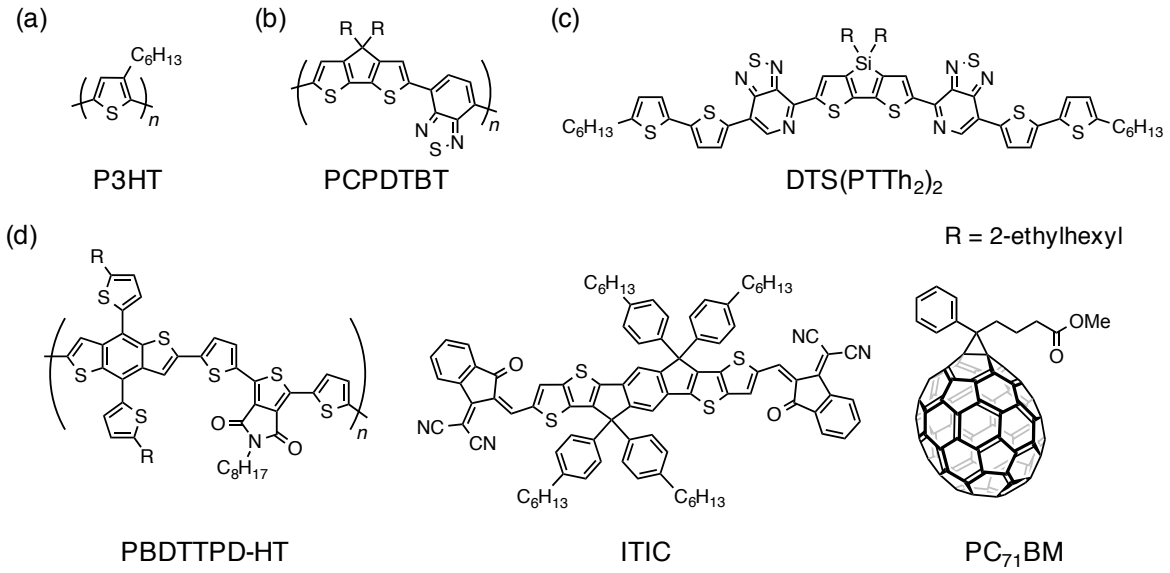

Figure 1-4. Molecular structures of OSC materials: (a) P3HT, (b) PCPDTBT, (c) DTS(PTTh$_2$)$_2$ and (d) PBDTTPD-HT, ITIC and PC$_{71}$BM.

Optimization of the electronic properties of the molecule and thin-film properties has played an essential role in improving the performance of OSC.

In 2017, the best PCE of OSC was reported as approximately 13% which is not an inferior value compared with dye-sensitized solar cells (PCE = 13%) and quantum-dot solar cells (PCE = 13.4%).[22, 25–26] On the other hand, perovskite solar cells and heterojunction with intrinsic thin-layer solar cell have been reported to attain higher PCEs (22.1% and 26.6%, respectively) compared with organic-based and quantum-dot solar cells.[27–28] However, these solar cells have some issues such as complex manufacturing processes or the use of harmful metals (Pb). In the case of OSCs, the active layer is easy to fabricate and harmless compared to the other solar cells. For commercialization of OSCs, it is necessary to improve PCE and to prevent degradation of the organic material.

1-3. Organic Phototransistors

1-3-1. Introduction to the Phototransistor Technology

Optoelectronic devices are used to convert optical energy into electrical energy. For applications with weak optical signals, the photodetectors with built-in amplification are used, which are called phototransistors. The phototransistor is a semiconductor device with high sensitivity to light irradiation. The phototransistors generate an output current in the order of milliamperes which is larger by ca. 1000 times compared to photodetectors without amplification such as photodiodes. The phototransistors based on Si semiconductor have applied in the field of photosensors such as detection of moving object, and biomedical monitoring devices, especially, wearable sensor devices.[29] Wearable sensors market is expected to grow from US$50 billion in 2017 to US$90 billion in 2020, at a compound annual growth rate of 22%. These sensors have poor adhesion to the human body because of their poor flexibility. Thus, inorganic phototransistors are not suitable for the biomedical wearable device.

1-3-2. Characteristics and Operating Principles of Organic Phototransistors

In a phototransistor based on the organic semiconductor, excellent bio-compatibility of organic materials is required for the wearable device. In addition, the wavelength sensitivity of the device can be modulated by the electronic structure of a molecule.

Organic phototransistor (OPT) has the same configuration of the bottom-gate-top-contact organic field-effect transistor (OFET) as shown in Figure 1-5.[31] It has three electrodes referred to as the source, drain, and gate. A heavily doped silicon wafer is often used as both the substrate and the gate electrode. A 300 nm-thick thermally grown SiO_2 layer is usually used as an insulating layer on the silicon surface. The organic active layer is deposited on the dielectric surface, and then the source and drain electrodes are deposited on top by vacuum evaporation through a shadow mask to give an OFET device.

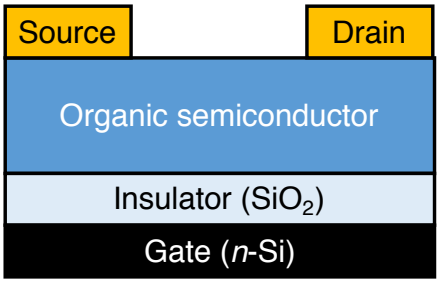

Figure 1-5. Illustration of bottom-gate-top-contact OFET devices.

In the operational mode of normal OFET the amount of current flowing (the source-drain current, I_{SD}) in the accumulated channel is controlled by the magnitude of gate voltage (V_G) at a given source to drain bias (V_{SD}) as shown in Figure 1-6b.[30] For OPTs the control of channel conductance is additionally enabled by the light absorption.[31] The channel of the device has not been formed at $V_G = 0$ V. Under illumination, a large number of photo-induced excitons are generated in the active layer. Then, they diffuse to the vicinity of the source or drain electrodes and are dissociated by the strong electric field near the interface between the organic material and the metal electrode. Under the action of the source-drain transverse electric field, photo-generated electrons drift and accumulate near the source while photo-generated holes drift and accumulate near the drain (Figure1-6c). It leads bent energy levels in the semiconductor. Compared with the situation in the dark, the hole injection barrier from the source apparently becomes lower due to the upward bent energy levels under illumination, and the threshold voltage (V_{th}) of the transfer characteristics becomes higher under illumination. It looks like that the field-effect characteristics of the device are activated. Increasing the negative V_G will result in the formation of a conductive channel by the accumulation of holes in the semiconductor. The photo-generated electrons dissociated at the source–organic interface quickly recombines with the holes injected by the source.

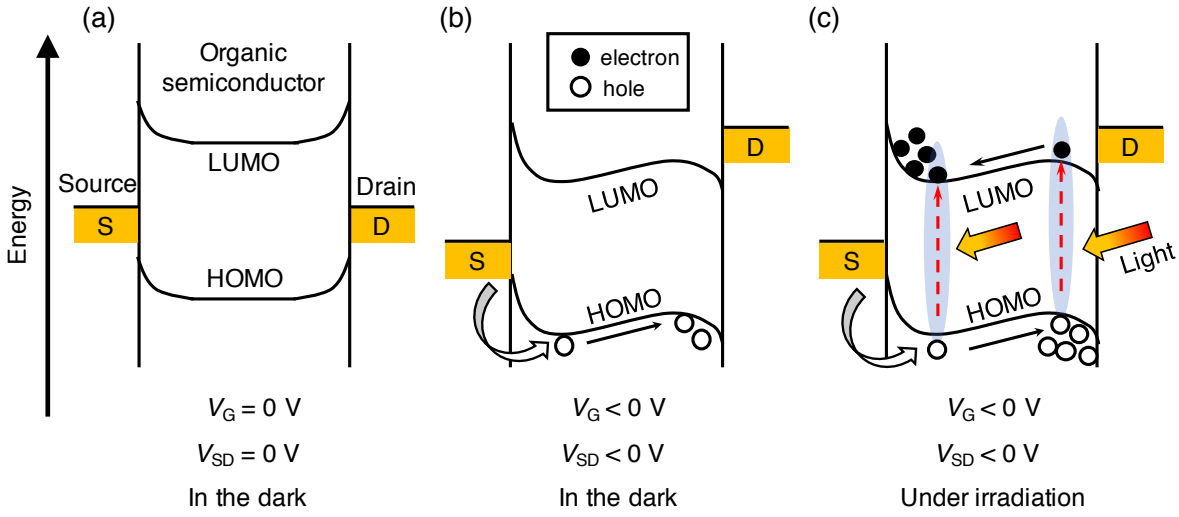

Figure 1-6. Schematic energy diagrams of OPT device: (a) no bias without light, (b) negative vias without light and (c) negative vias under irradiation.

1-3-3. Development and Current Status of Organic Phototransistors

This section describes the development of OPTs focusing on solution processed materials, and then present issues of them.

In the first report of OPTs, Narayan et al. demonstrated a photoresponse current on P3OT polymer-based OFET under irradiation (20 mW cm^{-2}) in 2001 (Figure1-7a).[4] It showed a photo-to-dark-current ratio (I_{ph}/I_{dark}) of ca. 100, which is lower than that for inorganic phototransistors.

Cho et al. reported that a four-arm shaped p-type material 4(HPBT) showed an I_{ph}/I_{dark} of 4 × 10^4 with a low power irradiation (30 μW cm^{-2}) in 2008 (Figure1-7b).[32] This high OPT performance, which is higher than that of amorphous Si-based phototransistors (I_{ph}/I_{dark} = 10^3), is attributed to their star-shaped molecular structure. The planar core part with four-armed π-conjugation in this molecule lead to effective absorption of incident light and efficient photo-carrier generation. This is the first report of OPTs based on solution-processed small molecule.

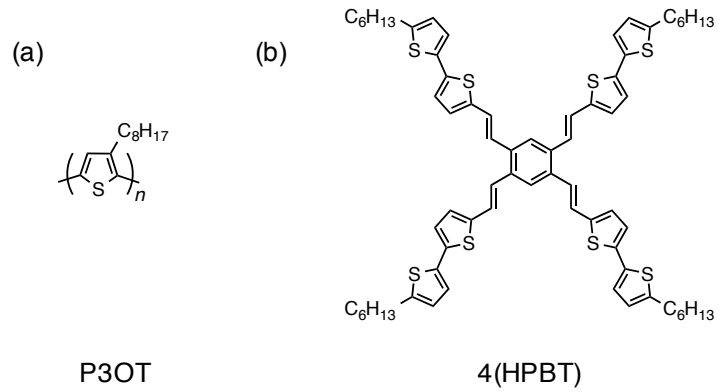

Figure 1-7. Molecular structures of OPT materials: (a) P3OT and (b) 4(HPBT).

The solution-processable OPTs are expected to show higher performances than inorganic phototransistors. These performances depend on the optoelectronic properties of the molecule in the active layer. However, the relationship between molecular structure and optoelectronic properties has many unknown aspects because of few reports.

The OPTs with a high photoresponse and flexibility are expected to be alternative sensors for inorganic phototransistors in the wearable device. Therefore, investigation of OPTs is worthwhile as fundamental research for supporting human health and comfortable life.

1-4. Aims and Outline of Research

The development of organic molecular dyes for optoelectronic applications has been supported by detailed molecular design based on computational chemistry to control the frontier molecular orbital energies and synthetic techniques using cross-coupling reactions for combining a number of π-building blocks. On the other hand, to improve the characteristics of the devices, it is also important to optimize and control not only the electronic properties of the molecule but also the properties of molecular assembly in the active layer. However, the structural factor of the molecule for the behavior of molecular assembly is not yet well understood.

The aims of this dissertation are to provide new knowledge regarding a correlation between the molecular structure and the thin-film properties affecting performances of the optoelectronic application. In each chapter, systematic evaluations are performed focused on different molecular structures: molecular linkage structure, the shape of molecule and structure of substituent.

As described in the previous sections, p-type materials were serving as the main photoabsorber. In order to construct the p-type materials with wide-range photoabsorption, porphycene-based extended π-systems are designed and synthesized. These optical properties and the potential of the conjugates as active-layer material in OSCs are discussed in Chapter 2.

The fullerene derivatives as n-type materials have been extensively investigated for their efficient BHJ-type OSC devices. However, one of the disadvantages for fullerene materials is a weak light absorption. In order to develop novel n-type materials which have strong light absorption ability, n-type materials with the 3D structure based on porphycene dimer are designed and synthesized. The 3D molecular architecture is expected to be enabled anisotropic electron transport. These 3D structures and the potential of the dimers as n-type materials in OSCs are described in Chapter 3.

Conjugated polymers with hydrophilic oligo(ethylene glycol) (OEG) chains have shown a smaller π–π and a higher OSC performance. However, the effect of hydrophilic chains on the small molecular system in the OSCs has been scarcely reported.[33–35] The comparison between the OEG and alkyl side chains in the small molecular DPP-based materials on single-crystal structure, thin film morphology and the photovoltaic properties are discussed in Chapter 4. In addition, the relationship between the substituents of the molecule and the photosensitivity on the OPTs has never been reported as far as I know. The OEG and alkyl chains effects on photosensitivity are also described in Chapter 4.

Finally, general conclusions of this dissertation are described in Chapter 5.

1-5. References

(1) Lipomi, D. J.; Tee, B. C.-K.; Vosgueritchian, M.; Bao, Z. Stretchable Organic Solar Cells. *Adv*. *Mater*. **2011**, *23* (15), 1771–1775.

(2) Kaltenbrunner, M.; White, M. S.; Głowacki, E. D.; Sekitani, T.; Someya, T.; Sariciftci, N. S.; Bauer, S. Ultrathin and Lightweight Organic Solar Cells with High Flexibility. *Nat*. *Commun*. **2012**, *3*, 770.

(3) Sekitani, T.; Nakajima, H.; Maeda, H.; Fukushima, T.; Aida, T.; Hata, K.; Someya, T. Stretchable Active-Matrix Organic Light-Emitting Diode Display Using Printable Elastic Conductors. *Nat*. *Mater*. **2009**, *8*, 494–499.

(4) Narayan, K. S.; Kumar, N. Light Responsive Polymer Field-Effect Transistor. *Appl. Phys. Lett.* **2001**, *79* (12), 1891–1893.

(5) Loo, Y.; McCulloch, I. Progress and Challenges in Commercialization of Organic Electronics. *MRS Bulletin* **2008**, *33* (7), 653–662.

(6) Wolfgang, L. *Application of Nanotechnologies in the Energy Sector*. Hessian Ministry of Economy, Transport, Urban and Regional Development: Wiesbaden, Germany, 2008; https://www.hessen-nanotech.de/mm/NanoEnergy_web.pdf.

(7) Gaëtan, M.; Mary, B. *SNAPSHOT OF GLOBAL PHOTOVOLTAIC MARKETS*. The International Energy Agency: Paris, France, 2016; http://www.iea-pvps.org/fileadmin/dam/public/report/statistics/IEA-PVPS_-_A_Snapshot_of_Global_PV_-_1992-2016__1_.pdf.

(8) Lee, H. K. H.; Li, Z.; Durrant, J. R.; Tsoi, W. C. Is Organic Photovoltaics Promising for Indoor Applications? *Appl. Phys. Lett.* **2016**, *108* (25), 253301–253306.

(9) Cowan, S. R.; Roy, A.; Heeger, A. J. Recombination in Polymer-Fullerene Bulk Heterojunction Solar Cells. *Phys. Rev. B* **2010**, *82* (24), 245207.

(10) De, S.; Pascher, T.; Maiti, M.; Jespersen, K. G.; Kesti, T.; Zhang, F.; Inganäs, O.; Yartsev, A.; Sundström, V. Geminate Charge Recombination in Alternating Polyfluorene Copolymer/Fullerene Blends. *J. Am. Chem. Soc.* **2007**, *129* (27), 8466–8472.

(11) Tang, C. W. Two-Layer Organic Photovoltaic Cell. *Appl. Phys. Lett.* **1986**, *48* (2), 183–185.

(12) Clarke, T. M.; Durrant, J. R. Charge Photogeneration in Organic Solar Cells. *Chem. Rev.* **2010**, *110* (11), 6736–6767.

(13) Halls, J. J. M.; Walsh, C. A.; Greenham, N. C.; Marseglia, E. A.; Friend, R. H.; Moratti, S. C.; Holmes, A. B. Efficient photodiodes from interpenetrating polymer networks. *Nature*

1995, *376* (6540), 498–500.

(14) Yu, G.; Heeger, A. J. Charge Separation and Photovoltaic Conversion in Polymer Composites with Internal Donor/Acceptor Heterojunctions. *J. Appl. Phys.* **1995**, *78* (7), 4510–4515.

(15) Yu, G.; Gao, J.; Hummelen, J. C.; Wudl, F.; Heeger, A. J. Polymer Photovoltaic Cells: Enhanced Efficiencies via a Network of Internal Donor-Acceptor Heterojunctions. *Science* **1995**, *270* (5243), 1789–1791.

(16) Hummelen, J. C.; Knight, B. W.; LePeq, F.; Wudl, F.; Yao, J.; Wilkins, C. L. Preparation and Characterization of Fulleroid and Methanofullerene Derivatives. *J. Org. Chem.* **1995**, *60* (3), 532–538.

(17) Schilinsky, P.; Waldauf, C.; Brabec, C. J. Recombination and Loss Analysis in Polythiophene Based Bulk Heterojunction Photodetectors. *Appl. Phys. Lett.* **2002**, *81* (20), 3885–3887.

(18) Li, G.; Shrotriya, V.; Huang, J.; Yao, Y.; Moriarty, T.; Emery, K.; Yang, Y. High-Efficiency Solution Processable Polymer Photovoltaic Cells by Self-Organization of Polymer Blends. *Nat. Mater.* **2005**, *4* (11), 864–868.

(19) Mühlbacher, D.; Scharber, M.; Morana, M.; Zhu, Z.; Waller, D.; Gaudiana, R.; Brabec, C. High Photovoltaic Performance of a Low-Bandgap Polymer. *Adv. Mater.* **2006**, *18* (21), 2884–2889.

(20) Sun, Y.; Welch, G. C.; Leong, W. L.; Takacs, C. J.; Bazan, G. C.; Heeger, A. J. Solution-Processed Small-Molecule Solar Cells with 6.7% Efficiency. *Nat. Mater.* **2011**, *11* (1), 44–48.

(21) Takimiya, K.; Osaka, I.; Nakano, M. π-Building Blocks for Organic Electronics: Revaluation of "Inductive" and "Resonance" Effects of π-Electron Deficient Units. *Chem. Mater.* **2013**, *26* (1), 587–593.

(22) Zhao, W.; Li, S.; Yao, H.; Zhang, S.; Zhang, Y.; Yang, B.; Hou, J. Molecular Optimization Enables Over 13% Efficiency in Organic Solar Cells. *J. Am. Chem. Soc.* **2017**, *139* (21), 7148–7151.

(23) Liu, Y.; Chen, C.-C.; Hong, Z.; Gao, J.; Michael Yang, Y.; Zhou, H.; Dou, L.; Li, G.; Yang, Y. Solution-Processed Small-Molecule Solar Cells: Breaking the 10% Power Conversion Efficiency. *Sci. Rep.* **2013**, *3* (1), 554–558.

(24) Lin, Y.; Wang, J.; Zhang, Z.-G.; Bai, H.; Li, Y.; Zhu, D.; Zhan, X. An Electron Acceptor Challenging Fullerenes for Efficient Polymer Solar Cells. *Adv. Mater.* **2015**, *27* (7), 1170–1174.

(25) Mathew, S.; Yella, A.; Gao, P.; Humphry-Baker, R.; Curchod, B. F. E.; Ashari-Astani, N.; Tavernelli, I.; Rothlisberger, U.; Nazeeruddin, M. K.; Grätzel, M. Dye-Sensitized Solar

Cells with 13% Efficiency Achieved Through the Molecular Engineering of Porphyrin Sensitizers. *Nat*. *Chem*. **2014**, *6* (3), 242–247.

(26) Sanehira, E. M.; Marshall, A. R.; Christians, J. A.; Harvey, S. P.; Ciesielski, P. N.; Wheeler, L. M.; Schulz, P.; Lin, L. Y.; Beard, M. C.; Luther, J. M. Enhanced Mobility CsPbI3 Quantum Dot Arrays for Record-Efficiency, High-Voltage Photovoltaic Cells. *Science Advances* **2017**, *3* (10), eaao4204.

(27) Yang, W. S.; Park, B.-W.; Jung, E. H.; Jeon, N. J.; Kim, Y. C.; Lee, D. U.; Shin, S. S.; Seo, J.; Kim, E. K.; Noh, J. H.; Seok, S. I. Iodide Management in Formamidinium-Lead-Halide-Based Perovskite Layers for Efficient Solar Cells. *Science* **2017**, *356* (6345), 1376–1379.

(28) Yoshikawa, K.; Kawasaki, H.; Yoshida, W.; Irie, T.; Konishi, K.; Nakano, K.; Uto, T.; Adachi, D.; Kanematsu, M.; Uzu, H.; Yamamoto, K. Silicon Heterojunction Solar Cell with Interdigitated Back Contacts for a Photoconversion Efficiency Over 26%. *Nat. Energy* **2017**, *2* (5), 17032.

(29) Guillaume, G.; Sébastien, C. *wearable electronics Sensors for wearable electronics & Mobile healthcare*, Yole Développement SA; Villeurbanne, France, 2015; http://www.yole.fr/iso_upload/News/2015/PR_MEMSforWearable_MarketOverview_YOLE_Jul2015.pdf.

(30) Mukherjee, B.; Mukherjee, M.; Choi, Y.; Pyo, S. Control Over Multifunctionality in Optoelectronic Device Based on Organic Phototransistor. *ACS Appl. Mater. Interfaces* **2010**, *2* (6), 1614–1620.

(31) Yao, B.; Li, Y.; Fang, Z.; Tan, Y.; Liu, S.; Peng, Y.; Xu, H. Investigation of the Source-Drain Electrodes/the Active Layer Contact-Effect on the Performance of Organic Phototransistor. *Synth*. *Met*. **2017**, *233*, 58–62.

(32) Cho, M. Y.; Kim, S. J.; Han, Y. D.; Park, D. H.; Kim, K. H.; Choi, D. H.; Joo, J. Highly Sensitive, Photocontrolled, Organic Thin-Film Transistors Using Soluble Star-Shaped Conjugated Molecules. *Adv. Funct. Mater.* **2008**, *18* (19), 2905–2912.

(33) Chen, X.; Zhang, Z.; Ding, Z.; Liu, J.; Wang, L. Diketopyrrolopyrrole-Based Conjugated Polymers Bearing Branched Oligo(Ethylene Glycol) Side Chains for Photovoltaic Devices. *Angew*. *Chem*. *Int*. *Ed*. **2016**, *55* (35), 10376–10380.

(34) Meng, B.; Song, H.; Chen, X.; Xie, Z.; Liu, J.; Wang, L. Replacing Alkyl with Oligo(Ethylene Glycol) as Side Chains of Conjugated Polymers for Close π–π Stacking. *Macromolecules* **2015**, *48* (13), 4357–4363.

(35) Chang, W.-H.; Gao, J.; Dou, L.; Chen, C.-C.; Liu, Y.; Yang, Y. Side-Chain Tunability

via Triple Component Random Copolymerization for Better Photovoltaic Polymers. *Adv. Energy Mater.* **2013**, *4* (4), 1300864–1300867.

Chapter 2

Synthesis and Photovoltaic Properties of Porphycene–Diketopyrrolopyrrole Conjugates

---

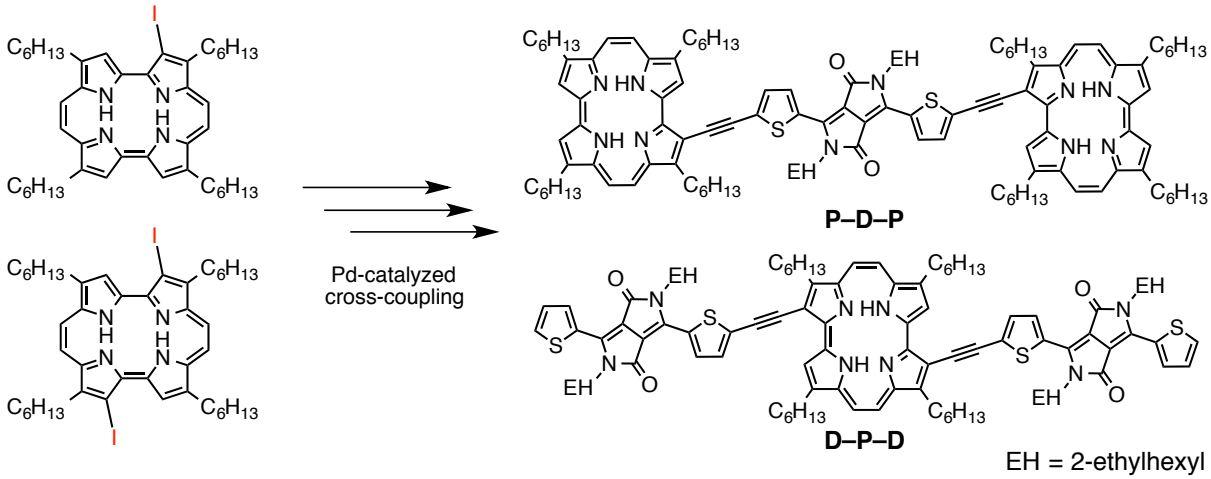

In this chapter, the selective iodination of porphycene and the optoelectronic and photovoltaic properties of porphycene–diketopyrrolopyrrole conjugates are described.

2-1. Introduction

The solar photon flux on the surface of the earth is highest at 500–900 nm (Figure 2-1).[1] Thus, primary requirements for well-performing photovoltaic materials include high photoabsorption capability at this range of wavelength. As for organic solar cells (OSCs), p-type semiconductors have been serving as main photoabsorber in the large majority of cases, while n-type materials have been limited mostly to fullerene derivatives that absorb only weakly, if not at all, over 400 nm.[2] Accordingly, much effort in the OSC research has been devoted to the development of p-type materials that are active in a wide range of the visible to near-infrared (NIR) region.[3–6] For example, Tang et al. reported a small-molecule p-type compound having the acceptor–donor–acceptor (A–D–A) configuration (3TBM, Figure 2-2a), in which benzodithiophene and methyldioxocyanopyridine were the donor and acceptor units, respectively.[3] This compound showed an absorption onset at 870 nm and afforded good power-conversion efficiencies (PCEs) of up to 6.3%. Other OSC materials with NIR absorption include squaraine derivatives and dipyrromethene boron difluoride (BODIPY) derivatives (Figure 2-2b).[7–9] However, the number of such compounds is rather limited, and their performance in OSCs has been only moderate in general. In another word, it remains a challenge to achieve a high-performance photoabsorber that covers a wide range of the visible to NIR region for use in OSCs.

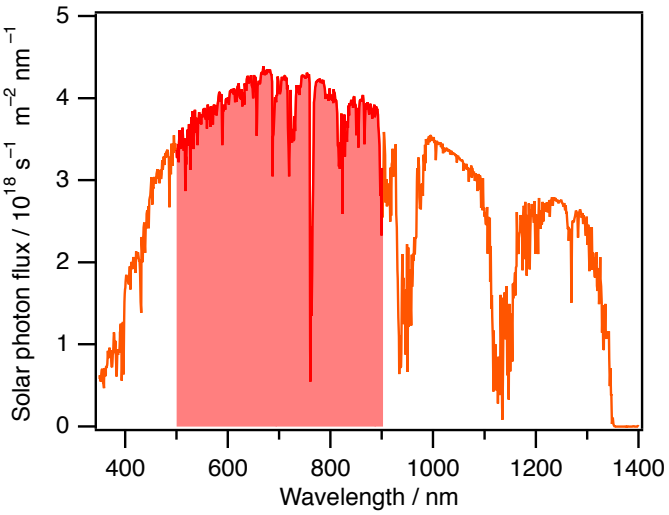

Figure 2-1. Solar photon flux spectrum. The red area is the highest photon flux at 500–900 nm.

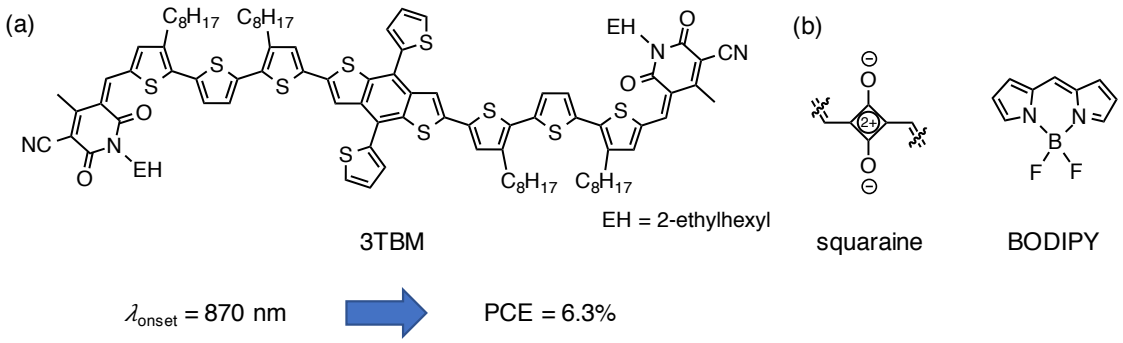

Figure 2-2. (a) Chemical structure of the A–D–A-type compounds reported by Tang et al.[3] (b) Chemical structures of squaraine and BODIPY.

Porphycene (Figure 2-3), a constitutional isomer of porphyrin, has relatively high absorptivity at 550–700 nm (Q-like band).[10–11] Therefore, its π-extension will easily lead to the achievement of efficient NIR absorbers. Furthermore, porphycene has a rigid and large π-framework, which is advantageous for forming effective charge-carrier paths in the condensed state. In view of these characteristics, porphycene will be a promising building unit of organic semiconductors for optoelectronic applications. Unfortunately, however, the chemical modification of porphycene has not been explored very well, resulting in few applications of

porphycene in organic electronics. Specifically, the so-far reported functionalized porphycenes are limited to sulfonated derivatives at the *β*-positions of the pyrrole moieties (SO_3-Pc, Scheme 2-1a),[12] *meso*-acetoxy derivatives (AcO-Pc, Scheme 2-1b)[13] and a few others including tetrabenzoporphycene.[14] While the sulfonate and acetoxy derivatives may be interesting for biomedical applications such as photodynamic therapy,[15–16] they are not ideal for constructing extended π-systems for optoelectronic applications—rather, halogenated derivatives that can be subjected transition-metal catalyzed cross-coupling reactions would be of high interest in the latter sense.

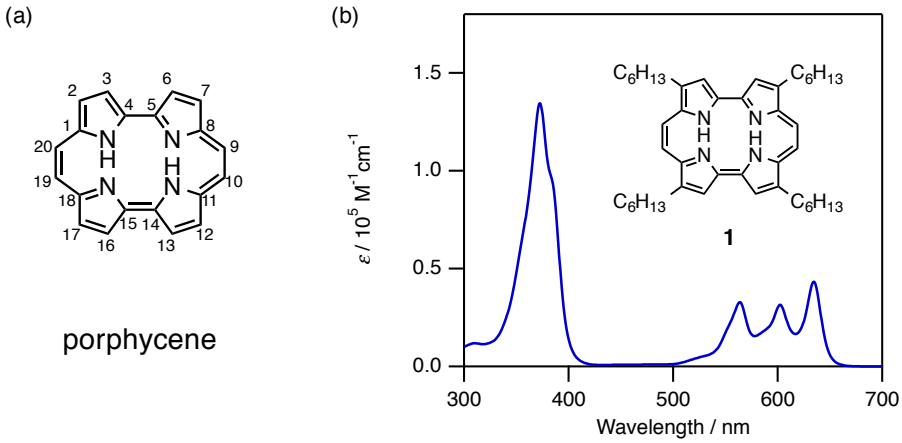

Figure 2-3. (a) Chemical structure of porphycene with its atom numbering; (b) Absorption spectra of 2,7,12,17-tetrahexylporphycene (**1**) in $CHCl_3$.

Scheme 2-1. Chemical structures of selected porphycene derivatives reported so far: (a) Sulfonates SO_3-Pc; (b) Acetates AcO-Pc.

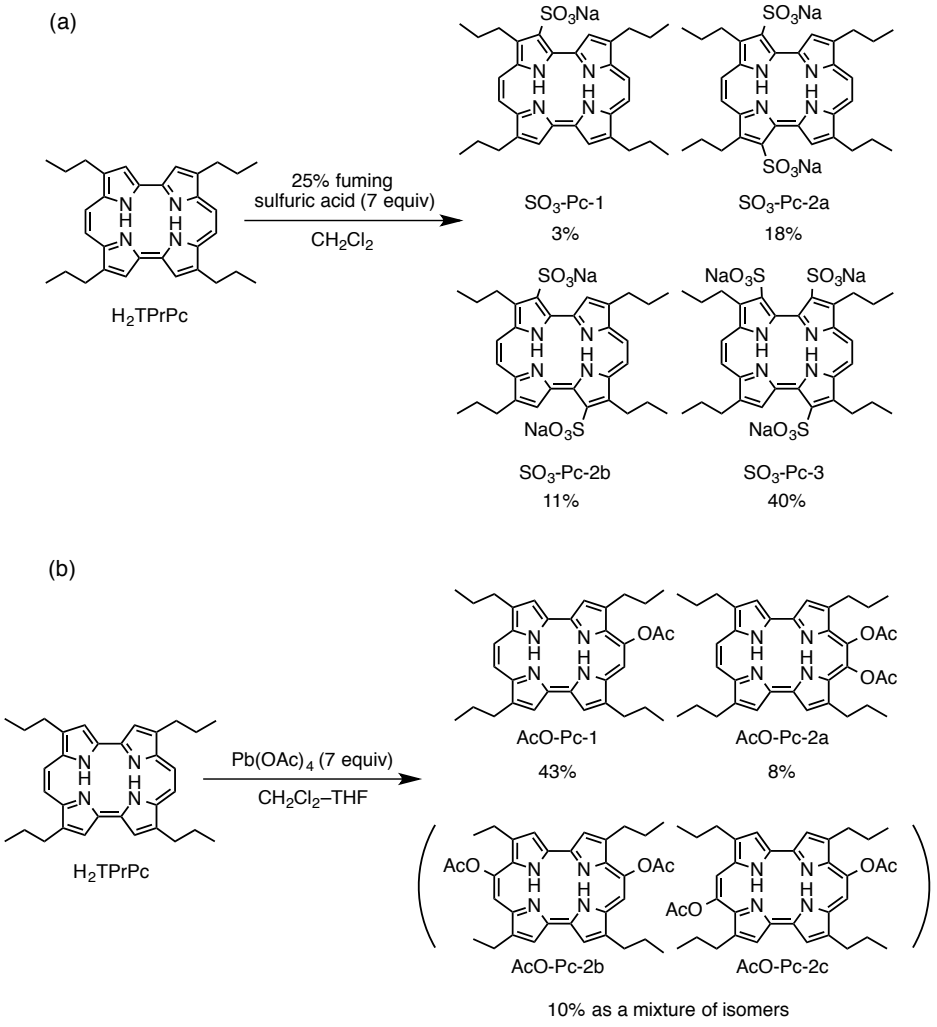

Taking into consideration of these backgrounds, this project aims for the establishment of selective and efficient iodination of porphycene, and for the synthesis of new porphycene-based photoabsorbers using the resulting iodides as key intermediates. The following sections in this chapter describe the controlled synthesis of mono and diiodoporphycenes **2** and **3a**, followed by preparation of conjugates comprising porphycene and dithienyldiketopyrrolopyrrole (ThDPP) shown in Figure 2-4. In addition, the potential of the conjugates as active-layer material in OSCs is examined in the latter part of this chapter.

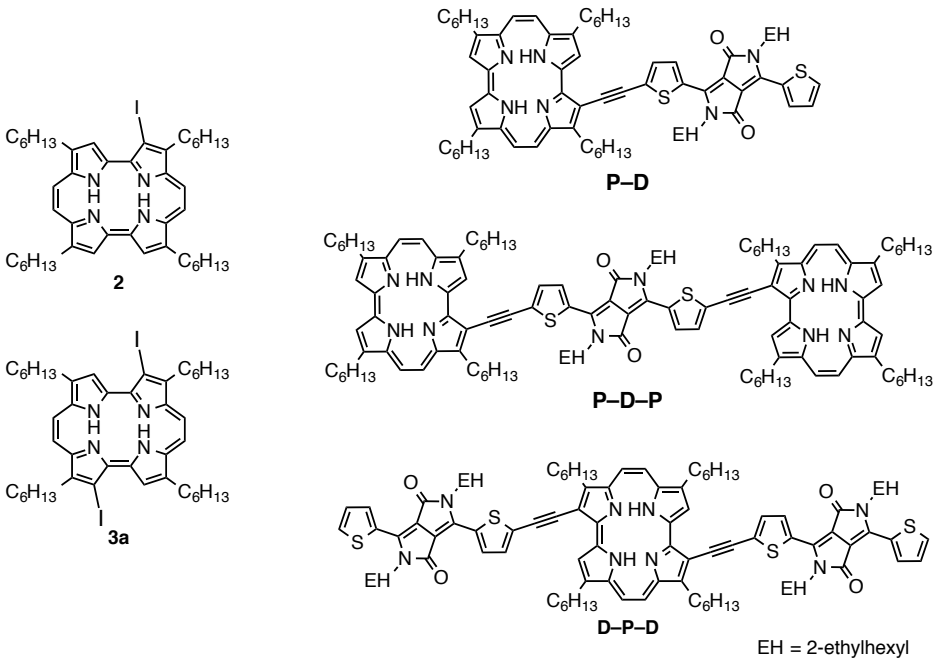

Figure 2-4. Chemical structures of iodoporphycenes **2** and **3a**, and porphycene–ThDPP conjugates synthesized in this work.

2-2. Establishing Controlled Iodination of Porphycene

There have been two preceding reports on the halogenation of porphycene. Shimakoshi et al. reported the bromination of 2,7,12,17-tetra-*n*-propylporphycene (H_2TPrPc) by bromine.[17] By changing the equivalence of bromine, mono-, di-, tri-, and tetra-brominated porphycenes Pc-Br, Pc-Br_2, Pc-Br_3, and Pc-Br_4 were prepared in different selectivities, respectively (Scheme 2-2a). Czerski et al. demonstrated the preparation of 2,7,12,17-tetra-*tert*-butyl-3,13-diiodoporphycene (H_2TBuPc) using 1.5 equiv of *N*-iodosuccinimide (NIS) as an iodonium cation source (Scheme 2-2b).[18] Unfortunately, their reaction gave the target 3,13-diiodoporphycene Pc-I_2 only in 12% yield as one of many other products including 3-bromo-13-iodoporphycene Pc-IBr (15% yield). The authors reasoned that the formation of brominated compounds was due to *N*-bromosuccinimide (NBS) included in the NIS reagent (95% purity) as a contaminant.

Scheme 2-2. Chemical structures of selected porphycene derivatives reported so far: (a) bromides Pc-Br_x; (b) iodidos Pc-I_2 and Pc-IBr.

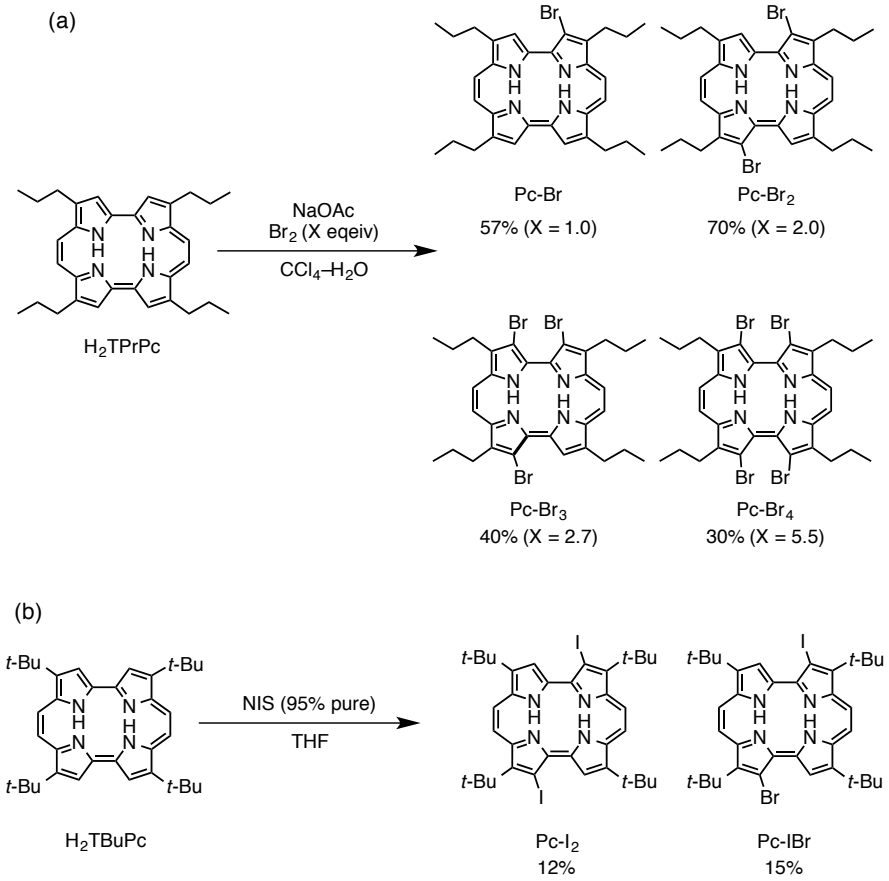

In this work, the iodination of porphycene with NIS was carefully optimized (Table 2-1). The reaction of 2,7,12,17-tetra-*n*-hexylporphycene (**1**) and NIS (98% purity, 1.1 equiv) in THF gave monoiodoporphycene **2** and diiodoporphycenes **3a** and **3b** (entry 1). While compound **2** was isolated by silica-gel column chlomatography in a yield of 36%, **3a** and **3b** could not be separated by the same method. Fortunately, the 3,13-diiodo isomer **3a** could be obtained in pure form in a yield of 12% by subjecting the **3a**/**3b** mixture to three repetitive recrystallizations from a $CHCl_3$ solution by adding hexanes. On the other hand, **3b** could not be isolated and its reaction yield (3%) was estimated based on the integrals of ^{1}H NMR peaks. As exemplified in Figure 2-5, compounds **3a** and **3b** can be distinguished in the aromatic proton region. Note that when the amount of NIS was increased to 2.5 equiv, porphycene **1** was not completely

consumed nor were tri- and tetra-iodinated porphycenes obtained (entry 4). These results suggest that the low reactivity induced by the steric hindrance associated with the large iodonium atom prevents multi-iodination of the porphycene framework.

The activation of NIS by trifluoroacetic acid (TFA)[19] or silica gel,[20] which are well-known efficient activators of NIS and NBS, was then attempted. Monoiodide **2** was predominantly obtained in 66% yield by the addition of an excess amount of TFA with 1.1 equiv of NIS (entry 2), while the use of 2.5 equiv of NIS with TFA gave diiodides **3a** and **3b** in 35% and 12% yields, respectively (entry 5). Interestingly, the yield of **3a** was increased to 54% by using silica gel as activator. In addition, the ratio between **3a** and **3b** varied from 35/12 with TFA (Figure 2-5) to 54/13 with silica gel. TFA not only activated NIS but also inactivated diiodonation reaction because the protonation of porphycene with TFA gave a porphycene dication.[21–23] On the other hand, silica gel provided hydrophilic reaction fields. Therefore, the efficient iodination of porphycene was accomplished by using NIS with either TFA or silica gel as activator to give the corresponding 3-iodo or 3,13-diiodo derivatives, respectively.

Table 2-1. Screening of reaction conditions for iodination of porphycene **1**.

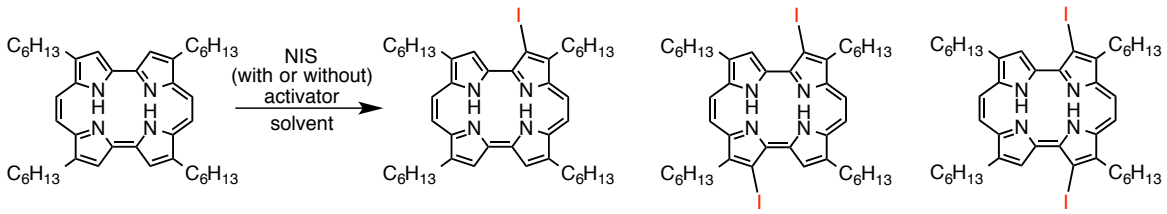

1 **2** **3a** **3b**

Entry	**1**:NIS equiv ratio	Activator	Solvent	Yield / %		
				2[a]	**3a**[a]	**3b**[b]
1	1.1	None	THF	36	12	3
2	1.1	TFA	THF	66	Trace	Trace
3	1.1	Silica gel	CH_2Cl_2	29	20	5
4	2.5	None	THF	42	7	1
5	2.5	TFA	THF	Trace	35	12
6	2.5	Silica gel	CH_2Cl_2	Trace	54	13

[a]Isolation yield. [b]Estimated based on ^{1}H NMR integrals.

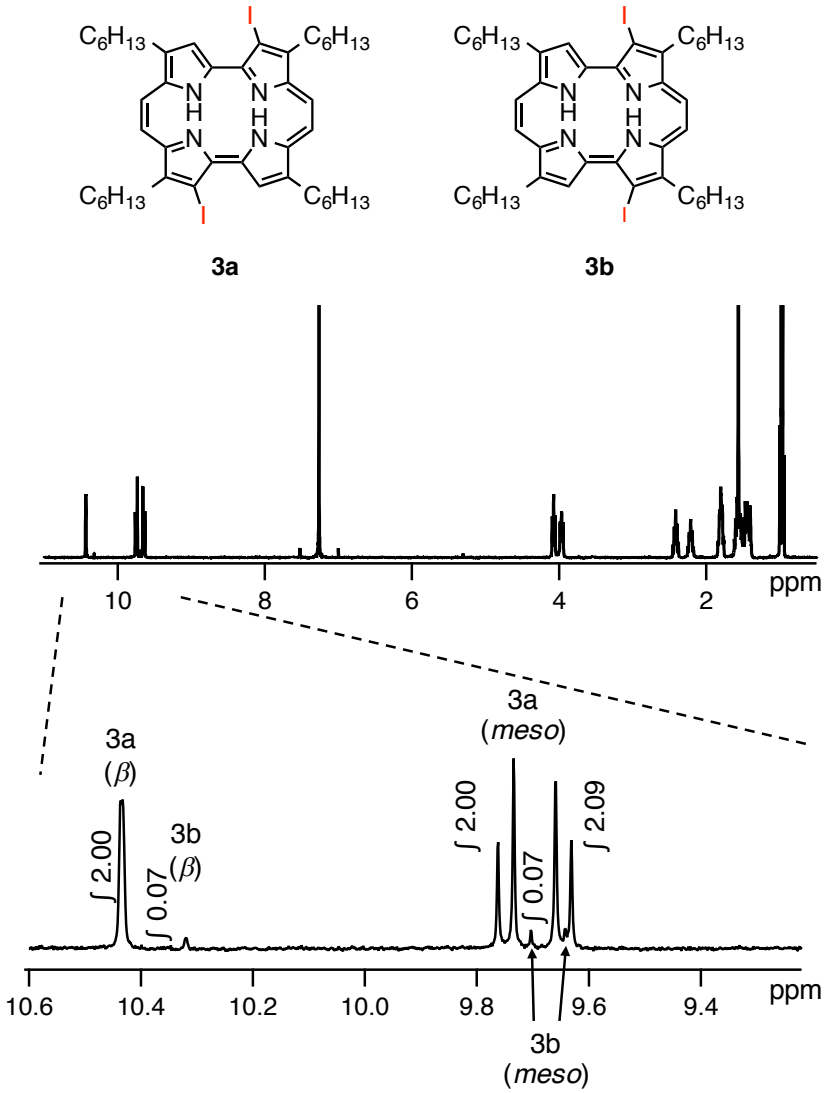

Figure 2-5. ^{1}H NMR spectrum (400 MHz, $CDCl_3$) of a mixture of diiodoporphycenes **3a** and **3b** obtained from the reaction of **1** with 2.5 equiv of NIS in THF.

The positions of the iodine atoms in **3a** were unambiguously elucidated by single-crystal X-ray diffraction analysis (Figure 2-6). The iodinated pyrroles show amine-type pyrrole of C2–N1–C5 bond angles with 107.0°, whereas other pyrroles are imine-type of C6–N2–C9 angles with 110.6°.[24] The side view shows that **3a** has a planar porphycene framework with a small mean-plane deviation of 0.040 Å, indicating that the steric repulsion between the iodine atom and the adjacent *β*-proton of pyrrole is minute.

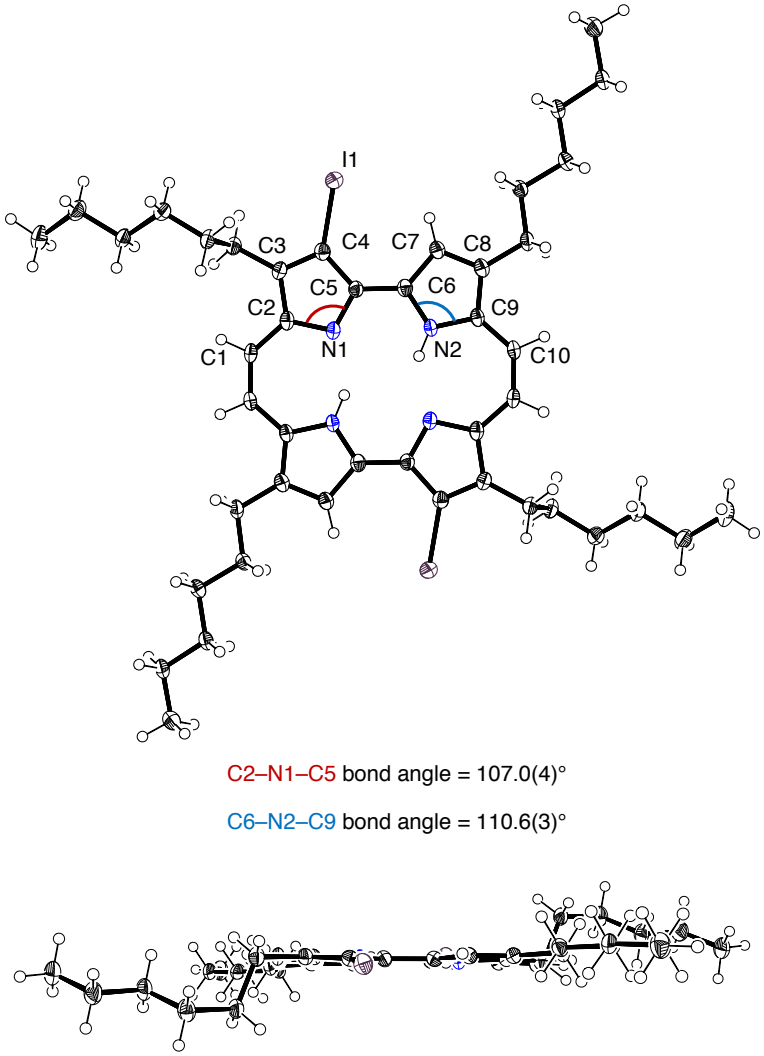

Figure 2-6. Molecular structure of **3a** determined by single-crystal X-ray diffraction analysis: (a) Top view; (b) Side view. Thermal ellipsoids represent 50% probability. A mean-plane deviation of a porphycene core unit is 0.040 Å.

Table 2-2. Crystal data and structure refinement for **3a**.

Empirical formula	$C_{44}H_{60}I_2N_4$
Formula weight	898.79
Temperature	103 K
Wavelength	0.71075 Å
Crystal sysmtem	triclinic
Space group	$P\bar{1}$
Unit cell dimensions	a = 7.7711(3) Å, b = 8.5531(4) Å, c = 16.1618(7) Å
	α = 75.4024(12)°, β = 89.3990(12)°, γ = 85.0834(11)°
Volume	1035.66(7) Å^3
Z	1
Density (calculated)	1.441 g cm^{-3}
Absorption coefficient	1.553 mm^{-1}
F(000)	458
Crystal size	0.100 × 0.040 × 0.010 mm^3
Theta range for data collection	3.07 to 25.36°
Index ranges	$-9 \leq h \leq 9$, $-10 \leq k \leq 10$, $-19 \leq l \leq 19$
Reflections collected	14676
Independent reflections	3805 (R_{int} = 0.0343)
Max. and min trasmission	0.985 and 0.678
Refinement method	Full-matrix least-squares on F^2
Data / restaraints / parameters	3805 / 0 / 228
Goodness-of-fit on F^2	1.128
Final R indices [$I > 2\sigma(I)$]	R_1 = 0.0386
R indices (all data)	wR_2 = 0.1071
Largest difference peak and hole	3.520 and −0.640 e$^-$ Å^{-3}

2-3. Development of Porphycene-Based Dyes for Organic Solar Cells

2-3-1. Molecular Design

The successful establishment of effective synthesis of monoiodide **2** and diiodide **3a** enables straightforward construction of porphycene-based extended π-systems via transition-metal catalyzed cross-coupling reactions. Along this line, three porphycene–ThDPP conjugates **P–D**, **P–D–P** and **D–P–D** with ethynyl linkages at the 3- or 3,13-positions of porphycene have been designed for use as active-layer materials in OSCs (Figure 2-7). The ThDPP chromophore has been chosen as a partner of porphycene, since it strongly absorbs around 450–600 nm at which porphycene has an absorption valley (Figure 2-8). In addition, the slim ethynyl linkage would allow the resulting extended π-systems to adopt fully planar conformations. This will bring about effective electronic interactions between the constituent chromophores, and may lead to narrowing of the optical band gap. Therefore, the conjugation of ThDPP and porphycene via the ethynyl linkage is likely to achieve wide photoabsorption range covering the visible to NIR region. In relation to this molecular design, ThDPP–porphyrin conjugate DPPEZnT-O was reported to exhibit a good absorption capability in the visible to NIR range, and to function as an excellent p-type material in bulk-heterojunction (BHJ) OSCs affording power conversion efficiencies (PCEs) of over 7% (Figure 2-9).[25]

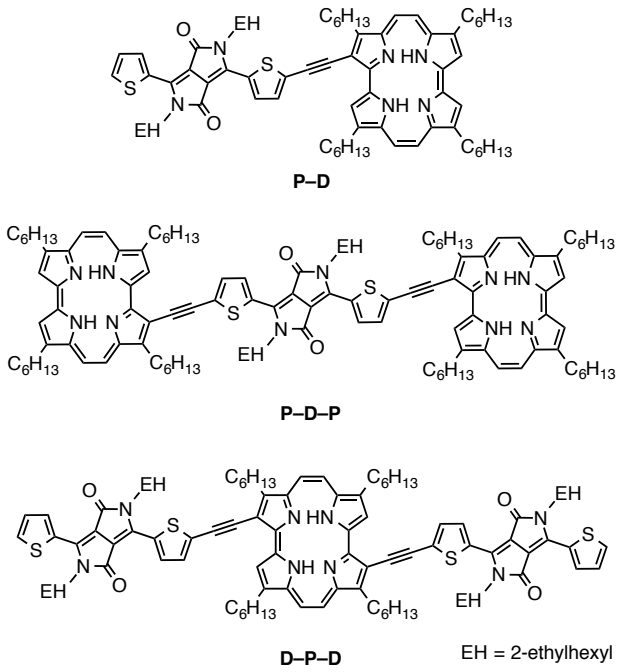

Figure 2-7. Structures of the porphycene–DPP conjugates **P–D**, **P–D–P** and **D–P–D**.

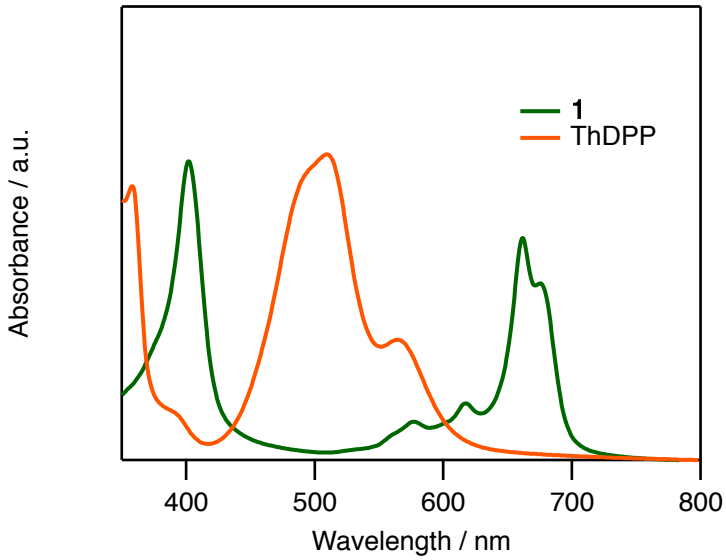

Figure 2-8. Absorption spectra of porphycene **1** and ThDPP in the thin film state.

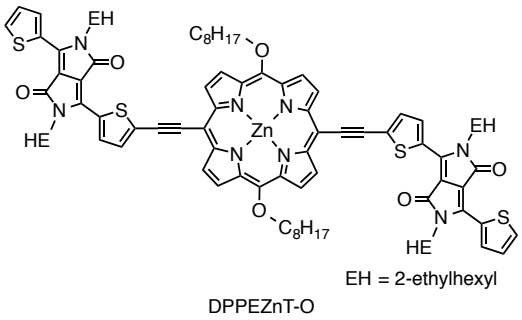

Figure 2-9. Molecular structures of porphyrin–ThDPP conjugate.

DFT calculations were performed on the designed molecules using the Gaussian 09 program package at the B3LYP/6-31G(d) level of theory.[26] Note that in these calculations the molecular structures were simplified by substituting the *n*-hexyl and 2-ethylhexyl groups with methyl as shown in Figure 2-10. The results show that the highest occupied molecular orbitals (HOMOs) of (**P–D**)′ and (**D–P–D**)′ localize mainly on the ThDPP moieties, while the lowest unoccupied molecular orbitals (LUMOs) on the porphycene units. Thus, porphycene behaves as electron acceptor, and ThDPP as electron donor in porphycene–ThDPP conjugates. (**P–D–P**)′ is slightly different from the other conjugates in that the LUMO is well delocalized over the entire molecule. Nevertheless, its HOMO is localized at the ThDPP unit, and thus the donor–acceptor relationship between ThDPP and porphycene is still valid in this case.

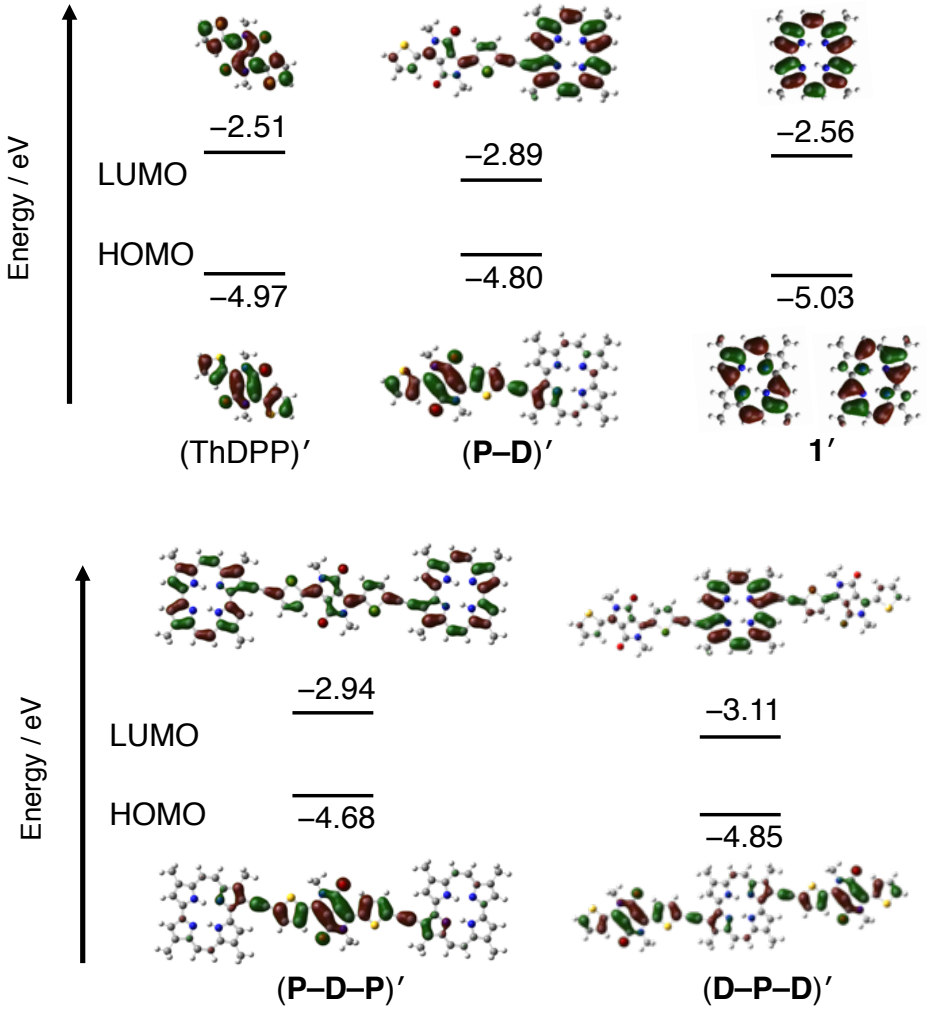

Figure 2-10. Frontier molecular orbital energies and their coefficient distributions of simplified model compounds of the three conjugates **P–D**, **P–D–P** and **D–P–D** and their building blocks **1** and ThDPP. Calculations were performed at the B3LYP/6-31G(d) level of theory.

2-3-2. Synthesis of Porphycene–Diketopyrrolopyrrole Conjugates

The synthesis of ethynyl-linked porphycene–ThDPP conjugates is shown in Scheme 2-3. Iodoporphycenes **2** and **3a** were subjected to Stille coupling with tributyl(trimethylsilylethynyl)tin to give **4** and **6** in 89% and 88% yields, respectively. The structure of **6** was confirmed by single-crystal X-ray diffraction analysis as shown in Figure 2-

11. Removal the trimethylsilyl groups of **4** and **6** by TBAF gave **5** and **7**, respectively. The porphycene–ThDPP dyad (**P–D**) was prepared from **5** by Sonogashira coupling with monobrominated ThDPP **8** in 55% yield. The porphycene–ThDPP triads, **P–D–P** and **D–P–D**, were synthesized similarly: **P–D–P** from **5** and **9** in 52% yield, and **D–P–D** from **7** and **8** in 75% yield, respectively. Structural characterization of these three porphycene–ThDPP conjugates were accomplished with ^{1}H NMR spectroscopy and high-resolution MALDI–TOF mass spectrometry.

Scheme 2-3. Synthesis of porphycene–ThDPP conjugates **P–D**, **P–D–P** and **D–P–D**.

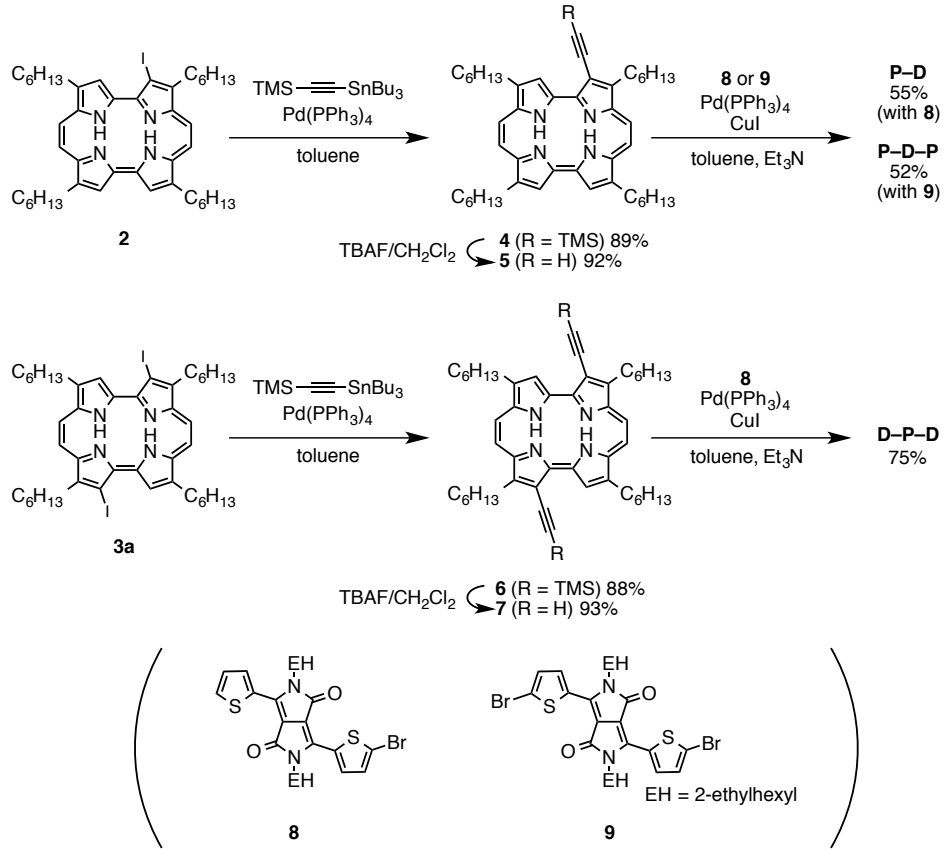

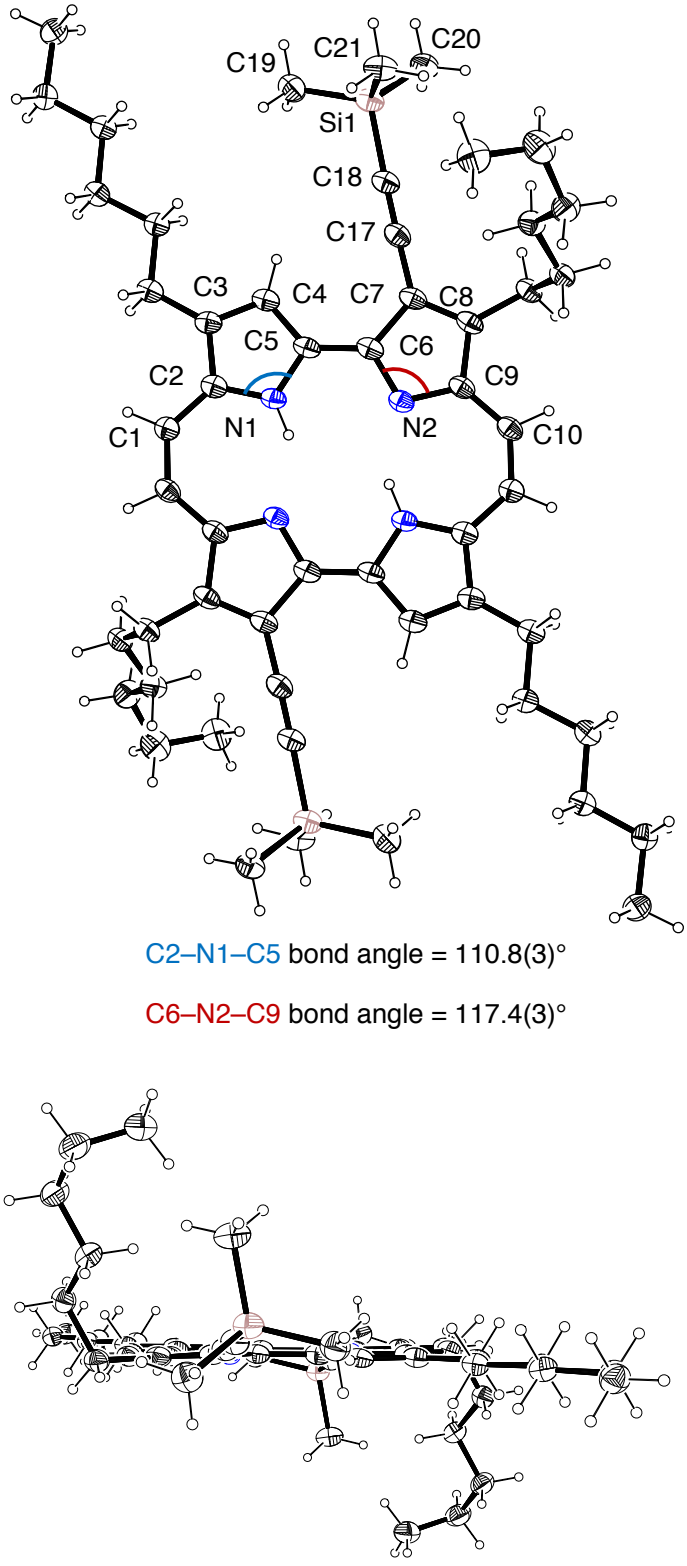

Figure 2-11. Molecular structure of **6** determined by single-crystal X-ray diffraction analysis. Thermal ellipsoids represent 25% probability. A mean-plane deviation of a porphycene core unit is 0.028 Å.

Table 2-3. Crystal data and structure refinement for **6**.

Empirical formula	$C_{54}H_{78}N_4Si_2$
Formula weight	839.41
Temperature	103 K
Wavelength	0.71075 Å
Crystal sysmtem	monoclinic
Space group	$P2_1/c$
Unit cell dimensions	a = 10.2001(13) Å, b = 6.7239(9) Å, c = 36.947(5) Å
	β = 93.358(3)°
Volume	2529.6(6) Å^3
Z	2
Density (calculated)	1.102 g cm^{-3}
Absorption coefficient	0.108 mm^{-1}
F(000)	916
Crystal size	0.400 × 0.070 × 0.010 mm^3
Theta range for data collection	3.08 to 25.33°
Index ranges	$-11 \leq h \leq 11$, $-7 \leq k \leq 7$, $-41 \leq l \leq 41$
Reflections collected	29504
Independent reflections	4012 (R_{int} = 0.1344)
Max. and min trasmission	0.999 and 0.434
Refinement method	Full-matrix least-squares on F^2
Data / restaraints / parameters	4012 / 0 / 276
Goodness-of-fit on F^2	1.128
Final R indices [$I > 2\sigma(I)$]	R_1 = 0.0897
R indices (all data)	wR_2 = 0.2136
Largest difference peak and hole	0.24 and −0.38 e$^-$ Å^{-3}

2-3-3. Optical and Electronic Properties

The UV–Vis absorption spectra of **P–D**, **P–D–P**, and **D–P–D** in $CHCl_3$ are shown in Figure 2-12. The absorption spectra of **1** and ThDPP in $CHCl_3$ are also provided in Figure 2-12 for reference. Porphycene **1** exhibits an intense Soret-like band with a peak top and a split shoulder peak at 372 and 386 nm, respectively, and broad Q-like band with moderate intensity three peaks at 564, 602 and 635 nm. ThDPP displays an absorption band at 450–570 nm. The maximum absorption peaks of the porphycene–DPP conjugates **P–D**, **D–P–D**, and **P–D–P** all show the Soret-like and Q-like bands in similar wavelength regions as observed for **1** and the absorption edges of **P–D–P** and **D–P–D** extend to 730 nm. The molar absorption coefficient of **P–D–P** at the Soret-like band is almost twice as high as those of **1**, **P–D**, and **D–P–D** because **P–D–P** contains two porphycene moieties in each molecule. The intensities of the Soret-like bands of **P–D** and **P–D–P** are similar to that of **1**. Interestingly, the intensities of the Q-like bands are significantly increased for all three porphycene–ThDPP conjugates compared to **1**. In particular, the molar absorption coefficient of **P–D–P** exhibits a maximum of 178 000 M^{-1} cm^{-1} at 653 nm. In addition, the absorption of the DPP components is not clearly evident within the range of 500–600 nm for all the three conjugates. These results indicate that electronic interactions occur between the ThDPP and porphycene moieties.

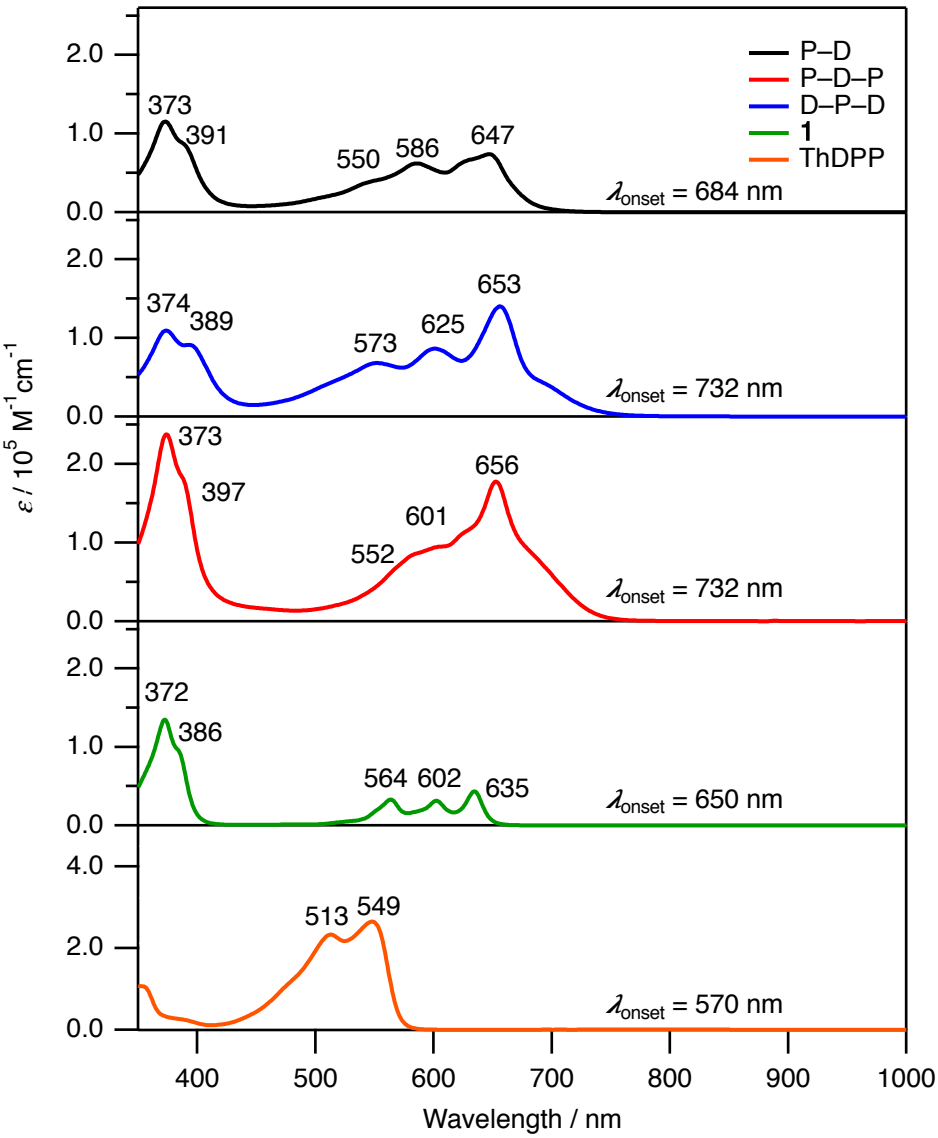

Figure 2-12. UV−Vis–NIR absorption spectra of **P–D** (black), **P−D−P** (red), **D−P−D** (blue) **1** (green), and ThDPP (orange) in $CHCl_3$ measured from low concentration: [**P–D**] = 6.1 × 10^{-7} M, [**P–D–P**] = 3.6 × 10^{-7} M, [**D–P–D**] = 7.3 × 10^{-7} M, [**1**] = 9.5 × 10^{-7} M and [ThDPP] = 7.0 × 10^{-7} M.

The absorption spectra of the conjugates, **1** and ThDPP in the thin-film state are shown in Figure 2-13. All the three porphycene–ThDPP conjugates show broader and red-shifted Q-like band in the thin-film state than in solution. The significant red-shift of the absorption band compared with solution states is attributed to the strong intermolecular π–π stacking in the solid state.[27] The absorption onsets of **1** and **P–D** in the thin-film state are approximately 40 nm red-shifted compared with those in solution. On the other hand, the absorption onsets of the thin

films of **P–D–P** and **D–P–D** are red-shifted by 90–100 nm. In addition, the absorption of the ThDPP components is evident at 500–600 nm for **P–D** and **D–P–D**. **D–P–D** has absorption maxima at 410, 533, 623, 679 and 772 nm and widely covers the visible to NIR region, which would be advantageous for use in OSCs.

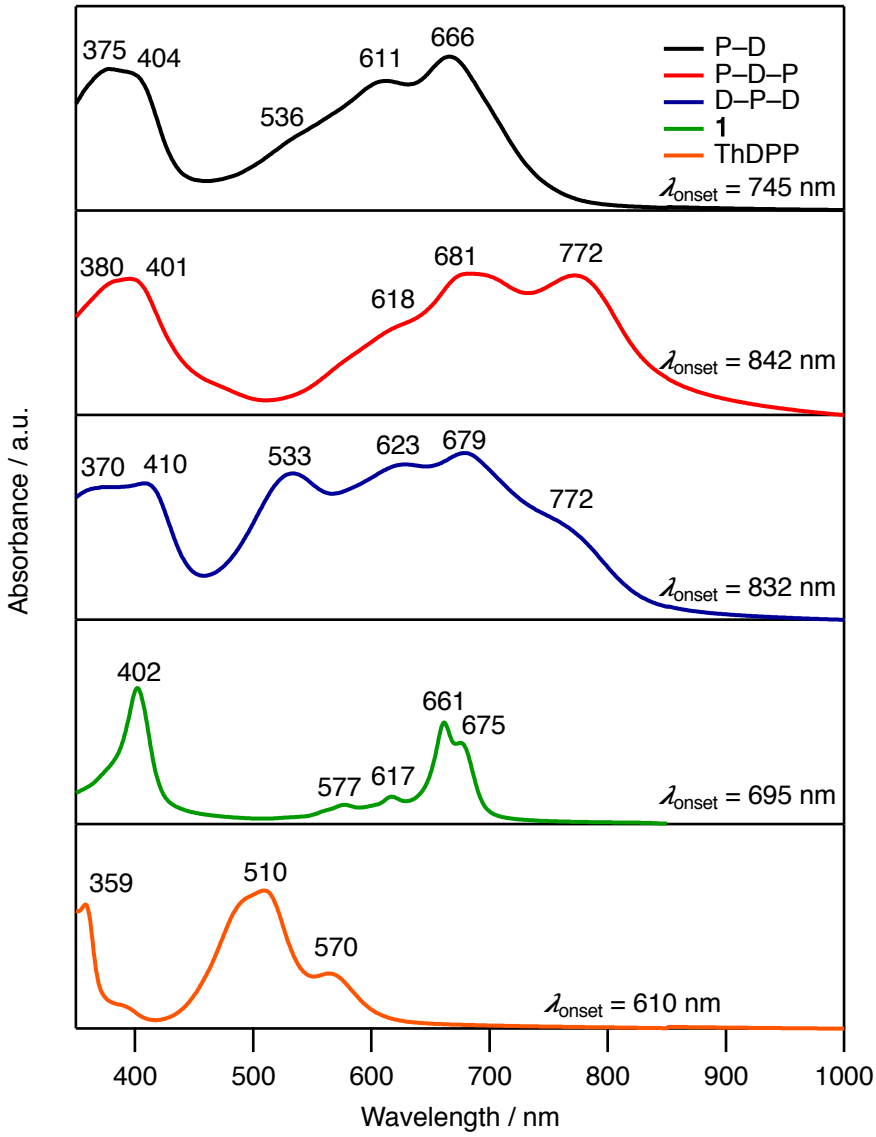

Figure 2-13. UV−Vis–NIR absorption spectra of **P–D** (black), **P−D−P** (red), **D−P−D** (blue) **1** (green), and ThDPP (orange) as thin film on glass prepared by spin-coating with a 5.0 mg mL^{-1} of solution in the $CHCl_3$ at 800 rpm for 30 s.

The electrochemical properties of the conjugates and reference compounds were studied by cyclic voltammetry (CV) and differential pulse voltammetry (DPV) in *o*-dichlorobenzene/acetonitrile (5:1) containing 0.1 M $^{n}Bu_4NPF_6$ at room temperature (Figure 2-14). The CV of reference compound **1** exhibits reversible redox processes at $E^{1/2}$ (vs Fc/Fc^{+}) = 0.47, –1.45 and −1.75 V. ThDPP shows reversible peaks at $E^{1/2}$ = 0.47 and −1.70 V. On the other hand, dyad **P–D** undergoes reversible two one-electron and a reversible one-electron oxidation at potentials of $E^{1/2}$ = 0.43 , 0.66 and 0.84 V, and its reversible reduction potentials of $E^{1/2}$ = −1.30, −1.52 and −1.75 V. Its first oxdation is observed a slightly lower compared with **1** and ThDPP, and its first reduction is less negative than that of **1** by 0.15 V. **P–D–P** exhibits reversible two two-electron and a one-electron reduction peaks and overlaped oxidation peaks. **D–P–D** shows reversible two one-electron and one two-electron oxidation peaks and two one-electron and one two-electron reduction peaks. The conjugates show broad redox peaks based on the interaction of porphycene and ThDPP units through the ethynylene linker.

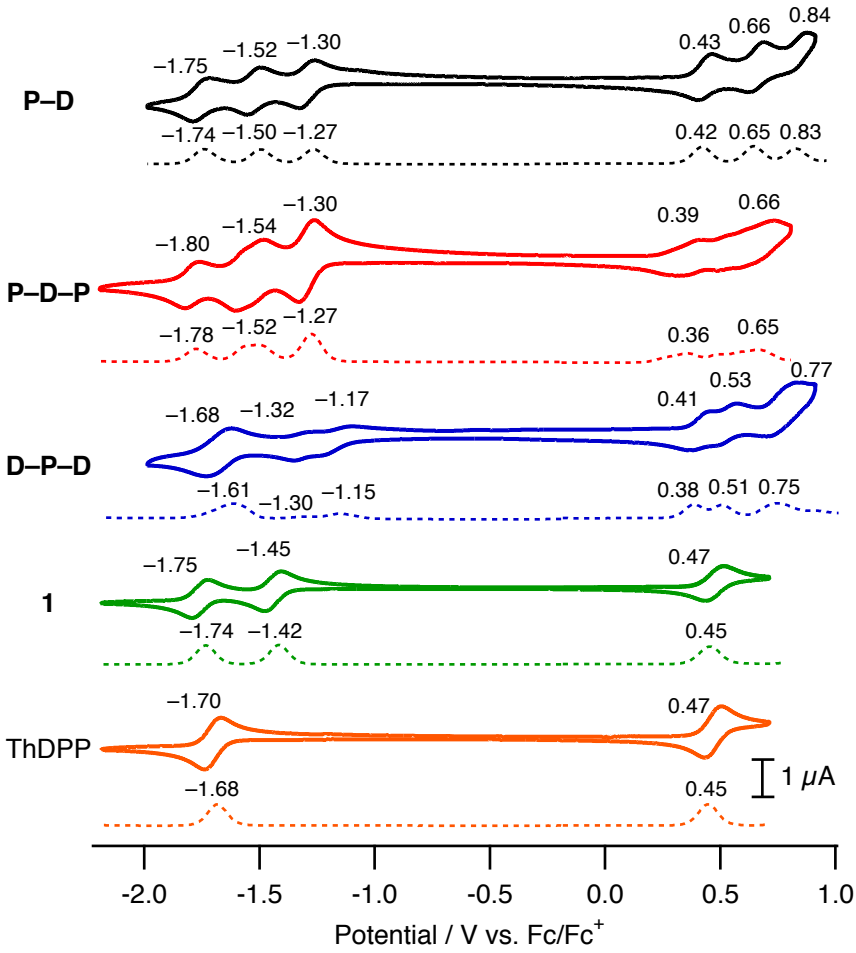

Figure 2-14. CVs (solid line) and DPVs (dotted line) of **P**−**D** (black), **P**−**D**−**P** (red), **D**−**P**−**D** (blue), **1** (green), and ThDPP (orange) in *o*-dichlorobenzene/acetonitrile (5:1) with 0.1 M $^{n}Bu_4NPF_6$. Scan rate = 100 mV s^{-1}. [**P**–**D**–**P** and **D**–**P**–**D**] = saturated, [**P**–**D**, **1** and ThDPP] = 1.0 mM. Working electrode: glassy carbon, counter electrode: Pt, reference electrode: $Ag/AgNO_3$.

In terms of organic electronic devices, determining the HOMO and LUMO energy levels of materials in thin films is important. For the OSC device, the energy difference between the HOMO of p-type material and the LUMO of n-type material correlates very well with the open-circuit voltage (V_{OC}) (Figure 1-2b).[28]

The HOMO levels of the conjugates in the thin-film state were estimated by the photoelectron spectroscopy in air to be −5.25–−5.29 eV (Figure 2-15). The optical energy gaps ($E_{g,\,opt}$) were calculated from the absorption onsets of the thin films to be 1.47–1.66 eV, and the LUMO levels were calculated as "HOMO + $E_{g,\,opt}$" to be −3.62–−3.80 eV. The HOMO and

LUMO levels in thin films and in solution are summarized in Table 2-4. These energy levels are higher than those of $PC_{61}BM$, a prototypical fullerene-based n-type material having HOMO and LUMO energy levels of −6.1 and −4.2 eV, respectively. Therefore, conjugates are expected to work as p-type material in OSCs with $PC_{61}BM$.

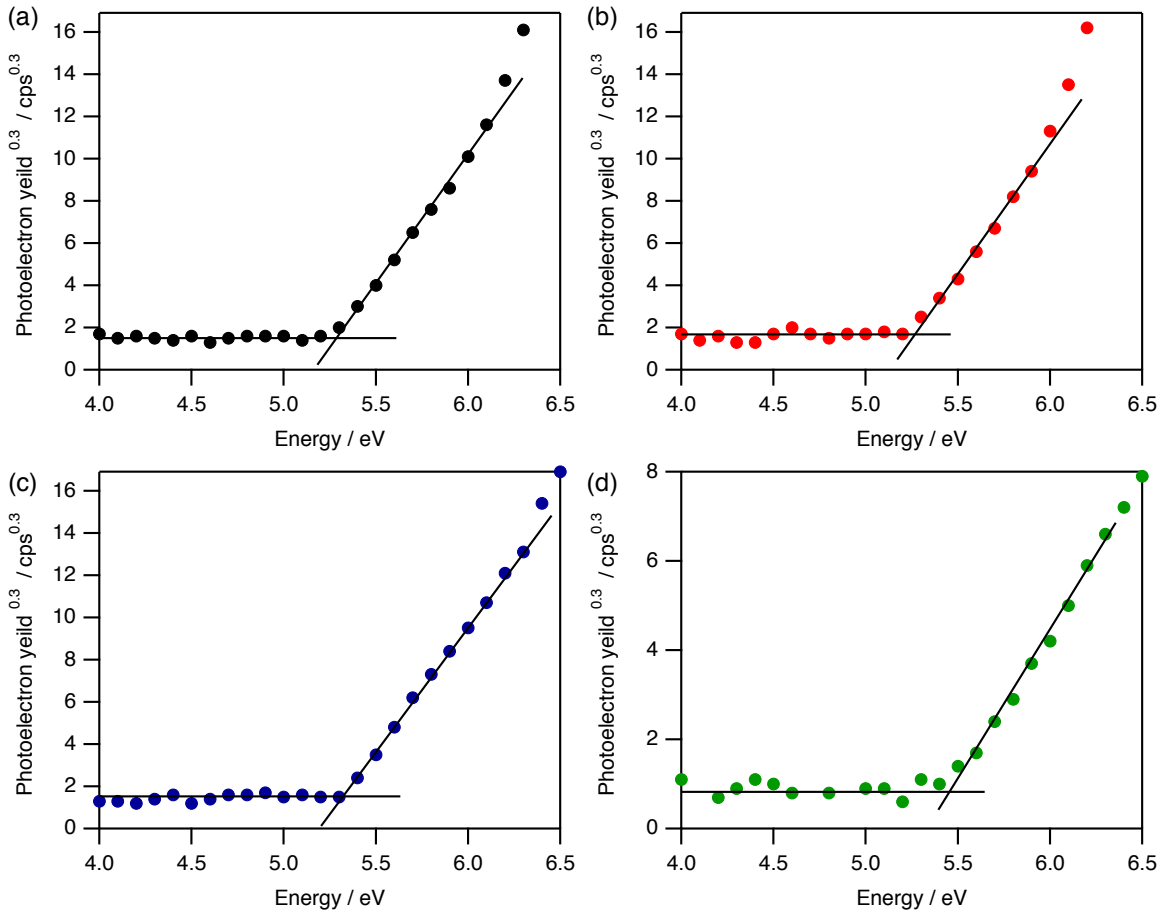

Figure 2-15. Photoelectron spectra of the neat film spin-coated on the ITO-glass: (a) **P–D**, (b) **P–D–P**, (c) **D–P–D** and (d) **1**.

Table 2-4. Electrochemical properties of compounds.

Compound	λ_{onset} / nm	$E_g{}^a$ / eV	HOMO^b / eV	LUMO^c / eV	HOMO$_{CV}{}^d$ / eV	LUMO$_{CV}{}^e$ / eV
P–D	745	1.66	−5.28	−3.62	−5.23	−3.50
P–D–P	842	1.48	−5.29	−3.81	−5.19	−3.50
D–P–D	832	1.45	−5.25	−3.80	−5.21	−3.63
1	695	1.78	−5.45	−3.67	−5.27	−3.35

[a]Calculated from λ_{onset}. [b]Determined by photoelectron spectroscopy in air, [c]LUMO = HOMO + E_g.[d]HOMO$_{CV}$ = −($E_{ox}{}^{1/2}$ + 4.80), [d]LUMO$_{CV}$ = −($E_{red}{}^{1/2}$ + 4.80).[29]

2-3-4. Evaluation of Organic Solar Cells

To investigate the effect of introduction of DPP moieties to porphycene on the photovoltaic performance, the bulk-heterojunction (BHJ) OSCs have been fabricated and evaluated comprising each of the porphycene–ThDPP conjugates as p-type material and $PC_{61}BM$ as n-type material. The BHJ films were incorporated into OSCs with a general device architecture of [ITO/PEDOT:PSS (30 nm)/p-type:$PC_{61}BM$/Ca (10 nm)/Al (70 nm)]. The weight ratios between p- and n-type materials were optimized for each conjugate and porphycene **1**. The optimum p:n ratio of **P–D**, **P–D–P**, **D–P–D** and **1** devices were assumed as 1:2, 2:3, 1:1 and 2:1, respectively (Table 2-5).

Table 2-5. Photovoltaic performance of OSCs based on p-type:$PC_{61}BM$ with different p:n weight ratios.

Device	p/n wt ratio	J_{SC} / mA cm^{-2}	V_{OC} / V	FF	PCE / %
P–D:$PC_{61}BM$	2:1	0.2	0.79	0.21	0.031
	1:1	0.6	0.78	0.23	0.11
	2:3	1.5	0.65	0.27	0.27
	1:2	1.3	0.65	0.36	0.30
P–D–P:$PC_{61}BM$	2:1	0.3	0.65	0.22	0.044
	1:1	0.3	0.61	0.23	0.35
	2:3	2.5	0.85	0.27	0.57
	1:2	2.1	0.63	0.27	0.35
	1:3	2.2	0.60	0.26	0.36
D–P–D:$PC_{61}BM$	2:1	0.09	0.83	0.19	0.014
	6:5	1.2	0.83	0.24	0.25
	1:1	4.3	0.82	0.49	1.74
	5:6	1.0	0.80	0.23	0.18
	1:2	0.6	0.62	0.14	0.048
1:$PC_{61}BM$	2:1	0.5	0.55	0.29	0.08
	1:1	0.5	0.44	0.29	0.07
	1:2	0.3	0.19	0.28	0.01

Active layers were prepared by spin-coating of a p:n blend solution in $CHCl_3$ (10 mg mL^{-1}) at 1500 rpm for 30 s.

Current density–voltage (*J–V*) curves of optimized devices under one sun illumination (AM1.5G, 100 mW cm^{-2}) are shown in Figure 2-16a and the photovoltaic parameters are summarized in Table 2-6. The external quantum efficiency (EQE) spectra of the OSC devices are also shown in Figure2-16b. The optimum active-layer thicknesses of **P–D**, **P–D–P**, **D–P–D** and **1**:$PC_{61}BM$ systems were experimentally determined as 72.5, 77.6, 66.8, and 76.7 nm, respectively.

Among the porphycene–ThDPP conjugates, **D–P–D** exhibits the best device performance with a J_{SC} of 4.3 mA cm^{-2}, V_{OC} of 0.82 V, FF of 0.49 and a corresponding PCE of 1.74%. In the case of **P–D** and **P–D–P** devices, reduced performances are observed (J_{SC} = 1.3 and 2.5 mA cm^{-2}, V_{OC} = 0.65 and 0.85 V, FF = 0.36 and 0.27, PCE = 0.30% and 0.57%, respectively). Series resistance (R_s) is one of the key parameters of OSC relating to the charge-transport property. The **D–P–D** device shows a lower R_s of 13.0 Ω cm^{-2} compared to the **P–D** and **D–P–D** devices (R_s = 116.0 and 150.3 Ω cm^{-2}, respectively). According to the DFT calculation as shown in Figure 2-10, **D–P–D** has a more delocalized HOMO compared with the other conjugates and may increase intermolecular HOMO overlap. It may have led to the improvement in the hole-transport property and the highest OSC performance in the conjugates. On the other hand, **1**:$PC_{61}BM$ blend device exhibits a significantly lower photovoltaic performance (J_{SC} = 0.5 mA cm^{-2}, V_{OC} = 0.55 V, FF = 0.25, PCE = 0.08%). The EQE spectra of the conjugates:$PC_{61}BM$ devices have onsets in the range of 740–830 nm which are longer than that of **1**:$PC_{61}BM$ device. It is consistent with the onsets of the broad absorption bands observed for the three conjugates.

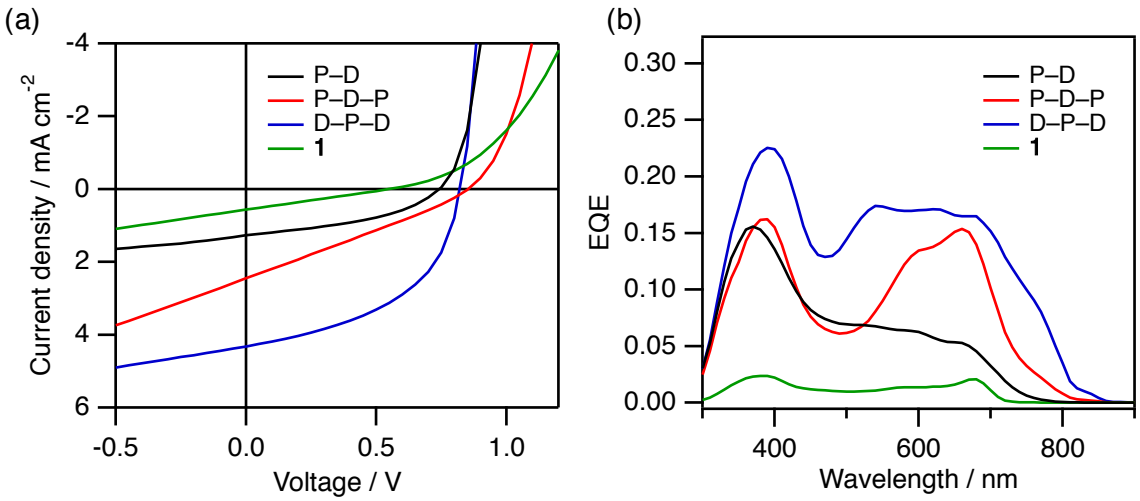

Figure 2-16. (a) *J–V* curves and (b) EQE spectra of the best-performing BHJ OSCs based on p-type:$PC_{61}BM$ blend.

Table 2-6. Photovoltaic parameters of optimized p-type:$PC_{61}BM$ blend.

Material	Thickness / nm	J_{SC} / mA cm^{-2}	V_{OC} / V	FF	PCE [a] / %	R_s / Ω cm^{-2}	R_{sh} / Ω cm^{-2}
P–D	72.5	1.3	0.65	0.36	0.30 (0.27 ± 0.01)	116.0	463.6
P–D–P	77.6	2.5	0.85	0.27	0.57 (0.54 ± 0.02)	150.3	374.6
D–P–D	66.8	4.3	0.82	0.49	1.74 (1.72 ± 0.02)	13.0	782.0
1	76.7	0.5	0.55	0.25	0.08 (0.07 ± 0.01)	778.4	966.0

[a]Highest values followed by averages and standard deviation of four devices in parentheses.

2-3-5. Film Morphology

To understand the difference of photovoltaic performances, the film morphology and crystallinity of the blend films were investigated by atomic force microscope (AFM) (Figure 2-17) and out-of-plane X-ray diffraction (XRD) (Figure 2-18). AFM height images of **P–D**, **P–D–P** and **1** films display larger grains which lead to poor exciton diffusion and dissociation at the p–n interface, since the exciton diffusion length in organic materials is limited to 5–20 nm.[30] It suggests that the porphycene unit show a stronger tendency for self aggregation. On the other hand, **D–P–D** forms smaller grains of approximately 20 nm and a smoother surface compared with other films. It indicates that the good miscibility of **D–P–D** with $PC_{61}BM$ is presumably owing to a favorable balance between self aggregation induced by π–π stacking and compatibility with $PC_{61}BM$ owing to the alkyl chains.

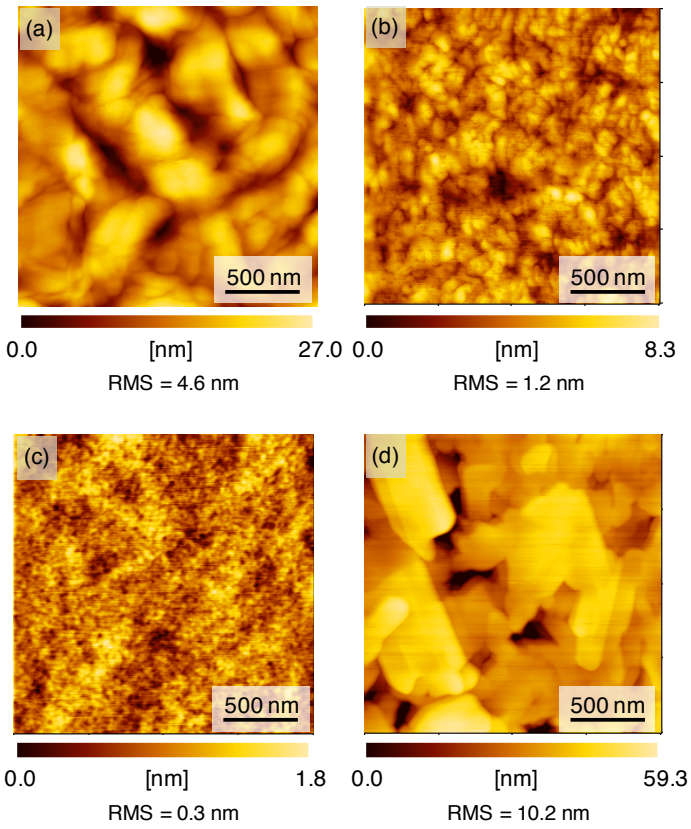

Figure 2-17. AFM height images of blend films on ITO/PEDOT:PSS: (a) **P–D**:$PC_{61}BM$, (b) **P–D–P**:$PC_{61}BM$, (c) **D–P–D**:$PC_{61}BM$ and (d) **1**:$PC_{61}BM$. The scan size for all images is 2 μm × 2 μm.

The XRD patterns of all blend films show diffraction peaks at $2\theta = 5.0–6.0^{o}$ ($d = 17.8–14.7$ Å) which correspond roughly to the length of the shorter molecular axis estimated from the optimized molecular structures as shown in Figure 2-19. These results seem that the porphycene units form edge-on-like orientation in the out-of-plane direction as shown in Figure 2-20, and **1** has a polymorphism in the thin-film state.

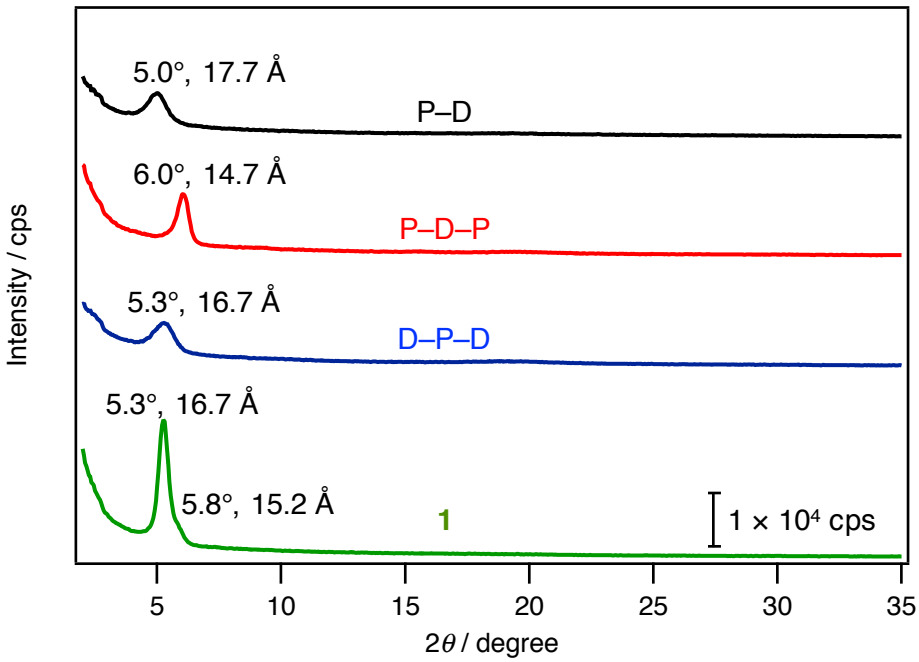

Figure 2-18. XRD patterns of BHJ blend films on ITO/PEDOT:PSS: **P–D**:$PC_{61}BM$ (black), **P–D–P**:$PC_{61}BM$ (red), **D–P–D**:$PC_{61}BM$ (blue) and **1**:$PC_{61}BM$ (green).

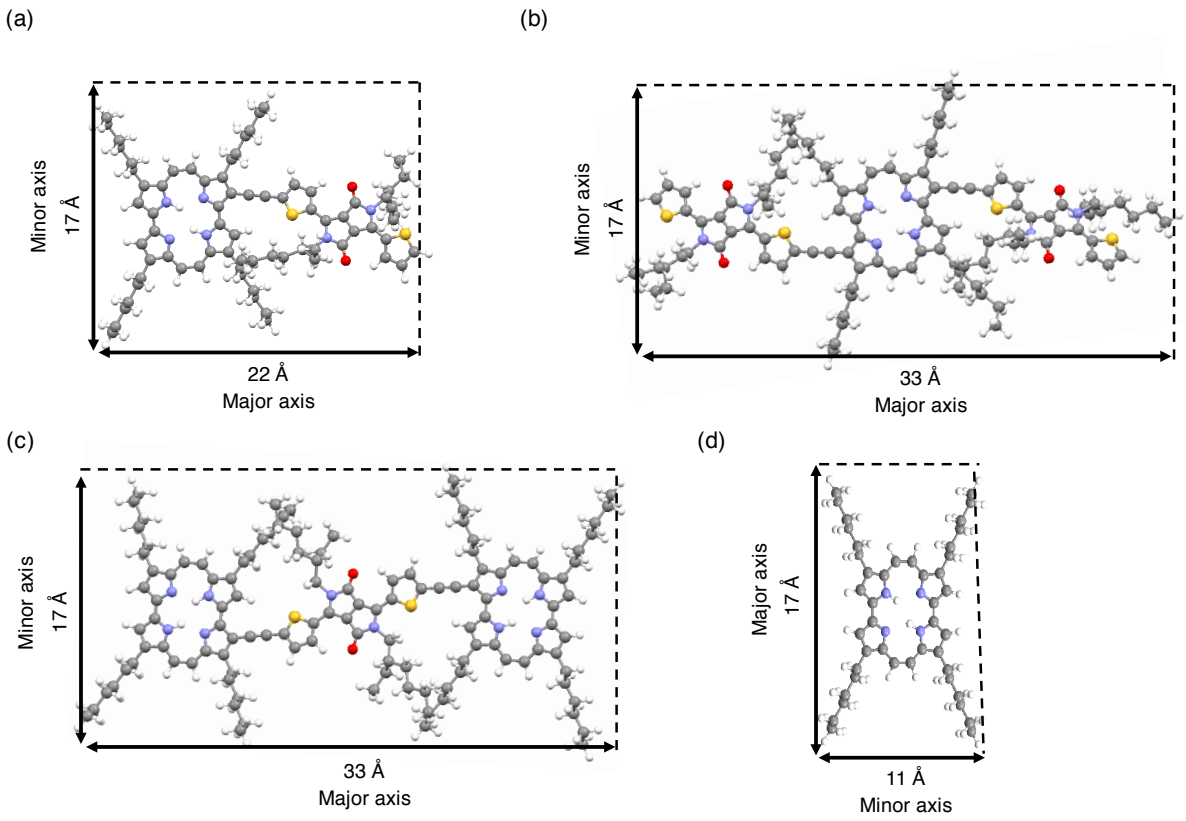

Figure 2-19. Optimized molecular structure of porphycenes calculated by MM2 molecular dynamics simulations: (a) **P–D**, (b) **P–D–P**, (c) **D–P–D** and (d) **1**.

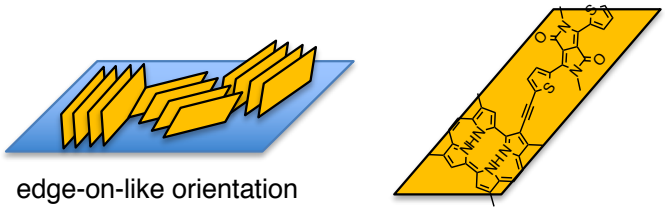

Figure 2-20. Illastration of edge-on-like orientation of porphycene derivatives.

The BHJ films were also investigated with two-dimensional glazing-incidence wide-angle X-ray diffractometry (2D GIWAXD). All the samples containing porphycene–ThDPP conjugates show a weak halo at $q = 0.36–0.50$ Å^{-1} ($d = 17.4–12.6$ Å) (Figure 2-21). Here again, these *d*-values are far from both the lengths of long molecular axes (ca. 22 Å, Figure 2-19) and π–π stacking distance (typically around 3.5 Å), while they are similar to the lengths of short molecular axes (Figure 2-19). Thus, the weak halos suggest that poorly defined stackings along

the short molecular axes exist without specific orientation. In addition, there is no clear diffraction derived from crystalline $PC_{61}BM$ domains which typically appears at q = 1.4 $Å^{-1}$.[31] These observations indicate low crystallinity of the blend films.

On the other hand, the **1**:$PC_{61}BM$ blend film shows a strong diffraction spot in the out-of-plane direction at q_z = 0.38 $Å^{-1}$ (d = 16.5 Å) associated with a relatively sharp ark-shaped diffraction. The d-value well correlates to the longer molecular dimension of **1** in a fully extended conformation (Figure 2-19d). Therefore, this diffraction pattern can be assigned to the order along the long molecular axis of **1** that preferentially, but not perfectly, orients in the out-of-plane direction. In other words, molecules of **1** prefer to arrange in an edge-on mode in the BHJ layer. Another halo at q = 1.75 $Å^{-1}$ (d = 3.59 Å) is also noticeable, which can be assigned to the π–π stacking and is not clearly observed in the cases of porphycene–ThDPP conjugates. The higher crystallinity of **1** may be ascribed to the smaller molecular size enabling smoother rearrangement of molecules during the deposition process.

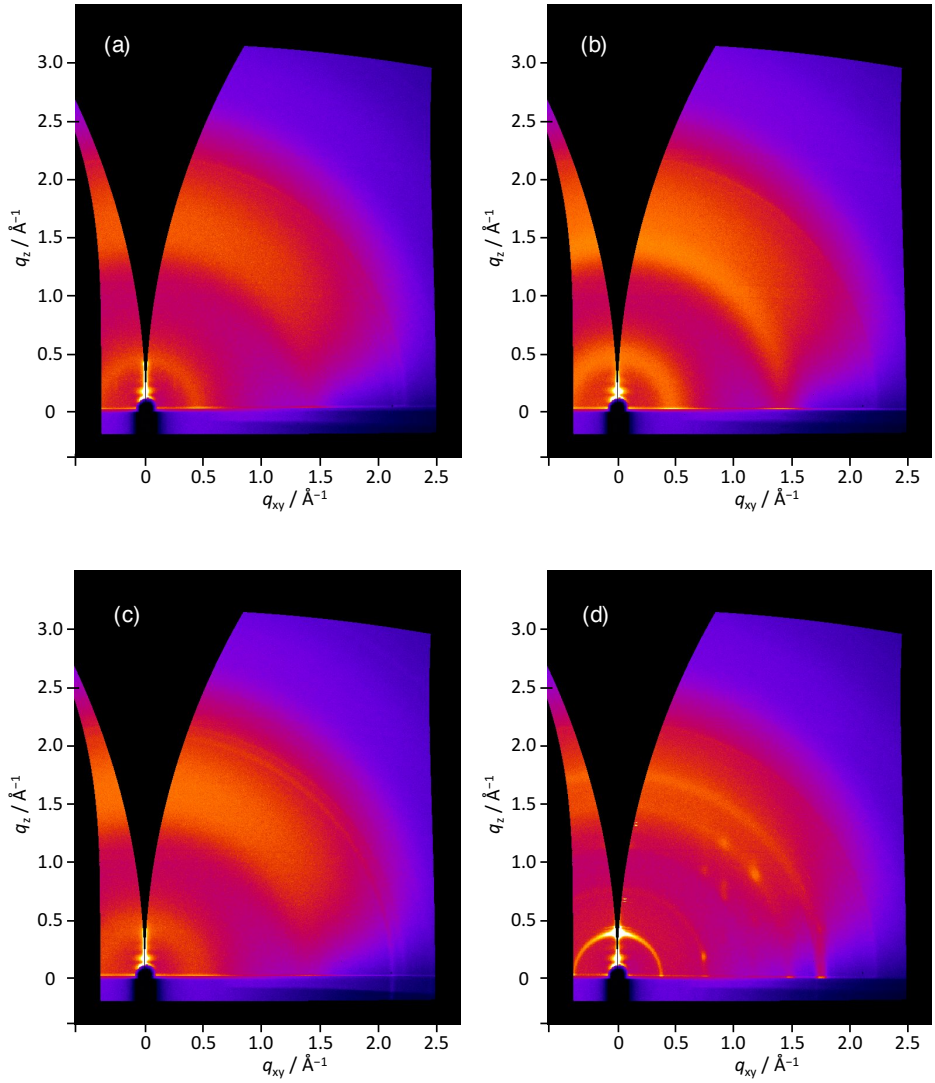

Figure 2-21. 2D-GIWAXD patterns of BHJ films on ITO/PEDOT:PSS: (a) **P–D**:$PC_{61}BM$, (b) **P–D–P**:$PC_{61}BM$, (c) **D–P–D**:$PC_{61}BM$ and (d) **1**:$PC_{61}BM$.

2-4. Summary and Outlook

The efficient regioselective iodination of 2,7,12,17-tetrahexylporphycene was accomplished by using NIS with either TFA or silica gel as activator to give the corresponding 3-iodo or 3,13-diiodo derivatives, respectively. In addition, the palladium-catalyzed cross-coupling reactions of the iodoporphycenes with a stannylated acetylene was found to proceed in good yields of near 90%. This is the first example in which the porphycene framework undergoes a cross-

coupling reaction, and enables the porphycene chromophore to be coupled with various π-systems for forming novel electronic and optoelectronic materials.

This work indeed demonstrated that the porphycene–ThDPP conjugates (**P–D–P** and **D–P–D**) could be accessed in three steps from either the mono or diiodoporphycene in good overall yields of around 50%. These conjugates can absorb at a wide range of wavelengths extending from the visible to NIR region, and serve as p-type materials in OSCs. In particular, the best PCE of 1.74% was obtained in a BHJ OSC based on **D–P–D** and $PC_{61}BM$, while the other conjugate **P–D–P** and the model compound **P–D** afforded considerably lower efficiencies of up to 0.27 and 0.36%, respectively. **D–P–D** has more delocalized HOMO and a lower R_s compared with other conjugates leading to the improvement in the hole-transport property. Observation of the surface morphology with AFM indicates that the difference in photovoltaic efficiency can be correlated at least partly to the miscibility of the porphycene conjugates with $PC_{61}BM$.

The preliminary device evaluation described in this chapter has clearly shown that porphycene-based small-molecule semiconductors can serve as p-type material in BHJ OSCs. However, the resulting devices are lower in J_{SC}, FF and thus PCE as compared to the current state-of-the-art OSCs that afford PCEs of over 10%. Considering the facts that the porphycene derivatives can absorb at wide ranges of wavelengths (Figure 2-13) and that the current density increases at (Figure 2-16a) negative bias voltages, the low efficiencies of the present systems may originate from problems in the charge-carrier transport process rather than charge-carrier generation.

Many studies have proven that J_{SC} and FF are strognly related to the morphology of the active layer.[32–40] An effective approach for morphological optimization is the side-chain engineering. For example, while a dithienosilole–DPP conjugate SIDPP-EE afforded low photovoltaic performance (J_{SC} = 2.1 mA cm^{-2}, V_{OC} = 0.82 V, FF = 0.38 and PCE = 0.5%), a

related derivative SIDPP-OE showed much higher performance (J_{SC} = 7.5 mA cm^{-2}, V_{OC} = 0.77 V, FF = 0.60 and PCE = 3.5%) in BHJ OSCs with $PC_{61}BM$, because of the improved crystallinity and more favorable molecular orientation (Figure 2-22a).[37] Another approach is the use of a high-boiling-point additive and/or post-deposition annealing as exemplified by the case of BHJ OSCs based on $DPP(TBFu)_2$ and $PC_{71}BM$. In this case, an active layer annealed with THF vapor showed significantly higher photovoltaic performance (J_{SC} = 11.7 mA cm^{-2}, V_{OC} = 0.78 V, FF = 0.56 and PCE = 5.2%) compared with non-annealed counterpart (J_{SC} = 2.1 mA cm^{-2}, V_{OC} = 0.95 V, FF = 0.28 and PCE = 0.55%) (Figure 2-22b).[38] The authors assumed that the solvent-vapor annealing effectively improved the crystallinity of $DPP(TBFu)_2$ domains.

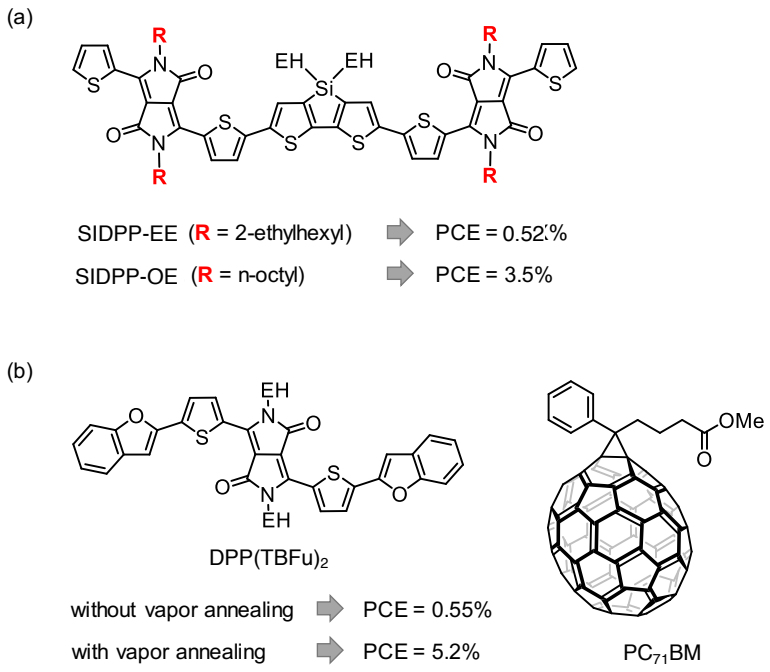

Figure 2-22. Improvement of photovoltaic performance through (a) side-chain engineering[37] and (b) solvent vapor annealing.[38] EH = 2-ethylhexyl.

Such morphological optimization will be definitely worth examining for the present cases of porphycene–ThDPP conjugates. The engineering of *N*-substituents on **D–P–D** is of special interest, considering its similarity in molecular structure to the successful example of SIDPP

system, as well as its relatively high photovoltaic performance among the derivatives examined in this work. It would be also interesting to further fine-tune the molecular electronic structure through the conjugation with other dyes than DPP. As porphycene is highly underrepresented in the field of organic electronics and optoelectronics, there still is much room to explore for new derivatives with unique properties. The synthetic development achieved in this work will serve as a solid basis for such diversity-oriented derivatization of porphycene.

2-5. Experimental Section

General method

All reactions were carried out under argon unless otherwise noted. “Room temperature” means 15–25 °C. Gravity column chromatography was performed on silica gel purchased from Kanto Chemical (Silica Gel 60N, 60 Å, 63–210 μm). Analytical TLC was conducted on Merck 200 μm thickness silica gel plates with a fluorescent indicator. Visualization was accomplished with UV light at 254 or 365 nm. GPC was performed on a JAI LC-9225NEXT recycle chromatography system equipped with JAIGEL 1H and 2H polystyrene gel columns (600 mm h × 40 mmϕ; bead size = 16 μm; pore size = 20–30 [1H] and 40–50 [2H] Å) using $CHCl_3$ as a mobile phase. ^{1}H NMR and $^{13}C\{^1H\}$ NMR spectra were recorded on a JEOL ECX 400P (400 MHz) or ECP-400 (400 MHz) spectrometer at 294 K using tetramethylsilane as internal standard. High-resolution ESI mass spectra were recorded on a JEOL JMS-MS T100LC spectrometer. High-resolution MALDI mass spectra were measured on a JEOL Spiral TOF/JMS-S3000 mass spectrometer. IR spectra were recorded on a JASCO FT/IR-4200 spectrometer. UV–Vis absorption spectra were recorded on a JASCO UV–Vis–NIR V-670 spectrometer. Electrochemical measurements were measured on an ALS 612D electrochemical analyzer in a solution of 0.1 M ^{n}Bu$_4$NPF$_6$ in dry *o*-dichlorobenzene/CH_3CN (5:1 vol) with a scan rate of 100 mV s^{-1} at room temperature in an argon-filled cell. A glassy carbon electrode and a Pt wire were used as a working and a counter electrode, respectively. An $Ag/AgNO_3$ electrode was used as a reference electrode, which was calibrated with the half-wave potential of Fc/Fc^+ redox couple. Ionization energies of thin films were determined from the onset of photoelectron spectra measured on a Riken Keiki AC-3 photoelectron spectrometer. The surface morphology of organic films was observed using an SII SPA400/SPI3800N AFM in

tapping mode with an SII SI-DF20 silicon probe at a resonant frequency of 138 kHz and a force constant of 16 N m^{-1}.

Single-crystal X-ray diffraction analysis

X-ray diffraction data were measured at 103 K on a Rigaku VariMax R-Axis RAPID imaging plate-based X-ray diffractometer system equipped with an RA-Micro7 X-ray source (Mo *K*α, λ = 0.71073 Å) operated at 1.2 kW. The diffraction data were processed with CrystalStructure of the Rigaku program, solved with the SIR-97 program[41–42] and refined with the SHELX-97 program.[43]

X-ray diffraction analysis of thin films

Out-of-plane XRD θ–2θ scans of thin films were measured on a Rigaku RINT-TTR III diffractometer equipped with a rotating anode (Cu *K*α, λ = 1.5418 Å) operated at 15 kW and a Rigaku D/teX Ultra 1D silicon strip detector. Measurements were performed at a scan rate of 3° min^{-1} with a scan range of 2–35°.

Two-dimensional grazing incidence wide-angle X-ray diffraction measurements

2D-GIWAXD measurements were performed in a HUBER multiaxis diffractometer installed in beamline BL-19B2 at SPring-8. The X-ray beam was monochromatized by a double-crystal Si(111) monochromator, and the X-ray energy was 12.398 keV. Scattered X-rays from samples were detected by a PILATUS 300 K X-ray photon counting pixel detector. The X-ray-beam incidence angle was set to 0.12°, and the sample-to-detector distance was 174.7 mm.

Materials

All solvents and chemicals were reagent grade obtained commercially, and used without further purification except otherwise noted. For spectral measurements, spectral grade and $CHCl_3$ were purchased from Nacalai Tesque. Prepared as described in the literature were 2,7,12,17-tetrahexylporphycene[14] and ThDPP.[44] $PC_{61}BM$ was purchased from Luminescence Technology Crop. and used as received.

Theoretical calculations

All calculations were performed using the Gaussian 09 program suite. Geometry optimizations were performed by DFT at the B3LYP/6-31G(d) level of theory. Vibrational frequencies were computed for all optimized structures to verify that the obtained structures were minima.

Fabrication and evaluation of photovoltaic cells

ITO-patterned glass substrates (20 × 20 mm^2, 15 Ω per square) were cleaned by gentle rubbing with an acetone-soaked wipe, then sequential sonication in detergent (Furuuchi Chemical, Semico Clean 53), distilled water (Wako Pure Chemical, reagent grade), and isopropyl alcohol (Kishida chemical, electronic grade) for 10 min each. After drying with N_2 blow and UV/O_3 treatment with a Bioforce Nanoscience TC-003 cleaner at room temperature for 20 min, PEDOT:PSS (Clevios, AI4083) was spin-coated onto the cleaned ITO surface. After being baked in air at 120 °C for 20 min, the substrates were transferred into a nitrogen-filled glove box (< 10 ppm O_2 and H_2O) for preparation of active layers. Bulk-heterojunction films were prepared by spin-coating of a p:n blend solution in $CHCl_3$ at 1500 rpm for 30 s. Finally, Ca (10 nm, 0.1 Å s^{-1}) and Al (70 nm, 0.3 Å s^{-1}) were vapor-deposited at high vacuum

(~10^{-4} Pa) through a shadow mask that defined an active area of 2 × 2 mm^2. The general device structure was [ITO/PEDOT:PSS (30 nm)/p:n/Ca (10 nm)/Al (70 nm)].

J–V curves were measured using a Keithley 2611B source mater unit under AM 1.5 G illumination at an intensity of 100 mW cm^{-2} using a Bunko Keiki CEP-2000RP solar simulator. The EQE spectra were obtained under illumination of monochromatic light using the same system.

Synthesis

Synthesis of 2,7,12,17-tetrahexyl-3-iodoporphycene (**2**)

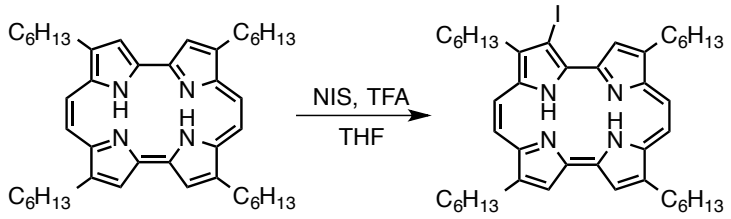

1 **2**

N-Iodosuccinimide (NIS) (39.0 mg, 173 µmol) was added to the mixture of 2,7,12,17-tetrahexylporphycene (**1**) (100 mg, 155 µmol) and TFA (0.5 mL) in THF (30 mL) at 0 °C in the dark. The reaction mixture was stirred at room temperature for 2 h and the solvent was removed under reduced pressure. The crude product was neutralized with 1% Et_3N/CH_2Cl_2 and purified by gravity silica gel column chromatography (CH_2Cl_2/hexanes, 1:9). Recrystallization from a $CHCl_3$ solution by adding methanol gave **2** as a purple solid (74.9 mg, 97.0 µmol, 66 %). ^{1}H NMR (400 MHz, $CDCl_3$): δ 10.18 (s, 1H, *β*-pyrrole), 9.43 (d, *J* = 11.4 Hz, 1H, *meso*), 9.39–9.35 (m, 2H, *meso*), 9.24 (d, *J* = 11.4 Hz, 1H, *meso*), 9.00 (s, 1H, *β*-pyrrole), 8.90 (s, 1H, *β*-pyrrole), 3.89–3.77 (m, 8H), 2.35–2.20 (m, 6H), 2.16–2.08 (m, 2H), 1.90 (br s, 1H, NH), 1.78–1.65 (m, 8H), 1.58–1.35 (m, 16H + 1H, alkyl + NH), 1.00–0.93 (m, 12H); ^{13}C{^{1}H} NMR (100 MHz, $CDCl_3$): δ 150.4, 148.5, 147.5, 145.0, 143.4, 142.3, 138.7, 137.8, 134.9, 131.5, 130.3, 123.5, 122.4, 121.3, 112.2, 111.6, 109.2, 108.1, 85.4, 32.8, 32.1, 32.0, 31.9, 31.8, 31.7, 30.3, 29.9, 29.8, 29.7, 29.7, 29.7, 28.4, 28.3, 28.1, 22.8, 22.8, 22.8, 14.2, 14.2; IR (ATR): $\bar{\nu}$ [cm^{-1}] 3010 (w, C(*sp*^{2})–H), 2923 (m, C(*sp*^{3})–H), 2854 (w, C(*sp*^{3})–H), 1459 (w), 1041 (s); UV–Vis ($CHCl_3$): λ_{max} (ε [M^{-1} cm^{-1}]) 374 (131 000), 385 (114 000), 570 (37 100), 610 (31 000), 644 (43 000); HRMS (ESI): *m/z* calcd for $C_{44}H_{62}IN_4^+$ ($[M + H]^+$) 773.4014, found 773.4045.

Synthesis of 2,7,12,17-tetrahexyl-3,13-diiodoporphycene (**3a**)

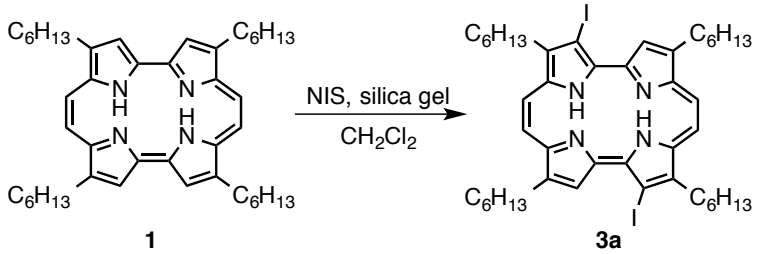

1 **3a**

NIS (20.0 mg, 88.9 μmol) and silica gel (2.00 g) were added to **1** (26.0 mg, 40.2 μmol) in CH_2Cl_2 (4 mL) at 0 °C in the dark. After stirring at room temperature for 2 h, the solvent was removed under a reduced pressure. The crude product was purified by gravity column chromatography on silica gel (CH_2Cl_2/hexanes, 1:9). Repetitive recrystallization three times from a $CHCl_3$ solution by adding hexanes gave **3a** as a purple solid (19.5 mg, 21.7 μmol, 54%). ^{1}H NMR (400 MHz, $CDCl_3$): δ 10.35 (s, 2H, *β*-pyrrole), 9.62 (d, J = 11.4 Hz, 2H, *meso*), 9.53 (d, J = 11.4 Hz, 2H, *meso*), 4.02 (t, J =7.8 Hz, 4H), 3.90 (t, J = 8.0 Hz, 4H), 2.42–2.34 (m, 4H), 2.21–2.13 (m, 4H), 1.82–1.37 (m, 8H), 1.60–1.37 (m, 16H), 1.17 (br s, 2H, NH), 0.96 (dt, J = 13.1, 5.0 Hz, 6H); ^{13}C{^{1}H} NMR (100 MHz, $CDCl_3$): δ 152.4, 147.9, 143.0, 137.1, 136.6, 130.3, 122.6, 113.2, 108.5, 86.5, 32.8, 32.2, 31.9, 30.4, 29.9, 29.7, 28.4, 22.8, 22.8, 14.2, 14.2; IR (ATR): $\bar{\nu}$ [cm^{-1}] 3054 (w, C (sp^2)–H), 2925 (w, C (sp^3)–H), 2854 (w, C (sp^3)–H), 1464 (m), 1216 (m), 1041 (s); UV–Vis ($CHCl_3$): λ_{max} (ε [M^{-1} cm^{-1}]) 379 (126 000), 386 (131 000), 575 (40 100), 617 (29 800), 652 (44 100); HRMS (ESI): *m/z* calcd for $C_{44}H_{61}I_2N_4^+$ ([M + H]$^+$) 899.2980, found 899.2964. Crystallographic data: $C_{44}H_{60}I_2N_4$, M = 898.79, triclinic, space group $P\bar{1}$, a = 7.7711(3) Å, b = 8.5531(4) Å, c = 16.1618(7) Å, α = 75.4024(12)°, β = 89.3990(12)°, γ = 85.0834(11)°, V = 1035.66(7) Å^3, Z = 1, T = 103 K, R_1 = 0.0386 (for $I > 2\sigma(I)$), wR_2= 0.1071 (for all data), GOF = 1.128. CCDC No. 1003914.

Synthesis of 2,7,12,17-tetrahexyl-3-[(trimethylsilyl)ethynyl]porphycene (**4**)

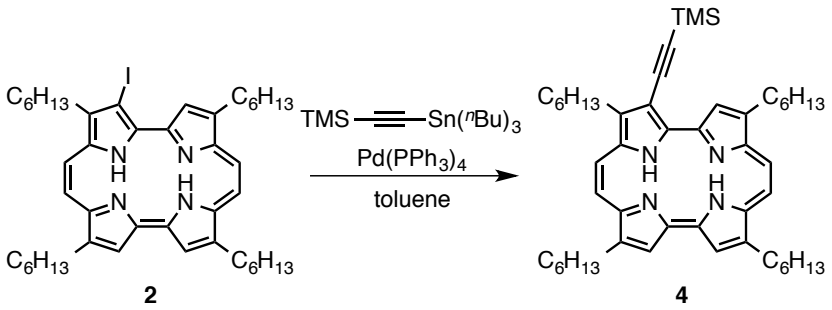

Trimethyl[(tributylsilyl)ethynyl]stannane (32.0 mg, 82.6 μmol) was added to a solution of **2** (60.0 mg, 77.7 μmol) and $Pd(PPh_3)_4$ (5.0 mg, 4.3 μmol) in toluene (10 mL). The mixture was degassed by bubbling nitrogen for 15 min and then was refluxed for 5 h. After being allowed to cool to room temperature, the solvent was removed under a reduced pressure. The crude product was purified by gravity silica gel column chromatography (CH_2Cl_2/hexanes, 1:6). Recrystallization from a $CHCl_3$ solution by adding hexanes gave **4** as a purple solid (51.0 mg, 68.7 μmol, 89%). ^{1}H NMR (400 MHz, $CDCl_3$): δ 10.12 (s, 1H, *β*-pyrrole), 9.72–9.63 (m, 4H, *meso*), 9.29 (s, 1H, *β*-pyrrole), 9.20 (s, 1H, *β*-pyrrole), 4.09–3.97 (m, 8H), 3.02 (br s, 1H, NH), 2.81 (br s, 1H, NH), 2.48–2.28 (m, 8H), 1.83–1.70 (m, 8H), 1.61–1.34 (m, 16H), 0.99–0.90 (m, 12H), 0.63 (s, 9H, -Si(CH_3)$_3$); ^{13}C{^{1}H} NMR (100 MHz, $CDCl_3$): δ 150.5, 147.0, 146.6, 144.5, 143.4, 142.5, 139.4, 139.0, 136.7, 135.0, 131.7, 130.6, 122.9, 122.1, 121.2, 119.1, 111.8, 110.9, 109.4, 108.5, 103.8, 102.1, 32.5, 31.6, 31.6, 31.5, 31.4, 31.2, 29.3, 29.3, 29.3, 29.2, 28.0, 27.9, 27.8, 27.3, 22.4, 22.4, 22.3, 13.8, 13.8; IR (ATR): $\bar{\nu}$ [cm^{-1}] 3008 (w, C (sp^2)–H), 2926 (w, C (sp^3)–H), 2852 (w, C (sp^3)–H), 2145 (m, C≡C), 1257 (m, Si–CH_3), 755 (s); UV–Vis ($CHCl_3$): λ_{max} (ε [M^{-1} cm^{-1}]) 376 (25 800), 387 (22 700), 575 (7 200), 615 (7 600), 647 (9 100); HRMS (ESI): *m/z* calcd for $C_{49}H_{71}N_4Si^+$ ([M + H]$^+$) 743.5443, Found 743.5466.

Synthesis of 3-ethynyl-2,7,12,17-tetrahexylporphycene (**5**)

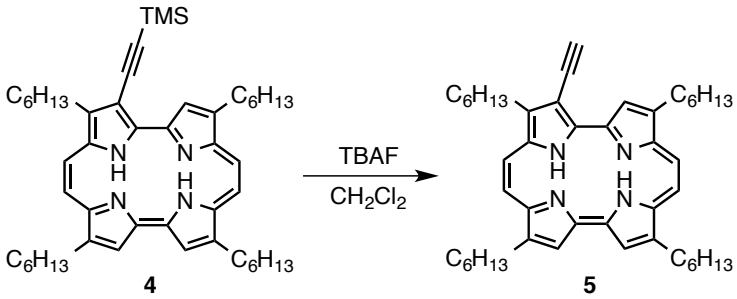

TBAF in THF (1.0 M, 0.1 mL) was added to a solution of **4** (52.0 mg, 7.00 µmol) in CH_2Cl_2 (17 mL). After stirring at room temperature for 5 min, the reaction mixture was washed with water and brine. The organic layer was dried over Na_2SO_4, filtered, and evaporated. Recrystallization from a $CHCl_3$ solution by adding methanol gave **5** as a purple solid. (43.0 mg, 64.1 µmol, 92%) ^{1}H NMR (400 MHz, $CDCl_3$): δ 10.05 (s, 1H, *β*-pyrrole), 9.73–9.63 (m, 4H, *meso*), 9.30 (s, 1H, *β*-pyrrole), 9.20 (s, 1H, *β*-pyrrole), 4.26 (s, 1H, C≡CH), 4.10–3.97 (m, 8H), 2.96 (br s, 1H, NH), 2.75 (br s, 1H, NH), 2.42–2.26 (m, 8H), 1.82–1.70 (m, 8H), 1.59–1.33 (m, 16H), 0.99–0.89 (m, 12H); ^{13}C{^{1}H} NMR (100 MHz, $CDCl_3$): δ 151.7, 147.8, 147.4, 144.9, 144.1, 143.1, 140.0, 139.4, 137.4, 135.5, 132.1, 131.1, 123.6, 122.5, 121.8, 118.3, 112.4, 111.6, 110.1, 109.0, 86.6, 80.9, 33.1, 32.3, 32.0, 32.0, 32.0, 31.9, 31.9, 29.7, 29.7, 28.4, 28.4, 28.2, 27.7, 22.8, 22.8, 22.7, 14.2, 14.2, 14.2; IR (ATR): $\bar{\nu}$ [cm^{-1}] 3310 (m, C (*sp*)–H), 3010 (w, C (sp^2)–H), 2925 (m, C (sp^3)–H), 2856 (m, C (sp^3)–H), 2102 (w, C≡C), 750 (s); UV–Vis ($CHCl_3$): λ_{max} (ε [M^{-1} cm^{-1}]) 375 (13 100), 385 (112 000), 573 (37 000), 613 (35 700), 646 (46 790); HRMS (ESI): *m/z* calcd for $C_{46}H_{63}N_4^+$ ([M + H]$^+$) 671.5047, found 671.5076.

Synthesis of 2,7,12,17-tetrahexyl-3,13-bis[(trimethylsilyl)ethynyl]porphycene (**6**)

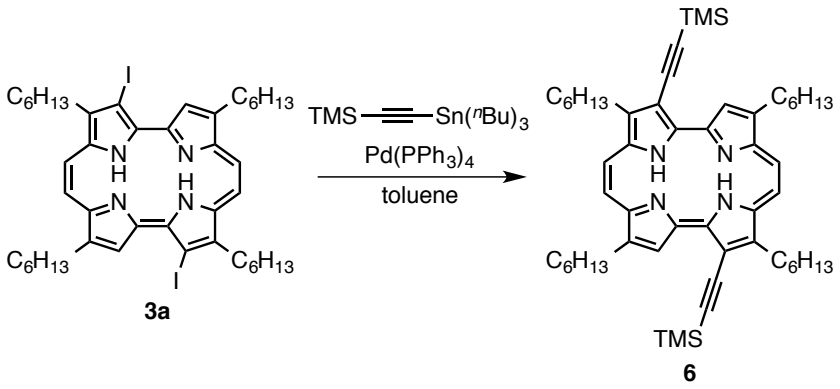

Trimethyl[(tributylsilyl)ethynyl]stannane (135 mg, 349 μmol) was added to a solution of **3a** (98.0 mg, 109 μmol) and $Pd(PPh_3)_4$ (14.0 mg, 12.1 μmol) in toluene (10 mL). The mixture was degassed by bubbling nitrogen for 15 min and was refluxed for 5 h. After being allowed to cool to room temperature, the solvent was removed under a reduced pressure. The crude product was purified by gravity silica gel column chromatography (CH_2Cl_2/hexanes, 1:1). Recrystallization from a $CHCl_3$ solution by adding hexanes gave **6** as a purple solid (80.0 mg, 95.4 μmol, 88%). ^{1}H NMR (400 MHz, $CDCl_3$): δ 10.12 (s, 2H, *β*-pyrrole), 9.71 (d, J = 11.4 Hz, 2H, *meso*), 9.67 (d, J = 11.4 Hz, 2H, *meso*), 4.05 (q, J = 7.0 Hz, 8H), 2.57 (br s, 2H, NH), 2.47–2.39 (m, 4H), 2.34–2.27 (m, 4H), 1.82–1.70 (m, 8H), 1.59–1.34 (m, 16H), 0.98–0.91 (m, 12H), 0.62 (s, 18H, -Si(CH_3)$_3$); ^{13}C{^{1}H} NMR (100 MHz, $CDCl_3$): δ 152.1, 147.1, 142.5, 137.3, 136.9, 130.0, 121.9, 120.0, 112.5, 108.7, 104.1, 101.9, 32.5, 31.6, 31.5, 31.2, 29.3, 29.2, 27.9, 27.3, 22.4, 22.3, 13.8; IR (ATR): $\bar{\nu}$ [cm^{-1}] 3004 (w, C (sp^2)–H), 2924 (w, C (sp^3)–H), 2854 (w, C (sp^3)–H) 2143 (m, C≡C), 1278 (m, Si–CH_3), 755 (s); UV–Vis ($CHCl_3$): λ_{max} (ε [M^{-1} cm^{-1}]) 377 (124 000), 391 (128 000), 587 (40 900), 627 (45 300), 661 (41 600); HRMS (ESI): *m/z* calcd for $C_{54}H_{79}N_4Si_2^+$ ([M + H]$^+$) 839.5838, found 839.5825. Crystallographic data: $C_{54}H_{78}N_4Si_2$, M = 839.41, monoclinic, space group $P2_1/c$, a = 10.2001(13) Å, b = 6.7239(9) Å, c = 36.947(5) Å, β = 93.358(3)°, V = 2529.6(6) Å^3, Z = 2, T = 103 K, R_1 = 0.0897(for $I > 2\sigma(I)$), wR_2 = 0.2136 (for all data), GOF = 1.129. CCDC No. 1003915.

Synthesis of 3,13-diethynyl-2,7,12,17-tetrahexylporphycene (**7**)

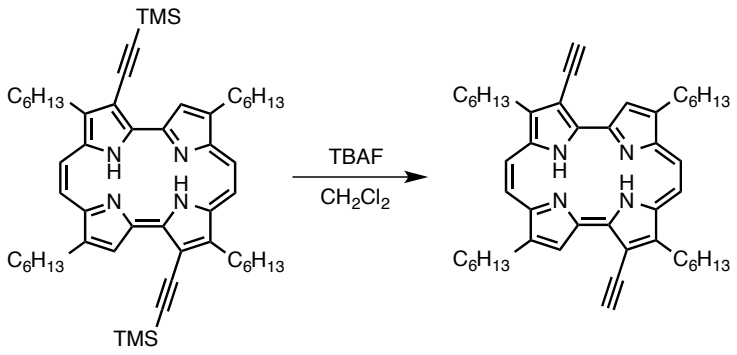

6 **7**

TBAF in THF (1.0 M, 0.2 mL) was added to a solution of **6** (49.0 mg, 58.4 µmol) in CH_2Cl_2 (17 mL). After stirring at room temperature for 5 min, the reaction mixture was washed with water and brine. The organic layers were dried over Na_2SO_4, filtered, and evaporated. Recrystallization from a $CHCl_3$ solution by adding methanol gave **7** as a purple solid (38.0 mg, 54.7 µmol, 93%). ^{1}H NMR (400 MHz, $CDCl_3$): δ 10.04 (s, 2H, *β*-pyrrole), 9.67 (d, 2H, J = 11.0 Hz, *meso*), 9.63 (d, 2H, J = 11.0 Hz, *meso*), 4.27 (s, 2H, -C≡CH), 4.05–4.00 (m, 8H), 2.41–2.24 (m + br s, 8H + 2H), 1.81–1.69 (m, 8H), 1.59–1.33 (m, 16H), 0.97 (t, J = 7.3 Hz, 9H), 0.92 (t, J = 7.3 Hz, 9H); ^{13}C{^{1}H} NMR (100 MHz, $CDCl_3$): δ 153.2, 147.3, 142.9, 137.5, 137.1, 130.1, 122.1, 119.0, 112.9, 109.0, 33.1, 32.2, 31.9, 31.8, 29.7, 28.3, 27.7, 22.8, 22.7, 14.2, 14.2; IR (ATR): $\bar{\nu}$ [cm^{-1}] 3309 (w, C (*sp*)–H), 3009 (w, C (sp^2)–H), 2955 (m, C (sp^3)–H), 2925 (m, C (sp^3)–H), 2102 (w, C≡C), 1526 (m), 1057 (m), 762 (s); UV–Vis ($CHCl_3$): λ_{max} (ε [M^{-1} cm^{-1}]) 376 (126 000), 388 (125 000), 583 (42 100), 624 (39 700), 658 (46 400); HRMS (ESI): *m/z* calcd for $C_{48}H_{63}N_4^+$ ([M + H]$^+$) 695.5047, found 695.5057.

Synthesis of **P–D**

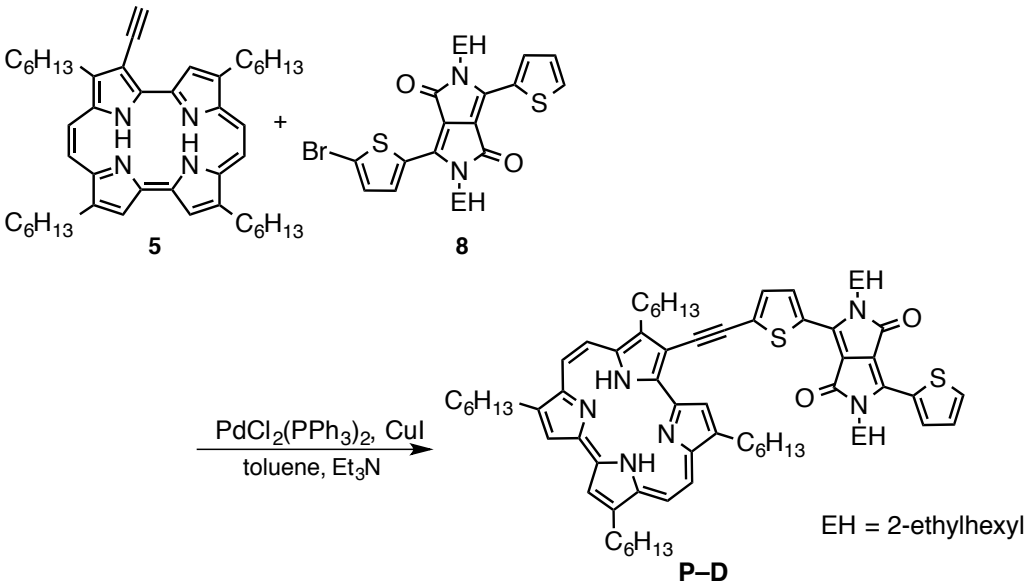

Triethylamine (360 mg, 3.56 mmol), $Pd(PPh_3)_4$ (6.0 mg, 5.2μmol) and CuI (1.5 mg, 7.9 μmol) were added to a solution of **8** (30.0 mg, 41.3 μmol) and **5** (33.0 mg, 54.8 μmol) in toluene (10 mL). The solvent was degassed by bubbling nitrogen for 15 min and the solution was heated at 80 °C for 19 h. After being allowed to cool to room temperature, the solvent was removed under a reduced pressure. The crude product was purified by gravity column chromatography on silica gel (CH_2Cl_2/hexanes, 1:1) and GPC. Recrystallization from a $CHCl_3$ solution by adding hexanes gave **P–D** as a purple solid (29.0 mg, 24.3 μmol, 55%). ^{1}H NMR (400 MHz, $CDCl_3$): δ 9.96 (s, 1H, *β*-pyrrole), 9.74–9.62 (m, 4H, *meso*), 9.30 (s, 1H, *β*-pyrrole), 9.20 (s, 1H, *β*-pyrrole), 9.15 (d, *J* = 4.1 Hz, 1H, thiophene), 8.96 (dd, *J* = 3.7, 1.1 Hz, 1H, thiophene), 7.77 (d, *J* = 4.1 Hz, 1H, thiophene), 7.66 (dd, *J* = 5.0, 1.1 Hz, 1H, thiophene), 7.30 (t, *J* = 4.6 Hz, 1H, thiophene), 4.15–3.95 (m, 8H + 4H, -C*H*$_2$C$_5$H$_{11}$ + -NC*H*$_2$-), 3.08 (br s, 1H, NH), 2.80 (br s, 1H, NH), 2.45–2.31 (m, 8H), 2.07–2.02 (m, 1H), 1.94–1.89 (m, 1H), 1.82–1.72 (m, 8H), 1.60–1.23 (m, 28H), 1.01–0.87 (m, 24H); ^{13}C{^{1}H} NMR (100 MHz, $CDCl_3$): δ 161.4, 161.4, 150.4, 148.1, 147.5, 145.1, 143.7, 142.7, 140.1, 139.5, 139.3, 138.9, 137.6, 136.0, 135.5, 135.1, 132.1, 131.5, 130.6, 130.5, 130.2, 129.8, 129.5, 128.4, 123.5, 121.8, 121.6, 118.2, 112.5, 111.5, 110.1, 108.7, 108.4, 107.9, 96.0, 91.7, 45.9, 45.8, 39.2, 39.1, 33.1, 32.0, 32.0, 32.0, 32.0, 31.9,

31.8, 31.7, 30.2, 30.2, 30.2, 30.2, 29.8, 29.7, 29.6, 28.4, 28.4, 28.4, 28.3, 28.2, 27.7, 23.6, 23.6, 23.5, 23.1, 22.8, 22.8, 22.8, 22.7, 14.2, 14.2, 14.2, 14.1, 10.5; IR (ATR): $\bar{\nu}$ [cm^{-1}] 3014 (w, C (sp^2)–H), 2925 (w, C (sp^3)–H), 2859 (w, C (sp^3)–H), 2361 (m, C≡C), 1666 (m, amide), 1232(m), 772 (s); UV–Vis ($CHCl_3$): λ_{max} (ε [M^{-1} cm^{-1}]) 373 (115 400), 390 (85 000), 585 (62 000), 648 (73 600); HRMS (MALDI–TOF, DCTB): *m/z* calcd for $C_{76}H_{101}N_6O_2S_2^+$ ($[M + H]^+$) 1193.7422, found 1193.7412.

Synthesis of **P–D–P**

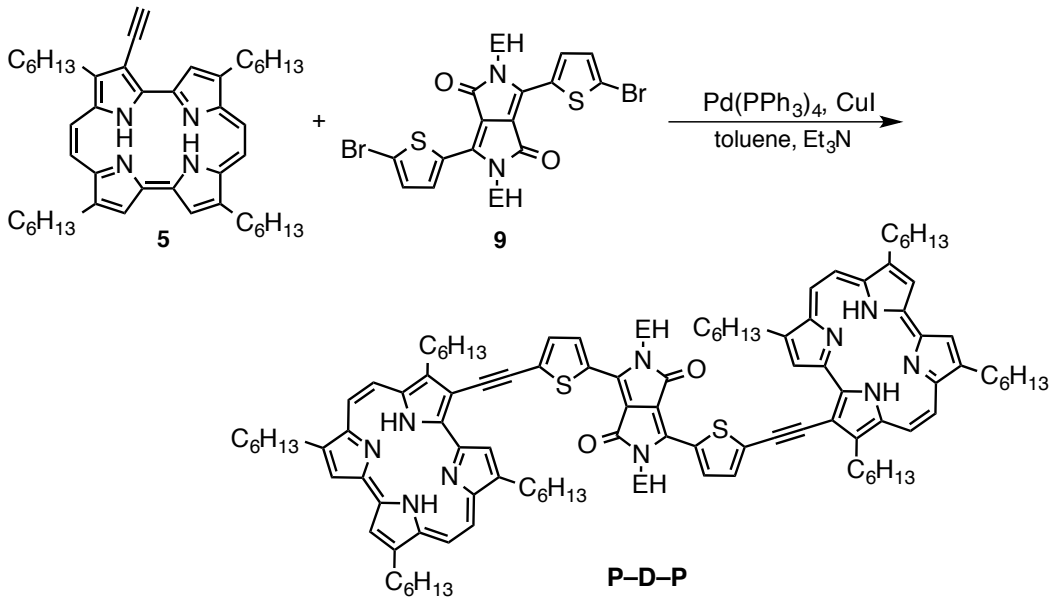

Triethylamine (870 mg, 8.60 mmol), $Pd(PPh_3)_4$ (14.0 mg, 12.1 μmol) and CuI (3.0 mg, 16 μmol) were added to a solution of **5** (75.0 mg, 11.2 μmol) and **9** (36.0 mg, 52.9 μmol) in toluene (25 mL). The solvent was degassed by bubbling nitrogen for 15 min and the solution was stirred at 80 °C for 13 h. The crude product was purified by gravity column chromatography on silica gel (CH_2Cl_2/hexanes, 1:2) and GPC. Recrystallization from a $CHCl_3$ solution by adding hexanes gave **P–D–P** as a purple solid (54.2 mg, 29.1 μmol, 52%). ^{1}H NMR (400 MHz, $CDCl_3$): δ 9.47 (s, 2H, *β*-pyrrole), 9.34 (d, J = 3.7 Hz, 2H, thiophene), 8.80 (s, 8H + 4H, *meso* + *β*-pyrrole), 7.79 (d, J = 4.1 Hz, 2H, thiophene), 4.28 (d, J = 7.3 Hz, 4H), 3.75–3.60 (m, 16H), 2.37–2.22 (m, 12H), 2.18–2.08 (m, 4H + 2H, alkyl + NH), 1.86–1.30 (m, 68H), 1.13–0.90 (m, 36H); ^{13}C{^{1}H} NMR (100 MHz, $CDCl_3$): δ 161.4, 149.5, 147.2, 146.7, 144.3, 142.9, 141.9, 139.2, 138.6, 137.9, 136.8, 136.6, 134.3, 132.2, 130.7, 130.4, 130.2, 129.8, 122.9, 121.3, 120.8, 118.0, 111.6, 110.6, 109.1, 108.7, 107.9, 96.6, 92.2, 46.3, 39.3, 33.1, 32.1, 32.1, 31.9, 31.8, 31.6, 30.4, 29.9, 29.8, 29.8, 29.7, 28.6, 28.3, 28.1, 28.0, 27.5, 23.8, 23.3, 22.9, 22.9, 22.8, 14.3, 14.3, 14.2, 10.6; IR (ATR): $\bar{\nu}$ [cm^{-1}] 3012 (w, C (sp^2)–H), 2924 (w, C (sp^3)–H), 2861 (w, C (sp^3)–H), 2341 (m, C≡C), 1667 (m, amide), 760 (s); UV–Vis ($CHCl_3$): λ_{max} (ε [M^{-1} cm^{-1}]) 374

(237 700), 603 (94 450), 625 (11 190), 654 (176 740); HRMS (MALDI–TOF, DCTB): *m/z* calcd for $C_{122}H_{161}N_{10}O_2S_2^+$ ($[M + H]^+$) 1862.2240, found 1862.2250.

Synthesis of **D–P–D**

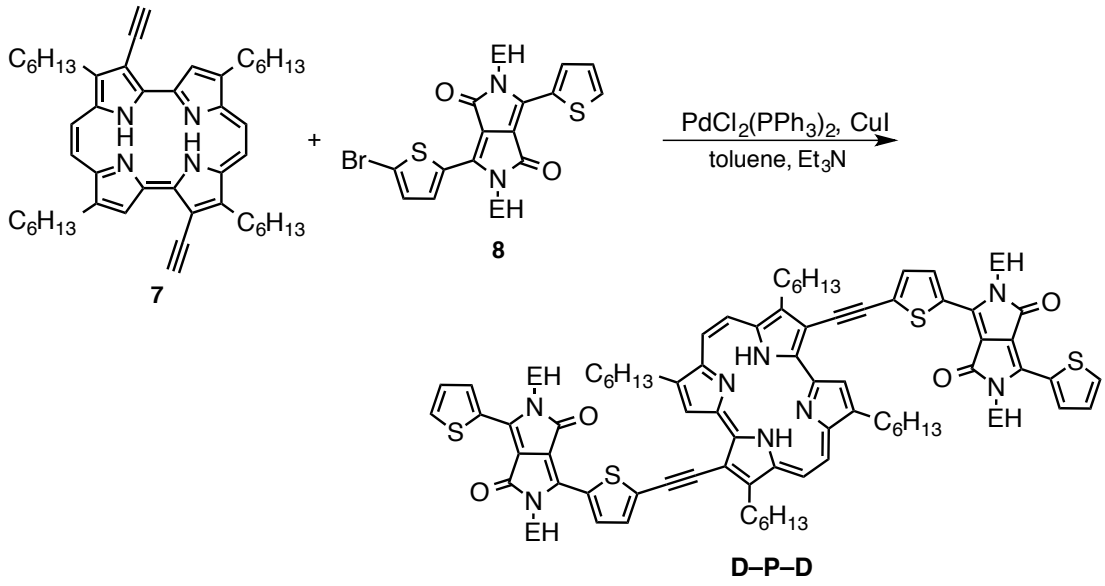

Triethylamine (1.50 g, 14.8 mmol), $Pd(PPh_3)_4$ (15.0 mg, 13.0 μmol) and CuI (2.0 mg, 11 μmol) were added to a solution of **7** (44.0 mg, 63.4 μmol) and **8** (84.0 mg, 139 μmol) in toluene (30 mL). The solvent was degassed by bubbling nitrogen for 15 min and the solution was stirred at 80 °C for 8.5 h. After removal of the solvent, the residue was purified by gravity column chromatography on silica gel (CH_2Cl_2/hexanes, 1:1) and GPC. Recrystallization from a $CHCl_3$ solution by adding hexanes gave **D–P–D** as a purple solid (87.0 mg, 50.0 μmol, 78%). ^{1}H NMR (400 MHz, $CDCl_3$): δ 9.77 (s, 2H, *β*-pyrrole), 9.46 (d, *J* = 11.4 Hz, 2H, *meso*), 9.40 (d, *J* = 11.4 Hz, 2H, *meso*), 9.06 (d, *J* = 4.1 Hz, 2H, thiophene), 8.90 (dd, *J* = 3.9, 1.1 Hz, 2H, thiophene), 7.71 (d, *J* = 4.1 Hz, 2H, thiophene), 7.60 (dd, *J* = 5.0, 1.4 Hz, 2H, thiophene), 7.23 (dd, *J* = 5.0, 3.9 Hz, 2H, thiophene), 4.04–3.95 (m, 16H), 2.42–2.22 (m, 8H), 2.04–1.95 (m, 2H, -$NCH_2CH(C_2H_5)C_4H_9$), 1.88–1.70 (m, 2H + 2H + 8H, -$NCH_2CH(C_2H_5)C_4H_9$ + NH + -$C_2H_4CH_2C_3H_7$), 1.59–1.29 (m, 48H), 1.00–0.88 (m, 36H); $^{13}C\{^1H\}$ NMR (100 MHz, $CDCl_3$): δ 161.4, 161.4, 152.1, 147.7, 142.8, 140.3, 139.2, 137.3, 137.0, 136.0, 135.6, 132.3, 130.7, 130.5, 129.8, 129.8, 129.4, 128.4, 121.6, 119.3, 113.1, 109.3, 108.5, 107.9, 95.7, 92.2, 46.0, 45.9, 39.2, 39.1, 33.1, 32.0, 32.0, 31.9, 30.2, 30.2, 29.7, 29.7, 28.4, 28.4, 28.3, 27.9, 23.7, 23.6, 23.5, 23.1, 22.8, 22.7, 14.2, 14.2, 14.1, 14.1, 10.5, 10.5; IR (ATR): $\bar{\nu}$ [cm^{-1}] 3006 (w, C (sp^2)–

H), 2956 (m, C (sp^3)–H), 2861 (w, C (sp^3)– H), 2185 (w, C≡C), 1668 (m, amide), 1261(m), 750 (s); UV–Vis ($CHCl_3$): λ_{max} (ε [M^{-1} cm^{-1}]) 306 (50 300), 374 (109 000), 393 (91 300), 552 (68 000), 601 (86 400), 656 (140 000); HRMS (MALDE–TOF, DCTB): *m/z* calcd for $C_{108}H_{139}N_8O_4S_4^+$ ($[M + H]^+$) 1739.9797, found 1739.9875.

NMR spectra

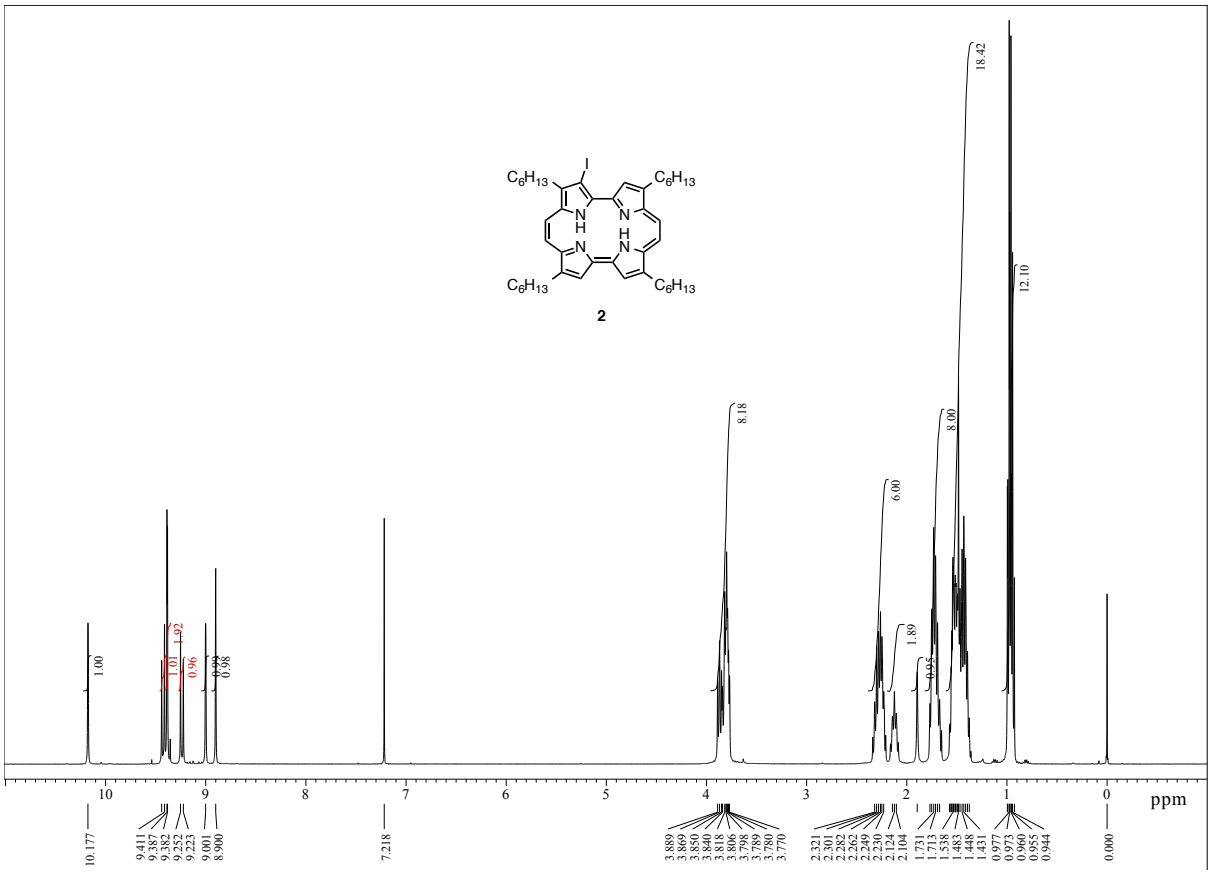

^{1}H NMR spectrum of **2** in $CDCl_3$.

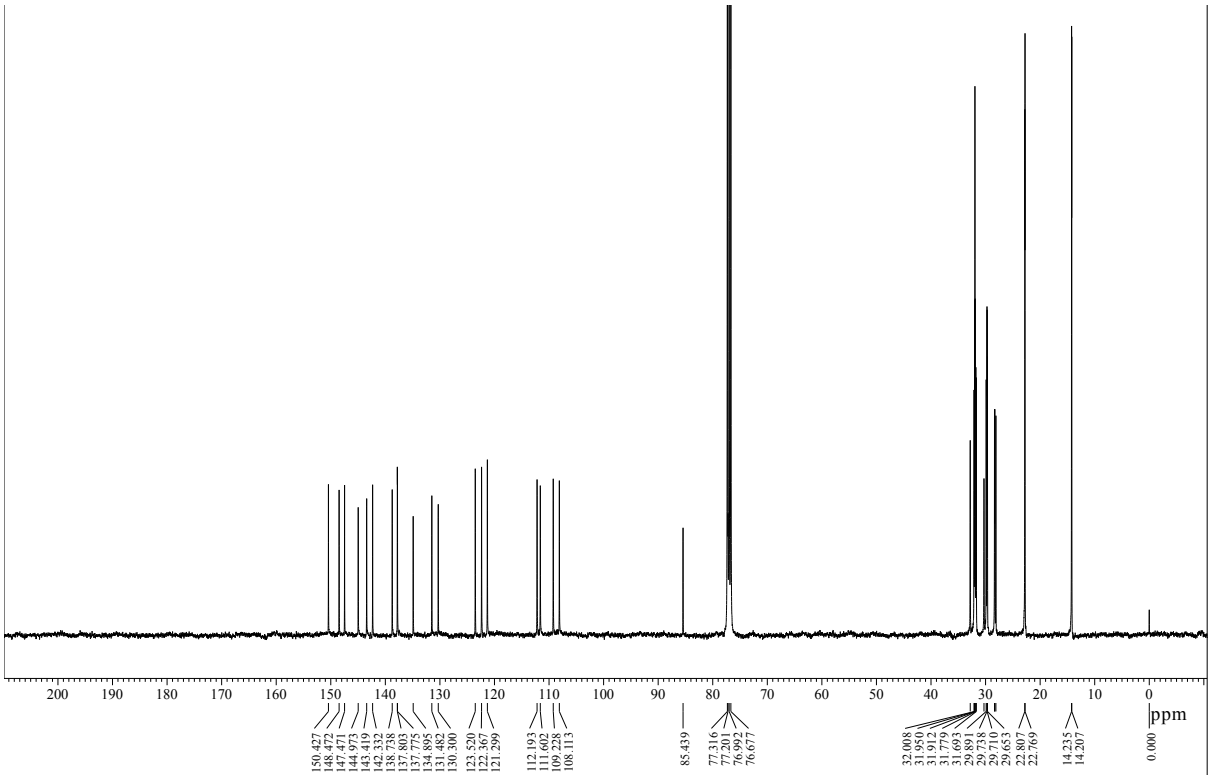

$^{13}C\{^{1}H\}$ NMR spectrum of **2** in $CDCl_3$.

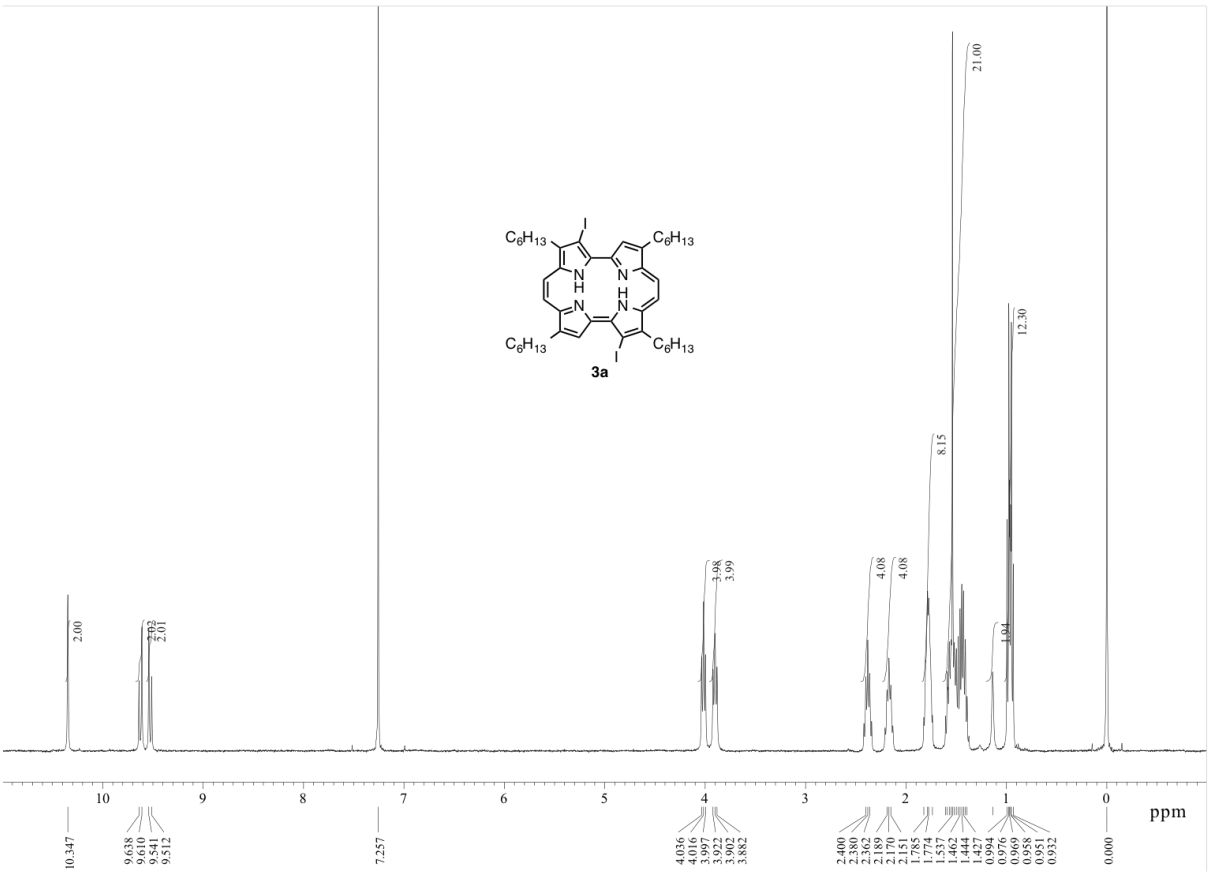

^{1}H NMR spectrum of **3a** in $CDCl_3$.

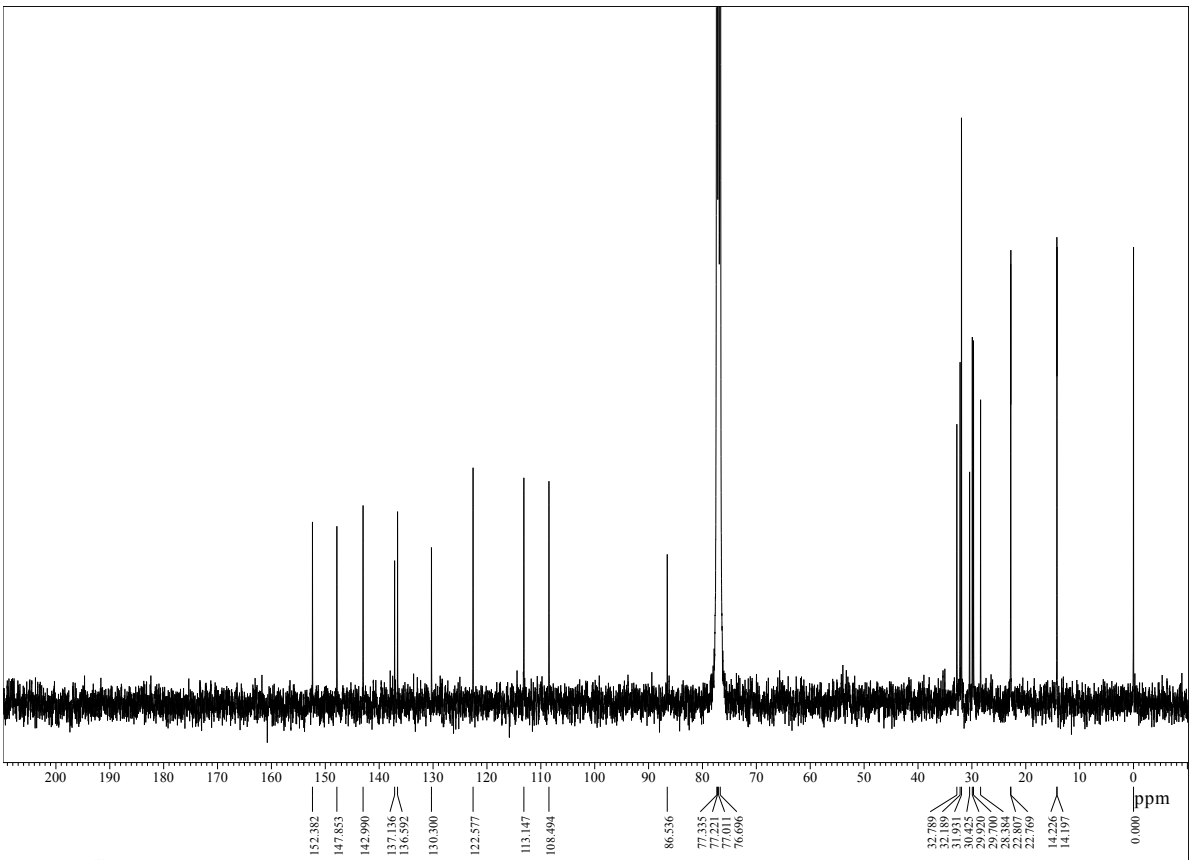

$^{13}C\{^{1}H\}$ NMR spectrum of **3a** in $CDCl_3$.

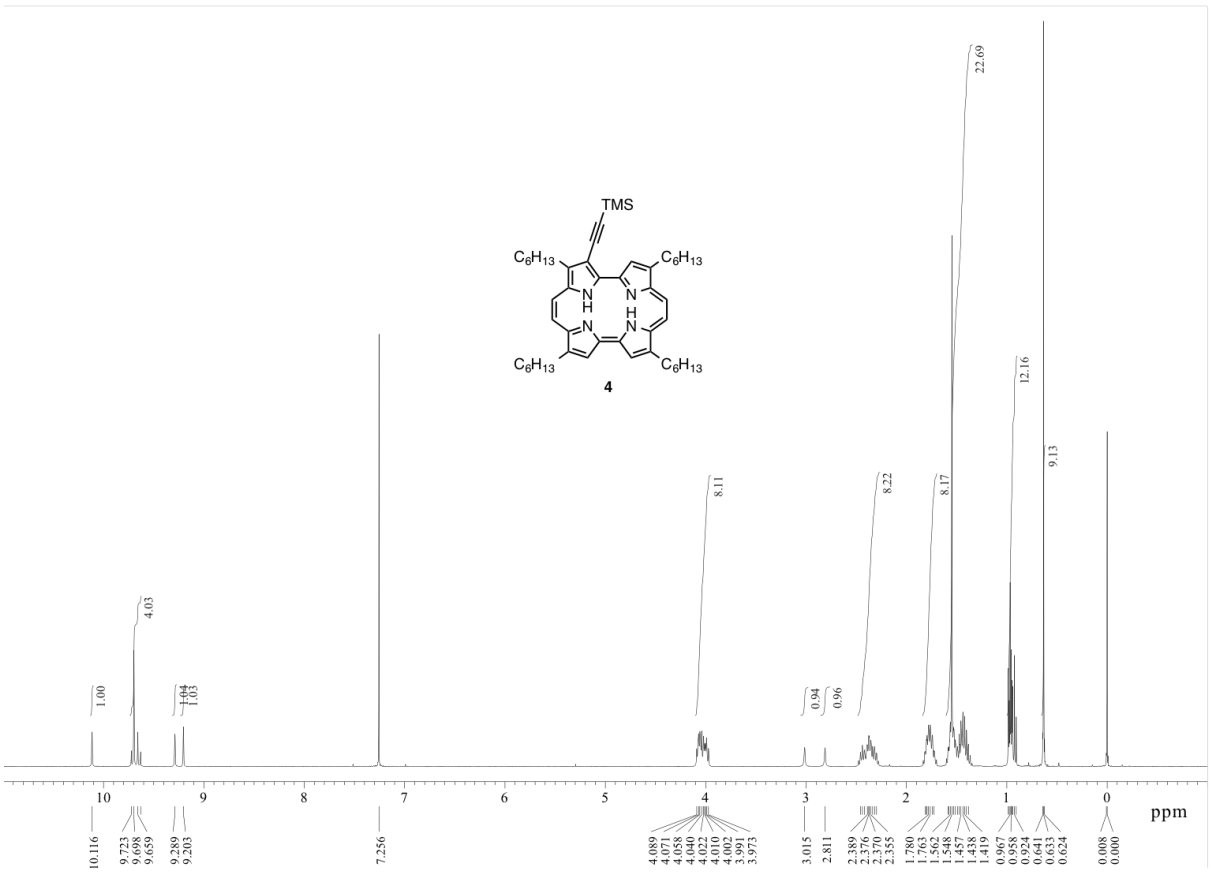

^{1}H NMR spectrum of **4** in $CDCl_3$.

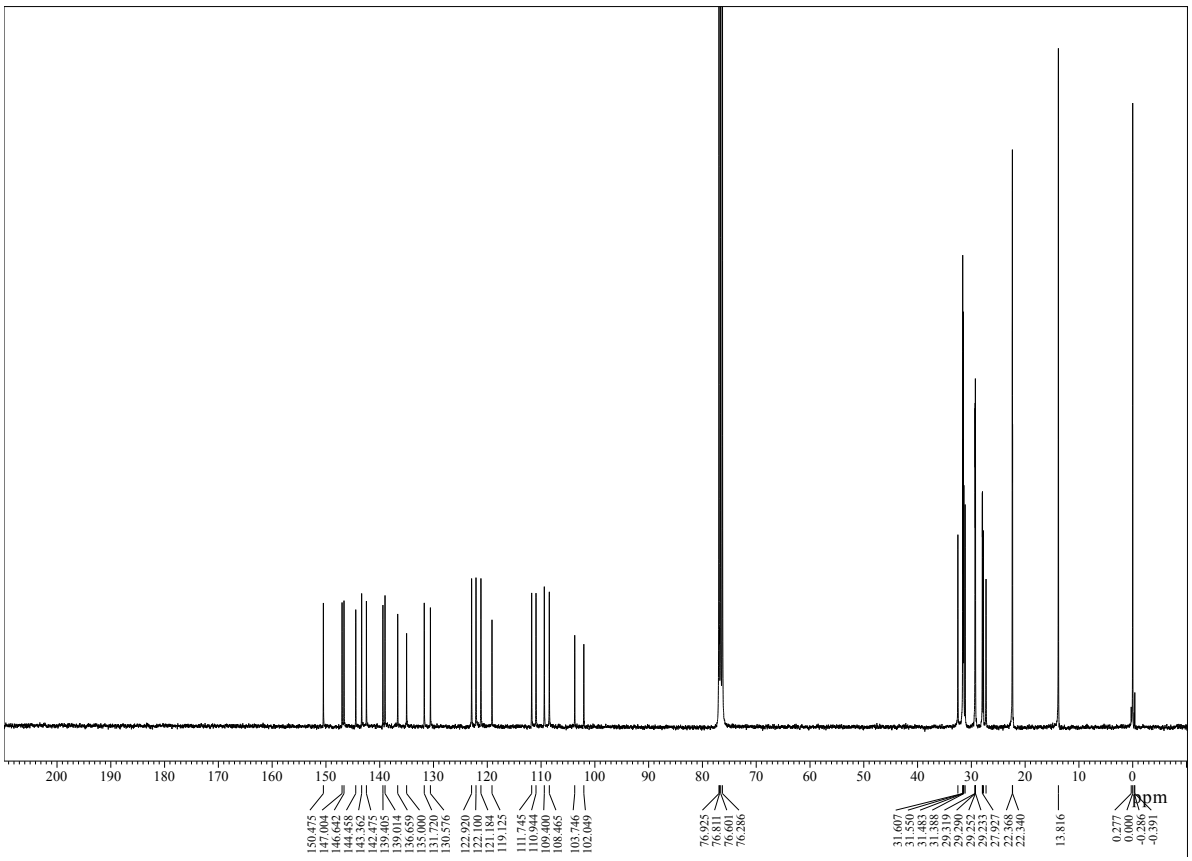

$^{13}C\{^{1}H\}$ NMR spectrum of **4** in $CDCl_3$.

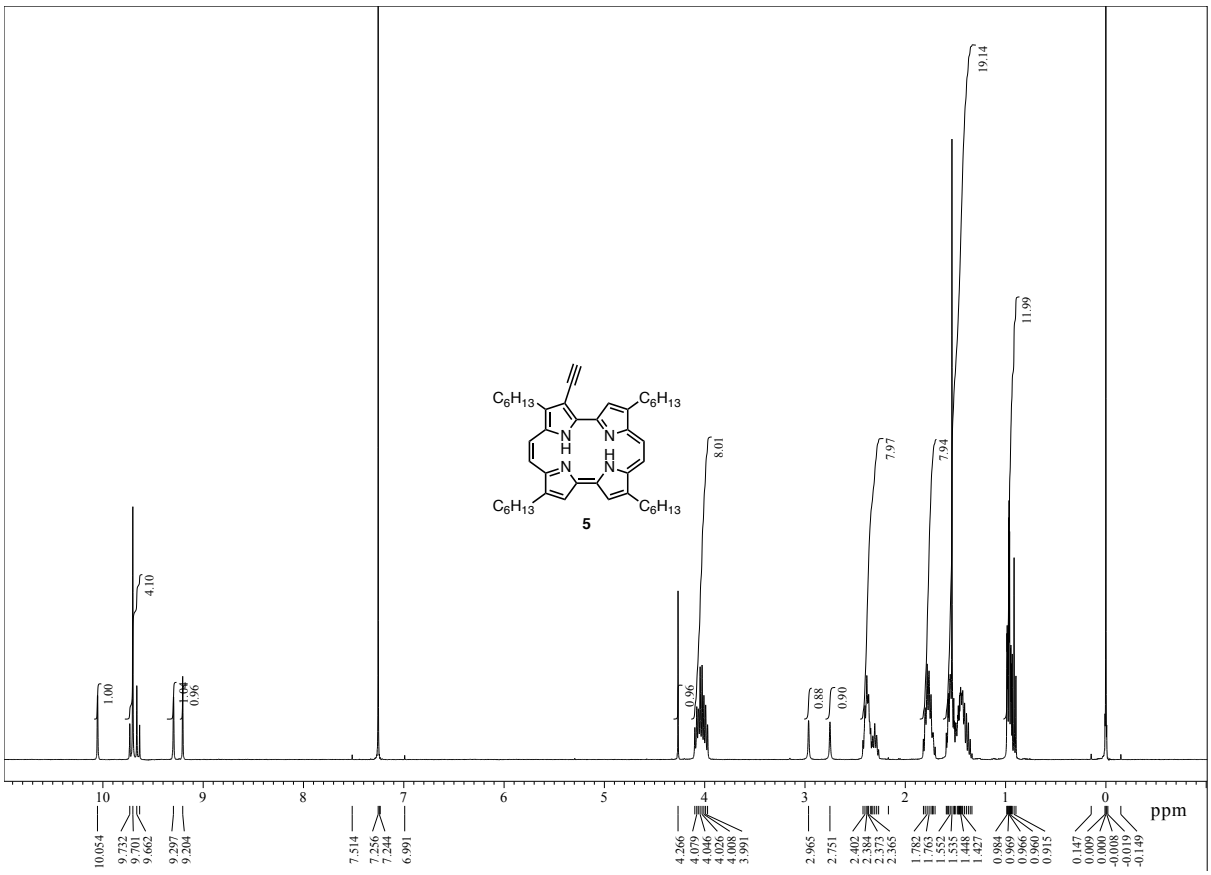

^{1}H NMR spectrum of **5** in $CDCl_3$.

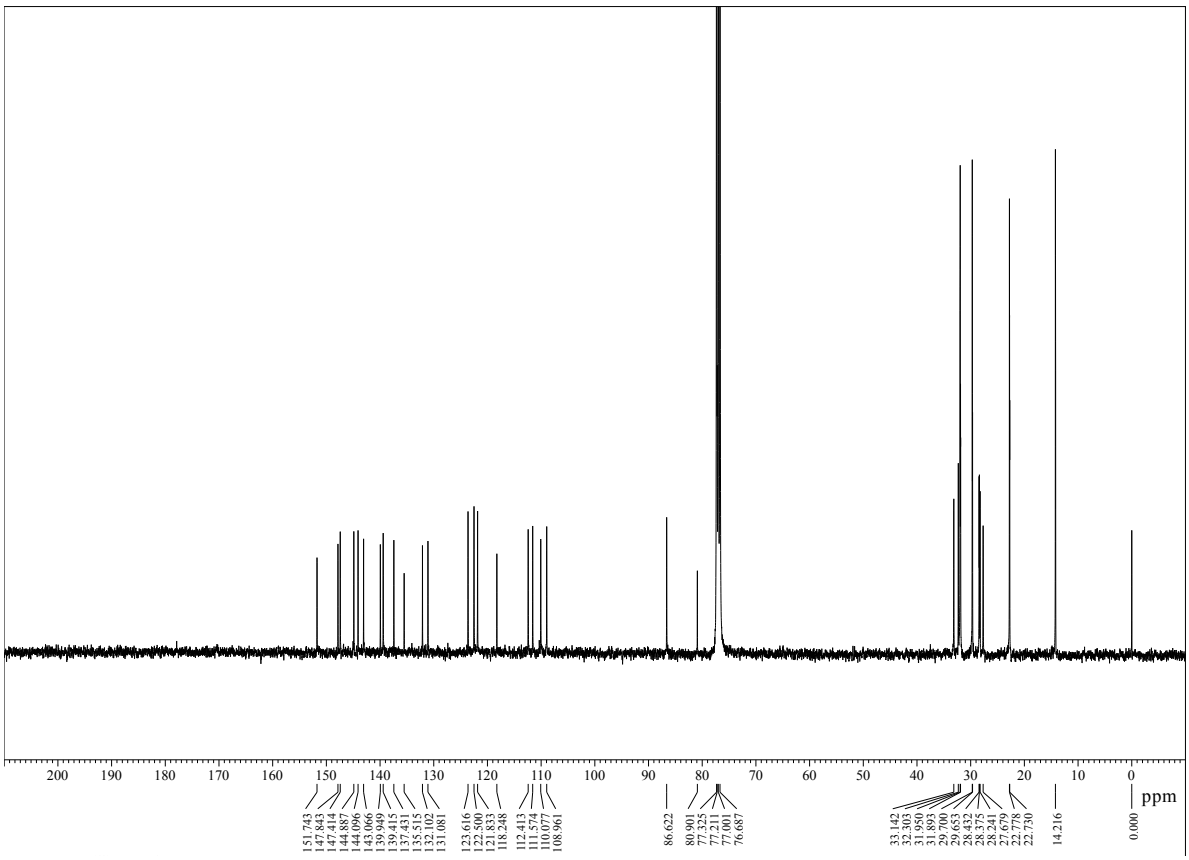

$^{13}C\{^{1}H\}$ NMR spectrum of **5** in $CDCl_3$.

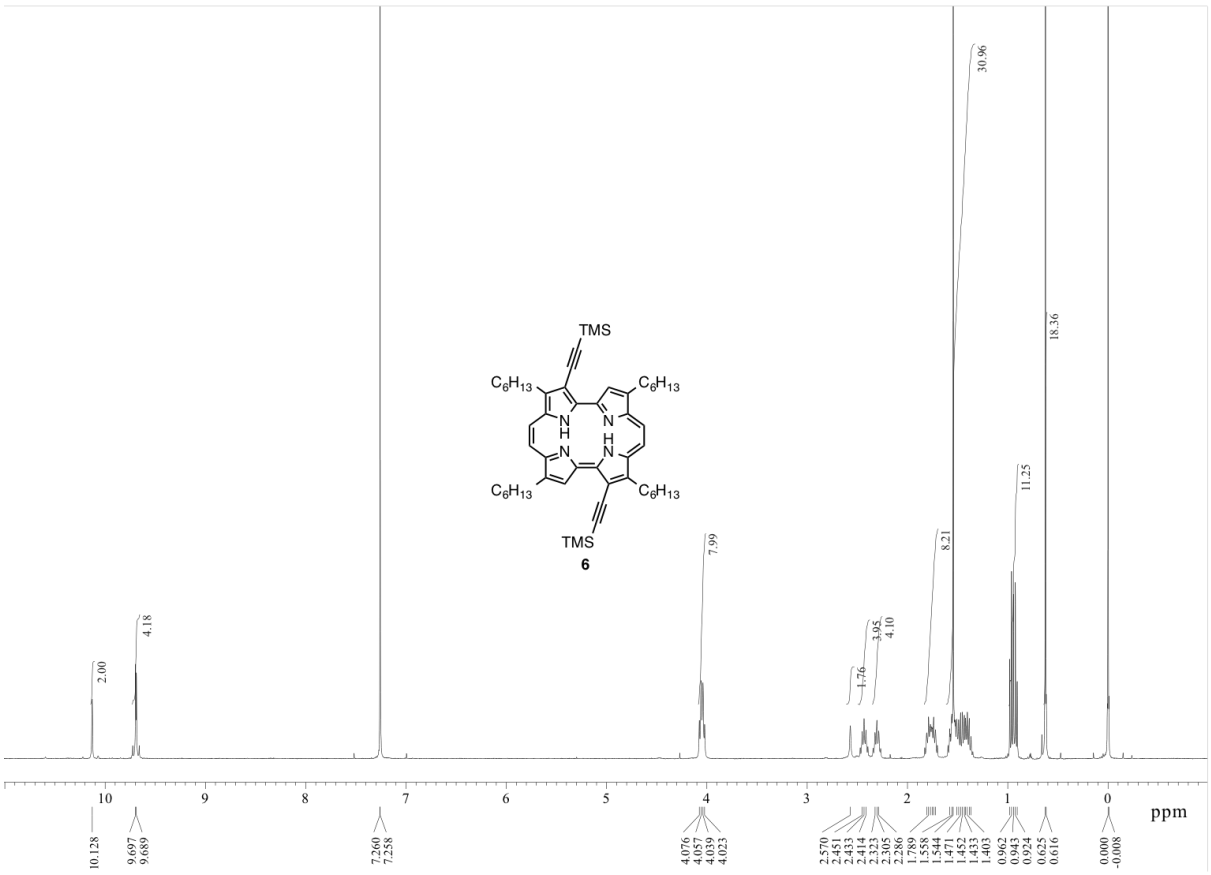

^{1}H NMR spectrum of **6** in $CDCl_3$.

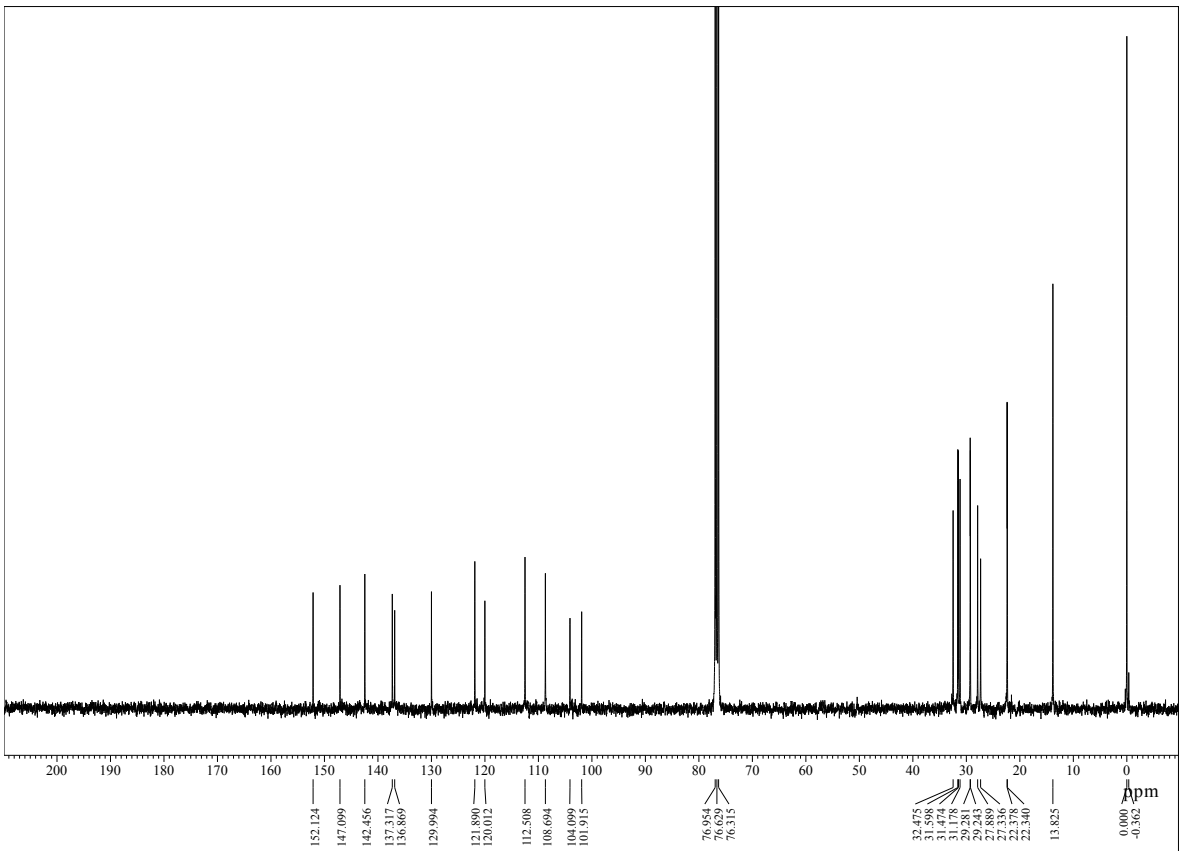

$^{13}C\{^1H\}$ NMR spectrum of **6** in $CDCl_3$.

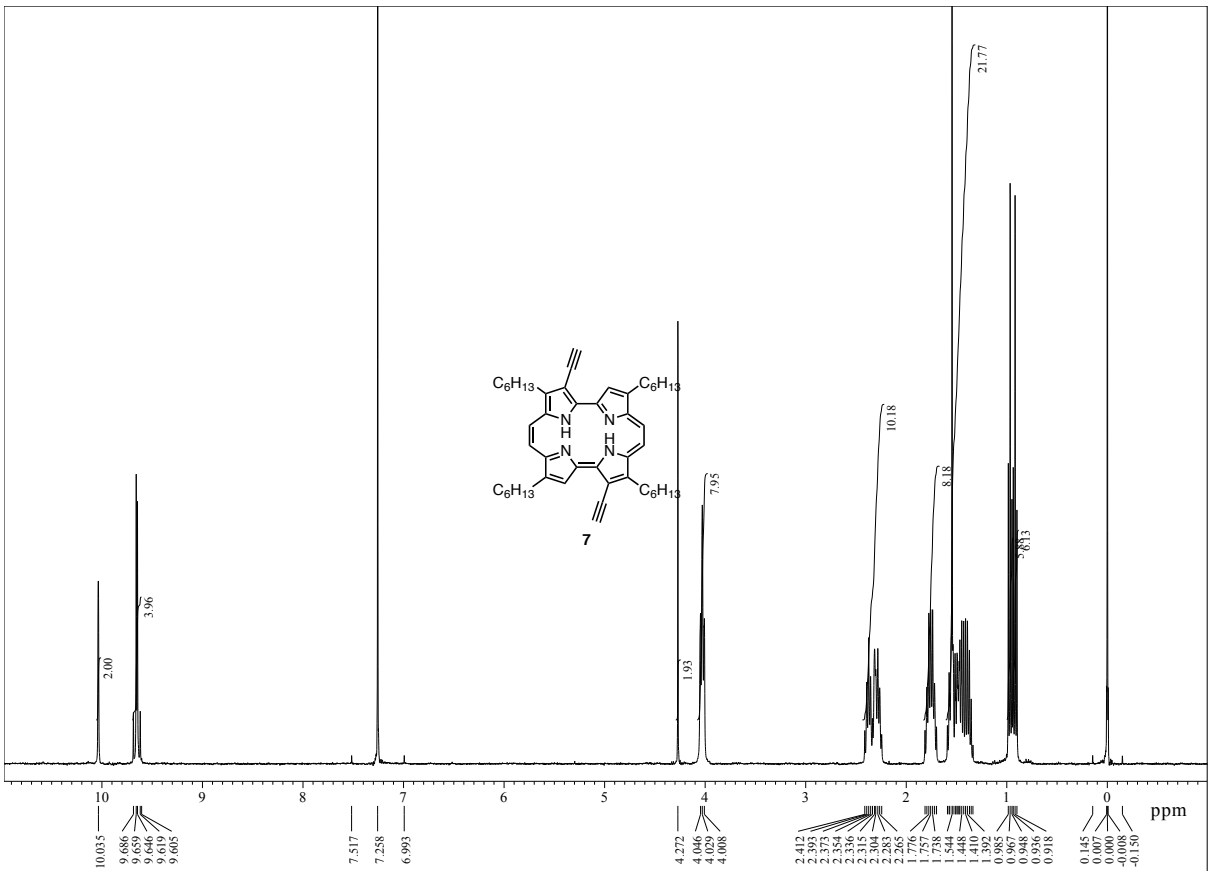

^{1}H NMR spectrum of **7** in $CDCl_3$.

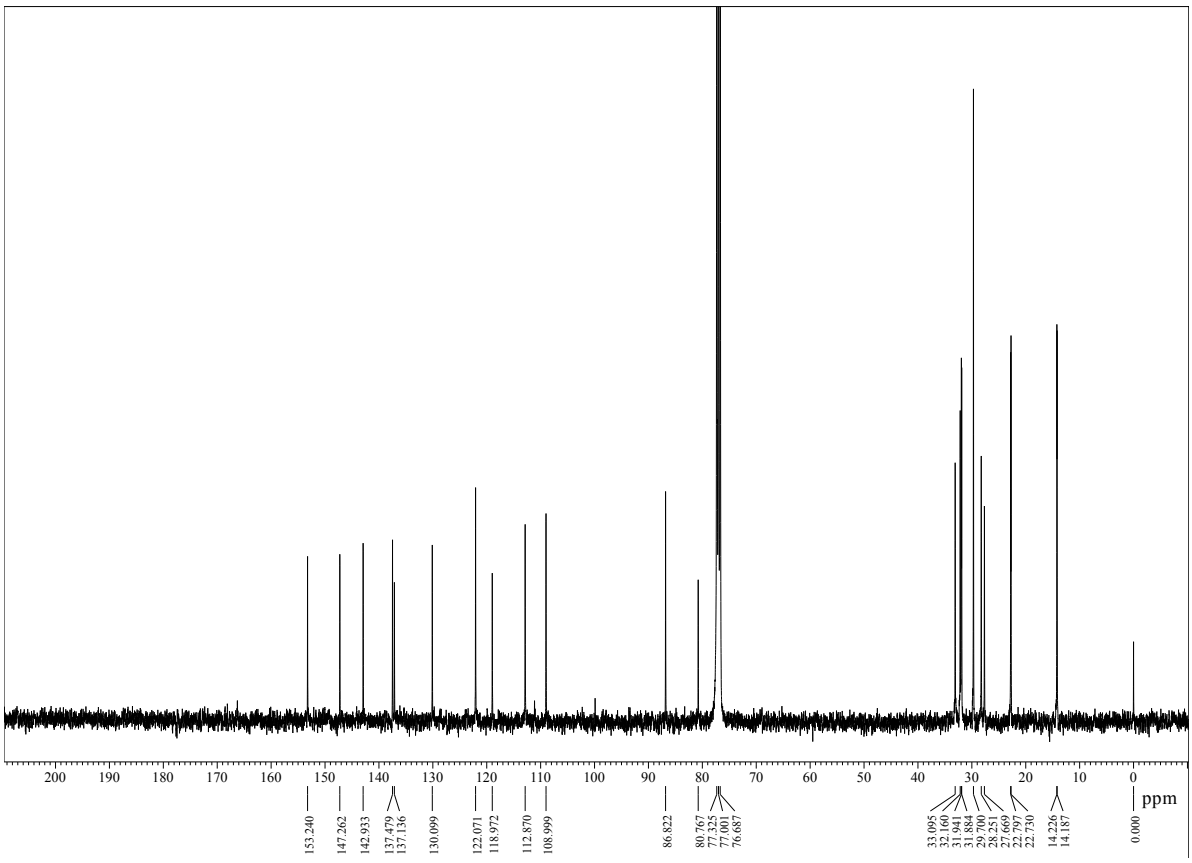

$^{13}C\{^{1}H\}$ NMR spectrum of **7** in $CDCl_3$.

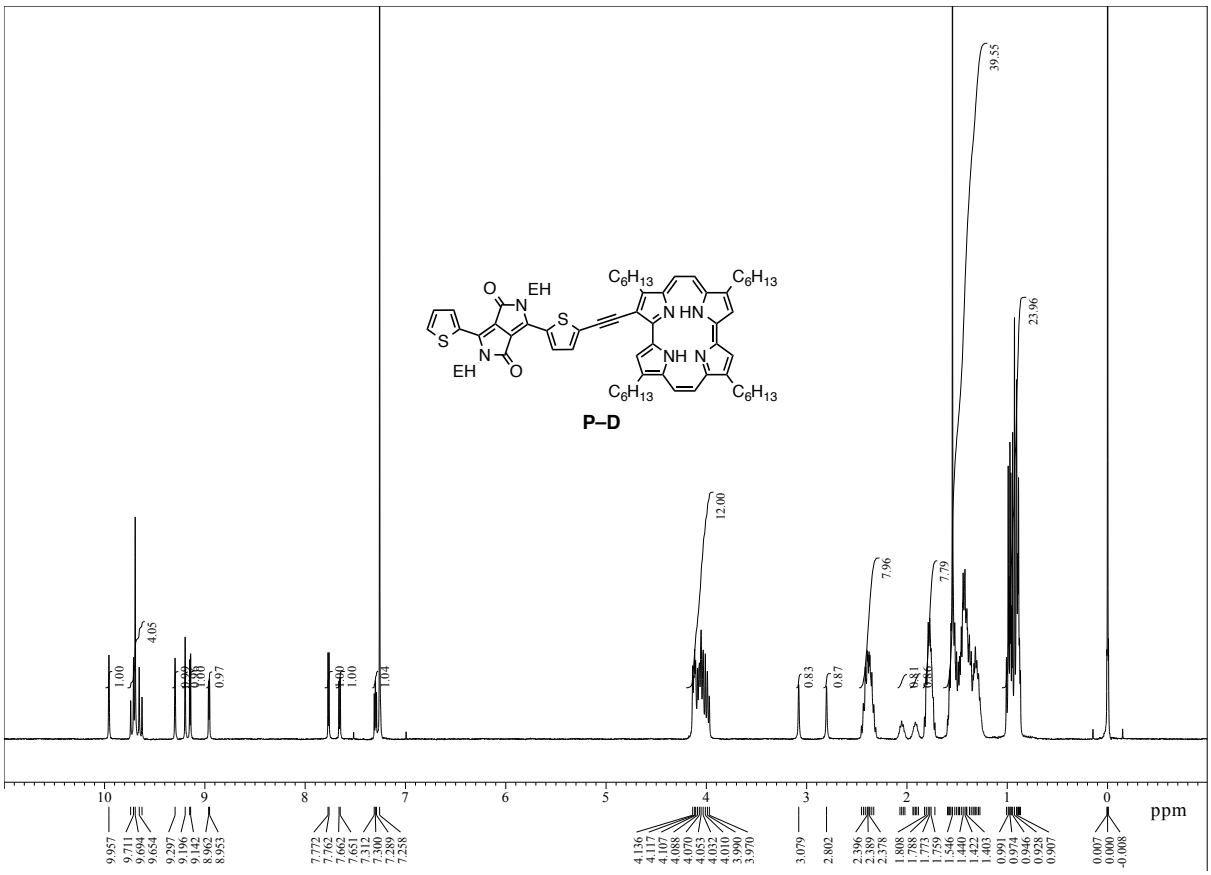

^{1}H NMR spectrum of **P–D** in $CDCl_3$.

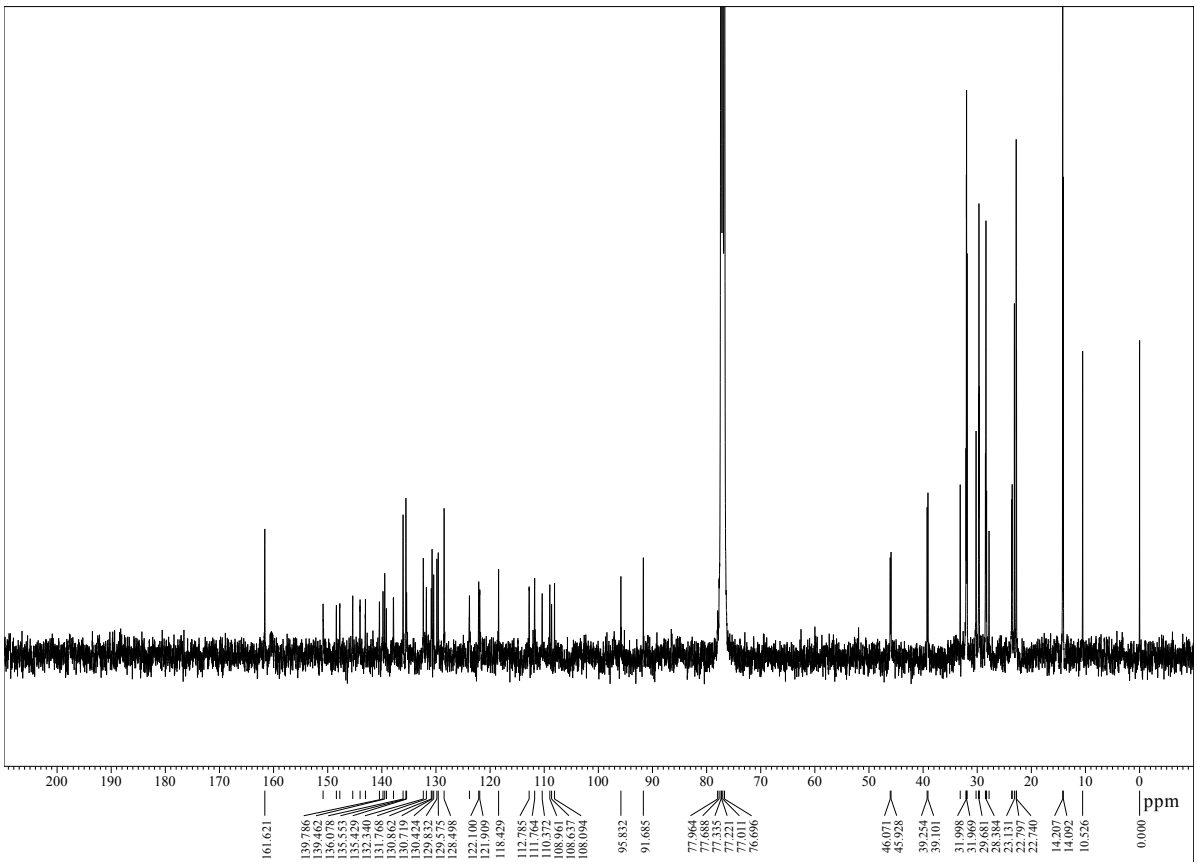

$^{13}C\{^{1}H\}$ NMR spectrum of **P–D** in $CDCl_3$.

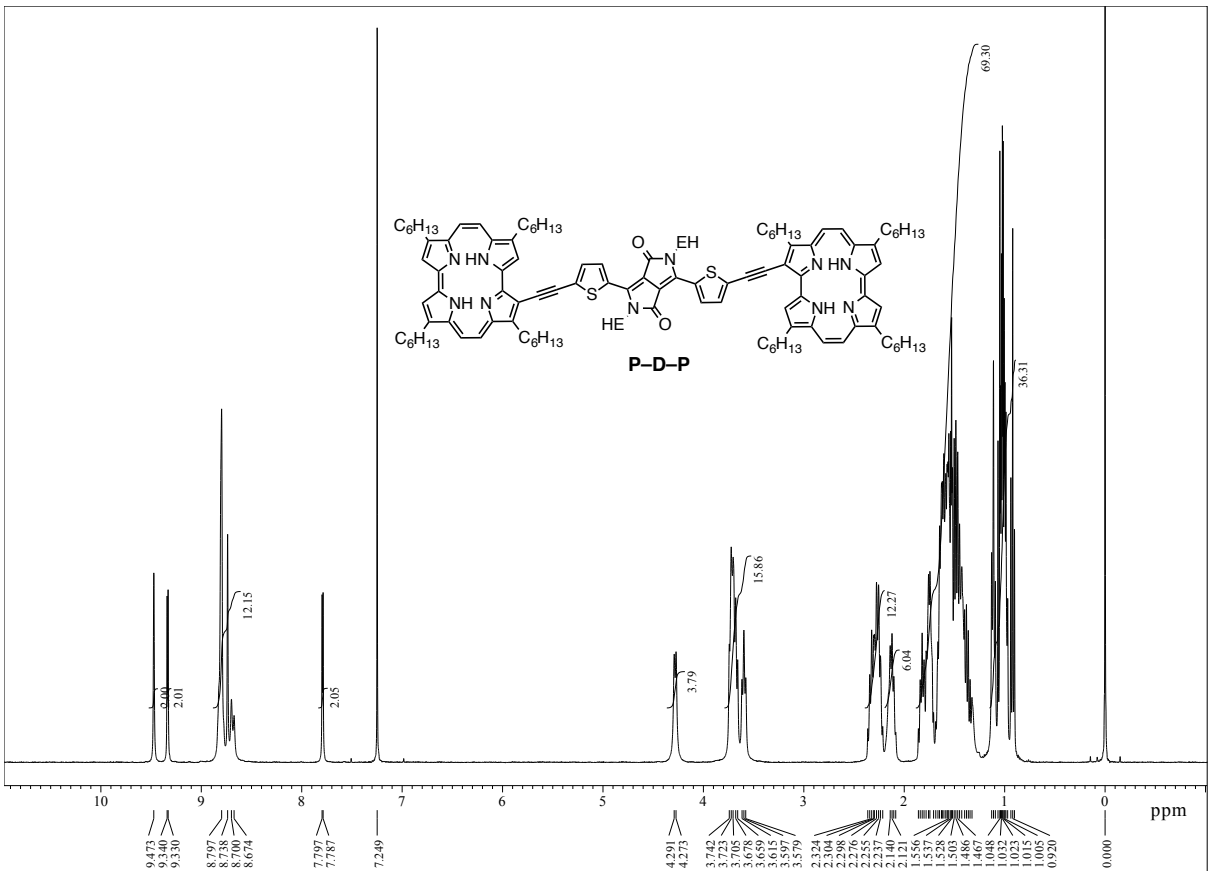

^{1}H NMR spectrum of **P–D–P** in $CDCl_3$.

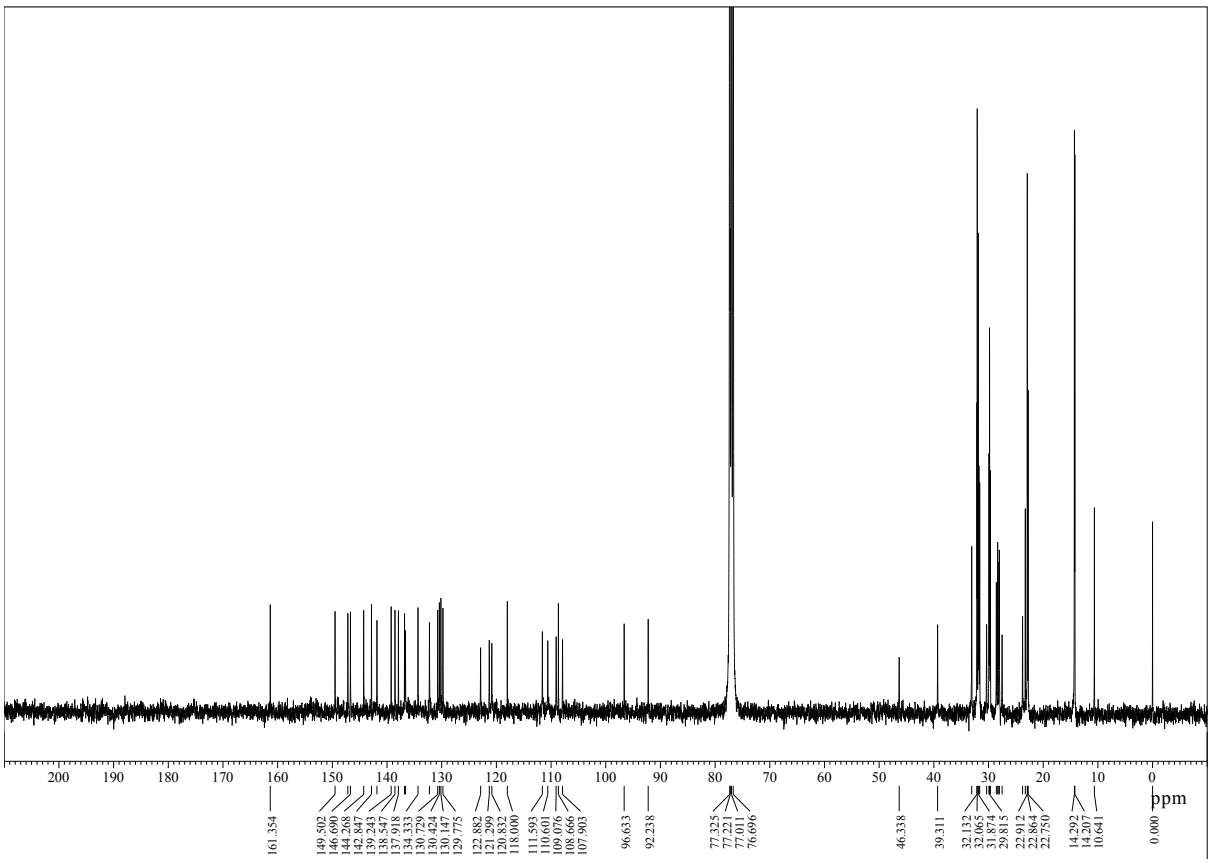

$^{13}C\{^{1}H\}$ NMR spectrum of **P–D–P** in $CDCl_3$.

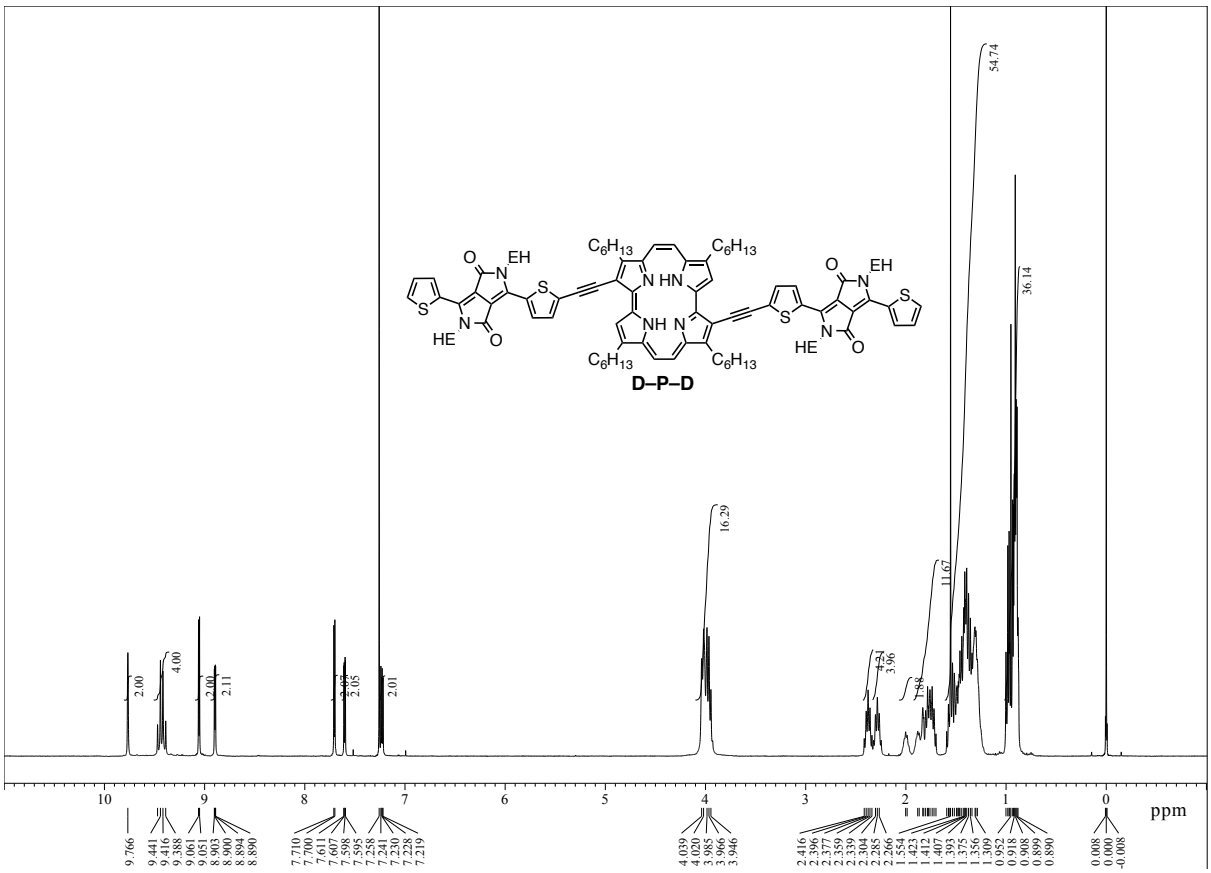

^{1}H NMR spectrum of **D–P–D** in $CDCl_3$.

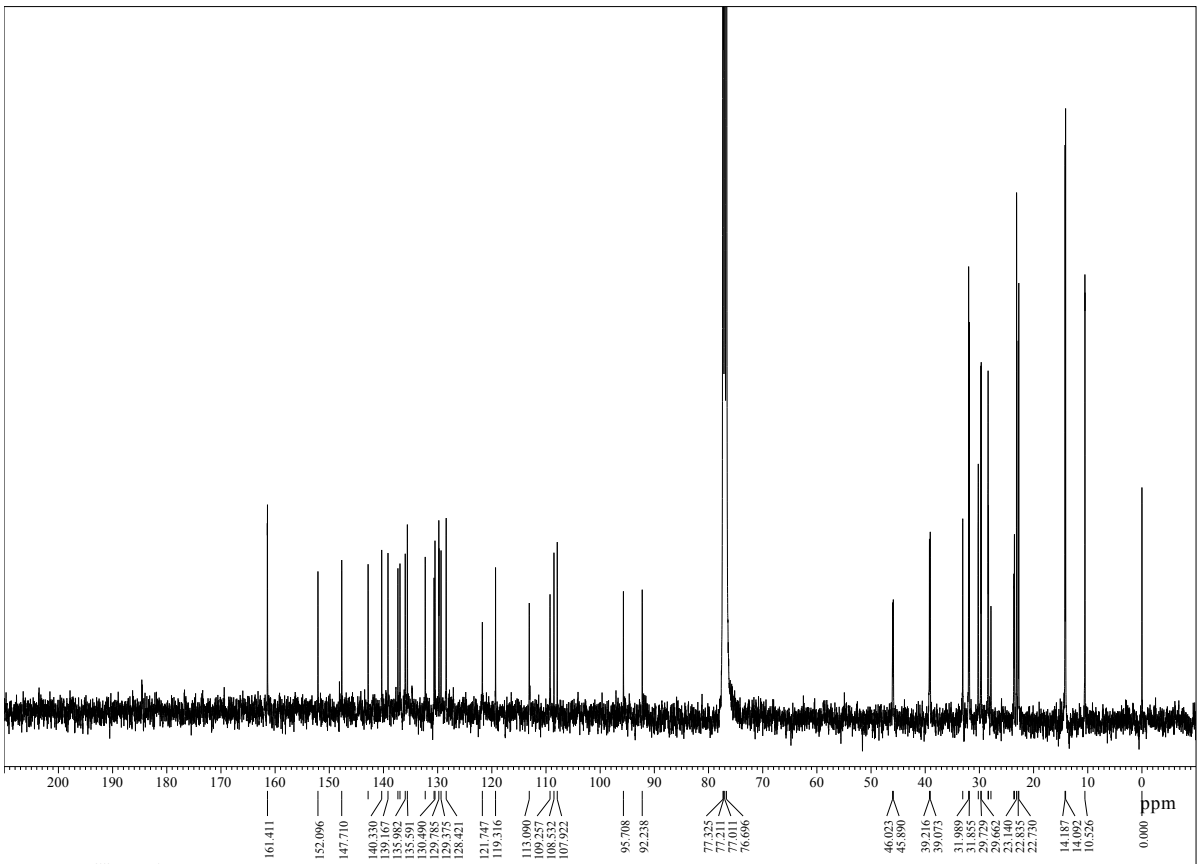

$^{13}C\{^{1}H\}$ NMR spectrum of **D–P–D** in $CDCl_3$.

2-6. Reference

(1) ASTM G173-03(2012), Standard Tables for Reference Solar Spectral Irradiances: Direct Normal and Hemispherical on 37° Tilted Surface, ASTM International, West Conshohocken, PA, 2012, www.astm.org.

(2) He, Y.; Li, Y. Fullerene Derivative Acceptors for High Performance Polymer Solar Cells. *Phys*. *Chem*. *Chem*. *Phys*. **2011**, *13* (6), 1970–1983.

(3) Tang, A.; Zhan, C.; Yao, J. Series of Quinoidal Methyl-Dioxocyano-Pyridine Based π-Extended Narrow-Bandgap Oligomers for Solution-Processed Small-Molecule Organic Solar Cells. *Chem. Mater.* **2015**, *27* (13), 4719–4730.

(4) Zhang, L.; Andrew, T. L. Improved Photovoltaic Response of a Near-Infrared Sensitive Solar Cell by a Morphology-Controlling Seed Layer. *Org*. *Electron*. **2016**, *33* (C), 135–141.

(5) Zitzler-Kunkel, A.; Lenze, M. R.; Kronenberg, N. M.; Krause, A.-M.; Stolte, M.; Meerholz, K.; Würthner, F. NIR-Absorbing Merocyanine Dyes for BHJ Solar Cells. *Chem. Mater.* **2014**, *26* (16), 4856–4866.

(6) Narayanaswamy, K.; Venkateswararao, A.; Gupta, V.; Chand, S.; Singh, S. P. NIR Absorbing D–π–A–π–D Structured Diketopyrrolopyrrole–Dithiafulvalene Based Small Molecule for Solution Processed Organic Solar Cells. *Chem. Commun.* **2015**, *52*, 210–213.

(7) Wang, S.; Hall, L.; Diev, V. V.; Haiges, R.; Wei, G.; Xiao, X.; Djurovich, P. I.; Forrest, S. R.; Thompson, M. E. *N*,*N*-Di Arylanilinosquaraines and Their Application to Organic Photovoltaics. *Chem. Mater.* **2011**, *23* (21), 4789–4798.

(8) Mayerhöffer, U.; Deing, K.; Gruß, K.; Braunschweig, H.; Meerholz, K.; Würthner, F. Outstanding Short-Circuit Currents in BHJ Solar Cells Based on NIR-Absorbing Acceptor-Substituted Squaraines. *Angew. Chem. Int. Ed.* **2009**, *48* (46), 8776–8779.

(9) Bura, T.; Leclerc, N.; Fall, S.; Lévêque, P.; Heiser, T.; Retailleau, P.; Rihn, S.; Mirloup, A.; Ziessel, R. High-Performance Solution-Processed Solar Cells and Ambipolar Behavior in Organic Field-Effect Transistors with Thienyl-BODIPY Scaffoldings. *J. Am. Chem. Soc.* **2012**, *134* (42), 17404–17407.

(10) Vogel, E.; Köcher, M.; Schmickler, H.; Lex, J. Porphycene—a Novel Porphin Isomer. *Angew*. *Chem*. *Int*. *Ed*. **1986**, *25* (3), 257.

(11) Waluk, J.; Muller, M.; Swiderek, P.; Kocher, M.; Vogel, E.; Hohlneicher, G.; Michl, J. Electronic States of Porphycenes. *J. Am. Chem. Soc.* **1991**, *113* (15), 5511–5527.

(12) Baba, T.; Shimakoshi, H.; Hisaeda, Y. Synthesis and Simple Separation of *β*-Pyrrole Sulfonated Porphycenes. *Tetrahedron Lett*. **2004**, *45* (31), 5973–5975.

(13) Okawara, T.; Abe, M.; Hisaeda, Y. Synthesis of a Series of Multiply Meso-Acetoxylated Porphycenes. *Tetrahedron Lett*. **2014**, *55* (45), 6193–6197.

(14) Kuzuhara, D.; Mack, J.; Yamada, H.; Okujima, T.; Ono, N.; Kobayashi, N. Synthesis, Structures, and Optical and Electrochemical Properties of Benzoporphycenes. *Chem*. *Eur*. *J*. **2009**, *15* (39), 10060–10069.

(15) Richert, C.; Wessels, J. M.; Müeller, M.; Kisters, M.; Benninghaus, T.; Goetz, A. E. Photodynamic Antitumor Agents: *β*-Methoxyethyl Groups Give Access to Functionalized Porphycenes and Enhance Cellular Uptake and Activity. *J. Med. Chem.* **1994**, *37* (17), 2797–2807.

(16) Gottfried, V.; Davidi, R.; Averbuj, C.; Kimel, S. In-vivo damage to chorioallantoic membrane blood-vessels by porphycene-induced photodynamic therapy. *J. Photochem*. *Photobiol*. *B* **1995**, *30*, 115–121.

(17) Shimakoshi, H.; Baba, T.; Iseki, Y.; Aritome, I.; Endo, A.; Adachi, C.; Hisaeda, Y. Photophysical and Photosensitizing Properties of Brominated Porphycenes. *Chem. Commun.* **2008**, *0* (25), 2882.

(18) Czerski, I.; Listkowski, A.; Nawrocki, J.; Urbańska, N.; Piwoński, H.; Sokołowski, A.; Pietraszkiewicz, O.; Pietraszkiewicz, M.; Waluk, J. The Long and Winding Road to New Porphycenes. *J*. *Porphyrins Phthalocyanines* **2012**, *16* (05n06), 589–602.

(19) Castanet, A.-S.; Colobert, F.; Broutin, P.-E. Mild and Regioselective Iodination of Electron-Rich Aromatics with *N*-Iodosuccinimide and Catalytic Trifluoroacetic Acid. *Tetrahedron Lett*. **2002**, *43* (29), 5047–5048.

(20) Smith, K.; James, D. M.; Mistry, A. G.; Bye, M. R.; Faulkner, D. J. A new method for bromination of carbazoles, *β*-carbolines and iminodibenzyls by use of *N*-bromosuccinimide and silica gel *Tetrahedron* **1992**, *48* (36), 7479.

(21) Waluk, J.; Muller, M.; Swiderek, P.; Köcher, M.; Vogel, E.; Hohlneicher, G.; Michl, J. Electronic states of porphycenes. *J*. *Am*. *Chem*. *Soc*. **1991**, *113* (15), 5511–5527.

(22) Sessler, J. L.; Brucker, E. A.; Lynch, V.; Choe, M.; Sorey, S.; Vogel, E. Solution Phase and Single Crystal Diffraction X-ray Analyses of Diprotonated Porphyrin Isomers—Etioporphyrin, Etioporphycene, and Etiocorrphycene Bishydroperchlorate Salts. *Chem*. *Eur*. *J*. **1996**, *2* (12), 1527–1532.

(23) Kuzuhara, D.; Sakaguchi, M.; Furukawa, W.; Okabe, T.; Aratani, N.; Yamada, H. Synthesis, Characterization and Protonation Behavior of Quinoxaline-Fused Porphycenes. *Molecules* **2017**, *22* (6), 908–915.

(24) Lau, K. S. F.; Zhao, S.; Ryppa, C.; Jockusch, S.; Turro, N. J.; Zeller, M.; Gouterman,

M.; Khalil, G. E.; Brückner, C. Synthesis, Structure, and Optical Properties of the Platinum(II) Complexes of Indaphyrin and Thiaindaphyrin. *Inorg. Chem.* **2009**, *48* (9), 4067–4074.

(25) Li, L.; Huang, Y.; Peng, J.; Cao, Y.; Peng, X. Enhanced Performance of Solution-Processed Solar Cells Based on Porphyrin Small Molecules with a Diketopyrrolopyrrole Acceptor Unit and a Pyridine Additive. *J. Mater. Chem. A* **2013**, *1* (6), 2144–2150.

(26) Frisch, M. J.; Trucks, G. W.; Schlegel, H. B.; Scuseria, G. E.; Robb, M. A.; Cheeseman, J. R.; Scalmani, G.; Barone, V.; Mennucci, B.; Petersson, G. A.; Nakatsuji, H.; Caricato, M.; Li, X.; Hratchian, H. P.; Izmaylov, A. F.; Bloino, J.; Zheng, G.; Sonnenberg, J. L.; Hada, M.; Ehara, M.; Toyota, K.; Fukuda, R.; Hasegawa, J.; Ishida, M.; Nakajima, T.; Honda, Y.; Kitao, O.; Nakai, H.; Vreven, T.; Montgomery, J. A., Jr.; Peralta, J. E.; Ogliaro, F.; Bearpark, M.; Heyd, J. J.; Brothers, E.; Kudin, K. N.; Staroverov, V. N.; Kobayashi, R.; Normand, J.; Raghavachari, K.; Rendell, A.; Burant, J. C.; Iyengar, S. S.; Tomasi, J.; Cossi, M.; Rega, N.; Millam, N. J.; Klene, M.; Knox, J. E.; Cross, J. B.; Bakken, V.; Adamo, C.; Jaramillo, J.; Gomperts, R.; Stratmann, R. E.; Yazyev, O.; Austin, A. J.; Cammi, R.; Pomelli, C.; Ochterski, J. W.; Martin, R. L.; Morokuma, K.; Zakrzewski, V. G.; Voth, G. A.; Salvador, P.; Dannenberg, J. J.; Dapprich, S.; Daniels, A. D.; Farkas, Ö .; Foresman, J. B.; Ortiz, J. V.; Cioslowski, J.; Fox, D. J. *Gaussian09*; Gaussian, Inc.: Wallingford, CT, 2009.

(27) Ariu, M.; Sims, M.; Rahn, M. D.; Hill, J.; Fox, A. M.; Lidzey, D. G.; Oda, M.; Cabanillas-Gonzalez, J.; Bradley, D. D. C. Exciton Migration in B-Phase Poly(9,9-Dioctylfluorene). *Phys. Rev. B* **2003**, *67* (19), 402–411.

(28) Scharber, M. C.; Mühlbacher, D.; Koppe, M.; Denk, P.; Waldauf, C.; Heeger, A. J.; Brabec, C. J. Design Rules for Donors in Bulk-Heterojunction Solar Cells—Towards 10 % Energy-Conversion Efficiency. *Adv. Mater.* **2006**, *18* (6), 789–794.

(29) Pommerehne, J.; Vestweber, H.; Guss, W.; Mahrt, R. F.; Bässler, H.; Porsch, M.; Daub, J. Efficient two layer leds on a polymer blend basis. *Adv. Mater.* **1995**, *7* (6), 551–554.

(30) van der Poll, T. S.; Love, J. A.; Nguyen, T.-Q.; Bazan, G. C. Non-Basic High-Performance Molecules for Solution-Processed Organic Solar Cells. *Adv. Mater.* **2012**, *24* (27), 3646–3649.

(31) Gomez, E. D.; Barteau, K. P.; Wang, H.; Toney, M. F.; Loo, Y.-L. Correlating the Scattered Intensities of P3HT and PCBM to the Current Densities of Polymer Solar Cells. *Chem. Commun.* **2011**, *47* (1), 436–438.

(32) Osaka, I.; Saito, M.; Koganezawa, T.; Takimiya, K. Thiophene-Thiazolothiazole Copolymers: Significant Impact of Side Chain Composition on Backbone Orientation and

Solar Cell Performances. *Adv. Mater.* **2013**, *26* (2), 331–338.

(33) Najari, A.; Beaupré, S.; Allard, N.; Ouattara, M.; Pouliot, J.-R.; Charest, P.; Besner, S.; Simoneau, M.; Leclerc, M. Thieno, Furo, and Selenopheno[3,4-*c*]pyrrole-4,6-dione Copolymers: Air-Processed Polymer Solar Cells with Power Conversion Efficiency Up to 7.1%. *Adv. Energy Mater.* **2015**, *5* (23), 1501213–1501219.

(34) Takahashi, K.; Kumagai, D.; Yamada, N.; Kuzuhara, D.; Yamaguchi, Y.; Aratani, N.; Koganezawa, T.; Koshika, S.; Yoshimoto, N.; Masuo, S.; Suzuki, M.; Nakayama, K.-I.; Yamada, H. Side-Chain Engineering in a Thermal Precursor Approach for Efficient Photocurrent Generation. *J. Mater. Chem. A* **2017**, *5* (27), 14003–14011.

(35) Zhang, G.; Zhang, K.; Yin, Q.; Jiang, X.-F.; Wang, Z.; Xin, J.; Ma, W.; Yan, H.; Huang, F.; Cao, Y. *J. Am. Chem. Soc.* **2017**, *139* (6), 2387.

(36) Deng, D.; Zhang, Y.; Zhang, J.; Wang, Z.; Zhu, L.; Fang, J.; Xia, B.; Wang, Z.; Lu, K.; Ma, W.; Wei, Z. Fluorination-Enabled Optimal Morphology Leads to Over 11% Efficiency for Inverted Small-Molecule Organic Solar Cells. *Nat. Commun.* **2016**, *7*, 1–9.

(37) Jung, M.; Yoon, Y.; Park, J. H.; Cha, W.; Kim, A.; Kang, J.; Gautam, S.; Seo, D.; Cho, J. H.; Kim, H.; Choi, J. Y.; Chae, K. H.; Kwak, K.; Son, H. J.; Ko, M. J.; Kim, H.; Lee, D.-K.; Kim, J. Y.; Choi, D. H.; Kim, B. Nanoscopic Management of Molecular Packing and Orientation of Small Molecules by a Combination of Linear and Branched Alkyl Side Chains. *ACS Nano* **2014**, *8* (6), 5988–6003.

(38) Sun, K.; Xiao, Z.; Hanssen, E.; Klein, M. F. G.; Dam, H. H.; Pfaff, M.; Gerthsen, D.; Wong, W. W. H.; Jones, D. J. The Role of Solvent Vapor Annealing in Highly Efficient Air-Processed Small Molecule Solar Cells. *J. Mater. Chem.* **2014**, *2* (24), 9048–9054.

(39) Li, G.; Shrotriya, V.; Huang, J.; Yao, Y.; Moriarty, T.; Emery, K.; Yang, Y. High-Efficiency Solution Processable Polymer Photovoltaic Cells by Self-Organization of Polymer Blends. *Nat. Mater.* **2005**, *4* (11), 864–868.

(40) Proctor, C. M.; Love, J. A.; Nguyen, T.-Q. Mobility Guidelines for High Fill Factor Solution-Processed Small Molecule Solar Cells. *Adv. Mater.* **2014**, *26* (34), 5957.

(41) Spek, A. L. PLATON, A Multipurpose Crystallographic Tool, Utrecht, The Netherlands, 2005.

(42) Particle Size Distribution and X-Ray Diffraction Peak Profiles in Supersaturated Solid Solutions. *Acta Crystallogr. Sect. A* **1990**, *46* (3), 187–194.

(43) Sheldrick, G. M. A Short History of SHELX. *Acta Cryst.* **2007**, *64* (1), 112–122.

(44) Zhou, E.; Wei, Q.; Yamakawa, S.; Zhang, Y.; Tajima, K.; Yang, C.; Hashimoto, K. Diketopyrrolopyrrole-Based Semiconducting Polymer for Photovoltaic Device with

Photocurrent Response Wavelengths Up to 1.1 μm. *Macromolecules* **2010**, *43* (2), 821–826. (1)

Chapter 3

Synthesis and Photovoltaic Performances of Porphycene Dimers as n-Type Materials

---

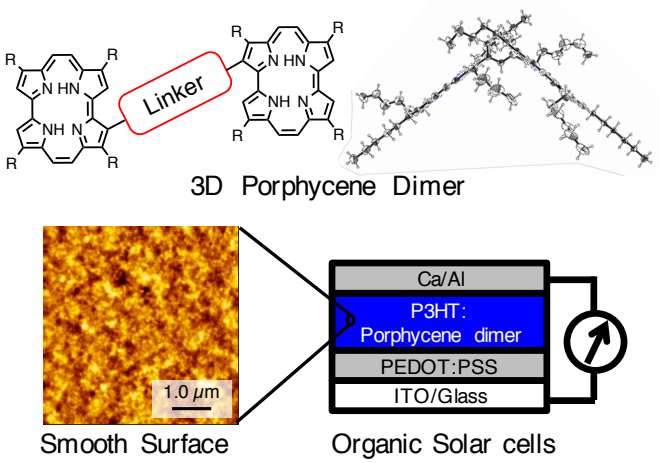

In this chapter, the 3D conformation tuning by choice of the linker unit in the porphycene dimer system, and the optoelectronic and photovoltaic properties of porphycene dimers as n-type semiconducting materials are described.

3-1. Introduction

Fullerene derivatives are known as superior n-type materials for organic solar cells (OSCs) because of the high electron affinity, good electron mobility, and provision of suitable morphology.[1–3] However, most of the fullerene derivatives, such as [6,6]-phenyl-C_{61}-butyric acid methyl ester ($PC_{61}BM$), have a poor absorption intensity in the visible to near-infrared (NIR) region (Figure 3-1).

In order to overcome this absorption problem of fullerene derivatives several three dimensional (3D) dimeric small molecules have been reported as non-fullerene n-type materials for OSCs.[4–11] These compounds show both of strong absorption in the visible to NIR regions and good electron mobility. Zhang et al. reported a perylene diimide (PDI) dimer as a novel non-fullerene n-type material in 2013 (Figure 3-2a).[4] A dimeric PDI (Bis-PDI-T-EG) showed a best PCE of 4.03%, whereas a PDI monomer gave a PCE of only 0.13% when they were each blended with the conjugated polymer PBDTTT-C-T. PDI has a highly planar structure and shows a strong π–π stacking which induces the strong aggregations leading to large phase separation domains in bulk-heterojunction (BHJ) blend films. In contrast, the dimeric structure of Bis-PDI-T-EG produced a 3D structure. Such 3D molecular architecture prevented the aggregation and created small domain morphology with p-type materials suitable for OSC in BHJ films. Also, the 3D molecular architecture enabled anisotropic electron transport.

In this context, the device performance of DBFI–EDOT showed a power-conversion efficienty (PCE) of 8.5% in combination with thiazolothiazole-dithienosilole copolymer (PSEHTT) and PBDTT-FTTE as a ternary blend system (Figure 3-2b).[5] However, the molecular variation of n-type materials is still limited to several skeletons. For the further development of OSCs, new generation of non-fullerene n-type materials would be highly beneficial.

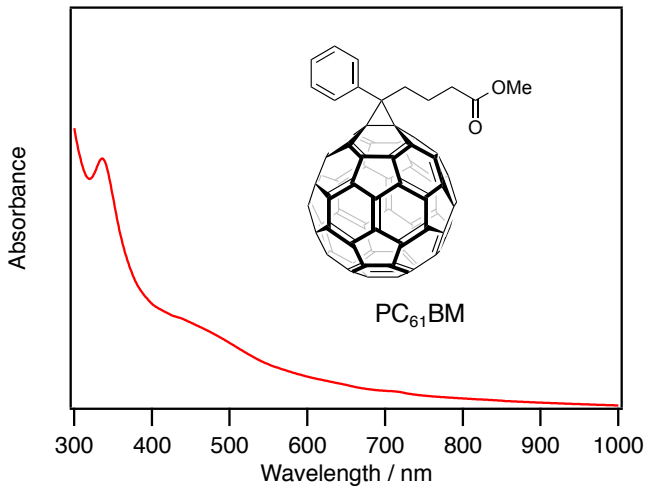

Figure 3-1. Molecular structure and UV–Vis–NIR absorption spectrum of a $PC_{61}BM$ thin film.

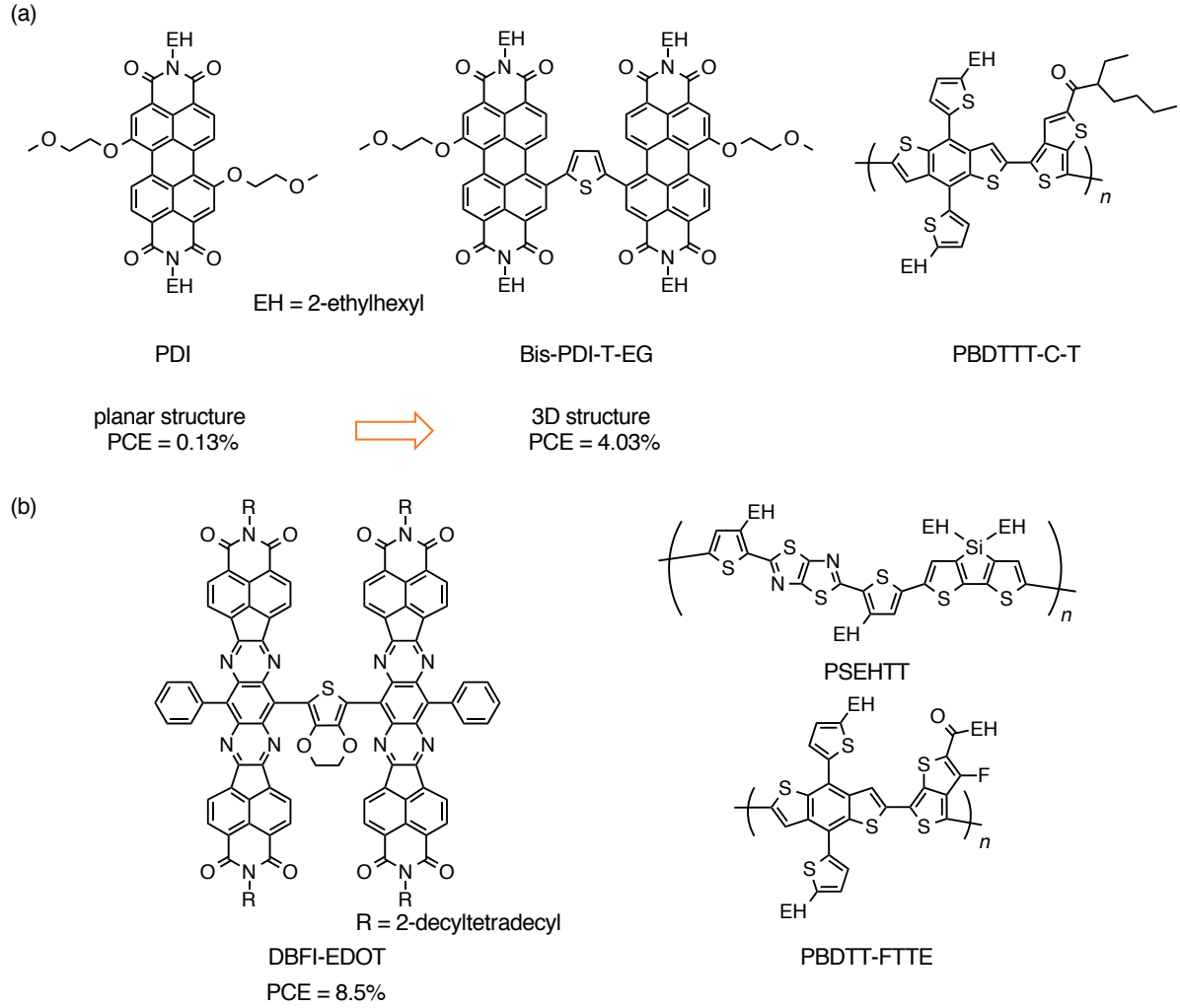

Figure 3-2. Non-fullerene n-type materials based on 3D dimeric structures: (a) PDI dimer Bis-PDI-T-EG system and (b) ternary blend system with DBFI-EDOT.

Chapter 2 has described that porphycene has a relatively small optical band gap associated with a low-lying LUMO, and is used as key building block electron acceptor unit and NIR absorbers (Figure 3-3).[12–14] This characteristic makes porphycene a promising building unit of dimeric n-type materials.

Taking into consideration of these backgrounds, this project aims for the development of novel n-type materials with 3D structure based on porphycene. The following sections in this chapter describe the synthesis of porphycene dimers with three types of linkage, *m*-phenylene (**Pc2-Ph**), 2,5-thienylene (**Pc2-Th**), and butadiyne (**Pc2-B**) and their 3D architectures revealed by single-crystal X-ray diffraction analysis (Figure 3-4). In addition, the potential of the dimers as n-type materials in OSCs is examined.

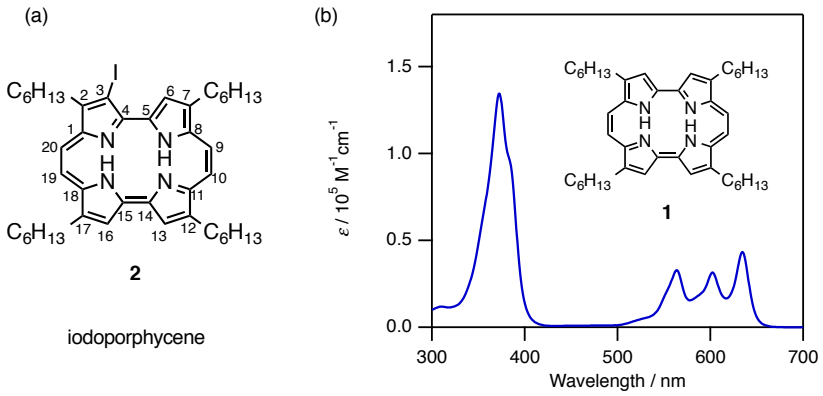

Figure 3-3. (a) Chemical structure of iodoporphycene with its atom numbering; (b) Absorption spectra of 2,7,12,17-tetrahexylporphycene (**1**) in $CHCl_3$.

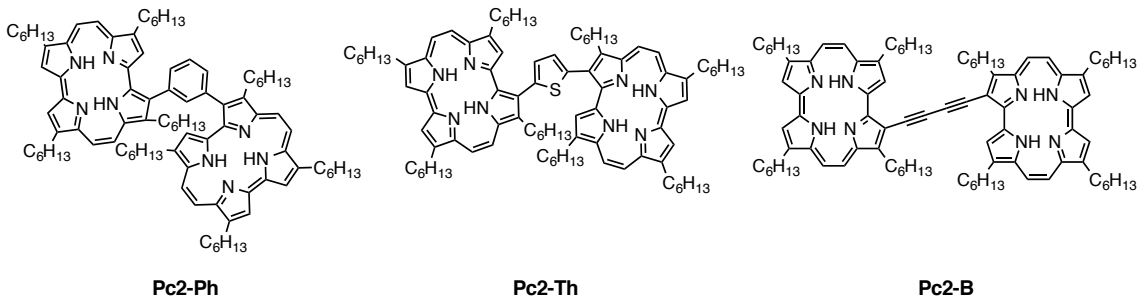

Figure 3-4. Chemical structures of the porphycene dimers synthesized in this work.

3-2. Synthesis

The synthetic scheme of porphycene dimers is shown in Scheme 3-1. The starting materials monoiodoporphycene **2** and monoethynylporphycene **5** were prepared on chapter 2. The *m*-phenylene dimer **Pc2-Ph** was prepared from **2** with *m*-phenyldiboronic acid bis(pinacol)ester by Suzuki–Miyaura coupling in 60%. The 2,5-thienylene dimer **Pc2-Th** was obtained from **2** with 2,5-bis(tributylstannyl)thiophene by Stille coupling in 35%. The butadiyne-linked dimer **Pc2-B** was prepared from **5** by the Glaser–Hay coupling using CuI and *N*,*N*,*N*′,*N*′-tetramethylethylenediamine (TMEDA) in 72% yield. Despite the use of an excess amount of CuI, **Pc2-B** was obtained in the free-base form without metal insertion to porphycene core. This is because an excessive amount of TMEDA traps Cu(II) ion as Cu(II)–TMEDA complex.

Scheme 3-1. Synthesis of porphycene dimers **Pc2-Ph**, **Pc2-Th** and **Pc2-B**.

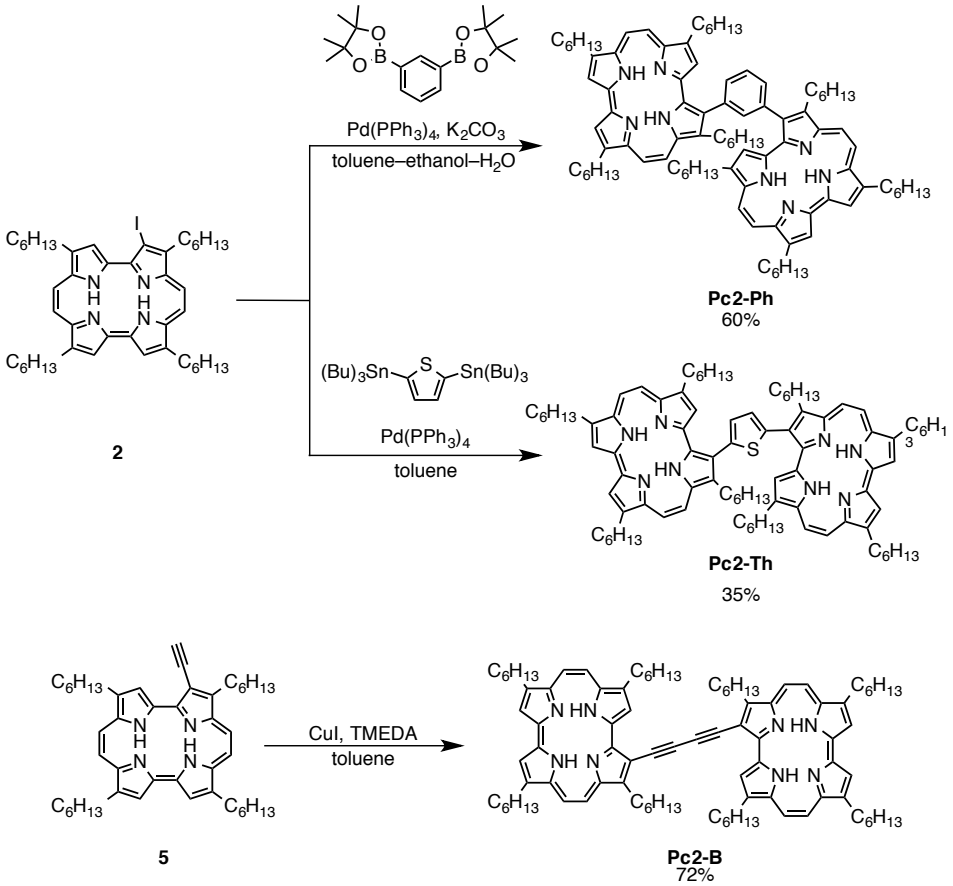

The structures of the all the three dimers, **Pc2-Ph**, **Pc2-Th** and **Pc2B**, were confirmed by single-crystal X-ray diffraction analysis as shown in Figure 3-5, 3-6 and 3-7. The

corresponding crystal data are summarized in Table 3-1. **Pc2-Ph** forms a highly bent conformation. The dihedral angles between porphycene and *m*-phenylene planes define by C2–C3–C45–C46 and C52–C53–C49–C48 atoms are 76° and 74°, respectively. The dihedral angle between each mean plane of porphycenes is 103°. On the other hand, the porphycene units in **Pc2-Th** and **Pc2-B** adepts coplanar with the dihedral angles of almost 0° because of the packing force. The cause of planar structure for **Pc2-B** seems the butadiyne linkage which is smaller and longer compared with phenylene and thienylene linkages. These results show that the 3D conformation of the porphycene dimers is tuned by choice of the linker unit.

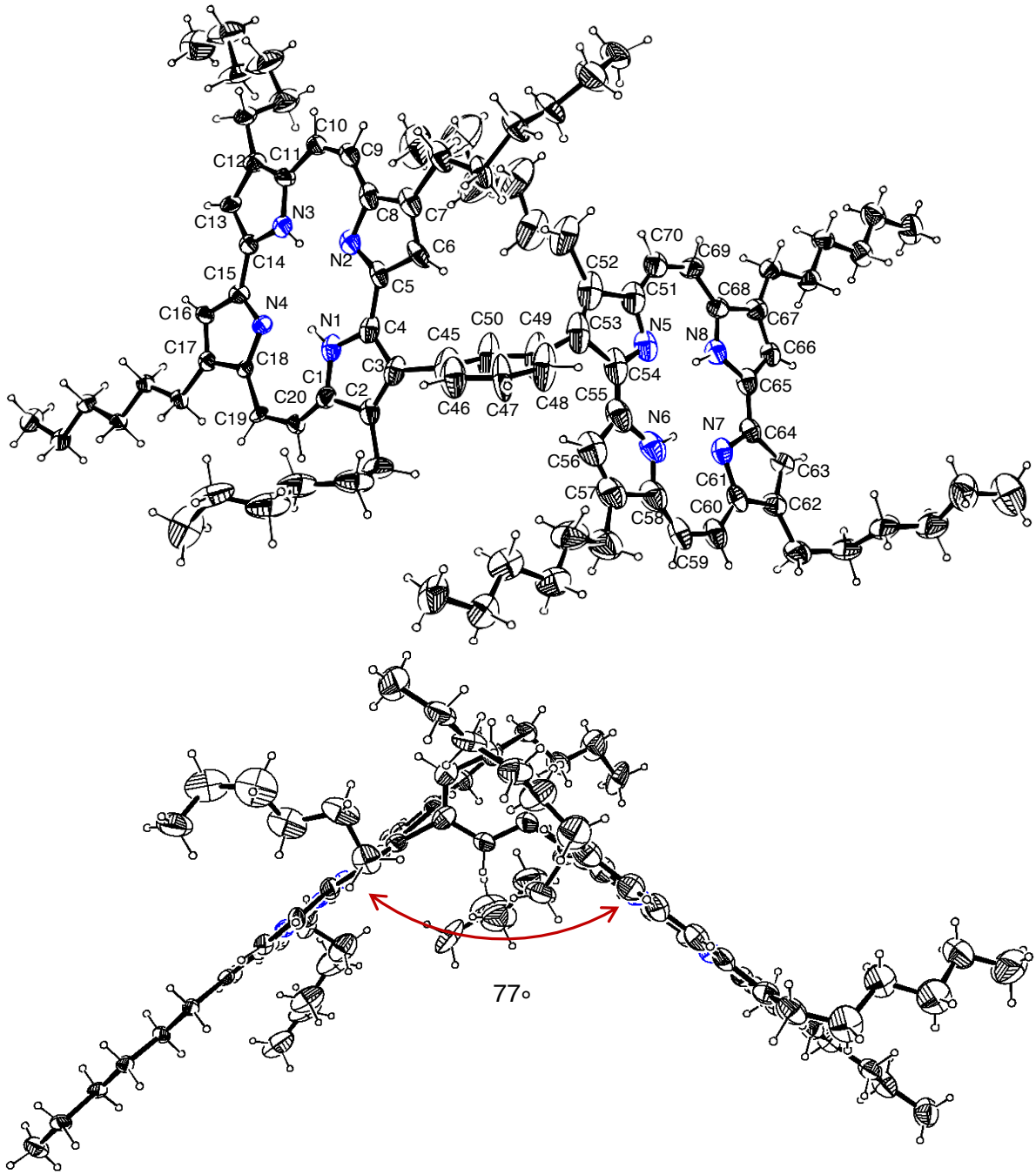

Figure 3-5. Molecular structure of **Pc2-Ph** determined by single-crystal X-ray diffraction analysis. Thermal ellipsoids represent 20% probability.

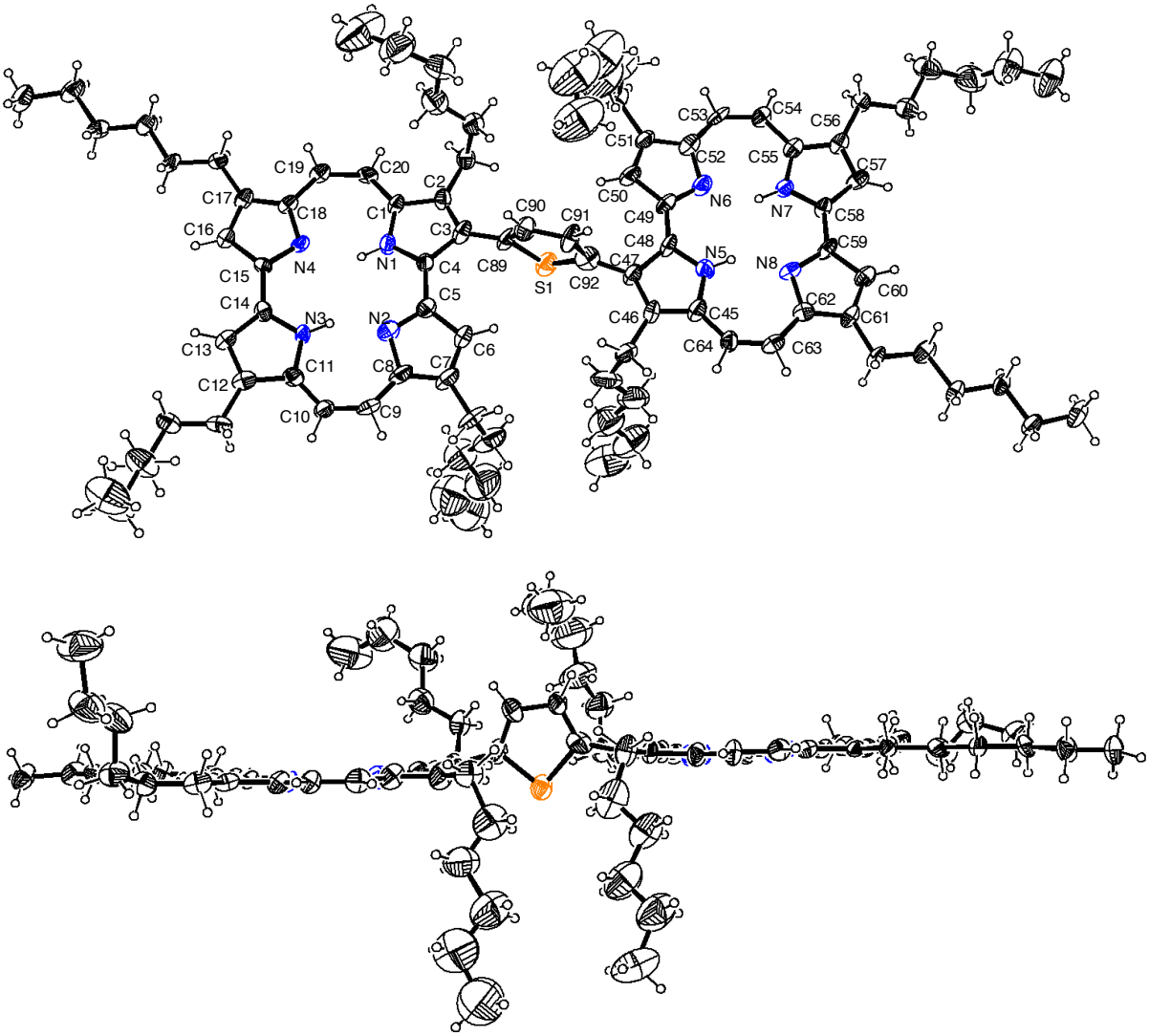

Figure 3-6. Molecular structure of **Pc2-Th** determined by single-crystal X-ray diffraction analysis. Thermal ellipsoids represent 20% probability.

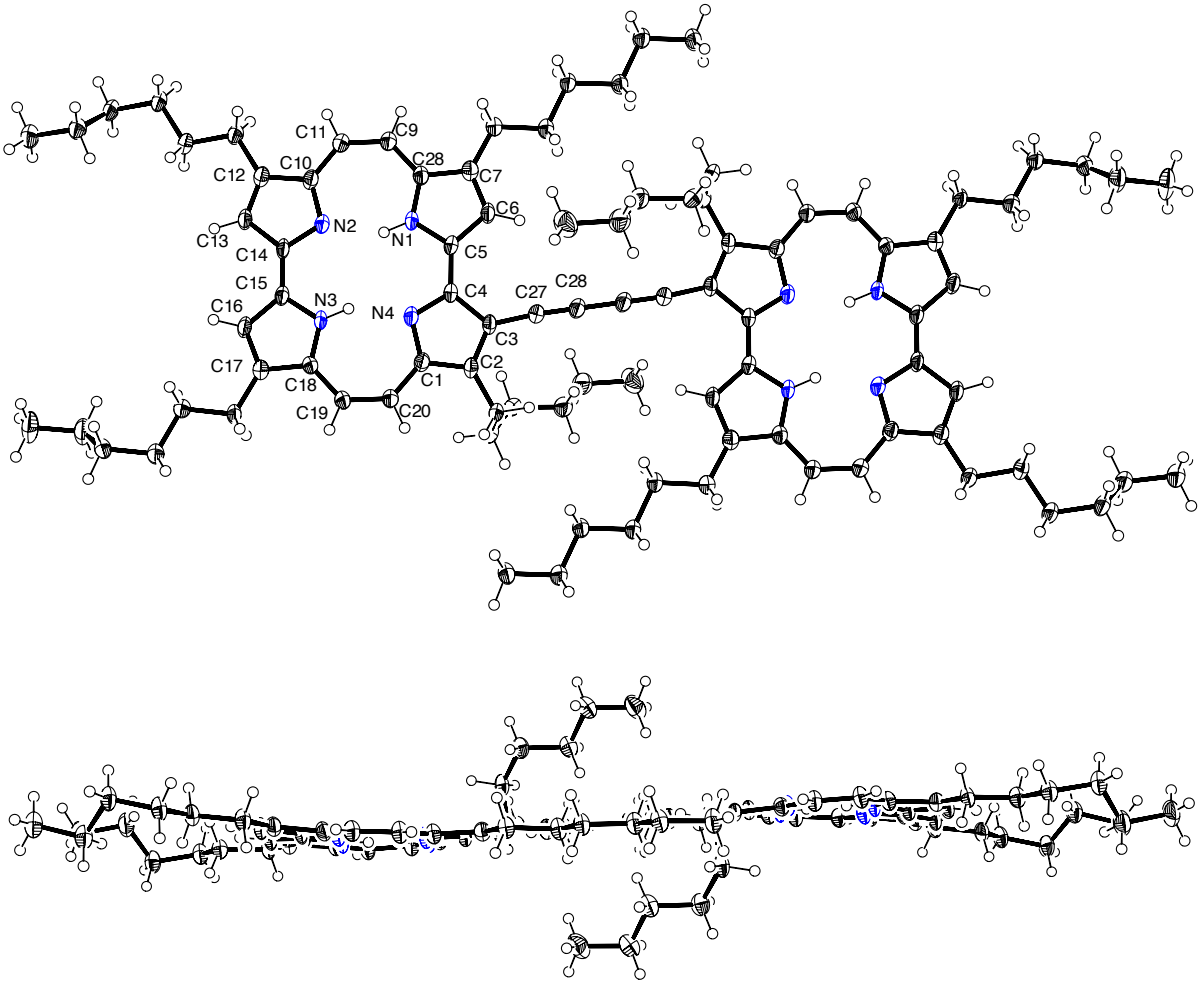

Figure 3-7. Molecular structure of **Pc2-B** determined by single-crystal X-ray diffraction analysis. Thermal ellipsoids represent 50% probability.

Table 3-1. Crystal data and structure refinement for porphycene dimers.

	Pc2-Ph	**Pc2-Th**	**Pc2-B**
Empirical formula	$C_{94}H_{126}N_8$	$C_{92}H_{124}N_8S$	$C_{92}H_{122}N_8$
Formula weight	1368.02	1374.04	1339.98
Temperature	90 K	90 K	103 K
Wavelength	0.71073 Å	0.71073 Å	0.78179 Å
Crystal sysmtem	triclinic	triclinic	triclinic
Space group	$P\bar{1}$	$P\bar{1}$	$P\bar{1}$
Unit cell dimensions	a = 9.182(6) Å,	a = 11.841(7) Å,	a = 9.6276(12) Å,
	b = 16.177(11) Å,	b = 16.170(9) Å,	b = 9.6276(12) Å,
	c = 28.18(2) Å,	c = 21.691(12) Å,	c = 16.671(2) Å,
	α = 92.513(15)°,	α = 70.485(9)°,	α = 105.532(5)°,
	β = 92.795(13)°,	β = 87.611(10)°,	β = 103.870(4)°,
	γ = 104.559(14)°	γ = 83.113(8)°	γ = 99.951(5)°
Volume	4040(5) Å^3	3886(4) Å^3	1944.6(5) Å^3
Z	2	2	1
Density (calculated)	1.125 g cm^{-3}	1.174 g cm^{-3}	1.144 g cm^{-3}
Absorption coefficient	0.065 mm^{-1}	0.094 mm^{-1}	0.066 mm^{-1}
F(000)	1492	1496	730
Crystal size	0.300 × 0.100 × 0.010 mm^3	0.200 × 0.030 × 0.010 mm^3	0.120 × 0.020 × 0.010 mm^3
Theta range for data collection	1.527 to 20.500°	1.732 to 22.000°	1.46 to 26.00°
Index ranges	$-8 \le h \le 9$, $-15 \le k \le 15$, $-27 \le l \le 22$	$-12 \le h \le 12$, $-17 \le k \le 17$, $-14 \le l \le 22$	$-10 \le h \le 10$, $-15 \le k \le 15$, $-18 \le l \le 18$
Reflections collected	13320	15677	21539
Independent reflections	7956 (R_{int} = 0.1640)	9443 (R_{int} = 0.2236)	5650 (R_{int} = 0.1194)
Max. and min trasmission	0.999 and 0.643	0.999 and 0.729	0.999 and 0.992
Refinement method	Full-matrix least-squares on F^2		
Data / restaraints / parameters	7956 / 725 / 915	9443 / 728 / 916	5650 / 0 / 455
Goodness-of-fit on F^2	0.997	1.008	1.033
Final R indices [$I > 2\sigma(I)$]	R_1 = 0.1264, wR_2 = 0.2652	R_1 = 0.1359, wR_2 = 0.2720	R_1 = 0.0722, wR_2 = 0.1628
R indices (all data)	R_1 = 0.3898, wR_2 = 0.3931	R_1 = 0.4204, wR_2 = 0.4260	R_1 = 0.1222, wR_2 = 0.1992
Largest difference peak and hole	0.299 and −0.211 e Å^{-3}	0.384 and −0.350 e Å^{-3}	0.324 and −0.336 e Å^{-3}

3-3. Optical and Electronic Properties

The UV–Vis–NIR absorption spectra of **Pc2-Ph**, **Pc2-Th**, **Pc2-B** and monomeric porphycene **1** in $CHCl_3$ are shown in Figure 3-8. In general, porphycene monomer has a Soret-like band with a split shoulder peak around 350–400 nm and moderate intense Q-like band with three peaks around 550–650 nm. Monomeric **1** shows absorption peaks of Soret- and Q-like band at 372 and 386 nm, and 564, 602 and 635 nm, respectively. The porphycene dimers display monomer-like absorption shapes, while the molar absorption coefficients of dimers are almost twice as high as that of **1**. The Soret band of dimers shows slightly larger split than that of monomar **1** because of a lower molecular symmetry compared with **1**. The absorption onset of **Pc2-B** is extended from 650 nm for monomer **1** to 670 nm because of interaction between the porphycene unit and butadiyne linkage. On the other hand, **Pc2-Ph** and **Pc2-Th** show very similar absorption shapes in the Q-like band, suggesting a weak intramolecular electronic interaction between the two porphycene units and no charge transfer characters between the porphycene unit and linkages.

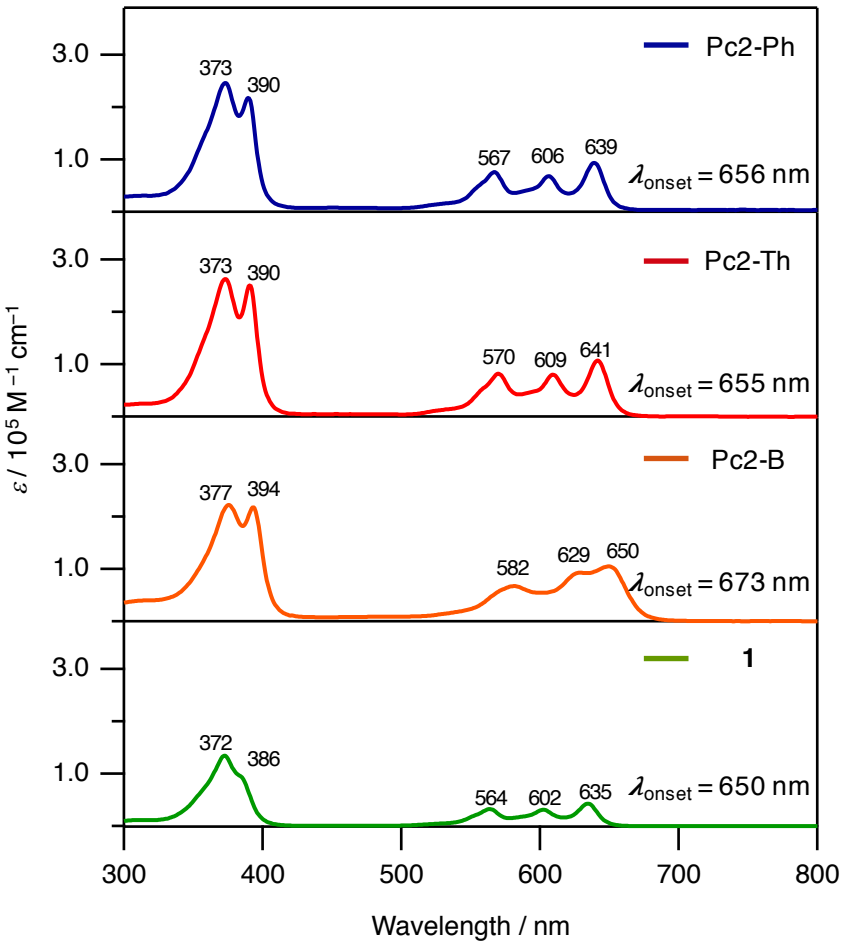

Figure 3-8. UV–Vis–NIR absorption spectra of **Pc2-Ph** (blue), **Pc2-Th** (red), **Pc2-B** (orange) and **1** (green) in $CHCl_3$ measured from low concentration: [**Pc2-Ph**] = 6.1×10^{-7} M, [**Pc2-Th**] = 3.6×10^{-7} M, [**Pc2-B**] = 7.3×10^{-7} M, and [**1**] = 9.5×10^{-7} M.

The absorption spectra of **Pc2-Ph**, **Pc2-Th**, **Pc2-B** and **1** in the thin-film state are shown in Figure 3-9. All the compounds show a broader and red-shifted Q-like band in the thin-film state than in solution. **Pc2-Ph** and **Pc2-Th** have Q-like bands with three peaks and slightly blue-shifted absorption onsets compared with **1**. On the other hand, **Pc2-B** shows a Q-like band with two peaks at 609 and 674 nm which are red-shifted compared with other porphycenes. It seems **Pc2-B** has stronger intra- and intermolecular interactions in the thin-film state than other dimers because of the lower steric hindrance of butadiyne linkage as compared to the phenylene and thienylene linkage.

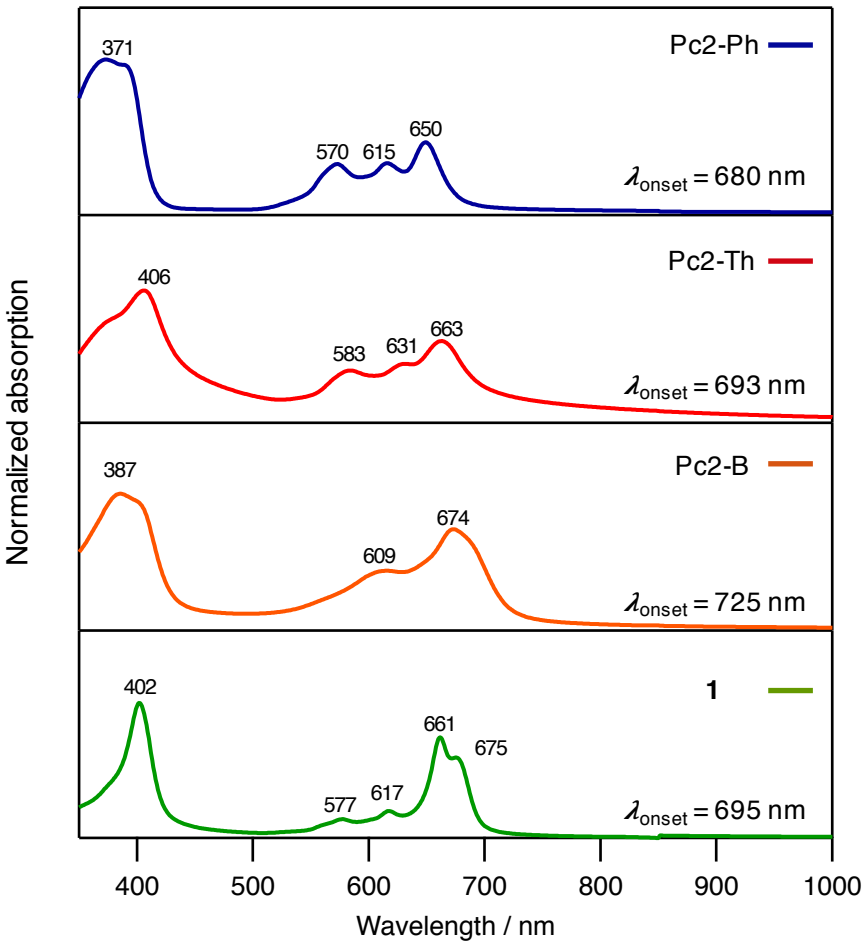

Figure 3-9. UV–Vis–NIR absorption spectra of **Pc2-Ph** (blue), **Pc2-Th** (red), **Pc2-B** (orange) and **1** (green) as thin-film on glass prepared by spin-coating with a 3.0 mg mL^{-1} of solution in the $CHCl_3$ at 800 rpm for 30 s.

The electrochemical properties of the dimers and reference compound were studied by cyclic voltammetry (CV) and differential pulse voltammetry (DPV) in *o*-dichlorobenzene/acetonitrile (5:1) containing 0.1 M $^{n}Bu_4NPF_6$ at room temperature (Figure 3-10). The CV of reference compound **1** exhibits reversible redox processes at $E^{1/2}$ (vs Fc/Fc^{+}) = 0.47, –1.45 and −1.75 V. All the porphycene dimers show reversible two-electron oxidation at a similar potential of $E^{1/2}$ = 0.48 V compared with **1**. The reversible two sets of two-electron reductions were observed at $E^{1/2}$ = −1.51 and −1.85 V for Pc2-Ph and −1.48 and −1.80 V for **Pc2-Th**. On the other hand, **Pc2-B** undergoes a two-electron and two sets of one-electron at slightly less negative potentials

of $E^{1/2}$ = −1.33, −1.59 and −1.68 V. These results indicate that porphycene units in **Pc2-Ph** and **Pc2-Th** are electrochemical independence, whereas porphycene units in **Pc2-B** are electrochemical non-independence.

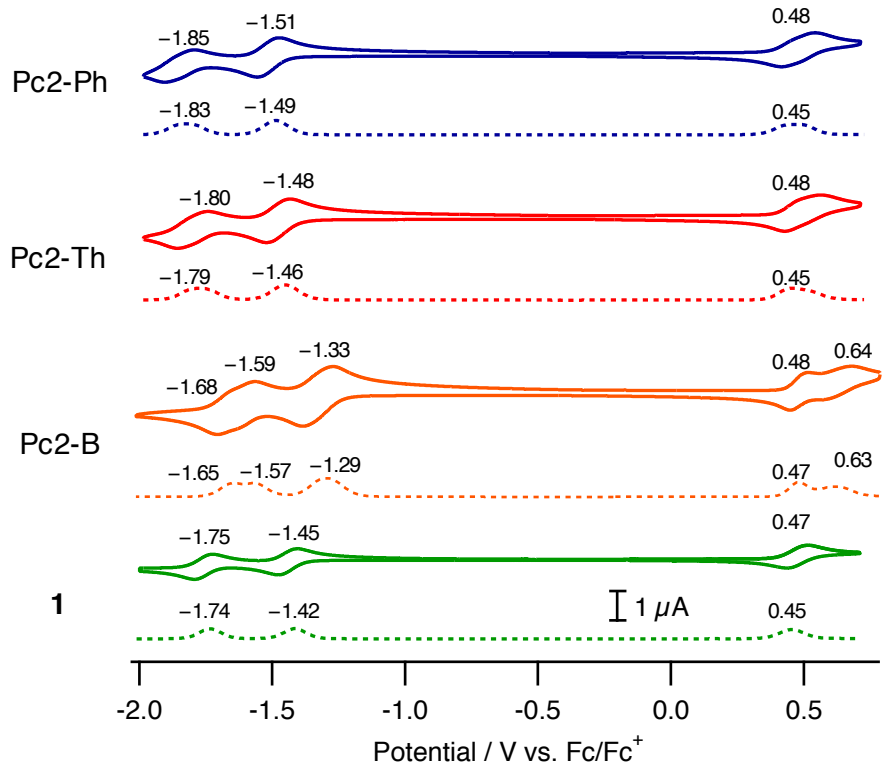

Figure 3-10. CVs (solid line) and DPVs (dotted line) of **Pc2-Ph** (blue), **Pc2-Th** (red), **Pc2-B** (orange) and **1** (green) in *o*-dichlorobenzene/acetonitrile (5:1) with 0.1 M $^{n}Bu_4NPF_6$. Scan rate = 100 mV s^{-1}. [**Pc2-Ph**, **Pc2-Th** and **1**] = 0.5 mM. [**Pc2-B**] = saturated. Working electrode: glassy carbon, counter electrode: Pt, reference electrode: $Ag/AgNO_3$.

The HOMO levels of the porphycene dimers in the thin-film state were estimated by the photoelectron spectroscopy in air to be −5.28–−5.71 eV (Figure 3-11). The optical energy gaps ($E_{g,\,opt}$) were calculated from the absorption onsets of the thin films to be 1.71–1.82 eV, and the LUMO levels were calculated as "HOMO + $E_{g,\,opt}$" to be −3.57–−3.89 eV. The HOMO and LUMO levels in thin films and in solution are summarized in Table 3-2. The frontier orbital energy levels of **1** have been described in chapter 2. The dimers have lower HOMO and LUMO levels than P3HT, a prototypical p-type material for OSCs, which shows the HOMO of −2.8 eV and LUMO of −4.7 eV. Therefore, these dimers may function as n-type materials in OSCs.

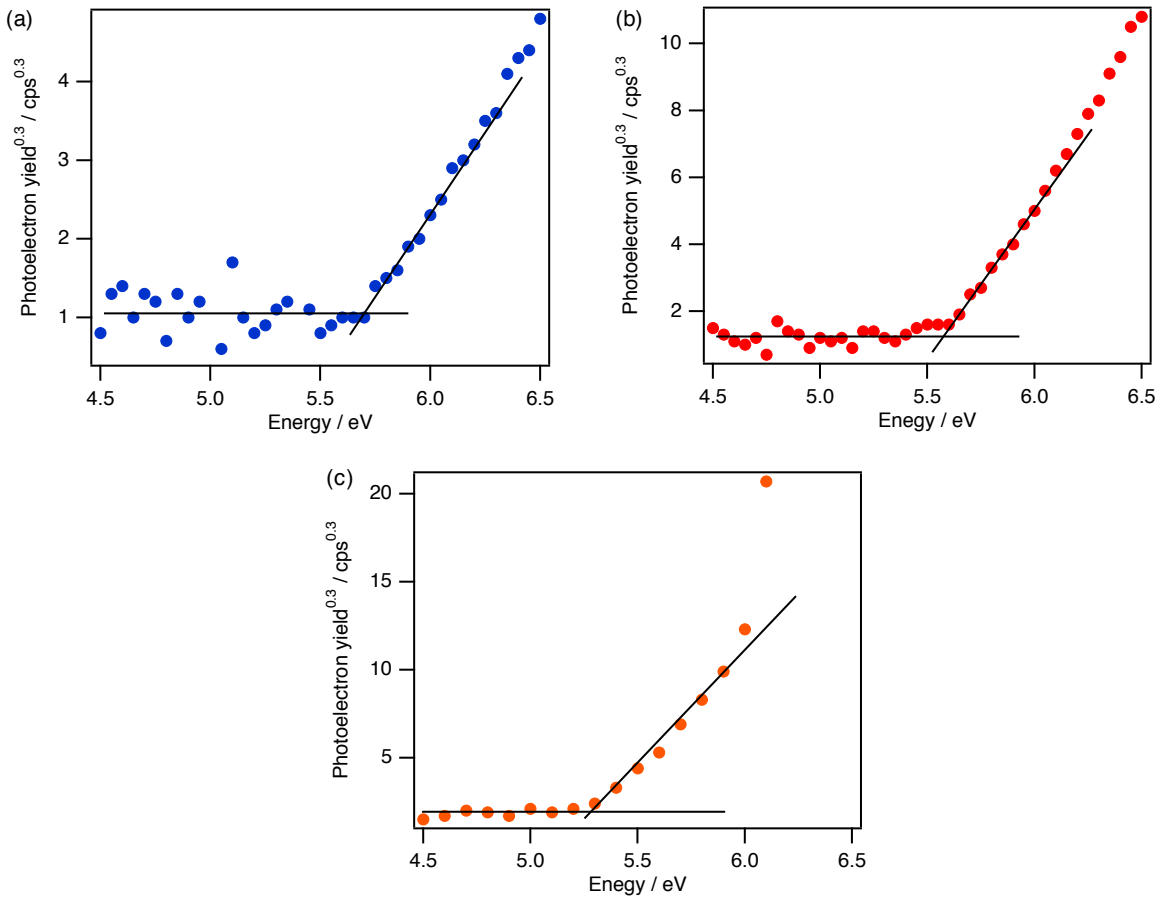

Figure 3-11. Photoelectron spectra of neat films spin-coated on ITO-glass: (a) **Pc2-Ph**, (b) **Pc2-Th** and (c) **Pc2-B**.

Table 3-2. Electrochemical properties of compounds.

Compound	λ_{onset} / nm	E_g[a] / eV	HOMO[b] / eV	LUMO[c] / eV	$HOMO_{CV}$[d] / eV	$LUMO_{CV}$[e] / eV
Pc2-Ph	680	1.82	−5.71	−3.89	−5.28	−3.29
Pc2-Th	693	1.79	−5.59	−3.82	−5.28	−3.32
Pc2-B	725	1.71	−5.28	−3.57	−5.28	−3.47
1	695	1.78	−5.45	−3.67	−5.27	−3.35

[a]Calculated from λ_{onset}. [b]Determined by photoelectron spectroscopy in air. [c]LUMO = HOMO + E_g.[d]$HOMO_{CV} = -(E_{ox}^{1/2} + 4.80)$, [d]$LUMO_{CV} = -(E_{red}^{1/2} + 4.80)$.[15]

3-4. Carrier Mobilities

To investigate the electron transport abilities of porphycene dimers, electron mobilities (μ_e) were measured by the space-charge-limited current (SCLC) method. Hole mobilities (μ_h) in the dimers were also measured for a comparison purpose. Organic solids are characterized by very low intrinsic charge carrier densities. Therefore in organic electronic devices, the charge carrier density in the organic active layer is governed by charge carriers injected from electrodes rather than by the intrinsic charge carriers. The maximum current that an organic semiconductor can sustain in the bulk is called the SCLC. It occurs when the charge carrier concentration is larger than the free carriers in a semiconductor. This drift current is dominated by the applied field. The Mott–Gurney law (equation 3-1) gives the single carrier SCLC and is commonly used to fit *J*–*V* data from diode device based on organic semiconductor to extract the carrier mobility.[16–17] The Mott–Gurney law is:

$$J = \frac{9}{8}\frac{\varepsilon\varepsilon_0\mu}{L^3}V^3 \tag{3-1}$$

where ε is the dielectric constant, ε_0 is the permittivity of free space, μ is the charge-carrier mobility, V is the applied voltage, and L is the thickness of the active layer. The dielectric constant ε is assumed to be 3, which is a typical value for organic semiconductors.

The obtained mobilities are summarized in Table 3-3. Electron-only devices with a general structure of [ITO/ZnO/active layer/LiF/Al] and a hole only devices with a general structure of [ITO/MoO_3/active layer/MoO_3/Al] were fabricated and characterized. The μ_es of neat films of **Pc2-Th**, **Pc2-B** and **1** are 0.32×10^{-5}, 5.1×10^{-5} and 1.5×10^{-5} cm^2 V^{-1} s^{-1}, respectively (Figure 3-12). The μ_e of the neat film of **Pc2-Ph** can not be observed. **Pc2-B** exhibit the highest μ_e among them, however, it is not evaluated for OSCs because of the low solubility.

The SCLC μ_hs of BHJ blend films with dimers and P3HT are similar to each other in the order of 10^{-4} cm^2 V^{-1} s^{-1} as shown in Figure 3-13. On the other hand, the μ_es of BHJ blend film of **Pc2-Ph** and **Pc2-Th** show one or two orders lower values of 2.6×10^{-5} and 2.7×10^{-6} cm^2 V^{-1} s^{-1} than the corresponding μ_es in neat films as shown in Figure 3-14. The electron mobility of BHJ blend film with **1** and P3HT could not be observed in the conditions examined. This means that porphycene dimer system improves the electronic characters, particularly electron mobility, in the BHJ blend films compared to monomer **1**.

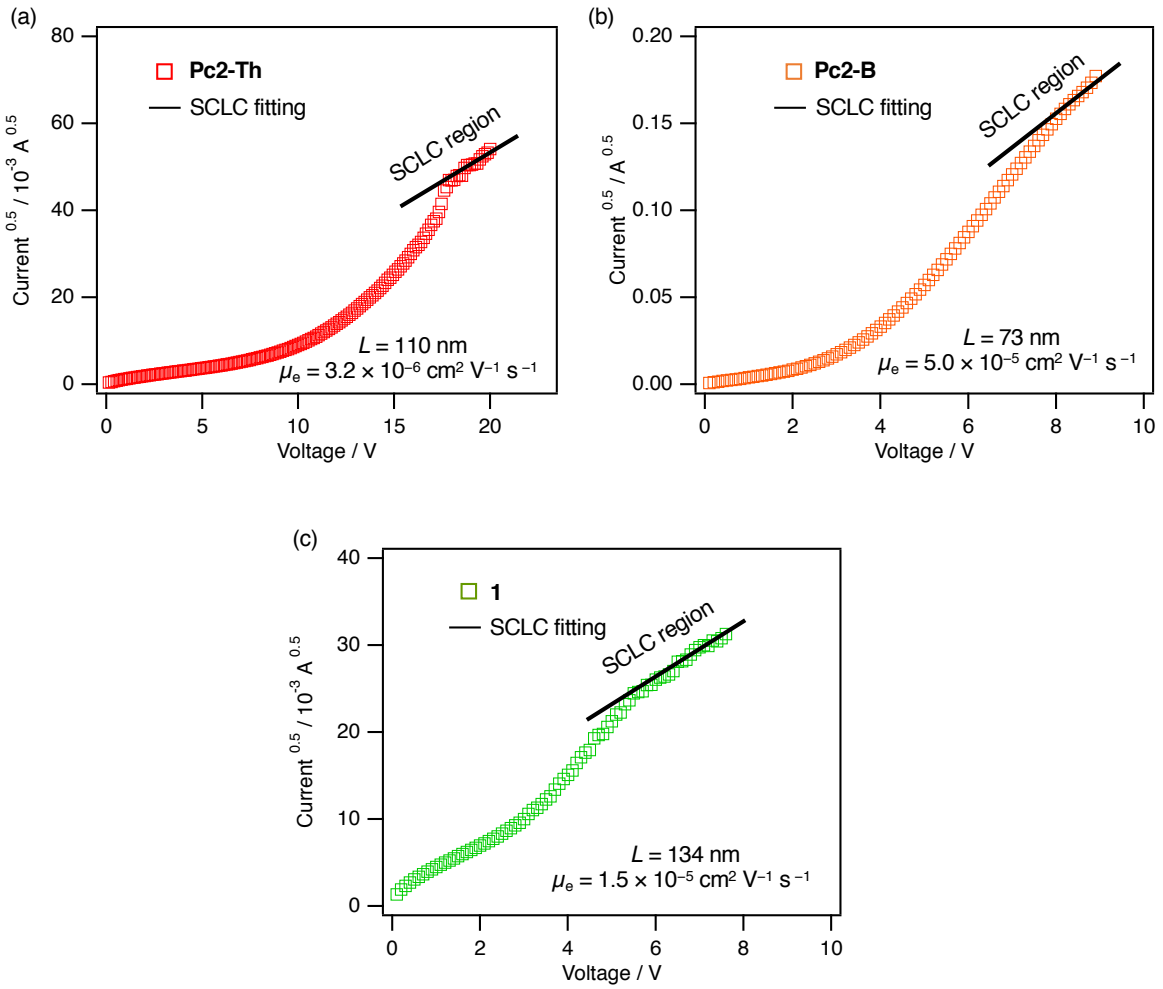

Figure 3-12. *I–V* curves and fitting lines to the Mott-Gurney Law for the electron-only devices of neat film: (a) **Pc2-Th**, (b) **Pc2-B** and (c) **1**. Active layer was prepared by spin-coating with a solution in the $CHCl_3$ at 800 rpm for 30 s. [**Pc2-Th** and **1**] = 10.0 mg mL^{-1}, [**Pc2-B**] = 5.0 mg mL^{-1}.

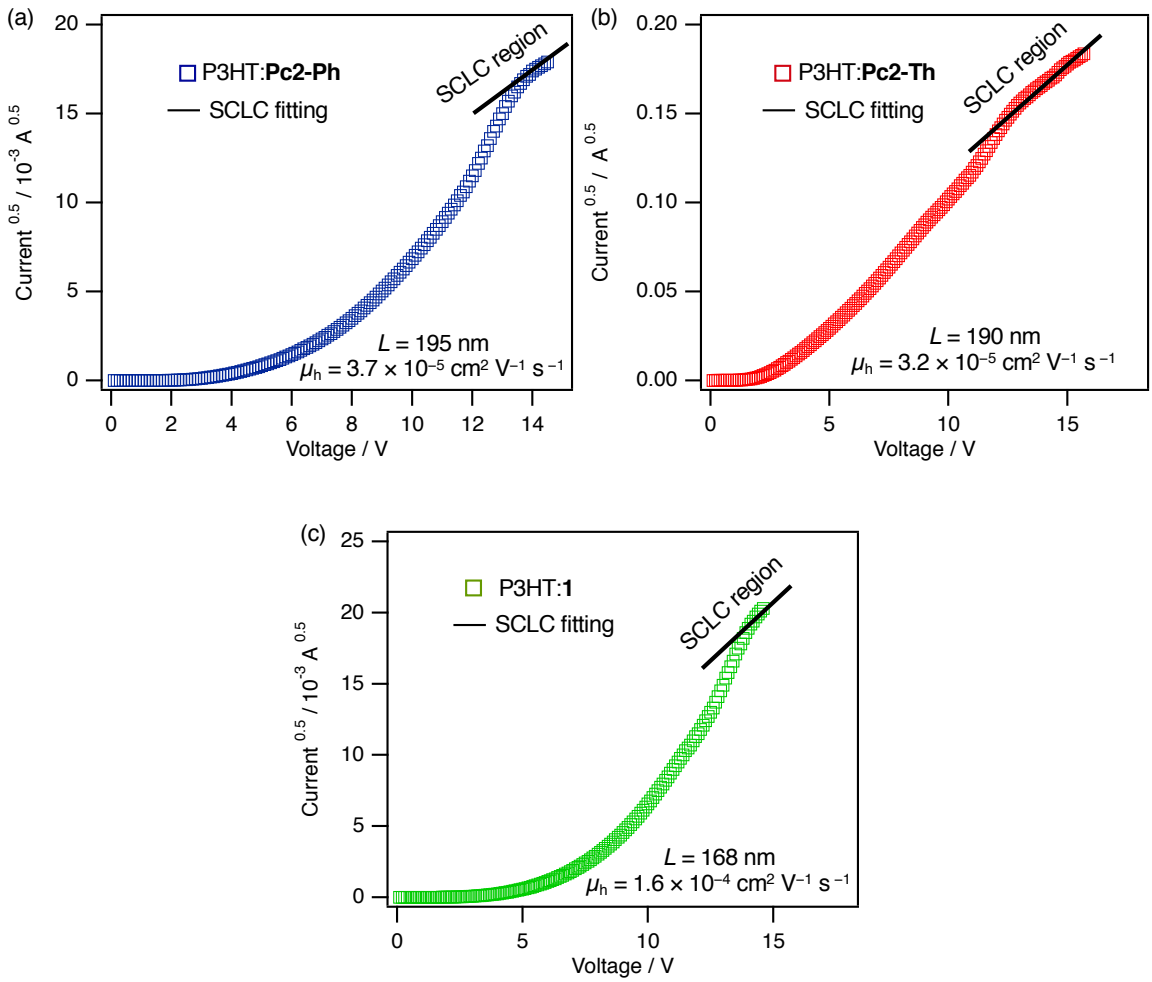

Figure 3-13. *I–V* curves and fitting lines to the Mott-Gurney Law for the hole-only devices of P3HT:n-type blend film: (a) **Pc2-Ph**, (b) **Pc2-Th** and (c) **1**. Active layer was prepared by spin-coating with a p:n (1:1 wt/wt) blend solution in the $CHCl_3$ (10 mg mL^{-1}) at 800 rpm for 30 s.

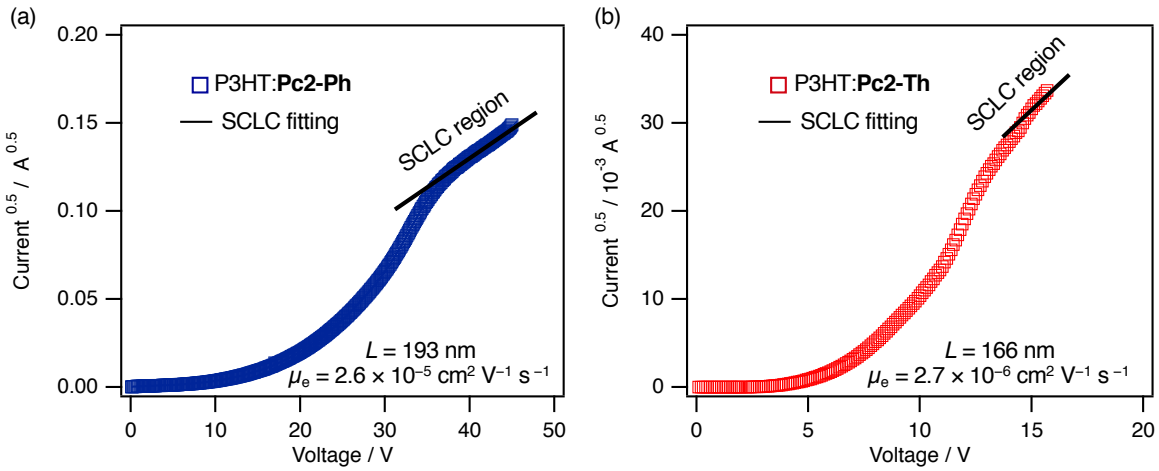

Figure 3-14. *I–V* curves and fitting lines to the Mott-Gurney Law for the electron-only devices of P3HT:n-type blend film: (a) **Pc2-Th** and (b) **Pc2-B**. Active layer was prepared by spin-coating with a p:n (1:1 wt/wt) blend solution in the $CHCl_3$ (10 mg mL^{-1}) at 800 rpm for 30 s.

Table 3-3. SCLC charge carrier mobilities of the neat films and BHJ blend films.

Compound	$\mu_{e,\,neat}$[a] / $cm^2\ V^{-1}\ s^{-1}$	$\mu_{e,\,blend}$[b] / $cm^2\ V^{-1}\ s^{-1}$	$\mu_{h,\,blend}$[c] / $cm^2\ V^{-1}\ s^{-1}$
Pc2-Ph	not observed	2.6×10^{-5}	3.7×10^{-4}
Pc2-Th	3.2×10^{-6}	2.7×10^{-6}	3.2×10^{-4}
Pc2-B	5.1×10^{-5}	cannot be fabricated	cannot be fabricated
1	1.5×10^{-5}	not observed	1.6×10^{-4}

[a]Electron-only SCLC devices of neat films [ITO/ZnO/neat film/LiF/Al]. [b]Electron-only SCLC devices of BHJ blend films [ITO/ZnO/P3HT:n-type/LiF/Al]. [c]Hole-only SCLC devices of BHJ blend films [ITO/MoO_3/P3HT:n-type/MoO_3/Al].

3-5. Film Morphology

To understand the difference in carrier mobilities, the film morphology and crystallinity of the neat and BHJ blend films were investigated by atomic force microscopy (AFM) (Figure 3-15) and out-of-plane X-ray diffraction analysis (XRD) (Figure 3-16).

It is well-known that the film morphology has implications for device performances.[18–26] The AFM height image of the neat film of **Pc2-Ph** shows a smooth surface, while that of **Pc2-Th** and **1** shows a high roughness surface. The XRD pattern of **Pc2-Ph** shows no diffraction peaks, which means that **Pc2-Ph** forms an amorphous film, while the XRD pattern of **Pc2–Th** shows a diffraction peak at $2\theta = 5.60°$ ($d = 15.8$ Å) from the 010 planes as shown in Figure 3-16a. On the other hand, the neat film of **1** gives a strong diffraction peak at 5.35° ($d = 16.5$ Å). This peak does not match with the simulated pattern from the single-crystal X-ray diffraction data of **1**. Since the *d*-spacings of them are close to the lateral molecular dimension (**1** [ca. 17 Å]) as shown in Figure 3-17b, it seems that porphycene units adopt on edge-on-like orientation in the thin film. These results suggest that the crystalline neat films form an electron-carrier path and show an electron mobility.

In the case of the blend film of P3HT:**Pc2-Ph**, a smooth and homogeneous surface is observed with AFM. The blend film of P3HT:**Pc2-Th** shows a less crystalline film structure compared with its neat film, but it still shows small island-like structures. The XRD pattern of P3HT:**Pc2-Ph** shows a diffraction peak at $2\theta = 5.30°$ ($d = 16.67$ Å), which corresponds to the diffraction peaks of P3HT. However, the diffraction peaks disappear at the higher 2θ region compared with the neat film of P3HT indicating the low crystallinity. On the other hand, the XRD pattern of P3HT:**Pc2-Th** shows multiple diffraction peaks at $2\theta = 5.00$, 5.65 6.60 and 10.65° corresponding to the *d*-spacings of 17.67, 15.64, 13.39 and 8.31 Å. Probably, BHJ blend film with P3HT:Pc2-Th contains of multiple molecular orientations induced by the mixing with **Pc2-Th** and P3HT. Therefore, the AFM image of P3HT:**Pc2-Th** spontaneously shows

homogeneous and island-like domains. The blend film of P3HT:**1** shows huge domains. The XRD pattern of P3HT:**1** shows a strong diffraction peak at $2\theta = 5.30°$, which matches to the 100 diffraction of P3HT.[27] These results show that the dimeric structures form the low crystalline films with or without P3HT, while **1** forms crystalline films. The isolated large grains of **1** in the BHJ film cannot form an electron-carrier path.

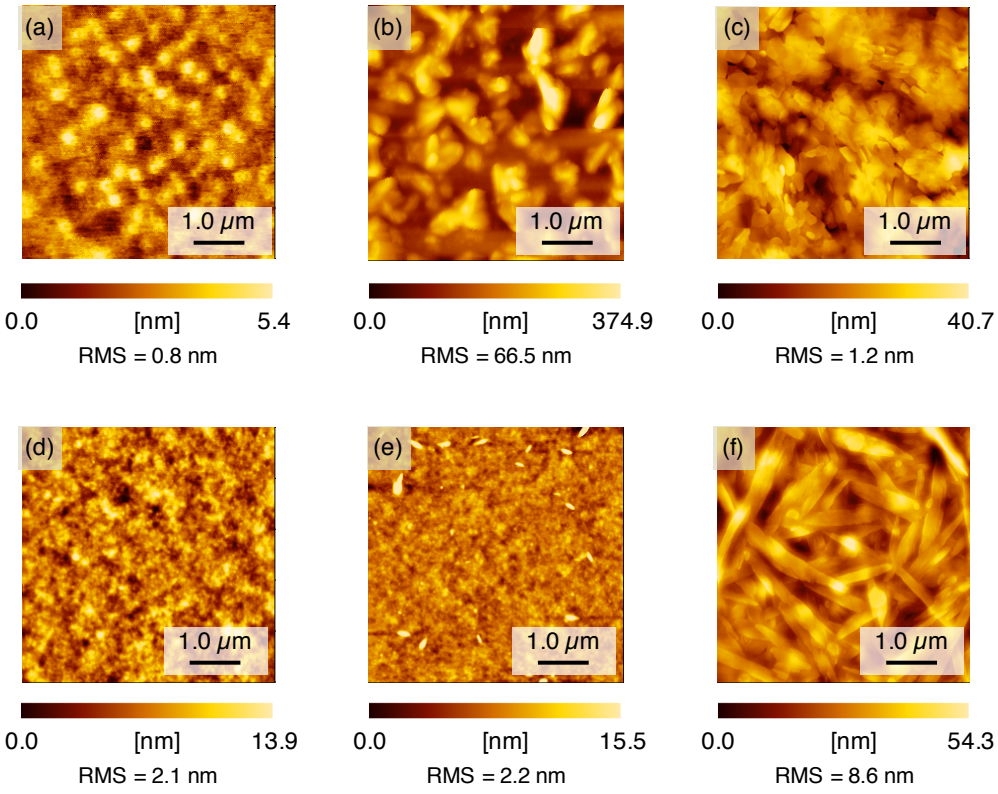

Figure 3-15. AFM height images of neat films on ITO/PEDOT:PSS: (a) Pc2-Ph, (b) Pc2-Th and (c) **1**, blend films on ITO/PEDOT:PSS: (d) P3HT:Pc2-Ph, (e) P3HT:Pc2-Th and (f) P3HT:**1**. The scan size is 5 μm × 5 μm for all images.

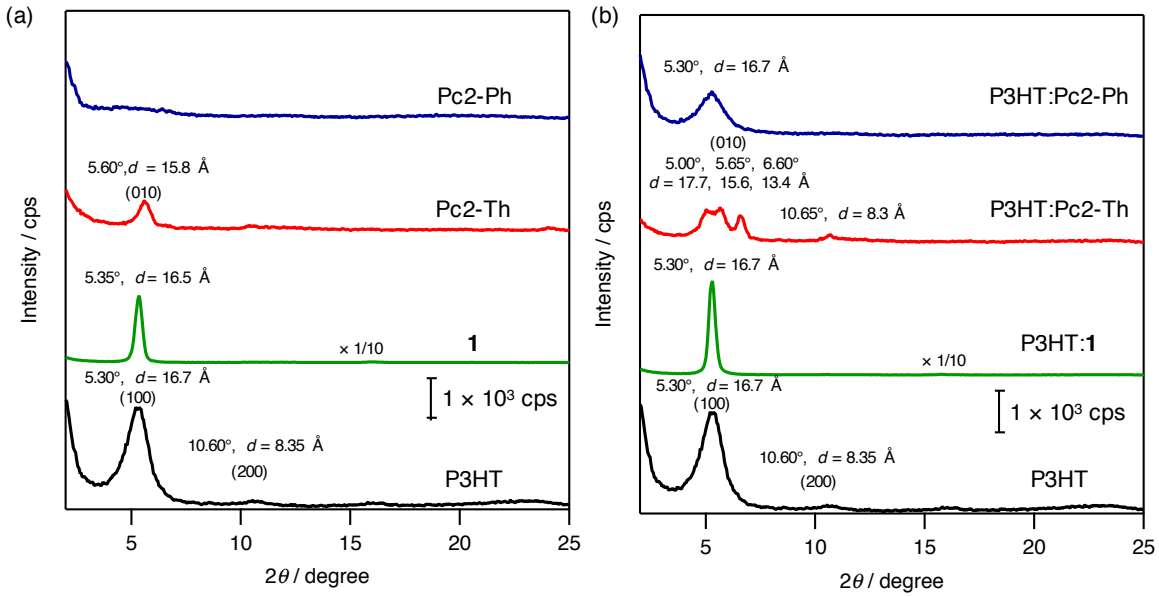

Figure 3-16. XRD patterns of (a) neat films on ITO/PEDOT:PSS: **Pc2-Ph** (blue), **Pc2-Th** (red), **1** (green) and P3HT (black), and blend films on ITO/PEDOT:PSS: P3HT:**Pc2-Ph** (blue), P3HT:**Pc2-Th** (red), P3HT:**1** (green) and P3HT neat film (black).

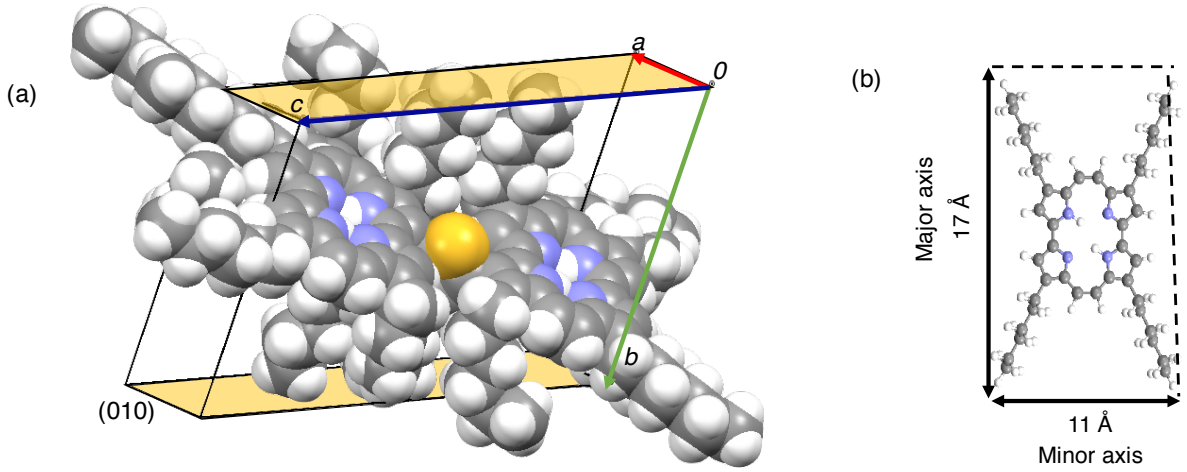

Figure 3-17. (a) A part of single-crystal structure of **Pc2-Th** and (b) optimized molecular structure of **1** at MM2 level.

3-6. Evaluation of Organic Solar Cells

The BHJ OSCs comprising each of the porphycene dimers as n-type material and P3HT as p-type material were fabricated. The BHJ films were incorporated into OSCs with a general device architecture of [ITO/PEDOT:PSS (30 nm)/P3HT:n-type/Ca (10 nm)/Al (70 nm)]. The active layers have been prepared by spin-coating at 1000 rpm for 30 s of a mixed $CHCl_3$ solution (10 mg mL^{-1}) of porphycenes and P3HT (1:1 wt/wt) in a nitrogen-filled glove box. After the deposition of the Al electrodes, the devices were sealed in the glove box to prevent the entrance of air and moisture. *J–V* curves of devices under one sun illumination (AM1.5G, 100 mW cm^{-2}) are shown in Figure 3-18a and the photovoltaic parameters are summarized in Table 3-4. The EQE spectra of the OSC devices are also shown in Figure3-18b.

The P3HT:**Pc2-Ph** BHJ shows the highest device performance with a short circuit current density (J_{SC}) of 0.33 mA cm^{-2}, an open circuit voltage (V_{OC}) of 0.89 V, a fill factor (FF) of 0.28, and a PCE of 0.081%. In the case of the P3HT:**Pc2-Th** blend devices, a slightly reduced performance is observed (J_{SC} = 0.33 mA cm^{-2}, V_{OC} = 0.84 V, FF = 0.27 and PCE = 0.075%). On the other hand, the P3HT:**1** exhibits a significantly lower OPV performance (J_{SC} = 0.12 mA cm^{-2}, V_{OC} = 0.82 V, FF = 0.22 and PCE = 0.022%) than that of dimers. The EQE spectra of the BHJ OSCs with porphycene dimers and P3HT show broad profiles over 300 to 700 nm with EQE values of 0.02%. The EQE values of P3HT:**1** are lower than those of P3HT: porphycene dimers.

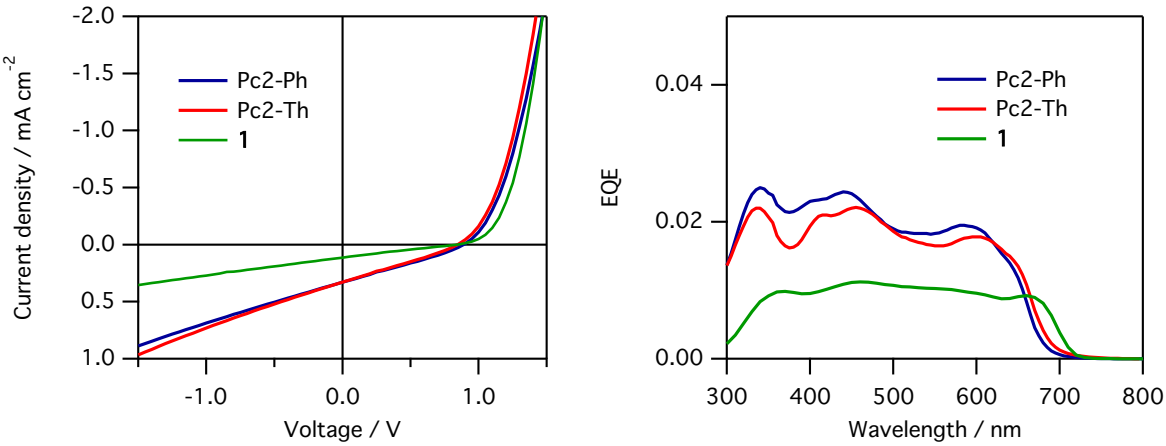

Figure 3-18. (a) *J*–*V* curves and (b) EQE spectra of the best-performing BHJ OSCs based on P3HT:n-type blend.

Table 3-4. Photovoltaic parameters of the P3HT:n-type blends.

Material	J_{SC} / mA cm^{-2}	V_{OC} / V	FF	PCE [a] / %
Pc2-Ph	0.33	0.89	0.28	0.081
Pc2-Th	0.33	0.84	0.27	0.075
1	0.12	0.82	0.22	0.022

Active layers were prepared by spin-coating of a p:n (1:1 wt/wt) blend solution in $CHCl_3$ (10 mg mL^{-1}) at 1000 rpm for 30 s

3-7. Summary and Outlook

The porphycene dimers with *m*-phenylene, thienylene and butadiyne linkages, **Pc2-Ph**, **Pc2-Th** and **Pc2-B**, have been successfully synthesized and their optical and electrochemical properties and single-crystal packings were characterized. The crystal structure of **Pc2-Ph** showed a twisted conformation, while **Pc2-Th** and **Pc2-B** formed nearly planar structures. Porphycene units in **Pc2-Ph** and **Pc2-Th** are electrochemical independence, whereas porphycene units in **Pc2-B** are electrochemical non-independence. The BHJ blend films with porphycene dimers and P3HT showed smooth surfaces and small domains, whereas the monomeric porphycene **1** and P3HT formed huge domains and a large RMS roughness value. Porphycene dimer-based OSCs showed 0.08% PCE at maximum which is twice as high as that

of the monomeric porphycene-based OSC. This is the first example in which porphycenes are used as n-type material in OSC.

Although porphycene dimer **Pc2-Ph** with 3D structure showed a high miscibility with P3HT and a wide light absorption up to ca. 700 nm, the corresponding OSC showed a lower PCE of 0.081% than other non-fullerene-based systems.[28–35] It seems that porphycene dimer-based OSC has low μ_e and μ_h values because of a weak intermolecular interaction induced a low crystallinity in the thin-film state.

Lu et al. have reported that BHJ OSCs based on P3HT and a PDI dimer with four ethylene glycol (EG) chains as shown in Figure 3-19.[35] The OSC with four substituted PDI (Bis-PDI-T-di-EG) showed a higher photovoltaic performance (J_{SC} = 3.8 mA cm^{-2}, V_{OC} = 0.67 V, FF = 0.60 and PCE = 1.5%) than that comprising a PDI dimer without EG chain (Bis-PDI-T) (J_{SC} = 0.4 mA cm^{-2}, V_{OC} = 0.43 V, FF = 0.47 and PCE = 0.41%). In this case, the EG chains induced a self-assembly of PDI dimers to effect nanoscale phase separation between p- and n-type materials and enhanced charge carrier mobility. The μ_h values of Bis-PDI-T-di-EG in BHJ blend increased to 0.26 cm^2 V^{-1} s^{-1} compared with that of Bis-PDI-T (6.4 × 10^{-4} cm^2 V^{-1} s^{-1}) with keeping a high μ_e (~10^{-4} cm^2 V^{-1} s^{-1}).

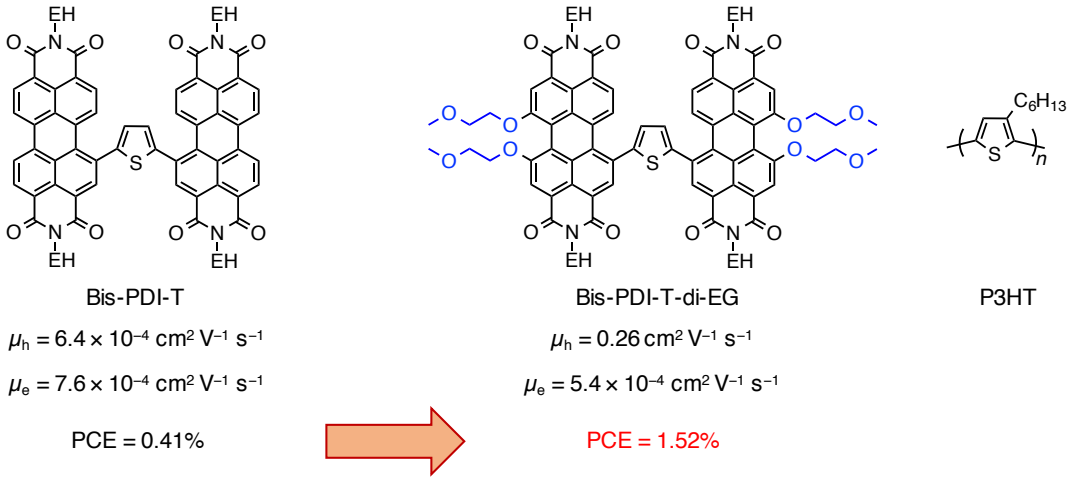

Figure 3-19. Improvement of photovoltaic performance through introduction of EG chains.

Such substitution with EG chains in the porphycene dimer may improve charge carrier mobility and photovoltaic performance. For example, it is possible to synthesize porphycene derivatives with EG chains on 12,17,12',17'-positions as shown in Figure 3-20. The 3D conformation tuning by choice of the linker in this work will serve as a basis of designing such 3D molecule for OSC materials.

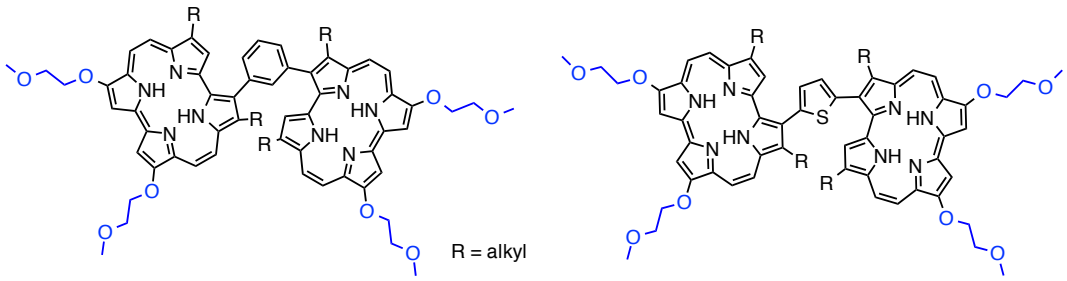

Figure 3-20. Potential porphycene dimers substituted with EG chains.

3-8. Experimental Section

General method

All reactions were carried out under nitrogen unless otherwise noted. “Room temperature” means 15–25 °C. Gravity column chromatography was performed on silica gel purchased from Kanto Chemical (Silica Gel 60N, 60 Å, 63–210 μm). Analytical TLC was conducted on Merck 200 μm thickness silica gel plates with a fluorescent indicator. Visualization was accomplished with UV light at 254 or 365 nm. GPC was performed on a JAI LC-9225NEXT recycle chromatography system equipped with JAIGEL 1H and 2H polystyrene gel columns (600 mm h × 40 mmϕ; bead size = 16 μm; pore size = 20–30 [1H] and 40–50 [2H] Å) using $CHCl_3$ as a mobile phase. ^{1}H NMR and $^{13}C\{^1H\}$ NMR spectra were recorded on a JEOL JNM-ECX400 (400 MHz) or JNM-ECX600 (600 MHz) spectrometer at 294 K or 363 K, and chemical shifts were calculated using 1,1,2,2-tetrachloroethane or tetramethylsilane as internal standards (1H: 6.00 ppm for 1,1,2,2-tetrachloroethane and 0.00 ppm for tetramethylsilane; $^{13}C\{^1H\}$: 73.78 ppm for 1,1,2,2-tetrachloroethane-d_2 and 0.00 ppm for tetramethylsilane). High-resolution MALDI mass spectra were measured on a JEOL Spiral TOF/JMS-S3000 mass spectrometer. UV–Vis absorption spectra were recorded on a JASCO UV–Vis–NIR V-670 spectrometer. Electrochemical measurements were measured on an ALS 612D electrochemical analyzer in a solution of 0.1 M ^{n}Bu$_4$NPF$_6$ in dry *o*-dichlorobenzene/CH_3CN (5:1 vol) with a scan rate of 100 mV s^{-1} at room temperature in an argon-filled cell. A glassy carbon electrode and a Pt wire were used as a working and a counter electrode, respectively. An Ag/$AgNO_3$ electrode was used as a reference electrode, which was calibrated with the half-wave potential of Fc/Fc$^+$ redox couple. Ionization energies of thin films were determined from the onset of photoelectron spectra measured on a Riken Keiki AC-3 photoelectron spectrometer. The surface morphology of organic films was observed using an SII SPA400/SPI3800N AFM in tapping mode with an

SII SI-DF20 silicon probe at a resonant frequency of 138 kHz and a force constant of 16 N m $^{-1}$.

Single-crystal X-ray diffraction analysis

X-ray diffraction data of Pc2-Ph and Pc2-Th were measured at 90 K on a Rigaku VariMax R-Axis RAPID imaging plate-based X-ray diffractometer system equipped with an RA-Micro7 X-ray source (Mo *K*α, λ = 0.71073 Å) operated at 1.2 kW.

X-ray diffraction data of Pc2-B was measured at 103 K on a Rigaku AFC10 diffractometer with a Rigaku Saturn 724 charge-coupled device (CCD) detector using synchrotron radiation at SPring-8 beam line BL40XU. The X-ray beam (λ = 0.78179 Å) was focused to 1.88 (vertical) × 3.86 (horizontal) μm^2 using a zoneplate.

The diffraction data were processed with CrystalStructure of the Rigaku program, solved with the SIR-97 program[36–37]and refined with the SHELX-97 program.[38]

X-ray diffraction analysis of thin films

Out-of-plane XRD θ–2θ scans of thin films were measured on a Rigaku RINT-TTR III diffractometer equipped with a rotating anode (Cu *K*α, λ = 1.5418 Å) operated at 15 kW and a Rigaku D/teX Ultra 1D silicon strip detector. Measurements were performed at a scan rate of 3° min^{-1} with a scan range of 2–35°.

Materials

All solvents and chemicals were reagent grade obtained commercially, and used without further purification except othersize noted. For spectral measurements, spectral grade and

$CHCl_3$ were purchased from Nacalai Tesque. P3HT (regioregular) was purchased from Sigma-Aldrich and used as received.

Fabrication and evaluation of space-charge-limited current electron-only devices

ITO-patterned glass substrates (20 × 20 mm^2, 15 Ω per square) were cleaned by gentle rubbing with an acetone-soaked wipe, then sequential sonication in detergent (Furuuchi Chemical, Semico Clean 53), distilled water (Wako Pure Chemical, reagent grade), and isopropyl alcohol (Kishida chemical, electronic grade) for 10 min each. After drying with nitrogen blow and UV/O_3 treatment with a Bioforce Nanoscience TC-003 cleaner at room temperature for 20 min. The ZnO layer was prepared on the ITO substrate by a sol–gel method using ZnO precursor[37]. The zinc acetate dihydrate (500 mg), 2-methoxyethanol (5 mL), and ethanolamine (140 μL) were mixed and stirred vigorously for 12 h in air. The ZnO precursor solution was spin-coated at 5000 rpm for 30 s on the ITO substrate. The films were annealed 250 °C for 1 h in air. The substrates were transferred into a nitrogen-filled glove box (< 10 ppm O_2 and H_2O) for preparation of active layers. The films were prepared by spin-coating of a porphycene solution or a p:n blend solution in $CHCl_3$ at 800 rpm for 30 s. Finally, LiF (1 nm, 0.01 Å s^{-1}) and Al (70 nm, 0.3 Å s^{-1}) were vapor-deposited at high vacuum (~10^{-4} Pa) through a shadow mask that defined an active area of 2 × 0.5 mm^2. The structure of electron-only devices was [ITO/ZnO/active layer/LiF (1 nm)/Al (70 nm)].

Current–voltage (*I–V*) characteristics of the space-charge-limited current (SCLC) devices were measured by using a Keithley 2400 Source Mater. The carrier mobility was extracted by fitting the *I–V* curves in the linear region according to the modified Mott–Gurney equation.

Fabrication and evaluation of space-charge-limited current hole-only devices

ITO-patterned glass substrates (20 × 20 mm^2, 15 Ω per square) were cleaned by the same procedure as described in "Fabrication and evaluation of space-charge-limited current electron-only devices". MoO_3 (15 nm, 0.1 Å s^{-1}) were vapor-deposited at high vacuum (~10^{-4} Pa) on the ITO substrate. The substrates were transferred into a nitrogen-filled glove box (< 10 ppm O_2 and H_2O) for preparation of active layers. The blend films were prepared by spin-coating of a p:n blend solution in $CHCl_3$ at 800 rpm for 30 s. Finally, MoO_3 (15 nm, 0.1 Å s^{-1}) and Al (70 nm, 0.3 Å s^{-1}) were vapor-deposited at high vacuum (~10^{-4} Pa) through a shadow mask that defined an active area of 2 × 0.5 mm^2. The structure of hole-only devices was [ITO/MoO_3 (15 nm)/active layer/MoO_3 (15 nm)/Al (70 nm)].

I–V characteristics of the SCLC devices were measured by the same method of SCLC hole-only devices.

Fabrication and evaluation of photovoltaic cells

ITO-patterned glass substrates (20 × 20 mm^2, 15 Ω per square) were cleaned by the same procedure as described in "Fabrication and evaluation of space-charge-limited current electron-only devices". PEDOT:PSS (Clevios, AI4083) was spin-coated onto the cleaned ITO surface. After being baked in air at 120 °C for 20 min, the substrates were transferred into a nitrogen-filled glove box (< 10 ppm O_2 and H_2O) for preparation of active layers. Bulk-heterojunction films were prepared by spin-coating of a p:n blend solution in $CHCl_3$ at 1500 rpm for 30 s. Finally, Ca (10 nm, 0.1 Å s^{-1}) and Al (70 nm, 0.3 Å s^{-1}) were vapor-deposited at high vacuum (~10^{-4} Pa) through a shadow mask that defined an active area of 2 × 2 mm^2. The general device structure was [ITO/PEDOT:PSS (30 nm)/p:n/Ca (10 nm)/Al (70 nm)].

Current density–voltage (*J–V*) curves were measured using a Keithley 2611B source mater unit under AM1.5G illumination at an intensity of 100 mW cm^{-2} using a Bunko Keiki CEP-

2000RP solar simulator. The EQE spectra were obtained under illumination of monochromatic light using the same system.

Synthesis

Synthesis of **Pc2-Ph**

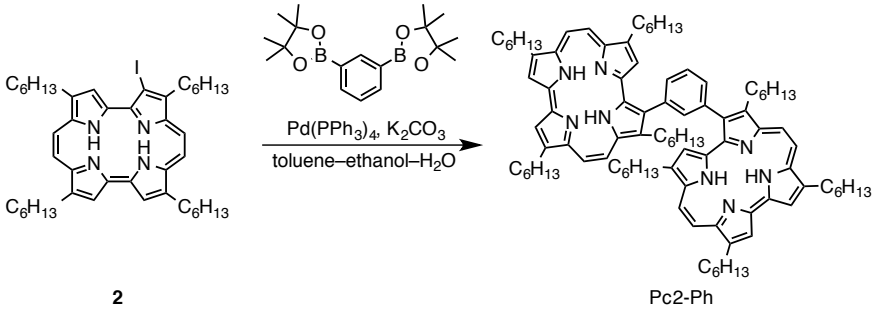

2 Pc2-Ph

1,3-Diborylbenzene pinacol diester (22.0 mg, 66.7 μmol) was added to a solution of 2,7,12,17-tetrahexyl-3-iodoporphycene **2** (50.1 mg, 64.8 mmol) and $Pd(PPh_3)_4$ (10.2 mg, 8.83 μmol) in toluene (5.0 mL), ethanol (2.5 mL) and 1.0 M K_2CO_3 aqueous solution (2.5 mL). The mixture was degassed by bubbling with nitrogen for 20 min and then refluxed for 48 h. The crude product was purified by gravity silica gel column chromatography (CH_2Cl_2/hexanes, 1:9) and GPC. Recrystallization from a $CHCl_3$ solution by adding methanol gave **Pc2-Ph** as a purple solid (26.6 mg, 19.3 μmol, 66 %). ^{1}H NMR (400 MHz, 1,1,2,2-tetrachloroethane-d_2, 363 K): δ 9.88–9.78 (m, 9H, *meso* + phenylene), 9.37 (s, 2H, *β*), 9.33 (s, 2H, *β*), 8.84–8.72 (m, 2H, *β*), 8.47 (br s, 2H, phenylene), 8.25 (t, J = 7.7 Hz, 1H, phenylene), 4.15–4.06 (m, 16H), 3.02 (br s, 4H, NH), 2.52–2.25 (m, 16H), 1.94–1.32 (m, 48H), 1.19–0.53 (m, 24H); ^{13}C{^{1}H} NMR (100 MHz, 1,1,2,2-tetrachloroethane-d_2, 363 K): δ 146.1, 145.3, 144.8, 144.0, 143.5 142.8, 142.1, 139.6, 138.1, 135.7, 134.6, 133.8, 123.1, 122.5, 110.9, 99.9, 32.5, 32.2, 32.2, 32.0, 31.9, 30.2, 30.1, 28.6, 28.6, 27.2, 22.8, 22.7, 22.7, 22.6, 14.2; UV–Vis ($CHCl_3$): λ_{max} (ε [M^{-1} cm^{-1}]) 373 (244 000), 390 (216 000), 567 (73 900), 606 (66 100), 639 (91 500); HRMS (MALDI–TOF, dithranol): *m/z* calcd for $C_{94}H_{127}N_8^+$ ([M + H]$^+$) 1368.0178, found 1368.0198.

Synthesis of **Pc2-Th**

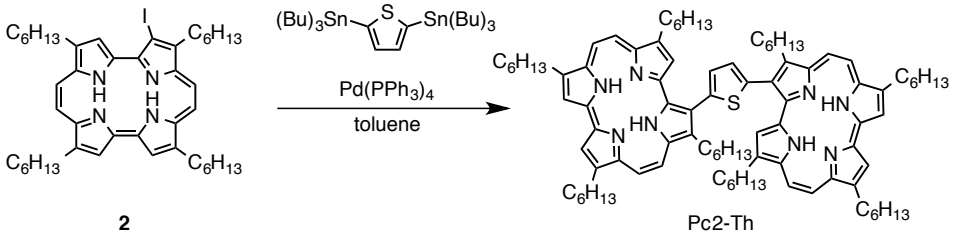

2,5-Bis(tributylstannyl)thiophene (22.5 mg, 34.0 μmol) was added to a solution of **2** (50.1 mg, 64.8 μmol) and $Pd(PPh_3)_4$ (10.0 mg, 8.65 μmol) in toluene (5.0 mL). The mixture was degassed by bubbling with nitrogen for 15 min and then refluxed for 44 h. The crude product was purified by gravity silica gel column chromatography (CH_2Cl_2/hexanes, 1:9) and GPC. Recrystallization from a $CHCl_3$ solution by adding methanol gave **Pc2-Th** as a purple solid (15.6 mg, 11.3 μmol, 35 %). ^{1}H NMR (400 MHz, $CDCl_3$, 294 K): δ 9.97 (d, J = 11.0 Hz, 2H, *meso*), 9.84 (d, J = 11.0 Hz, 2H, *meso*), 9.81 (s, 4H, *meso*), 9.41 (s, 2H, *β*), 9.34 (s, 2H, *β*), 9.29 (s, 2H, *β*), 8.12 (s, 2H, thienylene), 4.32 (t, J = 7.7 Hz, 4H), 4.15–4.06 (m, 12H), 3.02 (br s, 2H, NH), 2.96 (br s, 2H, NH), 2.54–2.34 (m, 16H), 1.91–1.73 (m, 16H), 1.63–1.32 (m, 32H), 0.98 (t, J = 7.1 Hz, 12H), 0.82 (t, J = 7.5 Hz, 12H) ^{13}C{^{1}H} NMR (100 MHz, $CDCl_3$): δ 146.6, 146.6, 146.1, 144.5, 144.3, 144.0, 141.6, 140.8, 139.7, 136.6, 135.9, 133.7, 132.7, 131.5, 131.0, 123.6, 123.4, 122.3, 112.3, 111.4, 110.1, 110.01, 34.6, 32.6, 32.2, 32.1, 12.1, 32.0, 30.3, 29.8, 28.8, 28.6, 28.5, 27.6, 22.9, 22.8, 14.3, 14.2, 14.1; UV–Vis ($CHCl_3$): λ_{max} (ε [M^{-1} cm^{-1}]) 373 (263 000), 385 (250 000), 570 (82 200), 609 (80 500), 641 (107 000); HRMS (MALDI–TOF, dithranol): *m/z* calcd for $C_{92}H_{125}N_8S^+$ ([M + H]$^+$) 1373.9742, found 1373.9757.

Synthesis of Pc2-B

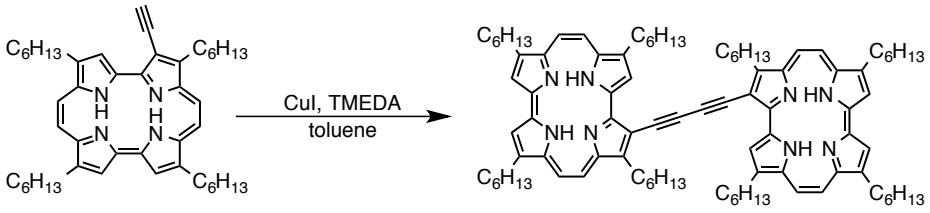

5 Pc2-B

3-Ethynyl-2,7,12,17-tetrahexylporphycene **5** (24.0 mg, 35.8 μmol), CuI (7.2 mg, 38 μmol), *N*,*N*,*N*′,*N*′-tetramethylethylenediamine (TMEDA, 0.1 mL) and THF (5.0 mL) were placed in flask. The mixture was stirred for 1 h under air at room temperature. After removal of the solvent under a reduced pressure, the crude product was purified by column chromatography on gravity silica gel (CH_2Cl_2/hexanes, 1:9). Recrystallization from a $CHCl_3$ solution by adding hexanes gave **Pc2-B** as a purple solid (17.2 mg, 12.8 μmol, 72%). ^{1}H NMR (400 MHz, $CDCl_3$, 294 K): δ 10.32 (s, 2H), 9.78 (d, *J* = 11.0 Hz, 2H), 9.74–9.70 (m, 4H), 9.68 (d, *J* = 11.0 Hz, 2H), 9.34 (s, 2H), 9.24 (s, 2H), 4.32 (t, *J* = 7.6 Hz, 4H), 4.15–4.10 (m, 12H), 3.10 (br s, 2H), 2.81 (br s, 2H), 2.55–2.37 (m, 16H), 1.94–1.35 (m, 44H), 1.26–1.17 (m, 4H), 0.99 (t, *J* = 7.3 Hz, 12H), 0.93 (t, *J* = 7.3 Hz, 6H), 0.62 (t, *J* = 7.3 Hz, 6H); ^{13}C{^{1}H} NMR (150 MHz, $CDCl_3$): δ 153.2, 148.7, 148.0, 145.7, 144.4, 143.1, 139.7, 139.3, 138.1, 136.5, 131.9, 130.9, 124.0, 122.8, 122.0, 118.7, 112.9, 112.0, 110.5, 109.0, 84.5, 81.7, 32.5, 32.6, 32.1, 32.1. 32.0, 31.9, 29.6, 29.8, 28.6, 28.4, 28.1, 22.9, 22.9, 22.7, 14.3, 14.0; UV–Vis ($CHCl_3$): λ_{max} (ε [M^{-1} cm^{-1}]) 377 (220 000), 394 (219 000), 582 (67 400), 629 (93 100), 650 (105 000); HRMS (MALDI–TOF, dithranol): *m/z* calcd for $C_{92}H_{123}N_8^+$ ([M + H]$^+$) 1339.9865, found 1339.9870. CCDC No. 1017232.

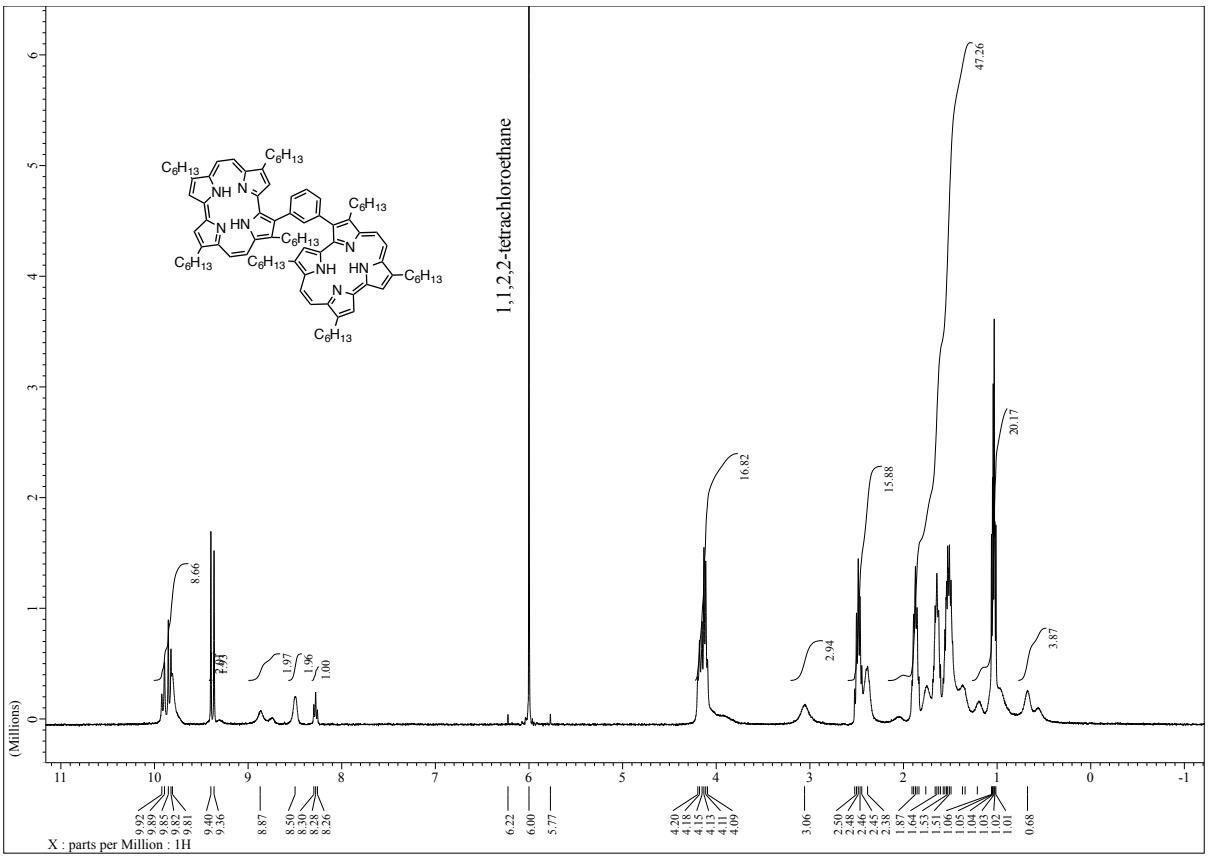

^{1}H NMR spectrum of **Pc2-Ph** in 1,1,2,2-tetrachloroethane-d_2.

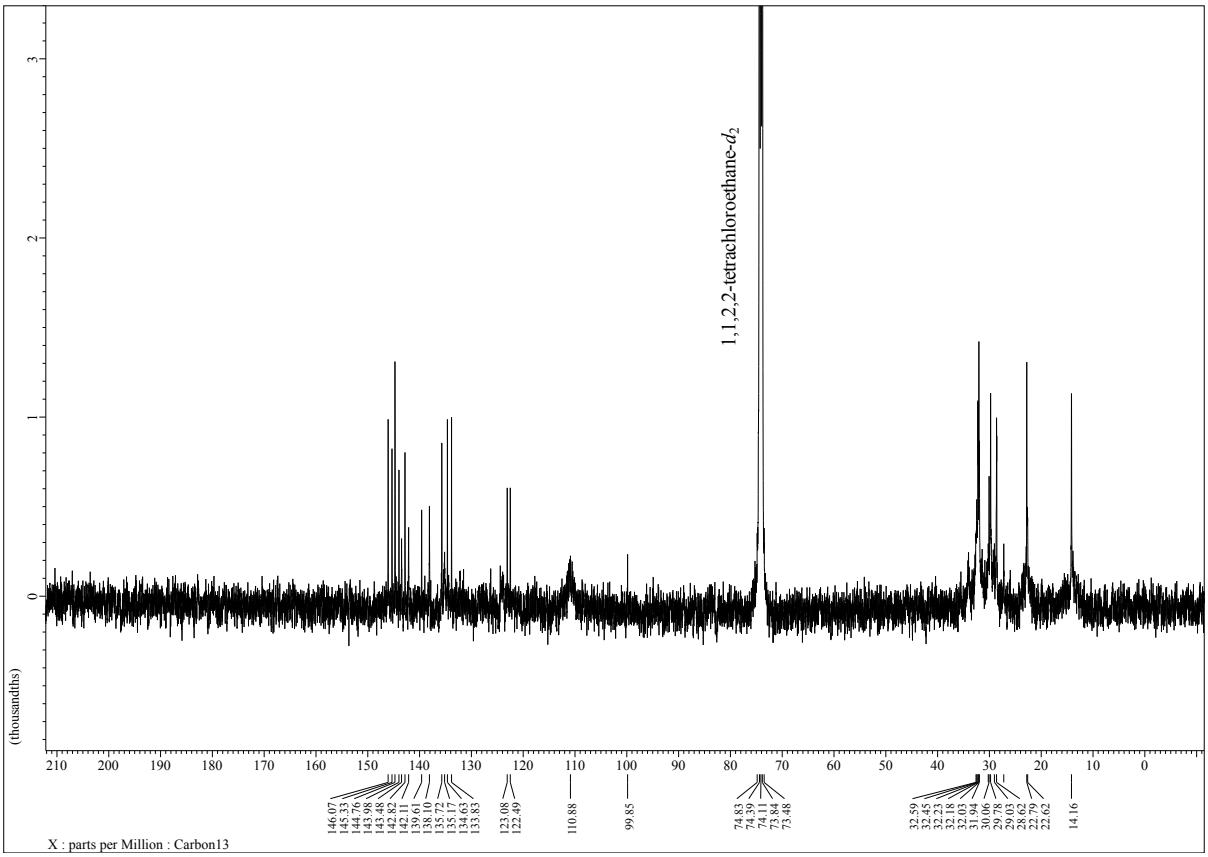

^{13}C{^{1}H} NMR spectrum of **Pc2-Ph** in1,1,2,2-tetrachloroethane-d_2.

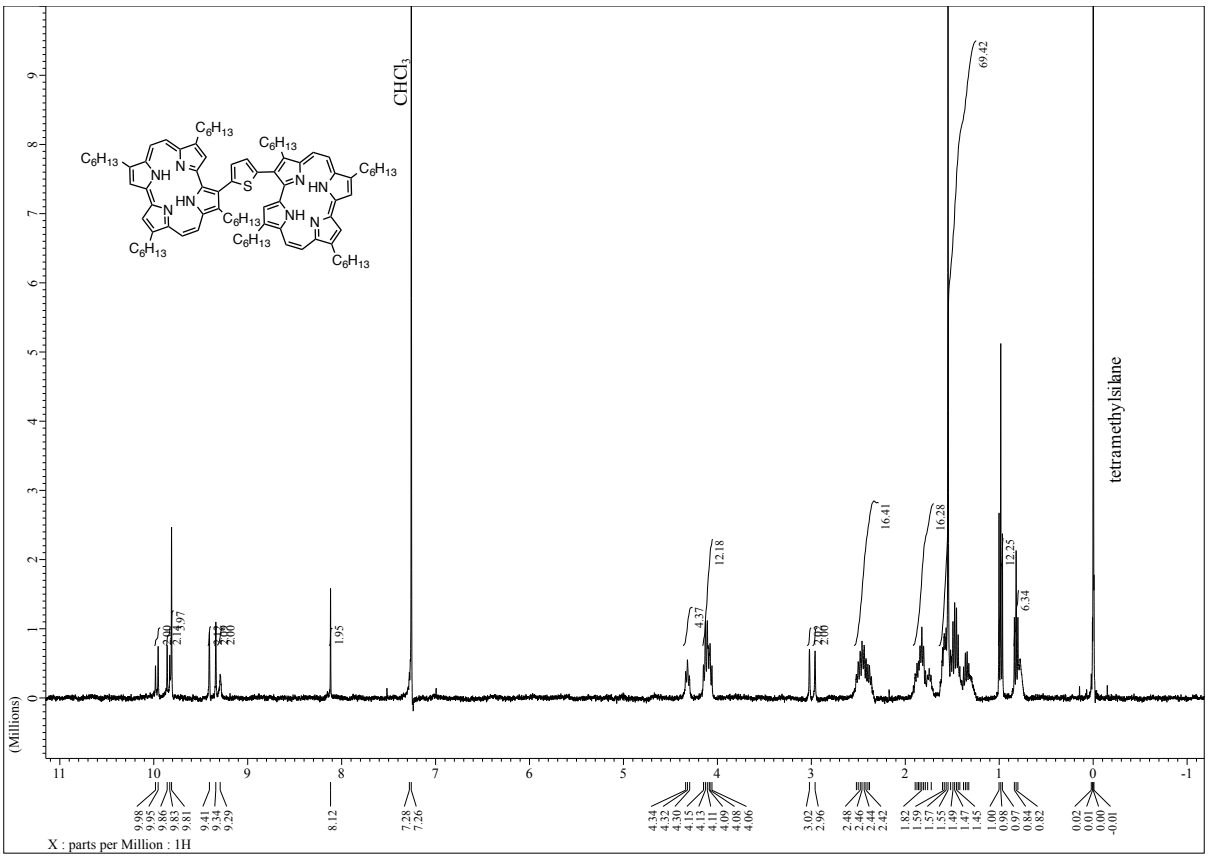

^{1}H NMR spectrum of **Pc2-Th** in $CDCl_3$.

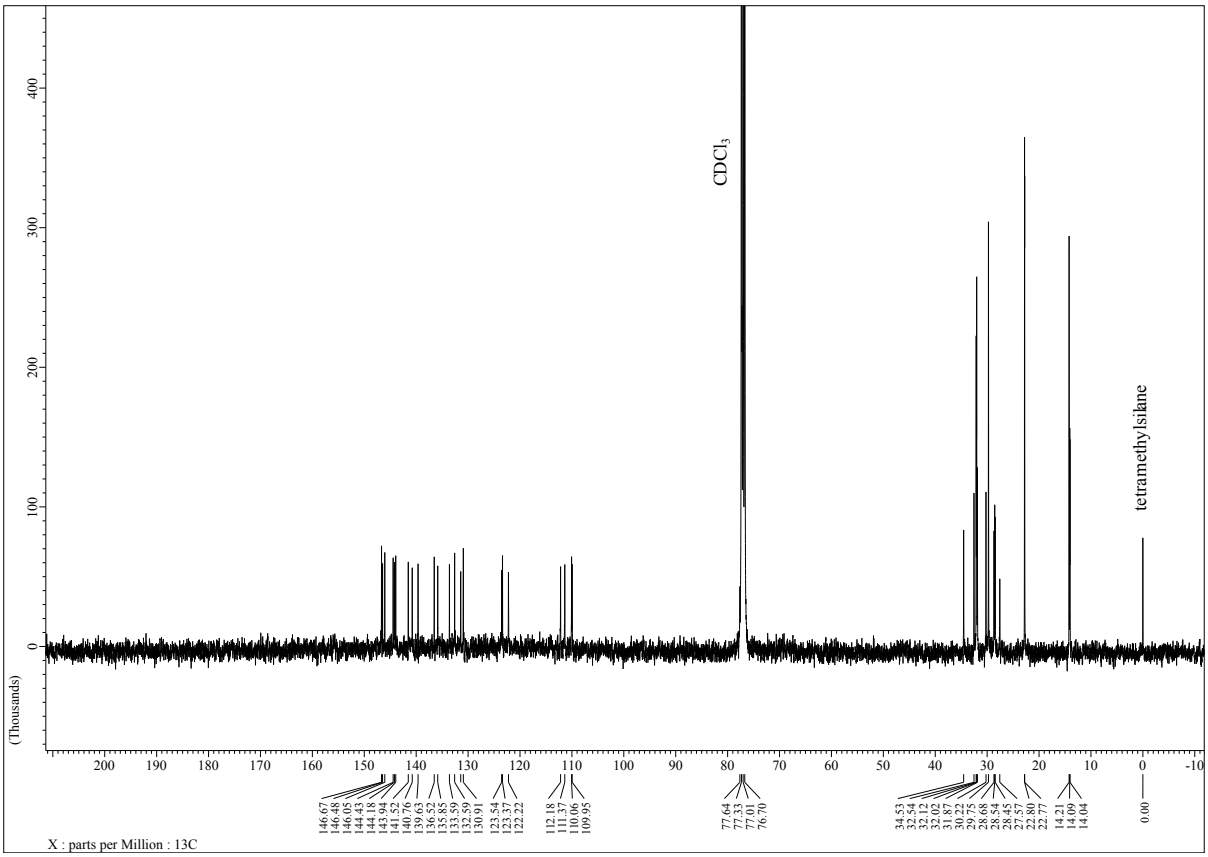

$^{13}C\{^{1}H\}$ NMR spectrum of **Pc2-Th** in $CDCl_3$.

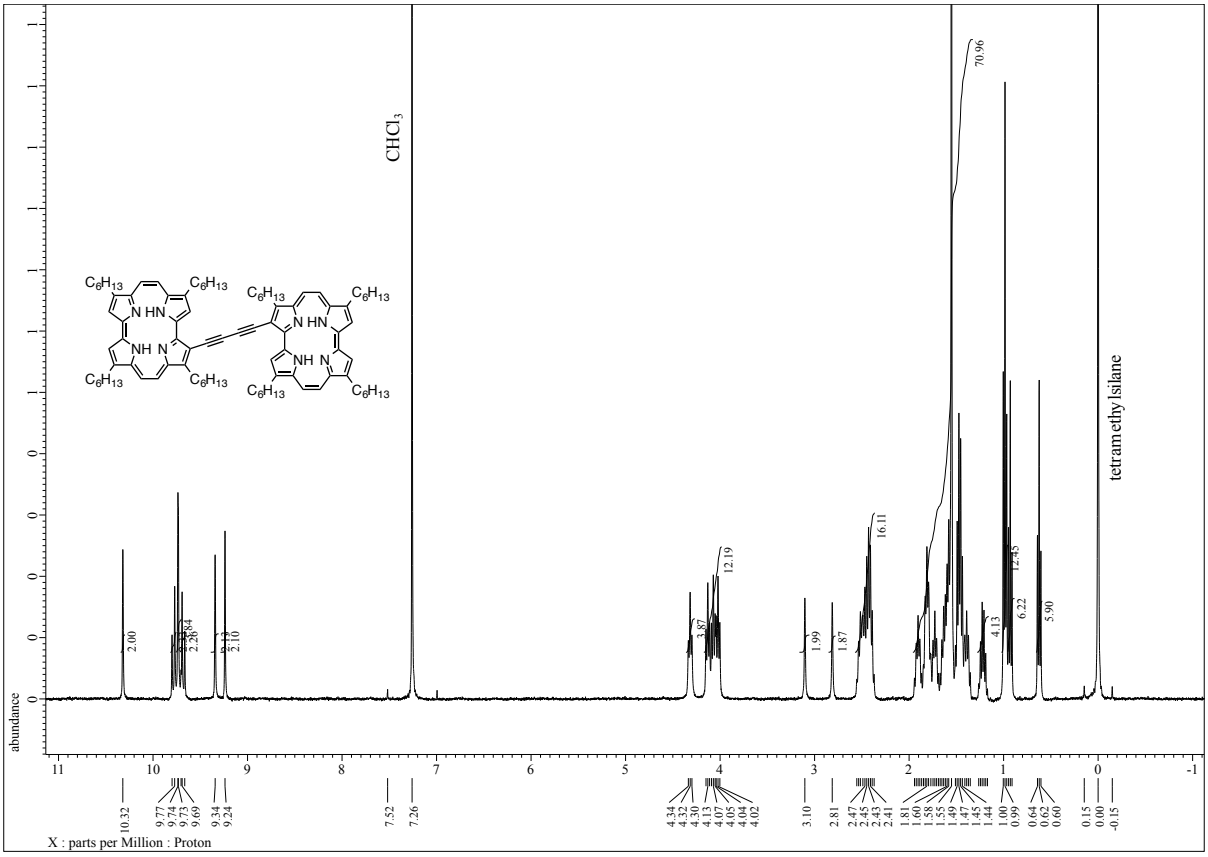

^{1}H NMR spectrum of **Pc2-B** in $CDCl_3$.

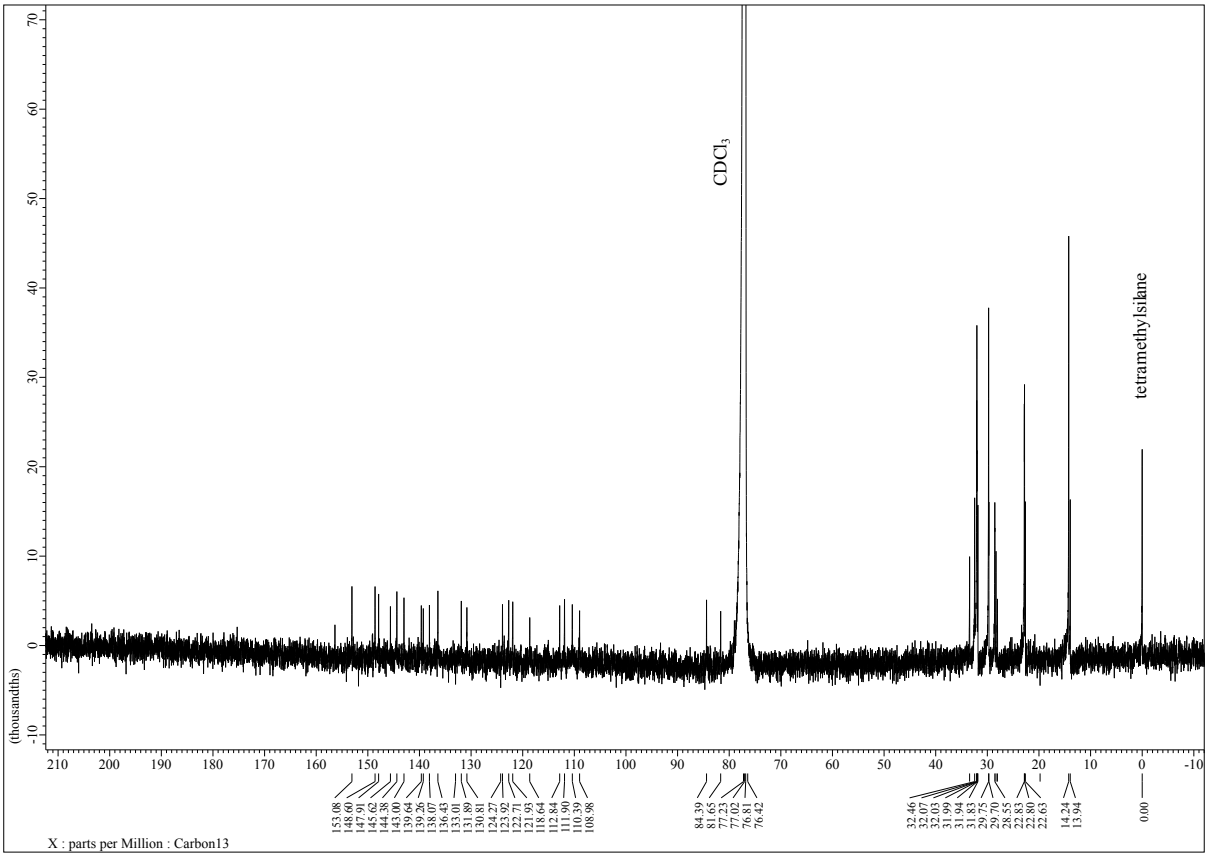

$^{13}C\{^{1}H\}$ NMR spectrum of **Pc2-B** in $CDCl_3$.

3-9. References

(1) Brabec, C. J.; Gowrisanker, S.; Halls, J. J. M.; Laird, D.; Jia, S.; Williams, S. P. Polymer-Fullerene Bulk-Heterojunction Solar Cells. *Adv. Mater.* **2010**, *22* (34), 3839–3856.

(2) He, Y.; Chen, H.-Y.; Hou, J.; Li, Y. Indene−C_{60} Bisadduct: A New Acceptor for High-Performance Polymer Solar Cells. *J. Am. Chem. Soc.* **2010**, *132* (4), 1377–1382.

(3) Varotto, A.; Treat, N. D.; Jo, J.; Shuttle, C. G.; Batara, N. A.; Brunetti, F. G.; Seo, J. H.; Chabinyc, M. L.; Hawker, C. J.; Heeger, A. J.; Wudl, F. 1,4-Fullerene Derivatives: Tuning the Properties of the Electron Transporting Layer in Bulk-Heterojunction Solar Cells. *Angew. Chem. Int. Ed.* **2011**, *50* (22), 5166–5169.

(4) Zhang, X.; Lu, Z.; Ye, L.; Zhan, C.; Hou, J.; Zhang, S.; Jiang, B.; Zhao, Y.; Huang, J.; Zhang, S.; Liu, Y.; Shi, Q.; Liu, Y.; Yao, J. A Potential Perylene Diimide Dimer-Based Acceptor Material for Highly Efficient Solution-Processed Non-Fullerene Organic Solar Cells with 4.03% Efficiency. *Adv. Mater.* **2013**, *25* (40), 5791–5797.

(5) Li, H.; Hwang, Y.-J.; Courtright, B. A. E.; Eberle, F. N.; Subramaniyan, S.; Jenekhe, S. A. Fine-Tuning the 3D Structure of Nonfullerene Electron Acceptors Toward High-Performance Polymer Solar Cells. *Adv. Mater.* **2015**, *27* (21), 3266–3272.

(6) Xia, D.; Gehrig, D.; Guo, X.; Baumgarten, M.; Laquai, F.; Müllen, K. A Spiro-Bifluorene Based 3D Electron Acceptor with Dicyanovinylene Substitution for Solution-Processed Non-Fullerene Organic Solar Cells. *J. Mater. Chem. A* **2015**, *3* (20), 11086–11092.

(7) Ie, Y.; Sakurai, T.; Jinnai, S.; Karakawa, M.; Okuda, K.; Mori, S.; Aso, Y. Three-Dimensional Electron-Accepting Compounds Containing Perylene Bis(Dicarboximide)s as N-Type Organic Photovoltaic Materials. *Chem. Commun.* **2013**, *49* (75), 8386–8388.

(8) Mao, Z.; Senevirathna, W.; Liao, J.-Y.; Gu, J.; Kesava, S. V.; Guo, C.; Gomez, E. D.; Sauvé, G. Azadipyrromethene-Based Zn(II) Complexes as Nonplanar Conjugated Electron Acceptors for Organic Photovoltaics. *Adv. Mater.* **2014**, *26* (36), 6290–6294.

(9) Xin, R.; Feng, J.; Zeng, C.; Jiang, W.; Zhang, L.; Meng, D.; Ren, Z.; Wang, Z.; Yan, S. Nonfullerene-Acceptor All-Small-Molecule Organic Solar Cells Based on Highly Twisted Perylene Bisimide with an Efficiency of Over 6%. *ACS Appl. Mater. Interfaces* **2017**, *9* (3), 2739–2746.

(10) Zhao, J.; Li, Y.; Lin, H.; Liu, Y.; Jiang, K.; Mu, C.; Ma, T.; Lai, J. Y. L.; Hu, H.; Yu, D.; Yan, H. High-Efficiency Non-Fullerene Organic Solar Cells Enabled by a Difluorobenzothiadiazole-Based Donor Polymer Combined with a Properly Matched Small Molecule Acceptor. *Energy Environ. Sci.* **2015**, *8* (2), 520–525.

(11) Li, H.; Earmme, T.; Ren, G.; Saeki, A.; Yoshikawa, S.; Murari, N. M.; Subramaniyan, S.; Crane, M. J.; Seki, S.; Jenekhe, S. A. Beyond Fullerenes: Design of Nonfullerene Acceptors for Efficient Organic Photovoltaics. *J. Am. Chem. Soc.* **2014**, *136* (41), 14589–14597.

(12) Vogel, E.; Köcher, M.; Schmickler, H.; Lex, J. Porphycene—a Novel Porphin Isomer. *Angew. Chem. Int. Ed.* **1986**, *25* (3), 257.

(13) Waluk, J.; Müller, M.; Swiderek, P.; Kocher, M.; Vogel, E.; Hohlneicher, G.; Michl, J. Electronic States of Porphycenes. *J. Am. Chem. Soc.* **1991**, *113* (15), 5511–5527.

(14) Okabe, T.; Kuzuhara, D.; Suzuki, M.; Aratani, N.; Yamada, H. Synthesis and Electrochemical Properties of Porphycene–Diketopyrrolopyrrole Conjugates. *Org. Lett.* **2014**, *16* (13), 3508–3511.

(15) Pommerehne, J.; Vestweber, H.; Guss, W.; Mahrt, R. F.; Bässler, H.; Porsch, M.; Daub, J. Efficient two layer leds on a polymer blend basis. *Adv. Mater.* **1995**, *7* (6), 551–554.

(16) Goh, C.; Kline, R. J.; McGehee, M. D.; Kadnikova, E. N.; Fréchet, J. M. J. Molecular-Weight-Dependent Mobilities in Regioregular Poly(3-Hexyl-Thiophene) Diodes. *Appl. Phys. Lett.* **2005**, *86* (12), 122110–122114.

(17) Chiu, F.-C. A Review on Conduction Mechanisms in Dielectric Films. *Adv. Mater. Sci. Eng.* **2014**, *2014* (7), 1–18.

(18) Osaka, I.; Saito, M.; Koganezawa, T.; Takimiya, K. Thiophene-Thiazolothiazole Copolymers: Significant Impact of Side Chain Composition on Backbone Orientation and Solar Cell Performances. *Adv. Mater.* **2013**, *26* (2), 331–338.

(19) Najari, A.; Beaupré, S.; Allard, N.; Ouattara, M.; Pouliot, J.-R.; Charest, P.; Besner, S.; Simoneau, M.; Leclerc, M. Thieno, Furo, and Selenopheno[3,4-*c*]Pyrrole-4,6-Dione Copolymers: Air-Processed Polymer Solar Cells with Power Conversion Efficiency Up to 7.1%. *Adv. Energy Mater.* **2015**, *5* (23), 1501213–1501219.

(20) Takahashi, K.; Kumagai, D.; Yamada, N.; Kuzuhara, D.; Yamaguchi, Y.; Aratani, N.; Koganezawa, T.; Koshika, S.; Yoshimoto, N.; Masuo, S.; Suzuki, M.; Nakayama, K.-I.; Yamada, H. Side-Chain Engineering in a Thermal Precursor Approach for Efficient Photocurrent Generation. *J. Mater. Chem. A* **2017**, *5* (27), 14003–14011.

(21) Zhang, G.; Zhang, K.; Yin, Q.; Jiang, X.-F.; Wang, Z.; Xin, J.; Ma, W.; Yan, H.; Huang, F.; Cao, Y. High-Performance Ternary Organic Solar Cell Enabled by a Thick Active Layer Containing a Liquid Crystalline Small Molecule Donor. *J. Am. Chem. Soc.* **2017**, *139* (6), 2387–2395.

(22) Deng, D.; Zhang, Y.; Zhang, J.; Wang, Z.; Zhu, L.; Fang, J.; Xia, B.; Wang, Z.; Lu, K.; Ma, W.; Wei, Z. Fluorination-Enabled Optimal Morphology Leads to Over 11% Efficiency for

Inverted Small-Molecule Organic Solar Cells. *Nat*. *Commun*. **2016**, *7*, 1–9.

(23) Jung, M.; Yoon, Y.; Park, J. H.; Cha, W.; Kim, A.; Kang, J.; Gautam, S.; Seo, D.; Cho, J. H.; Kim, H.; Choi, J. Y.; Chae, K. H.; Kwak, K.; Son, H. J.; Ko, M. J.; Kim, H.; Lee, D.-K.; Kim, J. Y.; Choi, D. H.; Kim, B. Nanoscopic Management of Molecular Packing and Orientation of Small Molecules by a Combination of Linear and Branched Alkyl Side Chains. *ACS Nano* **2014**, *8* (6), 5988–6003.

(24) Sun, K.; Xiao, Z.; Hanssen, E.; Klein, M. F. G.; Dam, H. H.; Pfaff, M.; Gerthsen, D.; Wong, W. W. H.; Jones, D. J. The Role of Solvent Vapor Annealing in Highly Efficient Air-Processed Small Molecule Solar Cells. *J. Mater. Chem. A* **2014**, *2* (24), 9048–9048.

(25) Li, G.; Shrotriya, V.; Huang, J.; Yao, Y.; Moriarty, T.; Emery, K.; Yang, Y. High-Efficiency Solution Processable Polymer Photovoltaic Cells by Self-Organization of Polymer Blends. *Nat*. *Mater*. **2005**, *4* (11), 864–868.

(26) Proctor, C. M.; Love, J. A.; Nguyen, T.-Q. Mobility Guidelines for High Fill Factor Solution-Processed Small Molecule Solar Cells. *Adv. Mater.* **2014**, *26* (34), 5957–5961.

(27) Gomez, E. D.; Barteau, K. P.; Wang, H.; Toney, M. F.; Loo, Y.-L. Correlating the Scattered Intensities of P3HT and PCBM to the Current Densities of Polymer Solar Cells. *Chem. Commun.* **2011**, *47* (1), 436–438.

(28) Yang, L.; Zhang, S.; He, C.; Zhang, J.; Yao, H.; Yang, Y.; Zhang, Y.; Zhao, W.; Hou, J. New Wide Band Gap Donor for Efficient Fullerene-Free All-Small-Molecule Organic Solar Cells. *J. Am. Chem. Soc.* **2017**, *139* (5), 1958–1966.

(29) Kwon, O. K.; Park, J.-H.; Kim, D. W.; Park, S. K.; Park, S. Y. An All-Small-Molecule Organic Solar Cell with High Efficiency Nonfullerene Acceptor. *Adv. Mater.* **2015**, *27* (11), 1951–1956.

(30) Bin, H.; Zhang, Z.-G.; Gao, L.; Chen, S.; Zhong, L.; Xue, L.; Yang, C.; Li, Y. Non-Fullerene Polymer Solar Cells Based on Alkylthio and Fluorine Substituted 2D-Conjugated Polymers Reach 9.5% Efficiency. *J. Am. Chem. Soc.* **2016**, *138* (13), 4657–4664.

(31) Rajaram, S.; Shivanna, R.; Kandappa, S. K.; Narayan, K. S. Nonplanar Perylene Diimides as Potential Alternatives to Fullerenes in Organic Solar Cells. *J*. *Phys*. *Chem*. *Lett*. **2012**, *3* (17), 2405−2408.

(32) Zhao, W.; Qian, D.; Zhang, S.; Li, S.; Inganäs, O.; Gao, F.; Hou, J. Fullerene-Free Polymer Solar Cells with Over 11% Efficiency and Excellent Thermal Stability. *Adv. Mater.* **2016**, *28* (23), 4734–4739.

(33) Li, S.; Ye, L.; Zhao, W.; Zhang, S.; Mukherjee, S.; Ade, H.; Hou, J. Energy-Level Modulation of Small-Molecule Electron Acceptors to Achieve Over 12% Efficiency in

Polymer Solar Cells. *Adv. Mater.* **2016**, *28* (42), 9423–9429.

(34) Zhao, W.; Li, S.; Yao, H.; Zhang, S.; Zhang, Y.; Yang, B.; Hou, J. Molecular Optimization Enables Over 13% Efficiency in Organic Solar Cells. *J. Am. Chem. Soc.* **2017**, *139* (21), 7148–7151.

(35) Lu, Z.; Zhang, X.; Zhan, C.; Jiang, B.; Zhang, X.; Chen, L.; Yao, J. Impact of Molecular Solvophobicity vs. Solvophilicity on Device Performances of Dimeric Perylene Diimide Based Solution-Processed Non-Fullerene Organic Solar Cells. *Phys. Chem. Chem. Phys.* **2013**, *15* (27), 11375–11385.

(36) Spek, A. L. PLATON, A Multipurpose Crystallographic Tool, Utrecht, The Netherlands, 2005.

(37) Particle Size Distribution and X-Ray Diffraction Peak Profiles in Supersaturated Solid Solutions. **1990**, *46* (3), 187–194.

(38) Sheldrick, G. M. A Short History of SHELX. *Acta Cryst* **2007**, *64* (1), 112–122.

(39) Sun, Y.; Seo, J. H.; Takacs, C. J.; Seifter, J.; Heeger, A. J. Inverted Polymer Solar Cells Integrated with a Low-Temperature-Annealed Sol-Gel-Derived ZnO Film as an Electron Transport Layer. *Adv. Mater. Weinheim* **2011**, *23* (14), 1679–1683.

Chapter 4

Effect of Side Chains on the Optoelectronic Properties of Diketopyrrolopyrrole-Based Small Molecules

---

In this chapter, the effect of the hydrophilic OEG side chain on the properties of small molecular DPP-based materials for the optoelectronic application are described.

4-1. Introduction

The side chains of organic semiconducting compounds can affect the solid-state morphology and determine the performance of organic electronic devices such as organic solar cells (OSCs) and organic field-effect transistors (OFETs).[1–5] The charge-carrier transport depends on the directionallity of π–π stacking, namely, molecular orientation. For instance, the combination of two different lengths of alkyl chains in the thiazolothiazole-based polymers PTzBT-14HD and PTzBT-BOHD induced molecular orientation and led to improving charge mobility and a power conversion efficiency (PCE) of OSC device from 4.5% to 7.5% (Figure4-1).[5]

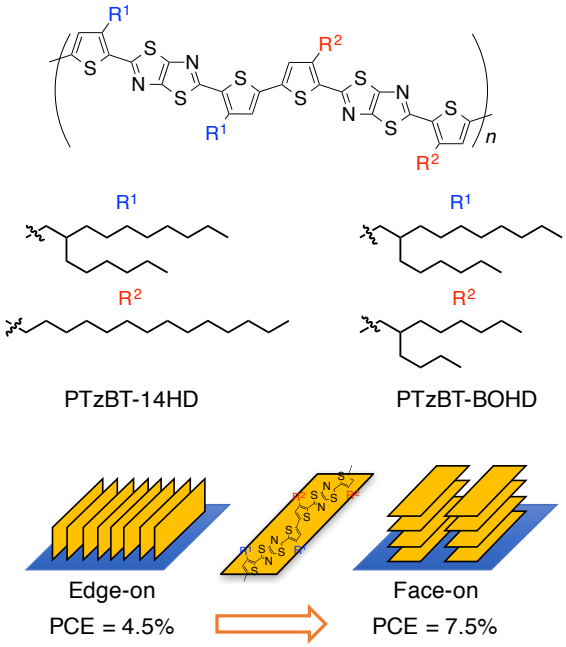

Figure 4-1. Molecular structures of PTzBT derivatives and illustration of molecular orientations in the thin-film state.

The photocurrent generation occurs at the interface between p-type and n-type materials, thus the miscibility of materials and the film morphology affect a OSC performance.[6–12] The incorporation of hydrophilic oligo (ethylene glycol) (OEG) into the side chains of π-conjugates alter the interactions among side chains and thus affect the packing and interactions among the

conjugated backbones.[13–15] Meng et al. have reported that the OEG chains of a conjugated polymer based on fluorene and benzothiadiazole, PFDTOBT-O2, led to facilitaing not only favorable miscibility with fullerene-based n-type materials but also π–π stacking of polymer backbones.[16] The effective π–π stacking induced to improve the charge carrier mobilities and photovoltaic performances compared with alkyl substituted polymer PFDTOBT (Figure 4-2a). In conjugated polymers, the CH_2–CH_2 interactions between hydrophobic alkyl chains impede π–π stacking of polymer backbones, whereas more flexible rotation of O–CH_2 in hydrophilic OEG chains removes the self-cohesion effect of alkyl chains and leads to more effective π–π stacking between polymer backbones.[16–18]

On the other hand, few small molecules having OEG chains showed semiconductive properties.[19–20] Chen et al. have reported that hydrophilic small molecule *p*-CDT(PTFu_2)$_2$ showed a low crystallinity in the thin film leading to prevent the photocurrent generation (Figure 4-2b).[20] A single-crystal structure of small molecule gives more detailed information on film structure compared with the polymers, however, this analysis has not been used to the investigation of the effect of side chains. Taking these backgrounds into consideration, this project aims to reveal the effect of the hydrophilic OEG side chain on the properties of small molecular materials for the optoelectronic application.

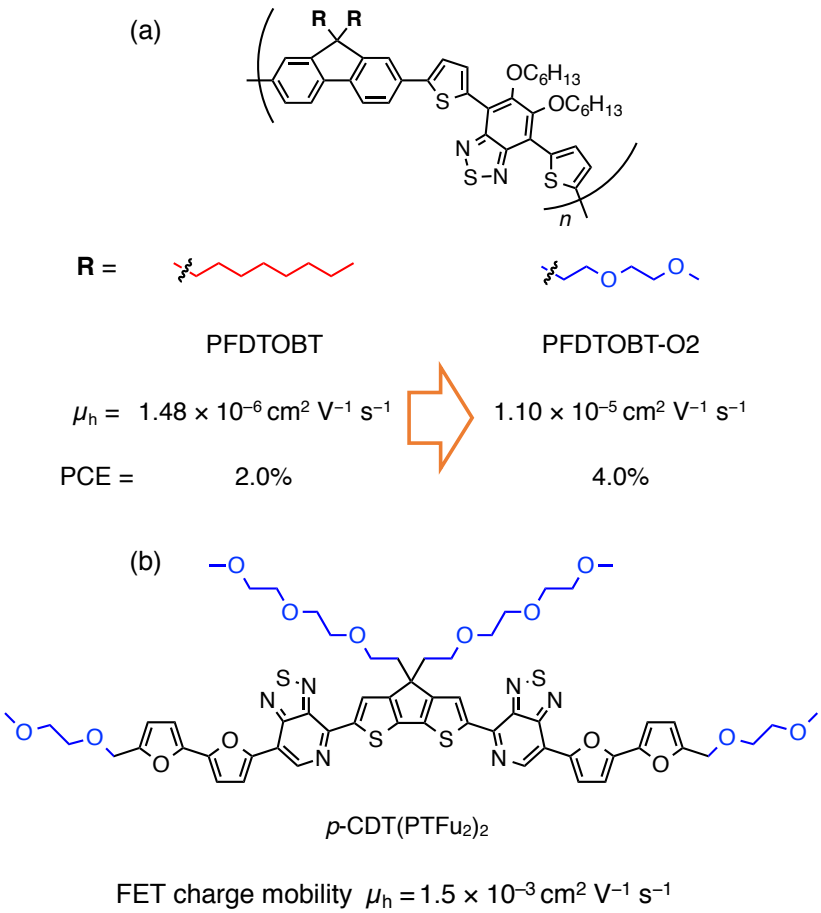

Figure 4-2. Chemical structures of hydrophilic materials: (a) fluorene and benzothiadiazole-based polymer PFDTOBT and PFDTOBT-O2 and (b) cyclopentadithiophene-based small molecule *p*-CDT(PTFu$_2$)$_2$.

DPP is a typical industrial pigment with a high photoabsorption. It has demonstrated that its valuable utility as a building block for use in constructing molecular semiconductors due to its facile synthesis, strong electron affinity that enables low frontier energy levels and ease of structural modification. For instance, the DPP-based small molecule, DPP(TBFu)$_2$, is well-known as a common p-type material, which was reported by Walker et al. (Figure 4-3a).[21] OSCs with DPP(TBFu)$_2$ and fullerene derivative such as [6,6]-phenyl-C$_{61}$-butyric acid methyl ester (PC$_{61}$BM) have achieved a power conversion efficiency (PCE) more than 4%.[22–26] In addition, DPP derivatives were found to exhibit moderate carrier mobilities in OFETs.[27–29] For example, Tantiwiwat et al. reported the DPP-based small molecule (DHT6DPPC6) with a maximum hole mobility of 0.02 cm^2 V^{-1} s^{-1} (Figure 4-3b).[30] Thus, the focusing on DPP

derivatives are expected to be obtained the knowledge of both OSC and OFET in the evaluation of the side-chain effect.

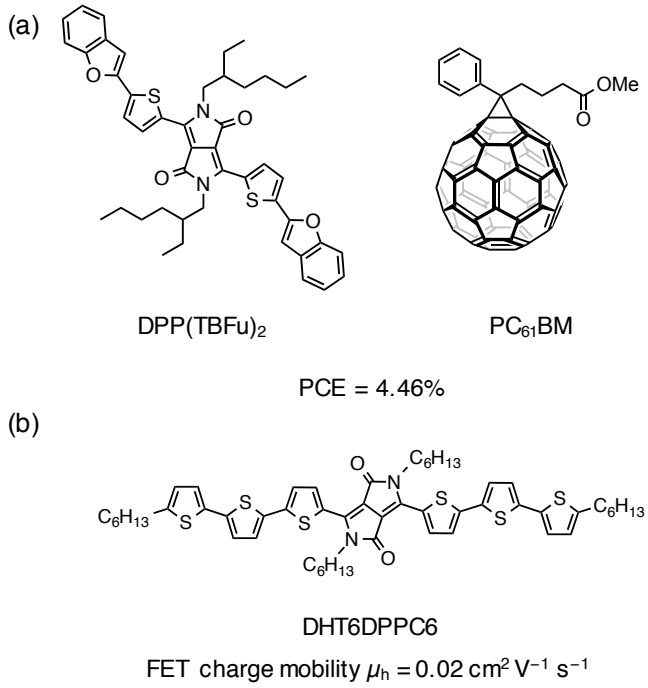

Figure 4-3. Chemical structures of DPP-based materials: (a) DPP(TBFu)$_2$ and PC$_{61}$BM system and (b) thieno[3,2-*b*]thiophene–DPP conjugated polymer P1.

The following sections in this chapter describe the comparison between the OEG and alkyl side chains in the small molecular DPP-based materials on single-crystal structure, thin film morphology, the photovoltaic and phototransistor properties (Figure4-4).

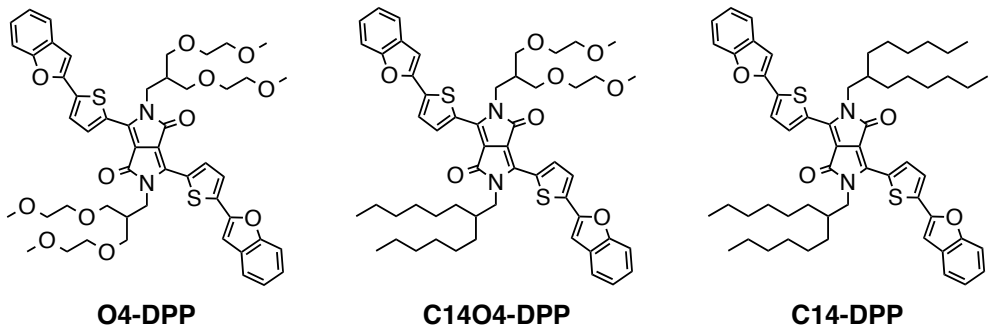

Figure 4-4. Chemical structures of the DPP derivatives synthesized in this work.

4-2. Synthesis

The *N*-alkylation of DPP was achieved under basic conditions to synthesize the alkylated DPPs as key-compounds. The synthetic scheme of DPP derivatives is shown in Scheme 4-1 according to the previously reported procedure.[16,22,31] The homo-substituted compounds, **13a** and **13c**, were synthesized using one-step *N*-alkylation, whereas the hetero-substituted compound **13b** was obtained in a step-by-step protocol via the mono-substituted intermediate **12b**. The DPPs which have either branched OEG chains (O4-DPP) or branched alkyl chains (C14-DPP) and both of OEG and alkyl chains (C14O4-DPP) were synthesized via bromination and Suzuki–Miyaura cross-coupling reaction.

Scheme 4-1. Synthesis of DPP derivatives.

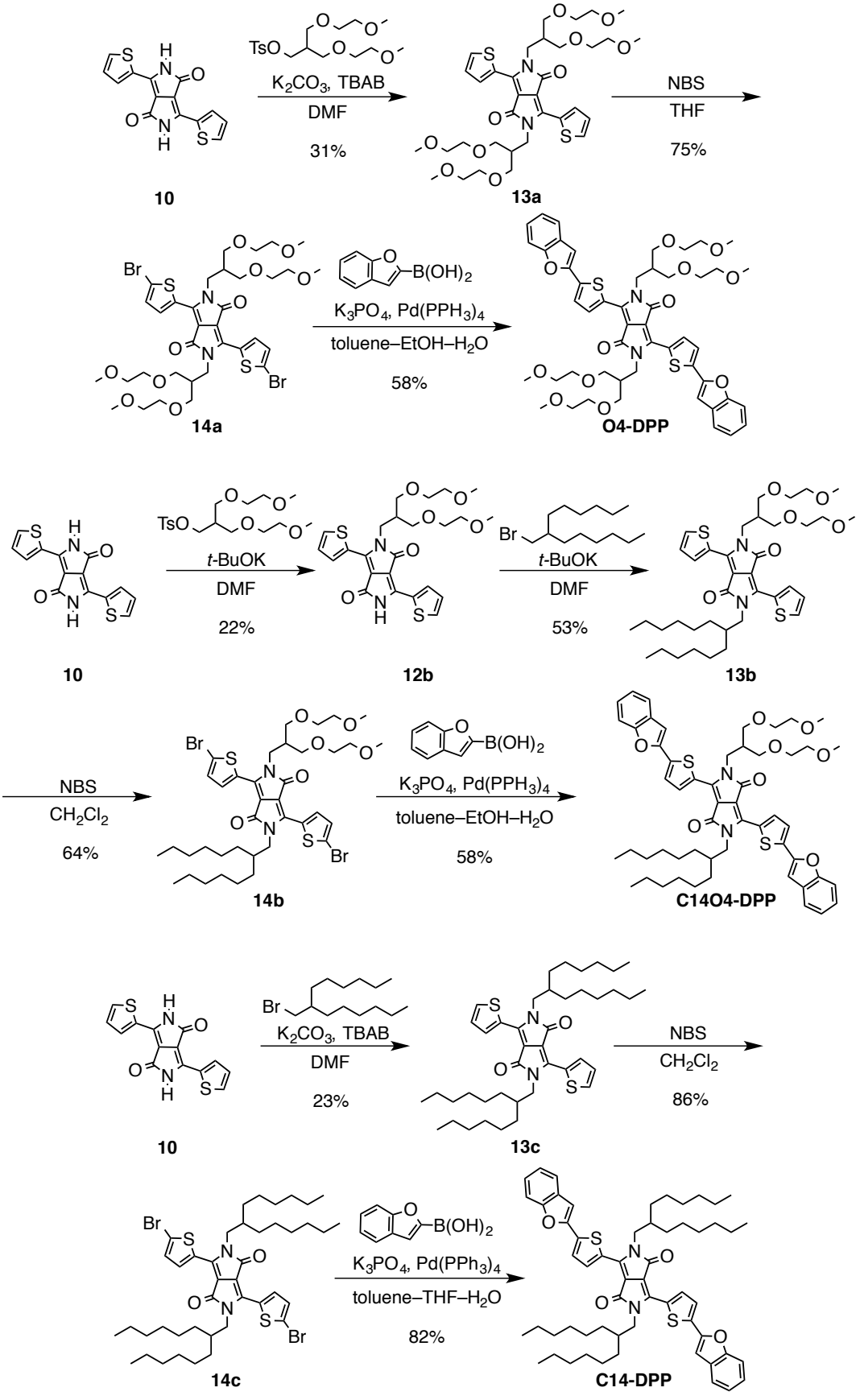

4-3. Optical and Electrochemical Properties

The light absorption and electrochemical properties in solution and in the thin-film state were investigated for comparison of the effect of side chains. The UV–Vis absorption spectra of **O4-DPP**, **C14O4-DPP** and **C14-DPP** in CH_2Cl_2 are shown in Figure 4-5. The absorption spectra of $DPP(TBFu)_2$ solution is also provided for reference. Although these DPPs have the different substituents, all the DPPs show a similar absorption shape compared with that of $DPP(TBFu)_2$ which has a strong absorption band with two peaks at 581 and 627 nm. It seems that the OEG chains and alkyl chains have little effect on the absorption spectrum in solution, therefore these substituents give no electronic effect on the DPP π-conjugation.

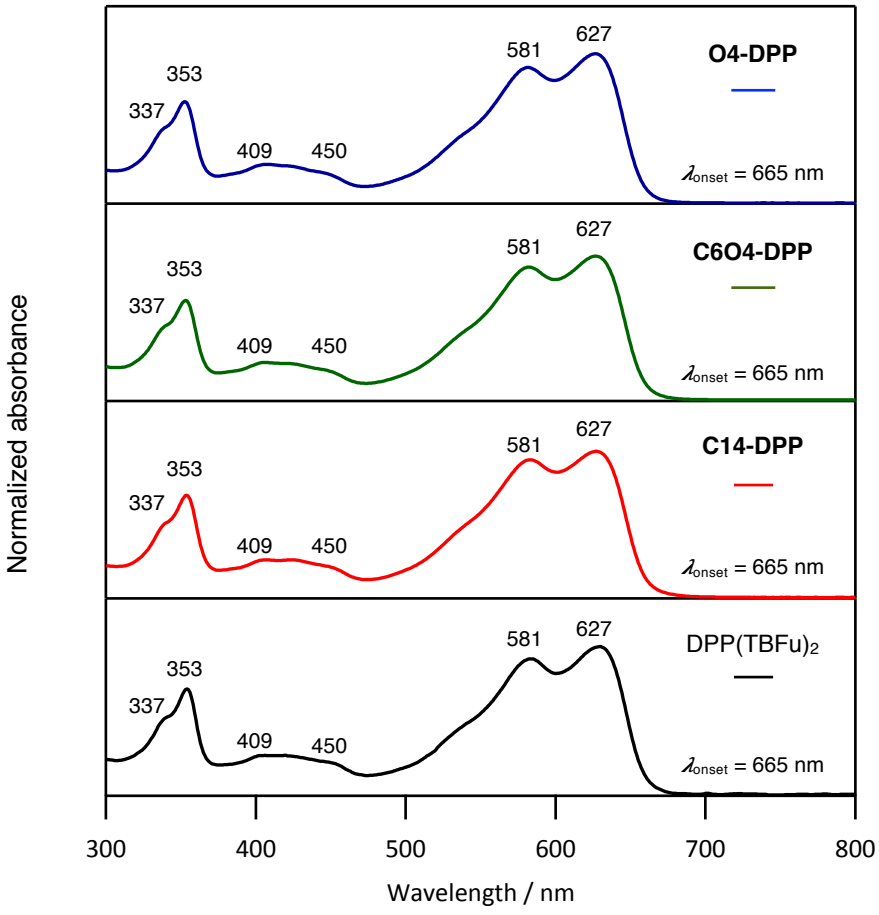

Figure 4-5. UV–Vis absorption spectra of **O4-DPP** (blue), **C14O4-DPP** (green), **C14-DPP** (red) and $DPP(TBFu)_2$ (black) in CH_2Cl_2 measured from low concentration: [**O4-DPP**, **C14O4-DPP** and **C14-DPP**] = 2×10^{-6} M and [$DPP(TBFu)_2$] = 1×10^{-6} M.

The electrochemical properties of the DPPs and the reference compound were studied by cyclic voltammetry (CV) and differential pulse voltammetry (DPV) in CH_2Cl_2 containing 0.1 M $^nBu_4NPF_6$ at room temperature (Figure 4-6). The CV of reference compound DPP(TBFu)$_2$ exhibits three one-electron reversible redox processes at $E_{1/2}$ (vs Fc/Fc$^+$) = 0.40, 0.66 and −1.52 V. The DPPs show reversible two one-electron oxidation and a one-electron reduction at similar potentials. The highest occupied molecular orbital (HOMO) and the lowest unoccupied molecular orbital (LUMO) levels were estimated based on the potentials of the first oxidation and reduction, respectively, as shown in Table 4-1. All the DPPs have similar HOMO and LUMO levels in the range of −5.20–−5.17 eV and −3.27–−3.29, respectively. Therefore, OEG and alkyl chains lead no effect on the frontier orbital energy levels in solution.

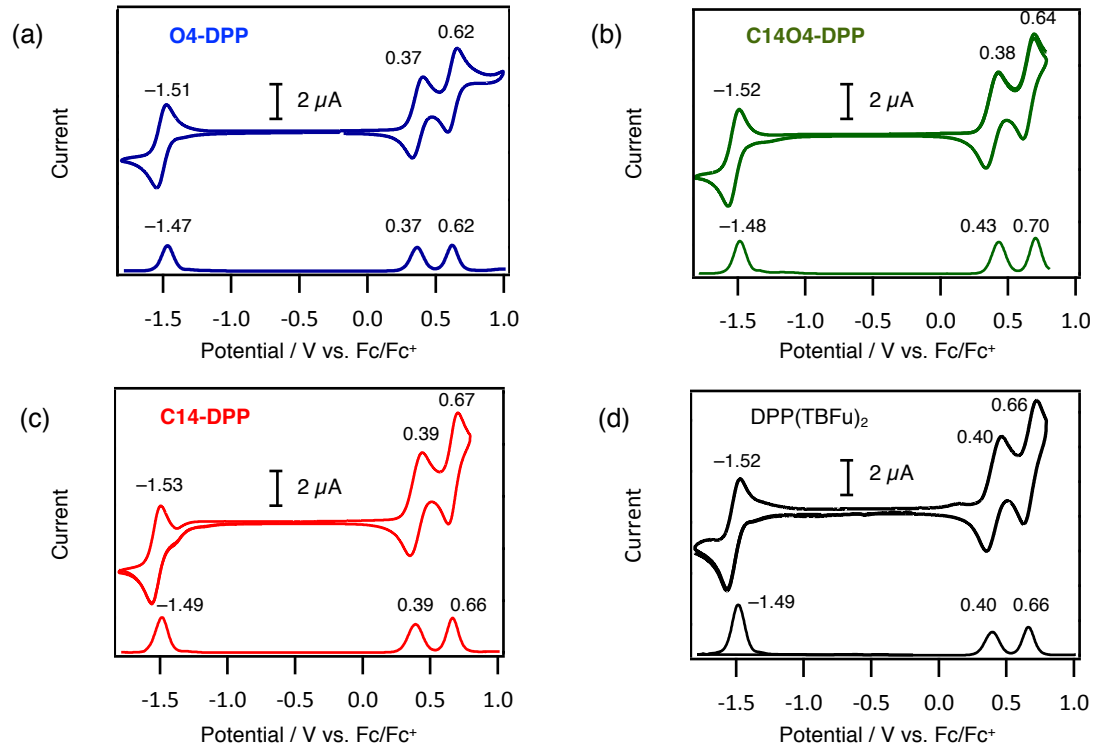

Figure 4-6. CVs (solid line) and DPVs (dotted line) of **O4-DPP** (blue), **C14O4-DPP** (green), **C14-DPP** (red) and DPP(TBFu)$_2$ (black) in CH_2Cl_2 with 0.1 M $^nBu_4NPF_6$. Scan rate = 100 mV s^{-1}. Concentration: 1.0 mM. Working electrode: glassy carbon, counter electrode: Pt, reference electrode: Ag/$AgNO_3$.

The absorption spectra of the DPPs in the thin-film state exhibit broader and red-shifted absorption band at 500–700 nm than in solution as shown in Figure 4-7. These absorption spectra are similar to the neat film of DPP(TBFu)$_2$ which shows a weaker absorption peak at 664 nm than other DPPs. On the other hand, **C14-DPP** shows a stronger peak at 669 nm than others. These results suggest that OEG and alkyl chains change intermolecular interaction in the thin-film state.

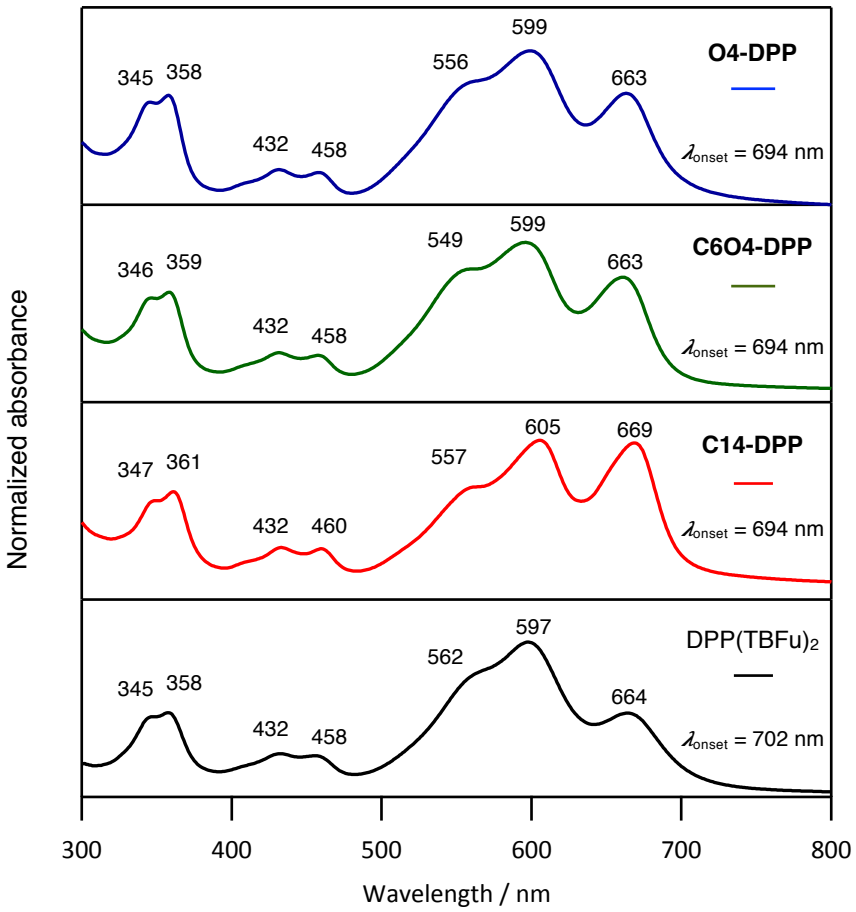

Figure 4-7. UV–Vis absorption spectra of **O4-DPP** (blue), **C14O4-DPP** (green), **C14-DPP** (red) and DPP(TBFu)$_2$ (black) as thin film on glass prepared by spin-coating with a 5.0 mg mL^{-1} of solution in the $CHCl_3$ at 800 rpm for 30 s.

The HOMO levels of the DPPs in the thin-film state were estimated by the photoelectron spectroscopy in air to be −5.29 eV for **O4-DPP**, −5.39 eV for **C14O4-DPP**, −5.50 eV for **C14-**

DPP and −5.37 eV for DPP(TBFu)$_2$ as shown in Figure 4-8. The optical energy gaps ($E_{g,\,opt}$) were calculated from the absorption onsets of the thin-films to be 1.76–1.79 eV, and the LUMO levels were calculated as "HOMO + $E_{g,\,opt}$" to be −3.50–−3.71 eV. The HOMO and LUMO levels in the thin films and in solution are summarized in Table 4-1. The energy levels of the DPPs in the thin-film state are higher with increasing the number of equipped OEG chains. This tendency of HOMO energy level changes is similar to the polymers with OEG side chains which have exhibited higher-lying HOMO levels than hydrophobic polymer.[18–19] In these polymer systems, the reason for the change in energy levels remains unknown. These electrochemical data indicate that the OEG side chains induce the shift of frontier orbital energy levels higher in the thin-film state than alkyl chains although the side chains do not affect energy levels in the solution.

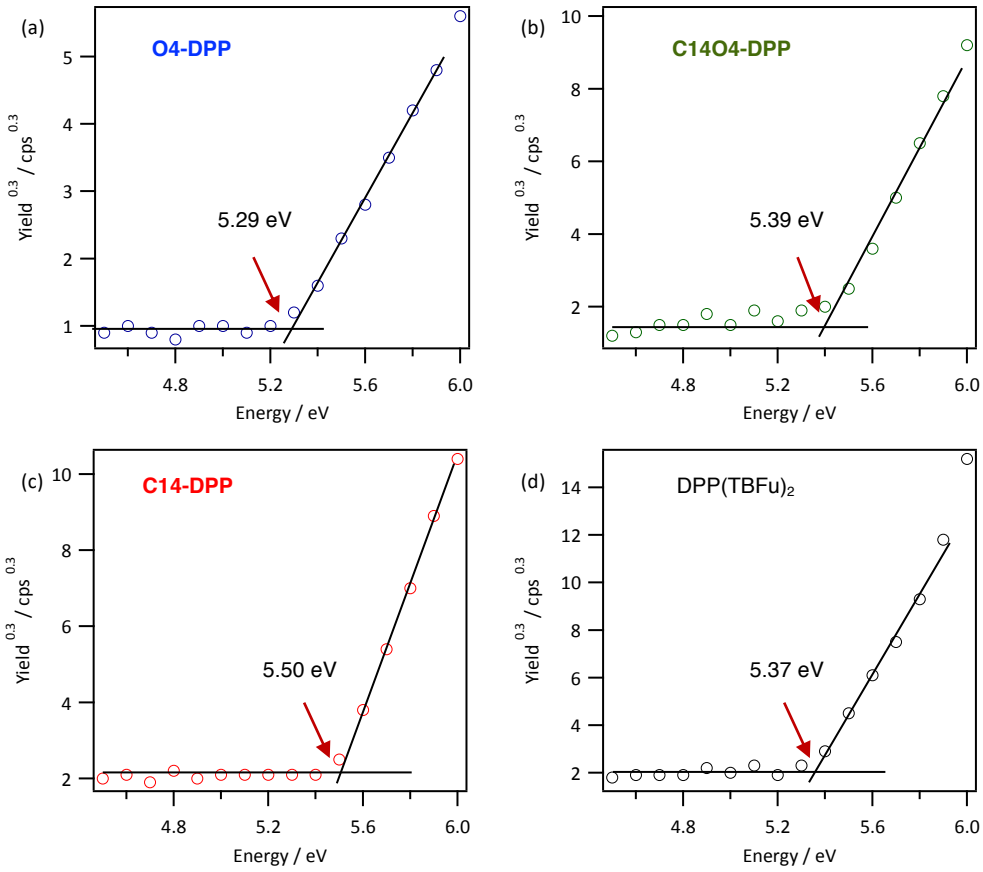

Figure 4-8. Photoelectron spectra of neat films spin-coated on ITO-glass: (a) **O4-DPP**, (b) **C14O4-DPP**, (c) **C14-DPP** and (d) DPP(TBFu)$_2$.

Table 4-1. Electrochemical properties of DPP compounds.

Compound	E_g[a] / eV	$HOMO_{film}$[b] / eV	$LUMO_{film}$[c] / eV	$HOMO_{CV}$[d] / eV	$LUMO_{CV}$[e] / eV
O4-DPP	1.79	−5.29	−3.50	−5.17	−3.29
C14O4-DPP	1.79	−5.39	−3.60	−5.18	−3.28
C14-DPP	1.79	−5.50	−3.71	−5.19	−3.27
DPP(TBFu)$_2$	1.76	−5.37	−3.61	−5.20	−3.28

[a]Calculated from λ_{onset}. [b]Determined by photoelectron spectroscopy in air, [c]$LUMO_{film} = HOMO_{film} + E_g$.[d]$HOMO_{CV} = -(E_{ox}^{1/2} + 4.80)$, [e]$LUMO_{CV} = -(E_{red}^{1/2} + 4.80)$.[32]

4-4. Surface Energies

The surface energy (γ) of the molecule which affect the miscibility of two materials in the blend film is changed by substitution of hydrophilic and hydrophobic groups. The surface energies were estimated by contact angles of *n*-octane and ethylene glycol droplets on the thin-film surface using Wu method as listed in Table 4-2.[33] The surface energies of **O4-DPP** and **C14O4-DPP** with OEG chains are 49.7 and 26.7 mN cm^{-2}, respectively, which are higher than those of **C14-DPP** (24.1 mN cm^{-2}) and DPP(TBFu)$_2$ (25.7 mN cm^{-2}) with two alkyl chains. A typical n-type material, $PC_{61}BM$, has the surface energy of 31.7 mN cm^{-2}.[34] The surface energies of **C14O4-DPP** and **C14-DPP** are close to that of $PC_{61}BM$. It suggests that these DPPs could have good miscibility with $PC_{61}BM$.

Table 4-2. The contact angles and the surface energies of DPPs.

Compound	Contact angle / °		γ / mN cm^{-2}
	n-octane	Ethylene glycol	
O4-DPP	3.9	12.8	49.7
C14O4-DPP	4.82	70.9	36.7
C14-DPP	3.3	76.8	24.1
DPP(TBFu)$_2$	4.2	76.2	25.7
PC$_{61}$BM	–	–	31.7[34]

Neat films were prepared by spin-coating of a solution in $CHCl_3$ (5 mg mL^{-1}) at 1000 rpm for 30 s on glass.

4-5. Single-Crystal and Thin-Film X-ray Diffraction Analysis

The single-crystal structures of DPPs were examined to investigate the effects of the side chain on the molecular packing. The single-crystals of **C14O4-DPP** and **C14-DPP** were obtained by slow diffusion of *n*-octane into a 1,2-dichloroethane solution. The single-crystal of **O4-DPP** was obtained by the same method using cyclohexane and 1,2-dichloromethane. The single-crystal structure of DPP(TBFu)$_2$ has been reported.[23]

The crystallographic data are summarized in Figure 4-9 and Table 4-3. All the DPPs are very similar in molecular conformation (Figure 4-9a, c, e and g). The π–π overlappings of **O4-DPP**, **C14O4-DPP** and **C14-DPP** are localized thiophene and benzofuran groups (Figure 4-9b, d and f), whereas DPP(TBFu)$_2$ overlaps on the entire molecule and slightly slips (Figure 4-9h). All DPP derivatives exhibit similar π–π stacking distance of 3.4 Å, indicating that the OEG side chains cannot affect the π–π stacking distance of conjugated backbone in the DPP-based small molecule crystal structure in contrast to the polymer system.[16]

The molecular packing in single-crystal can be different from thin film state. It is evaluated by comparing the experimental thin film X-ray diffraction (XRD) pattern with a simulated powder pattern based on the single-crystal diffraction data. Figure 4-10 shows the experimental

and simulated XRD patterns of DPPs. **O4-DPP** shows a diffraction peak at smaller 2θ by 0.7° from simulated one, in other words, a longer *d*-spacing by 1.8 Å than simulated values. This means that the O4-DPP molecular packing in the film is different from that in single-crystal structure. On the other hand, the experimental patterns of **C14O4-DPP** and **C14-DPP** and DPP(TBFu)$_2$ agree with the simulation, therefore their packing in the film is assumed to be similar to the single-crystal packing.

DPP(TBFu)$_2$ forms a larger intermolecular overlapping compared with **C14-DPP** in the thin film state as shown in Figure 4-11. To investigate this effect on the energy levels, single point energies of one to six molecules from the single crystal structures of **C14-DPP** and DPP(TBFu)$_2$ were calculated by density functional theory (DFT) at the B3LYP/6-31G(d) level as summarized in Table 4-4. HOMO levels of one molecule are similar: –4.86 eV for C14-DPP and –4.85 eV for DPP(TBFu)$_2$. The HOMO levels of DPP(TBFu)$_2$ are higher with increasing the number of surrounding molecules, whereas **C14-DPP** shows similar HOMO levels even in multiple molecules. These results suggest that the short chains induce large overlapped molecular packing and correspond to high energy levels.

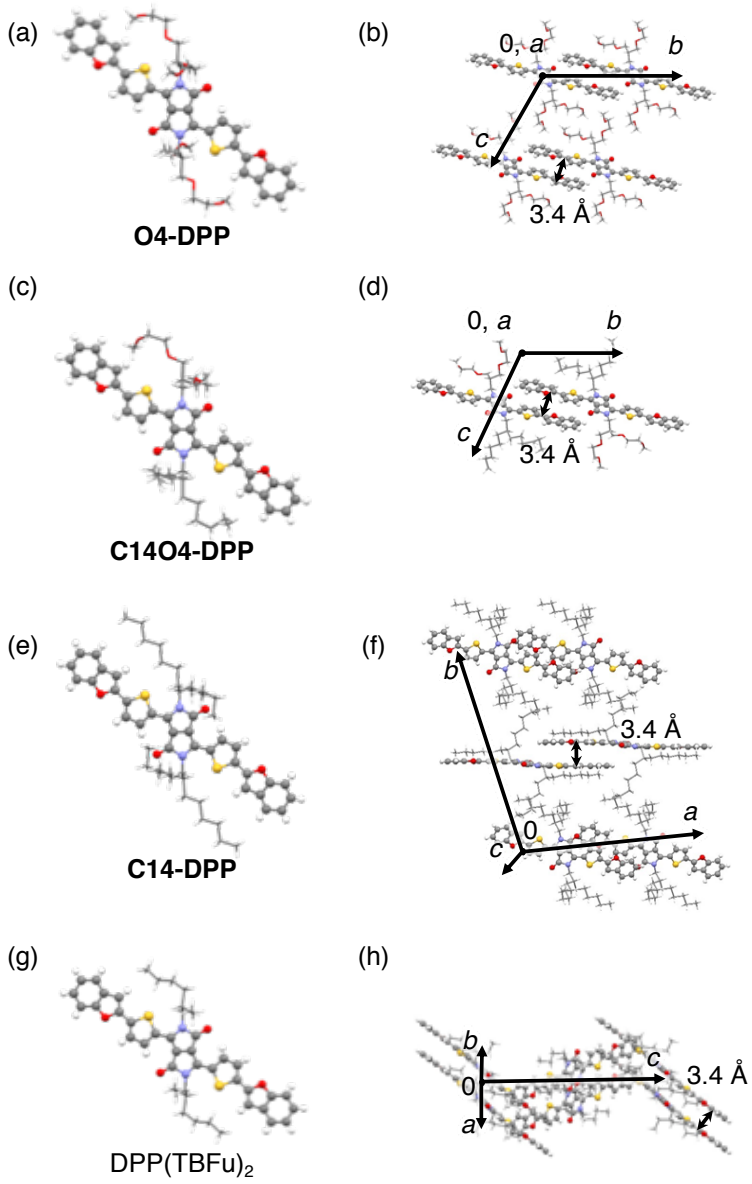

Figure 4-9. Comparison of DPP derivatives obtained as single-crystals: (a, c, e, g) molecular structures and (b, d, f, h) packing structures of unit cell of **O4-DPP**, **C14O4-DPP**, **C14-DPP** and DPP(TBFu)$_2$, respectively.

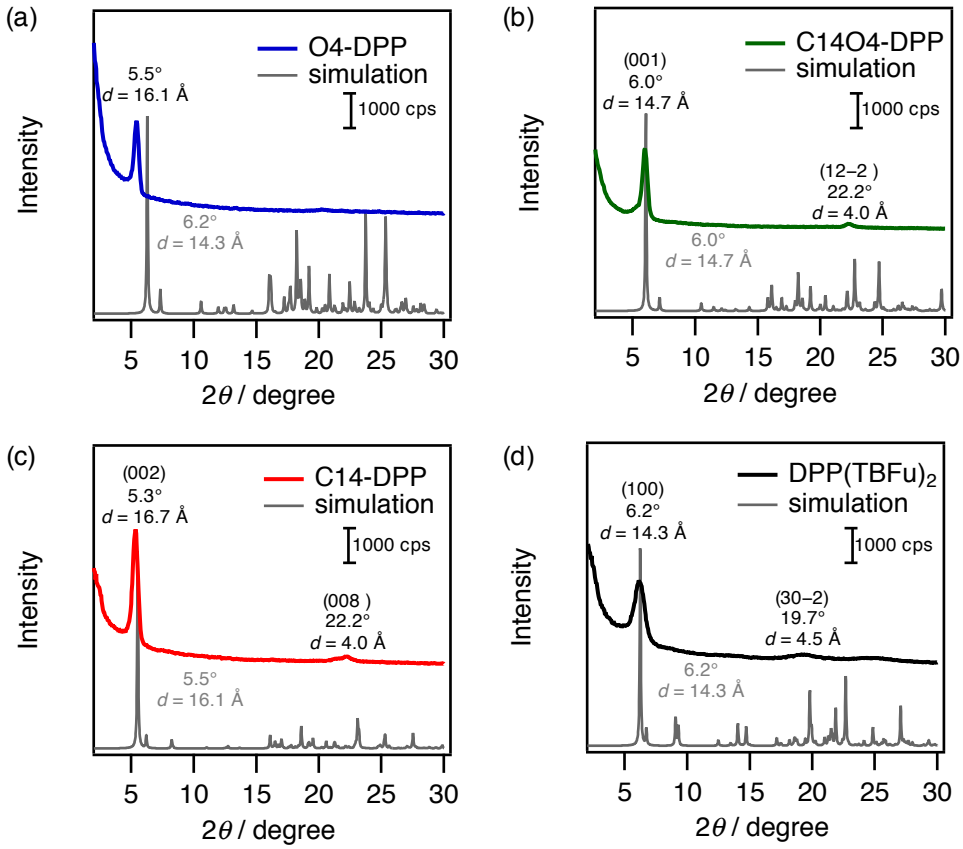

Figure 4-10. Experimentally measured XRD patterns of the thin film (top) and simulation calculated from single-crystal X-ray diffraction data (bottom) of (a) **O4-DPP**, (b) **C14O4-DPP**, (c) **C14-DPP** and (d) DPP(TBFu)$_2$.

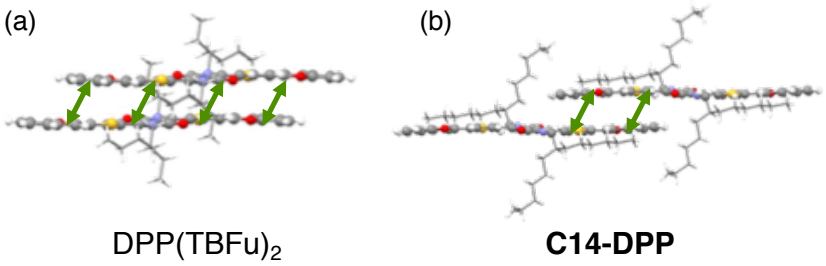

Figure 4-11. Intermolecular overlapping of (a) DPP(TBFu)$_2$ and (b) **C14-DPP**.

Table 4-3. Crystal data and structure refinement for porphycene dimers.

	O4-DPP	**C14O4-DPP**	**C14-DPP**
Empirical formula	$C_{50}H_{56}N_2O_{12}S_2$	$C_{54}H_{64}N_2O_8S_2$	$C_{58}H_{72}N_2O_4S_2$
Formula weight	941.12	933.19	925.34
Temperature	103 K	103 K	103 K
Wavelength	0.71075 Å	0.71075 Å	0.71075 Å
Crystal sysmtem	triclinic	triclinic	monoclinic
Space group	$P\bar{1}$	$P\bar{1}$	$C12/c1$
Unit cell dimensions	a = 5.6571(11) Å, b = 14.471(3) Å, c = 15.161(3) Å, α = 109.362(8)°, β = 96.907(7)°, γ = 97.334(7)°	a = 5.6812(5) Å, b = 14.5801(13) Å, c = 15.8017(15) Å, α = 109.832(8)°, β = 96.361(7)°, γ = 99.939(7)°	a = 28.5315(17) Å, b = 5.6071(3) Å, c = 32.1128(19) Å, β = 90/869(6)°,
Volume	1143.7(4) Å^3	1192.4(2) Å^3	5136.7(5) Å^3
Z	1	1	4
Density (calculated)	1.366 g cm^{-3}	1.300 g cm^{-3}	1.196 g cm^{-3}
Absorption coefficient	0.184 mm^{-1}	0.170 mm^{-1}	0.151 mm^{-1}
F(000)	498	498	1992
Crystal size	0.300 × 0.080 × 0.010 mm^3	0.300 × 0.150 × 0.010 mm^3	0.300 × 0.020 × 0.010 mm^3
Theta range for data collection	3.033 to 25.350°	3.049 to 25.349°	3.108 to 24.406°
Index ranges	$-6 \le h \le 6$, $-17 \le k \le 17$, $-18 \le l \le 18$	$-6 \le h \le 6$, $-17 \le k \le 17$, $-19 \le l \le 19$	$-32 \le h \le 32$, $-6 \le k \le 6$, $-36 \le l \le 36$
Reflections collected	15122	16175	30568
Independent reflections	4177 (R_{int} = 0.1148)	4343 (R_{int} = 0.0785)	4232 (R_{int} = 0.1793)
Max. and min trasmission	0.998 and 0.256	0.998 and 0.499	0.998 and 0.679
Refinement method	Full-matrix least-squares on F^2		
Data / restaraints / parameters	4177 / 2 / 300	4343 / 94 / 381	4232 / 0 / 300
Goodness-of-fit on F^2	1.082	1.048	1.105
Final R indices [I > 2σ(I)]	R_1 = 0.0806, wR_2 = 0.2024	R_1 = 0.0973, wR_2 = 0.2680	R_1 = 0.0931, wR_2 = 0.2265
R indices (all data)	R_1 = 0.1172 wR_2 = 0.2294	R_1 = 0.1462, wR_2 = 0.3069	R_1 = 0.1427, wR_2 = 0.2524
Largest difference peak and hole	0.653 and −0.391 e Å^{-3}	0.492 and −0.411 e Å^{-3}	0.83 and −0.29 e Å^{-3}

Table 4-4. Calculated and experimentally HOMO levels of **C14-DPP** and DPP(TBFu)$_2$.

	$HOMO_{calc}$[a] / eV				$HOMO_{film}$[b] / eV
	1 molecule	2 molecules	4 molecules	6 molecules	
C14-DPP	–4.86	–4.87	–4.82	–4.82	–5.50
DPP(TBFu)$_2$	–4.85	–4.75	–4.70	–4.64	–5.37

[a]Single-point energies from single crystal structure were calculated by B3LYP/6-31G(d). [b]Determined by photoelectron spectroscopy in air

4-6. Evaluation of Organic Solar Cells

The bulk-heterojunction (BHJ) OSCs comprising each of DPP derivatives as p-type material and $PC_{61}BM$ as n-type material have been fabricated and evaluated. The BHJ films were incorporated into OSCs with a general device architecture of [ITO/poly(3,4-ethylenedioxythiophene) doped with poly(styrene sulfonate) (PEDOT:PSS) (30 nm)/p-type:$PC_{61}BM$/LiF (1 nm)/Al (70 nm)]. The current density–voltage (*J*–*V*) curves under illumination AM1.5G with a light intensity of 100 mW cm^{-2} are shown in Figure 4-12a and the OSC parameters are summarized in Table 4-5. Among the DPPs, **C14-DPP** exhibits the best device performance with the short-circuit current density (J_{SC}) of 9.1 mA cm^{-2}, open-circuit voltage (V_{OC}) of 0.95 V, fill factor (FF) of 0.55 and a corresponding PCE of 4.7%. This PCE is comparable to reported DPP$(TBFu)_2$:$PC_{61}BM$ device.[29]

On the other hand, unlike the hydrophilic polymers, **O4-DPP** and **C14O4-DPP** with OEG chains show lower performances (J_{SC} = 3.7 and 6.4 mA cm^{-2}, V_{OC} = 0.71 and 0.83 V, FF = 0.40 and 0.49 and PCE = 1.0 and 2.6%, respectively) compared to hydrophobic **C14-DPP** and DPP$(TBFu)_2$. The HOMO levels of p-type materials correlate with the observed trend in V_{OC},[35] thus, an increase in HOMO due to the introduction of the OEG chains causes a decrease in the V_{OC} of the OSCs. **C14-DPP** device shows a higher V_{OC} of 0.95 V compared to DPP$(TBFu)_2$ device which exhibits V_{OC} of 0.89 V, consistent with the low-lying HOMO level. The equipped OEG chains give higher HOMO levels of DPPs corresponding to lower V_{OC}s of these OSCs compared to alkyl chains. The tendency of OSC performances on DPP derivatives is unlike the behavior of hydrophilic polymers because OEG chains changed active layer morphologies and HOMO levels. The external quantum efficiency (EQE) spectra of the OSCs are shown in Figure 4-12b. The all devices exhibit consistent with the magnitude of each spectrum correlate with the observed J_{SC}s. **C14-DPP** shows a distinctive spectrum which is similar to its film absorption spectrum and has a higher intensity band at 660 nm compared with other devices.

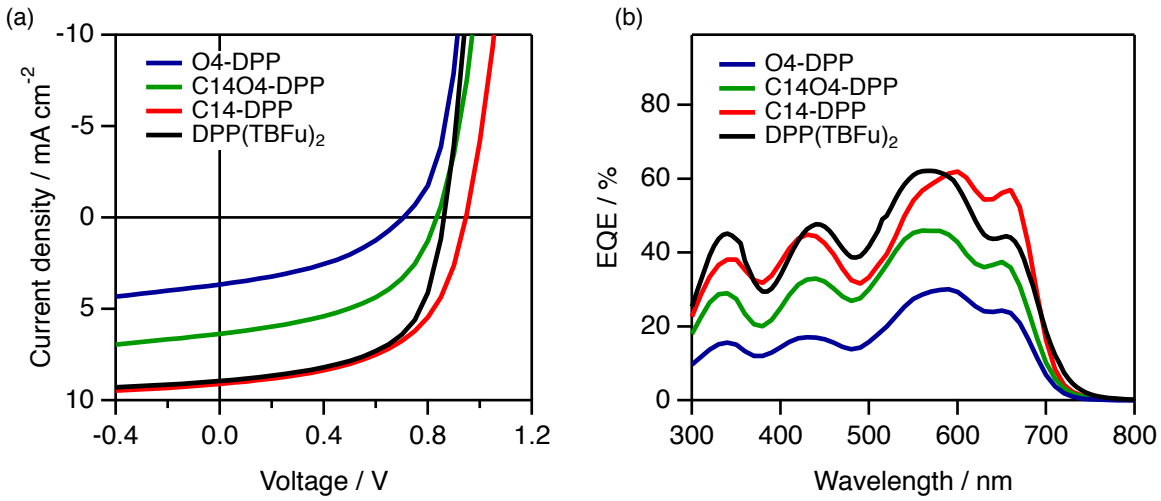

Figure 4-12. (a) *J–V* curves and (b) EQE spectra of the best-performing BHJ OSCs based on p-type:$PC_{61}BM$ blend.

Table 4-5. Summary of OSC devices characteristics of DPP derivatives.

Compound	J_{SC} / mA cm^{-2}	V_{OC} / V	FF	PCE [a] / %	μ^a / 10^{-4} cm^2 V^{-1} s^{-1}		
					μ_h^{neat}	μ_h^{blend}	μ_e^{blend}
O4-DPP	3.7	0.71	0.40	1.0 (0.99 ± 0.07)	3.0 (2.4 ± 0.5)	1.8 (1.5 ± 0.4)	4.0 (3.3 ± 0.5)
C14O4-DPP	6.4	0.83	0.49	2.6 (2.4 ± 0.10)	1.5 (1.3 ± 0.1)	1.6 (1.1 ± 0.4)	3.5 (3.0 ± 0.5)
C14-DPP	9.1	0.95	0.55	4.7 (4.6 ± 0.11)	2.6 (2.5 ± 0.1)	1.2 (1.1 ± 0.1)	4.2 (4.2 ± 0.1)
DPP(TBFu)$_2$	8.9	0.89	0.58	4.5 (4.19 ± 0.26)	3.1 (2.6 ± 0.5)	3.0 (2.4 ± 0.6)	5.0 (3.3 ± 1.2)

[a]The average values of 5 devices are shown in parentheses. [b]The average of 4 devices. [c]Measured by SCLC method with hole-only device [ITO/MoO_3 (15 nm)/active layer/MoO_3 (15 nm)/Al (70 nm)]. [d]Measured by SCLC method with electron-only device [ITO/ZnO (20 nm)/active layer/LiF (1 nm)/Al (70 nm)].

4-7. Space-Charge-Limited Current Carrier Mobilities

Hole mobility (μ_h) and electron mobility (μ_e) of each neat and blend films were measured using the space-charge-limited current (SCLC) method. Current density–voltage (*J–V*) characteristics are shown Figure 4-13, 4-14 and 4-15, and SCLC mobilities are also summarized in Table 4-5. Hole only devices with a general structure of [ITO/MoO_3/active

layer/MoO_3/Al] and electron-only devices with a general structure of [ITO/ZnO/active layer/LiF/Al] were fabricated and characterized. DPP neat films exhibit similar the hole mobilities of **O4-DPP** (3.0×10^{-4} cm^2 V^{-1} s^{-1}), **C14O4-DPP** (1.5×10^{-4} cm^2 V^{-1} s^{-1}), **C14-DPP** (2.6×10^{-4} cm^2 V^{-1} s^{-1}) and DPP(TBFu)$_2$ (3.1×10^{-4} cm^2 V^{-1} s^{-1}), indicating that the OEG side chains do not affect the hole transport properties. The both of hole and electron mobilities of BHJ films of DPPs give magnitude in the order of 10^{-4}, which is comparable to DPP(TBFu)$_2$:$PC_{61}BM$ system ($\mu_h = 3.0 \times 10^{-4}$ cm^2 V^{-1} s^{-1} and $\mu_e = 5.0 \times 10^{-4}$ cm^2 V^{-1} s^{-1}). These results indicate that BHJ films with p-type:$PC_{61}BM$ have the charge carrier transport pathway and J_{SC}s difference is not depend on charge carrier properties.

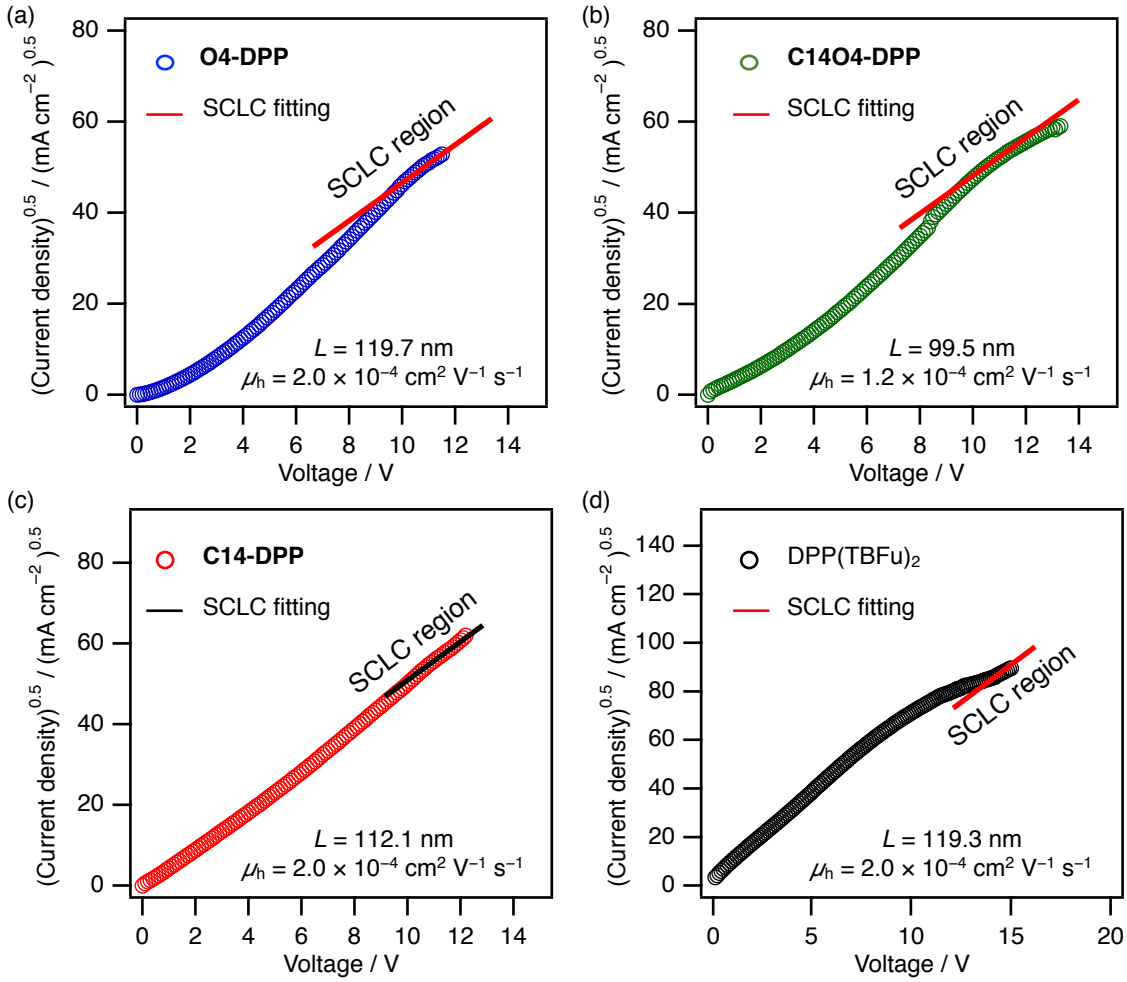

Figure 4-13. *J–V* curves and fitting lines to the Mott-Gurney Law for the electron-only devices of neat film: (a) **O4-DPP,** (b) **C14O4-DPP,** (c) **C14-DPP** and (d) DPP(TBFu)$_2$. Active layer was prepared by spin-coating with a solution in the $CHCl_3$ (10.0 mg mL^{-1}) at 800 rpm for 30 s.

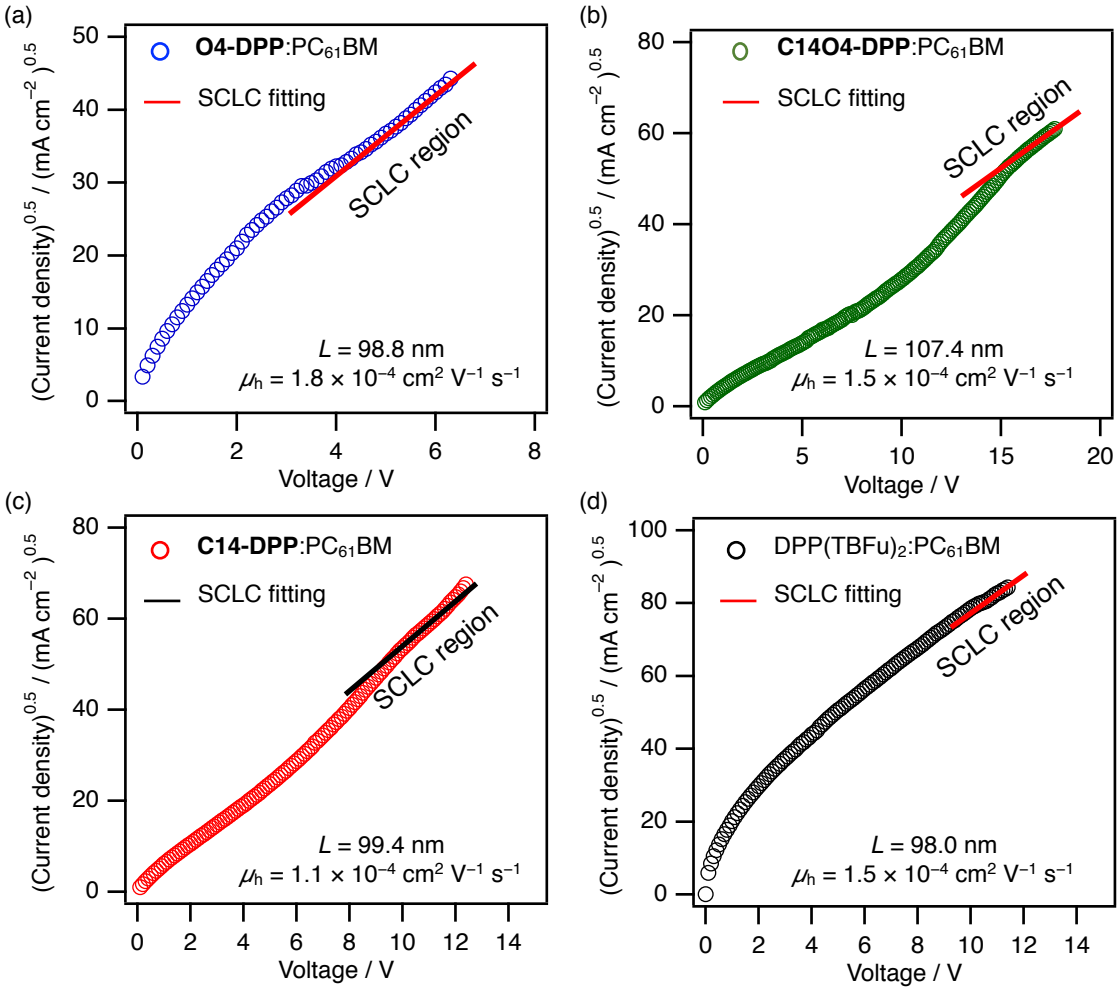

Figure 4-14. *J–V* curves and fitting lines to the Mott-Gurney Law for the hole-only devices of p-type:$PC_{61}BM$ blend film: (a) **O4-DPP**, (b) **C14O4-DPP**, (c) **C14-DPP** and (d) $DPP(TBFu)_2$. Active layer was prepared by spin-coating with a p:n (1:1 wt/wt) solution in the $CHCl_3$ (10.0 mg mL^{-1}) at 800 rpm for 30 s.

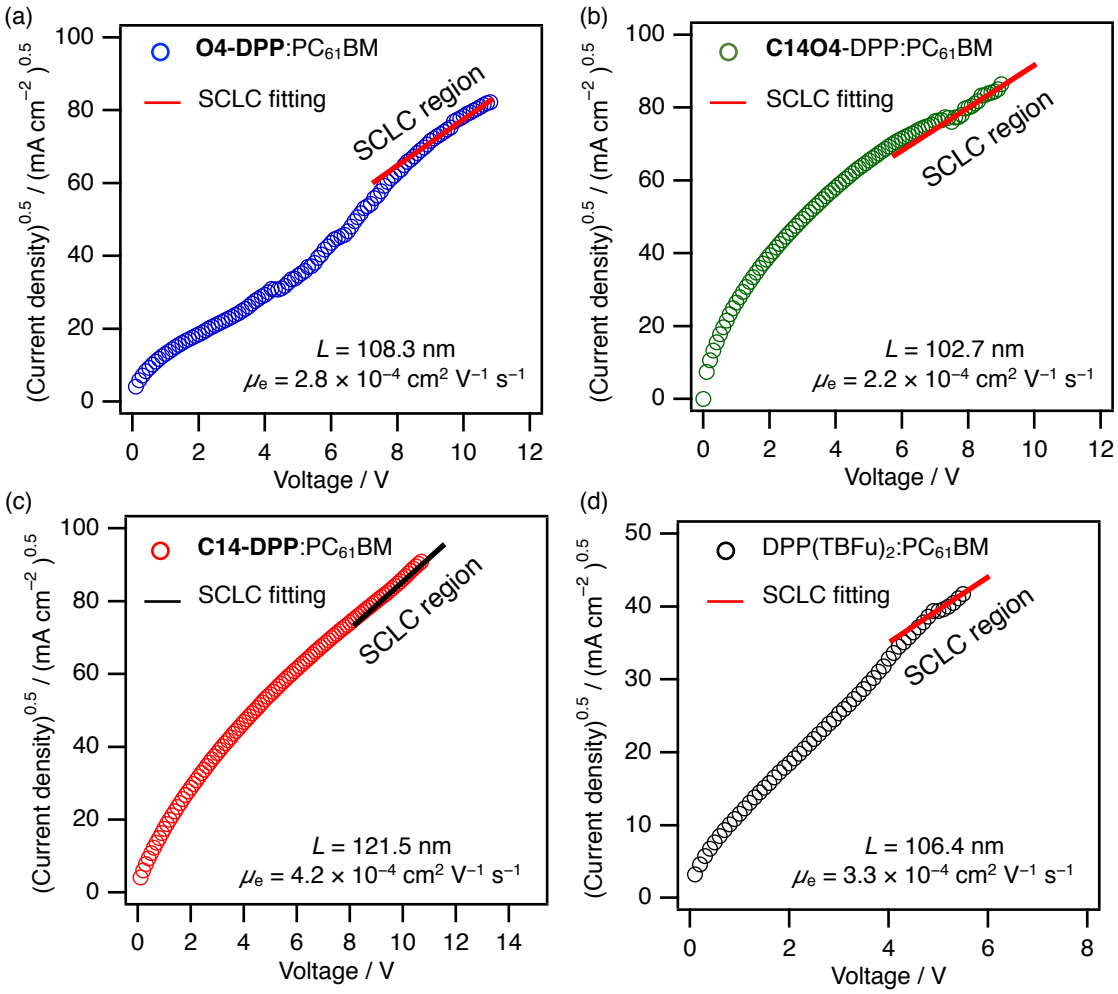

Figure 4-15. *J–V* curves and fitting lines to the Mott-Gurney Law for the electron-only devices p-type:$PC_{61}BM$ blend film: (a) **O4-DPP**, (b) **C14O4-DPP**, (c) **C14-DPP** and (d) $DPP(TBFu)_2$. Active layer was prepared by spin-coating with a p:n (1:1 wt/wt) solution in the $CHCl_3$ (10.0 mg mL^{-1}) at 800 rpm for 30 s.

4-8. Film Morphology

To understand the difference of photovoltaic performances, the film morphology of the blend films were investigated by atomic force microscope (AFM) (Figure 4-16) and out-of-plane XRD (Figure 4-17). **O4-DPP**:$PC_{61}BM$ blend film forms a large aggregation indicating a larger phase separation owing to the higher surface energy contrast between **O4-DPP** (γ = 49.7 mN cm^{-2}) and $PC_{61}BM$ (γ = 31.7 mN cm^{-2}) which lead to poor exciton diffusion and dissociation at the interface between p- and n-type materials (Figure 4-16a). These domains have the size

in the range of 130–200 nm. In contrast, the **C14-DPP**:$PC_{61}BM$ blend film shows small size domains of approximately 20 nm and a very smooth surface indicating good compatibility of **C14-DPP** with $PC_{61}BM$ (Figure 4-16c). **C14O4-DPP**:$PC_{61}BM$ blend exhibits middle domain size in the range of 50–90 nm compared with **O4-DPP** and **C14-DPP** (Figure 4-16b). DPP$(TBFu)_2$:$PC_{61}BM$ blend film has small size domains similar to **C14-DPP** despite as rough surface as **C14O4-DPP** (Figure 4-16d).

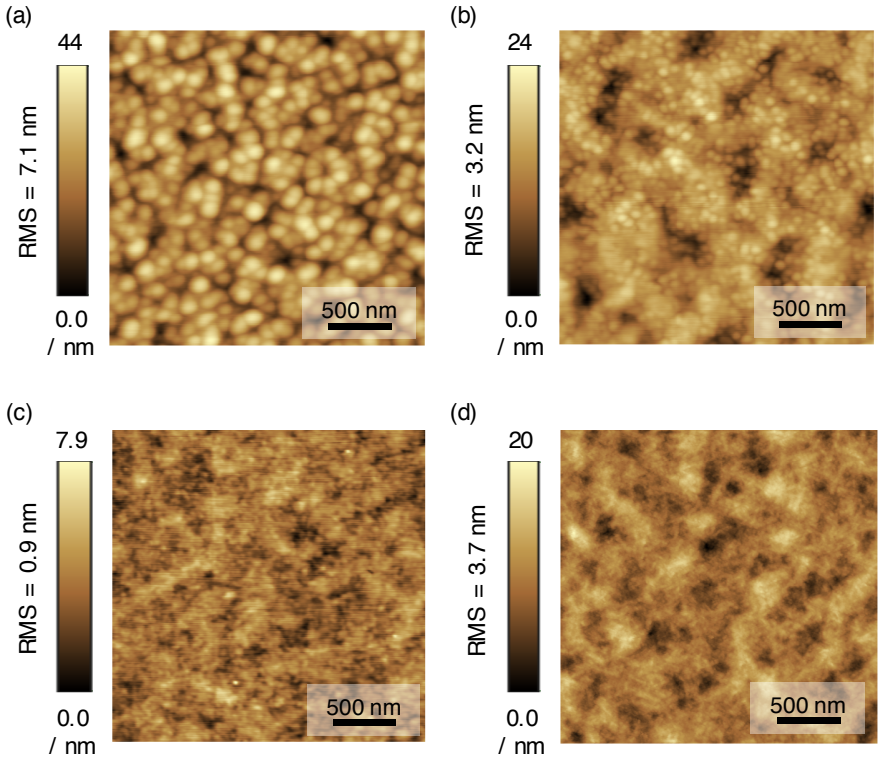

Figure 4-16. AFM height images of blend films on ITO/PEDOT:PSS: (a) **O4-DPP**:$PC_{61}BM$, (b) **C14O4-DPP**:$PC_{61}BM$, (c) **C14-DPP**:$PC_{61}BM$ and (d) DPP$(TBFu)_2$:$PC_{61}BM$. The scan size images is 2.5 μm × 2.5 μm for all.

The XRD patterns of BHJ films of **O4-DPP** and **C14O4-DPP** show diffraction peaks at 2θ = 5.5 and 5.4° (d = 16.1 and 16.4 Å), respectively, which correspond roughly to the length of the shorter molecular axis estimated from the optimized molecular structures as shown in Figure 4-18. **C14-DPP** and DPP(TBFu)$_2$ show the 002 and 100 planes diffractions, respectively. These results seem that the conjugates adopt edge-on-like orientations against the substrate (Figure 4-18e).

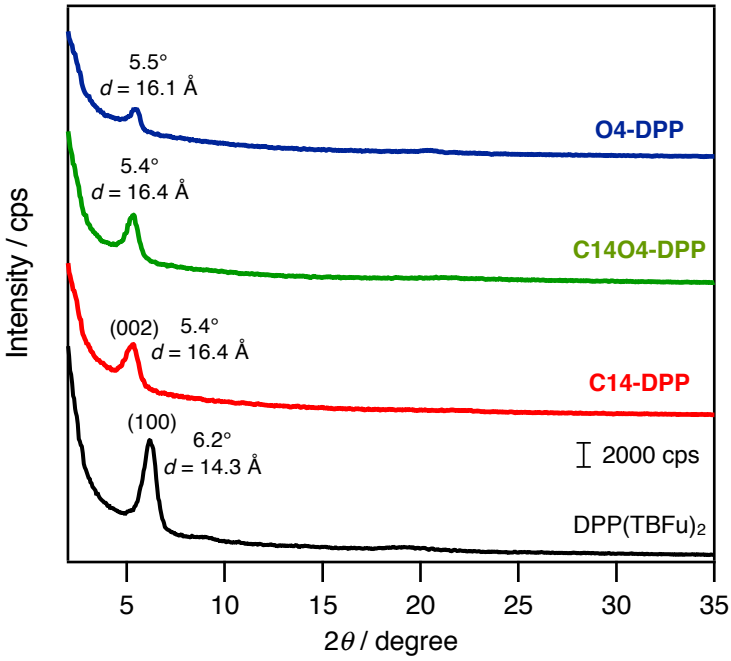

Figure 4-17. XRD patterns of blend films on ITO/PEDOT:PSS: **O4-DPP**:$PC_{61}BM$ (blue), **C14O4-DPP**:$PC_{61}BM$ (green), **C14-DPP**:$PC_{61}BM$ (red) and DPP(TBFu)$_2$:$PC_{61}BM$ (black).

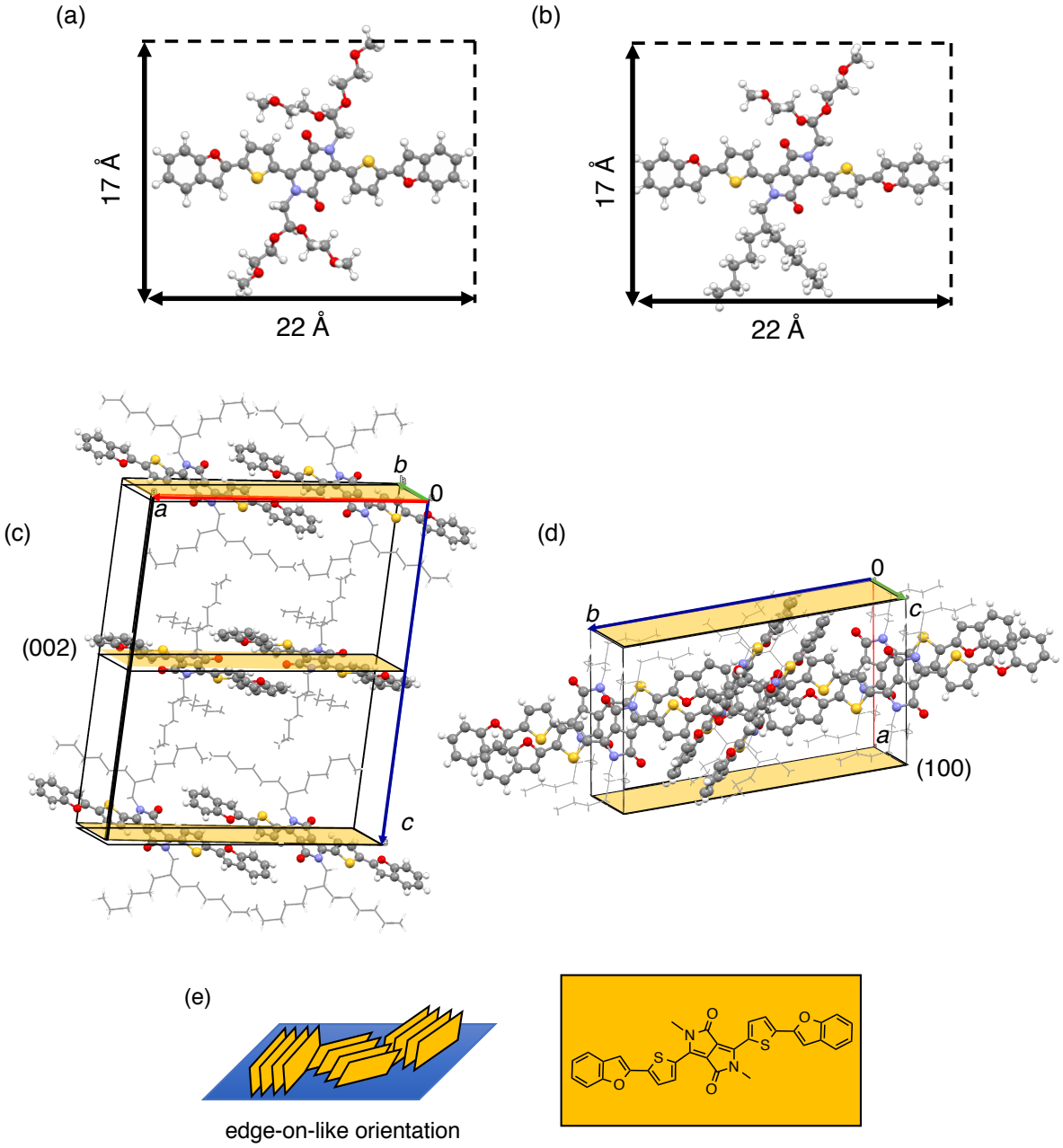

Figure 4-18. Optimized molecular structure of (a) **O4-DPP** and (b) **C14O4-DPP** at MM2 level and parts of single-crystal structures of (d) **C14-DPP** and (d) DPP(TBFu)$_2$ and (e) illastration of edge-on-like orientation.

4-9. Organic Field-Effect Transistor and Optoelectronic Performances

To investigate the effect of OEG chains on the OFET carrier mobility and optoelectronic performances, the p-channel OFET devices have been fabricated and evaluated comprising each of the DPP derivatives. Bottom-gate/top-contact OFETs were fabricated from drop-casted films prepared with a chlorobenzene solution on highly doped n-type silicon wafers as the gate electrode, 300 nm of SiO_2 as the gate dielectric and Au as the contact electrodes. The OFET characteristics of DPPs as shown in Figure 4-19 and the OFET performance data were extracted from the transfer curves and are summarized in Table 4-6. The OFET μ_hs of **O4-DPP**, **C14O4-DPP** and **C14-DPP** are similar to each other in the order of 10^{-4} cm^2 V^{-1} s^{-1}. On the other hand, DPP(TBFu)$_2$ shows a higher μ_h of 2.8×10^{-4} cm^2 V^{-1} s^{-1}, probably because the molecular packing of DPP(TBFu)$_2$ forms a larger intermolecular overlapping compared with other DPPs (Figure 4-11).

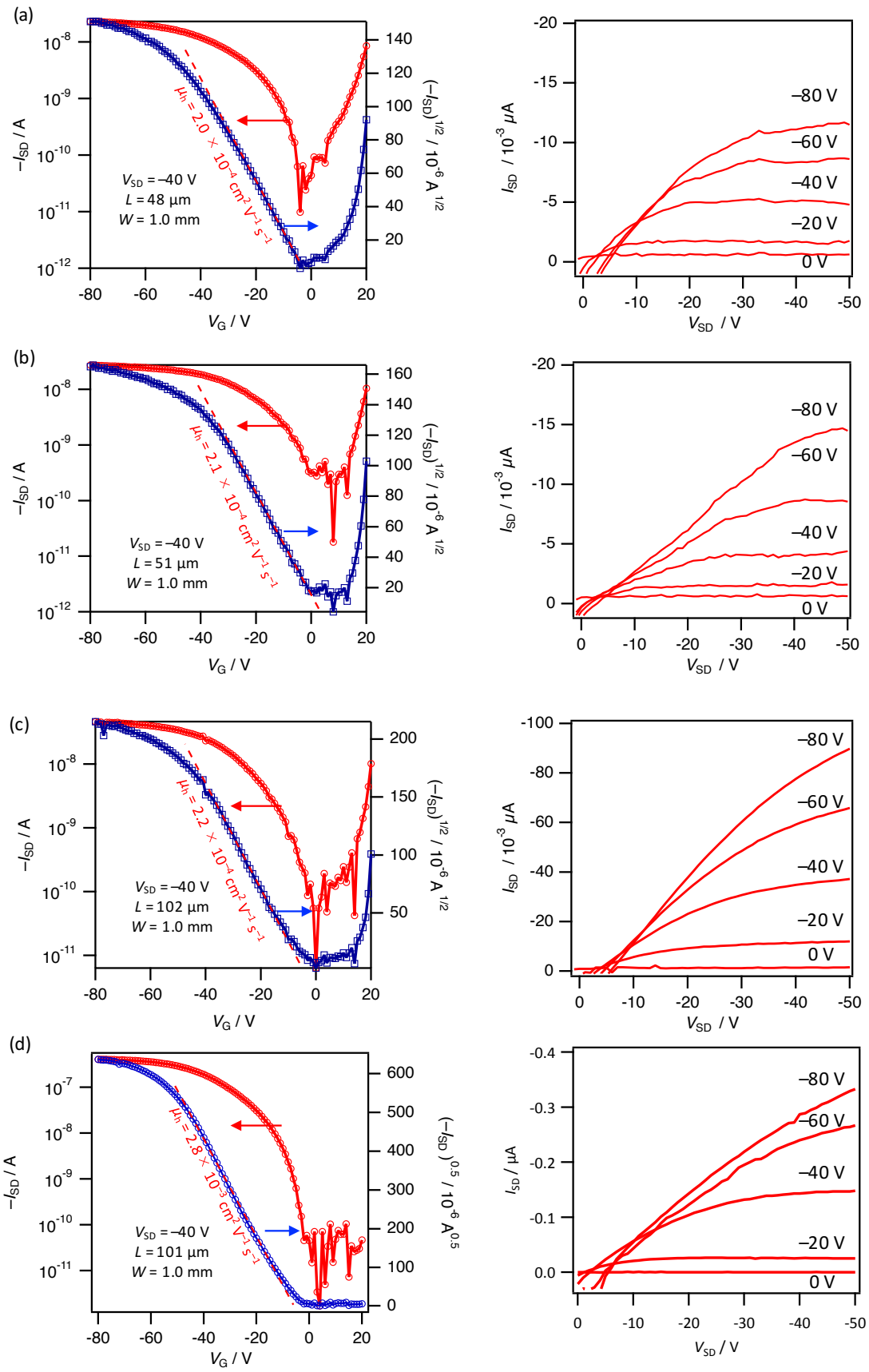

Figure 4-19. Transfer curve (left) and output curves (right) of FETs of DPPs: **O4-DPP** (a), **C14O4-DPP** (b), **C14-DPP** (c), and DPP(TBFu)$_2$ (d).

Table 4-6. FET characteristics of DPPs-based OFET.

Compound	$\mu_{h,\,FET}{}^{a}$ / 10^{-4} cm^2 V^{-1} s^{-1}	V_{th} / V	I_{on} /I_{off}
O4-DPP	2.0 (1.7)	−3.2	2.3×10^3
C14O4-DPP	2.1 (1.4)	3.7	1.5×10^3
C14-DPP	2.2 (1.8)	−3.2	7.2×10^3
$DPP(TBFu)_2$	28 (20)	−4.0	2.4×10^5

[a]The average values of 5 devices are shown in parentheses.

The OFETs based on organic molecular dyes with a light absorption have been studied for not only electronic circuit applications but also photodetector, called organic phototransistor (OPT). These organic sensors enable apply optoelectronic application such as the biomedical sensor, wearable device and imaging device. The OPT performances depend on the optoelectronic properties of the molecule in the active layer. However, the relationship between molecular structure and optoelectronic properties has many unknown aspects because of few reports. For instance, Cho et al. have demonstrated that a four-arm shape p-type material 4(HPBT) showed a high photo-to-dark-current ratio (I_{ph}/I_{dark}) of 4×10^4 with a low power irradiation (30 μW cm^{-2}) (Figure 4-20).[36] However previous work has not focused on the effect of OEG and alkyl side chains.

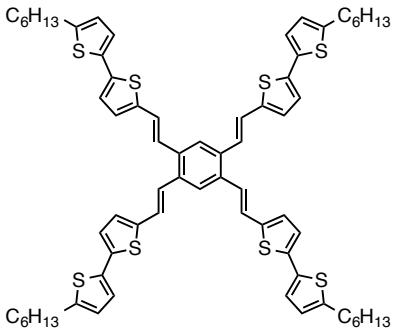

4(HPBT)

$I_{ph}/I_{dark} = 4 \times 10^4$
(30 μW cm^{-2}, 436 nm)

Figure 4-20. Chemical structure of four-arm shape p-type material 4(HPBT).

To perceive the relationship between phototransistor performances and irradiation wavelength, series of monochromatic lights (400, 600, 660 and 800 nm) with a light power of 2.5 mW cm^{-2} was incident onto the channel region of OFET devices. The irradiation wavelengths were chosen for the position of a weak absorption region as 400 nm, strong two peaks at 600 and 660 nm, and a region of no absorption as 800 nm on the absorption spectra of DPPs. Transfer characteristics of DPPs-based FETs measured in the dark and under irradiation are shown in Figure 4-21. **O4-DPP** and **C14O4-DPP** show increased source-drain current (I_{SD}) and positively shifted threshold voltage (V_{th}) under irradiation at 400, 600 and 660 nm compared with the curve measured in the dark. Outstanding I_{ph}/I_{dark} values at V_{th} of the dark condition of **O4-DPP** and **C14O4-DPP** up to ca. 100 and 150 are obtained with irradiation at 660 and 400 nm, respectively. The monochromatic light at 800 nm induces no photocurrent because DPP cannot absorb it. On the other hand, **C14-DPP** and DPP$(TBFu)_2$ exhibit poor optical responses with all series of monochromatic light. It seems that OEG and alkyl chains effect on the behavior of either the photoinduced excitons or charge carriers under applied source-drain voltage.

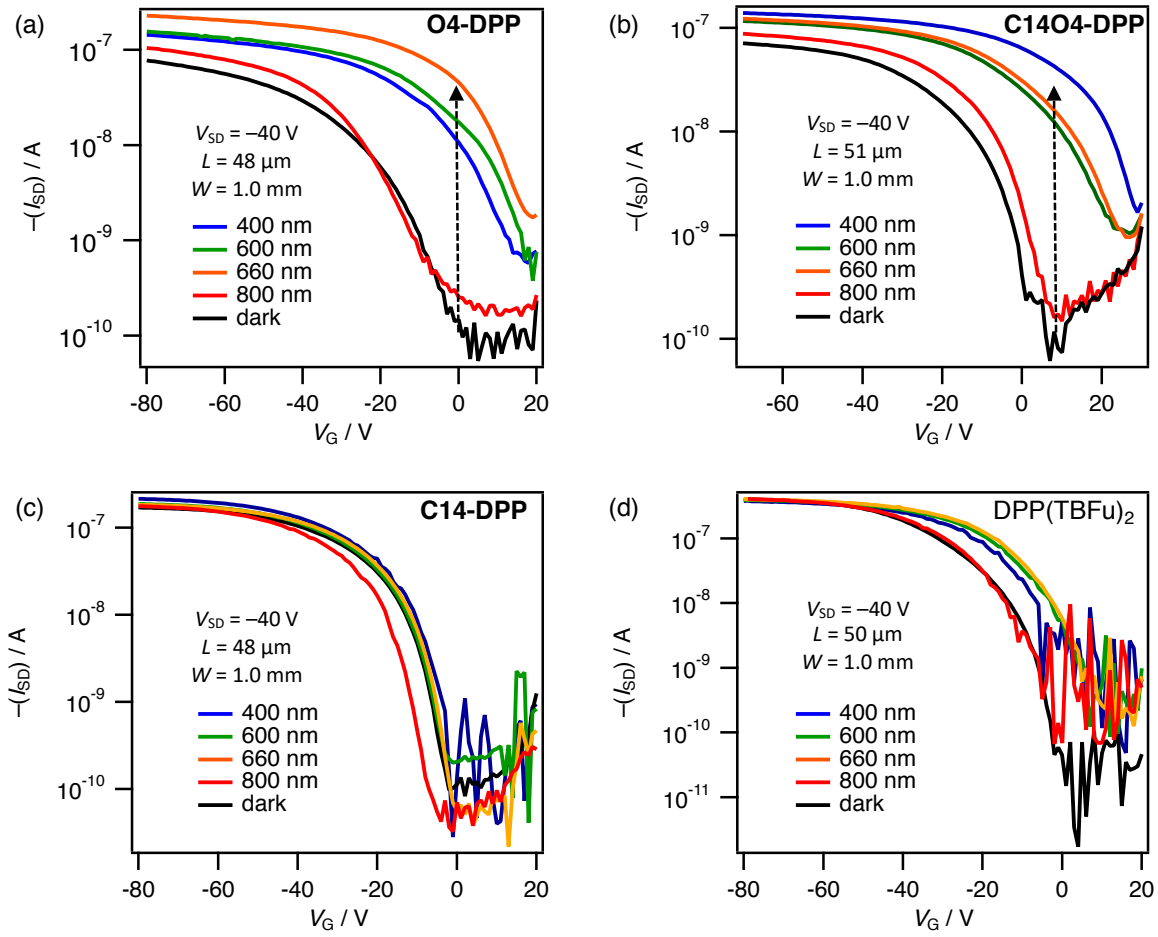

Figure 4-21. Transfer characteristics measured in the dark and under series of monochromic lights (400, 600, 660 and 800 nm) of FETs based on DPPs: **O4-DPP** (a), **C14O4-DPP** (b), **C14-DPP** (c), and DPP(TBFu)$_2$ (d). The light intensity was 2.5 mW cm^{-2}.

4-10. Summary and Outlook

In the case of a polymer system, it has been reported that replacing hydrophobic alkyl chains with hydrophilic OEG chains in the conjugate polymer such as PFDTOBT-O2 led a smaller π–π distance and higher-lying HOMO and lower-lying LUMO levels compared with hydrophobic alkyl chains (PFDTOBT). The former property induced a higher hole mobility and a higher J_{SC}, and the latter property led a red-shifted light absorption and a lower V_{OC} than those of PFDTOBT (Figure4-2a).[16]

In this work, the OEG chains in the DPP-based small molecules, **O4-DPP** and **C14O4-DPP**, lead a higher-lying HOMO and lower V_{OC} values compared with alkyl chains in **C14-DPP**, in agreement with a polymer system. On the other hand, **O4-DPP** and **C14-DPP** show a higher-lying LUMO level with keeping E_g and no large effects on π–π distance, optical properties, charge carrier mobilities. Moreover, these hydrophilic DPPs exhibit a larger phase separation in BHJ film and lower J_{SC} values than those of **C14-DPP** and DPP(TBFu)$_2$. These trends depend on the number of OEG chains which lead slightly different molecular packings and increasing surface energy. On the other hand, the bulky alkyl chains on **C14-DPP** induce small overlapped molecular packing and the corresponding a lower HOMO level of −5.50 eV than that of small side chains on DPP(TBFu)$_2$ ($HOMO_{film}$ = −5.37 eV). This difference also effects V_{OC} values of those OSC devices.

To improve OSC performance, it is necessary to realize both of a high V_{OC} and a high J_{SC}, however, there is a trade-off between these parameters. The energy difference between the HOMO of p-type material and the LUMO of n-type material correlates very well with the V_{OC}.[35] Tuning of frontier orbital energy levels with keeping the energy gap leads to improvement of photon energy loss at OSC. It is expected that the introduction of the OEG chains to n-type materials lead high-lying HOMO and LUMO levels and the corresponding high V_{OC} with keeping a E_g.

Armin et al. have reported that n-type materials based on cyclopentadithiophene–benzothiadiazole conjugates with OEG chains (DG) or alkyl chains (DA) as shown in Figure 4-22a.[37] DG showed lower-lying HOMO and LUMO levels and an unchanged E_g in the thin-film state, but those V_{OC} values in the OSC device were not measured. Further, Lu et al. have reported that perylene diimide (PDI) dimers with two or four ethylene glycol chains, Bis-PDI-T-EG and Bis-PDI-T-di-EG, respectively, as shown in Figure 4-22b.[38] Bis-PDI-T-di-EG-based OSC with poly(3-hexylthiophene) (P3HT) exhibited a higher V_{OC} of 0.67 V compared with

Bis-PDI-T-EG (V_{OC} = 0.59 V) with keeping E_g, but those frontier orbital energy levels in the thin-film state were not observed.

The tuning of V_{OC} by the side chains on a small molecule is of special interest, considering no changing π–conjugated structure. It would be also interesting to further fine-tune miscibility between p- and n-type materials in BHJ film by the hydrophilicity and hydrophobicity contrast. Therefore, the relationship between side chains, frontier orbital energy levels and V_{OC} values of OSC in this work will serve as molecular design guideline of n-type materials with a high V_{OC}.

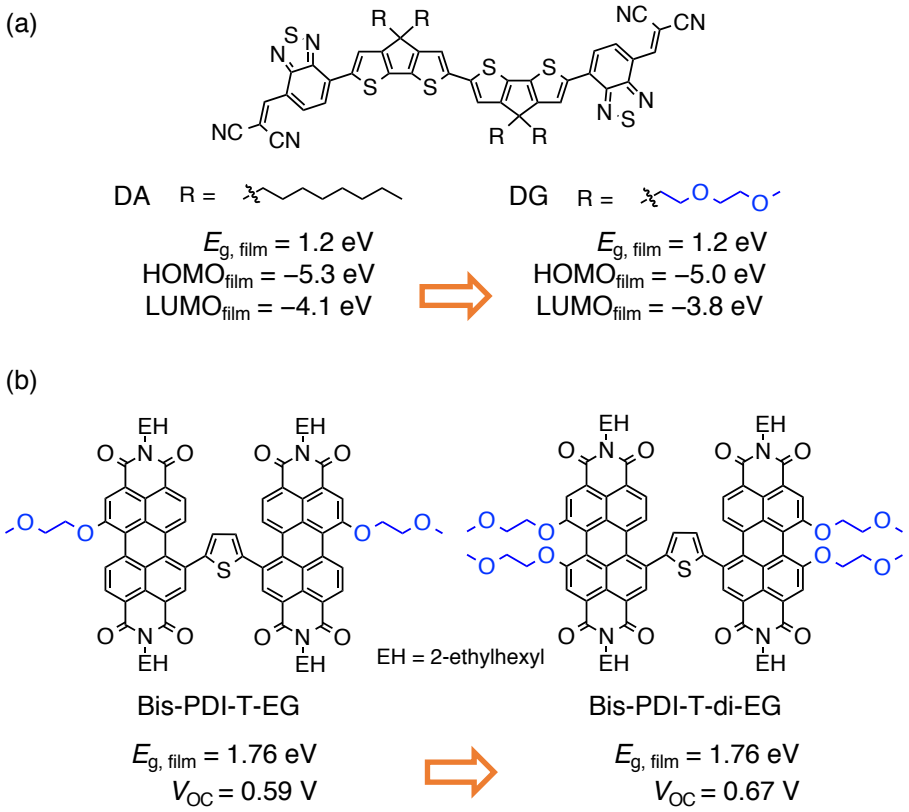

Figure 4-22. Chemical structures of n-type materials with or without OEG chains: (a) cyclopentadithiophene–benzothiadiazole conjugates and (b) PDI dimers.

The OEG chains improve a higher phototransistor performances (I_{ph}/I_{dark} = 100 for **O4-DPP** and I_{ph}/I_{dark} = 150 for **C14O4-DPP**) than that of alkyl chains (I_{ph}/I_{dark} = 0 for **C14-DPP**), though their OFETs show similar hole mobilities in the order of 10^{-4} cm^2 V^{-1} s^{-1}.

It has been reported a relationship between carrier mobilities and phototransistor properties. For instance, the phototransistors based on benzodithiophene dimer with vinylene linker (BBDTE) or acetylene linker (BBDTY) have been reported by Zhao et al. as shown in Figure 4-23.[39] BBDTE showed two order of magnitude higher I_{ph}/I_{dark} of 10^5 compared with BBDTY ($I_{ph}/I_{dark} = 4 \times 10^3$) due to the poorer charge transport properties (μ_h = 1.62 cm^2 V^{-1} s^{-1} for BBDTE and μ_h = 0.062 cm^2 V^{-1} s^{-1} for BBDTY). However, the relationship between the substituent and the photosensitivity in materials with the similar order of magnitude mobilities is unknown.

This is the first example in which the side chains switch the phototransistor response. It seems that OEG chain and alkyl chains effect on the behavior of either the photoinduced excitons or charge separation under applied source-drain voltage. The effect of the side chains on photosensitivity in this work will serve as a basis for the materials of the organic photodetector.

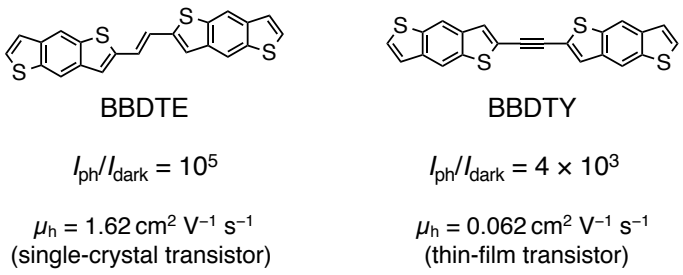

Figure 4-23. Chemical structures of benzodithiophene-dimers and their phototransistor performances.

4-11. Experimental Section

General method

All reactions were carried out under nitrogen unless otherwise noted. “Room temperature” means 15–25 °C. Gravity column chromatography was performed on silica gel purchased from Kanto Chemical (Silica Gel 60N, 60 Å, 63–210 μm). Analytical thin-layer chromatography (TLC) was conducted on Merck 200 μm thickness silica gel plates with a fluorescent indicator. Visualization was accomplished with UV light at 254 or 365 nm. GPC was performed on a JAI LC-9225NEXT recycle chromatography system equipped with JAIGEL 1H and 2H polystyrene gel columns (600 mm*h* × 40 mmϕ; bead size = 16 μm; pore size = 20–30 [1H] and 40–50 [2H] Å) using $CHCl_3$ as a mobile phase. ^{1}H NMR and ^{13}C{^{1}H} NMR spectra were recorded on a JEOL JNM-ECX400 (400 MHz) or JNM-ECX500 (500 MHz) spectrometer at 294 K, and chemical shifts were calibrated using $CHCl_3$, 1,1,2,2-tetrachloroethane or tetramethylsilane (TMS) as internal standards (^{1}H: 7.26 ppm for $CHCl_3$, 6.00 ppm for 1,1,2,2-tetrachloroethane and 0.00 ppm for TMS; ^{13}C{^{1}H}: 77.00ppm for $CHCl_3$ and 0.00 ppm or TMS). High-resolution matrix-assisted laser desorption/ionization (MALDI) mass spectra were measured on a JEOL Spiral TOF/JMS-S3000 mass spectrometer. UV–Vis absorption spectra were recorded on a JASCO UV–Vis–NIR V-670 spectrometer. Electrochemical measurements were measured on an ALS 612D electrochemical analyzer at room temperature in an argon-filled cell. A glassy carbon electrode and a Pt wire were used as a working and a counter electrode, respectively. An $Ag/AgNO_3$ electrode was used as a reference electrode, which was calibrated with the half-wave potential of Fc/Fc^+ redox couple. Ionization energies of thin films were determined from the onset of photoelectron spectra measured on a Riken Keiki AC-3 photoelectron spectrometer. The surface morphology of organic films was observed using a Shimazu SPM-9700 atomic force microscope in tapping mode with an SII SI-DF20 silicon probe at a resonant frequency of 137 kHz and a force constant of 16 N m^{-1}.

Contact angle measurement

Contact angles of organic thin-films on glass were observed using a Kyowa Interface Science CA-X150 contact angle analyzer and each result is an average of five measurements per samples. Surface energies were estimated by the contact angles of the two probe liquids, *n*-octane and ethylene glycol, with the Wu equation:

$$\gamma_{pl}(1 + \cos\theta) = 4(\gamma_{pl}^{d}\ \gamma_{s}^{d}) / (\ \gamma_{pl}^{d} + \gamma_{s}^{d}) + 4(\gamma_{pl}^{p}\ \gamma_{s}^{p}) / (\ \gamma_{pl}^{p} + \gamma_{s}^{p})$$

where γ_{pl} and γ_{s} are the surface energies of the probe liquid and the sample, respectively.[33] The superscripts d and p refer to the dispersion and polar components of the surface energy, respectively.

Single-crystal X-ray diffraction analysis

X-ray diffraction data of **O4-DPP**, **C14O4-DPP** and **C14-DPP** were measured at 103 K on a Rigaku VariMax R-Axis RAPID imaging plate-based X-ray diffractometer system equipped with an RA-Micro7 X-ray source (Mo *K*α, λ = 0.71073 Å) operated at 1.2 kW. The diffraction data were processed with CrystalStructure of the Rigaku program, solved with the SIR-97 program[40–41]and refined with the SHELX-97 program.[42]

X-ray diffraction analysis of thin films

Out-of-plane XRD θ–2θ scans of thin films were measured on a Rigaku RINT-TTR III diffractometer equipped with a rotating anode (Cu *K*α, λ = 1.5418 Å) operated at 15 kW and a Rigaku D/teX Ultra 1D silicon strip detector. Measurements were performed at a scan rate of 3° min^{-1} with a scan range of 2–30°.

Materials

All solvents and chemicals were reagent grade obtained commercially, and used without further purification except otherwise noted. For spectral measurements, spectral grade CH_2Cl_2 and $CHCl_3$ were purchased from Nacalai Tesque. Prepared as described in literature were 3,6-dithiophen-2-yl-2,5-dihydropyrrolo[3,4-*c*]pyrrole-1,4-dione (**10**),[44] 3-(2-methoxyethoxy)-2-((2-methoxyethoxy)methyl)propyl 4-methylbenzenesulfonate, compounds **13a** and **14a**,[17] 7-(bromomethyl)tridecane,[45] and DPP(TBFu)$_2$.[21] [6,6]-Phenyl-C_{61}-butyric acid methyl ester ($PC_{61}BM$) was purchased from Luminescence Technology Crop. and used as received.

Fabrication and evaluation of space-charge-limited current electron-only devices

ITO-patterned glass substrates (20 × 20 mm^2, 15 Ω per square) were cleaned by gentle rubbing with an acetone-soaked wipe, then sequential sonication in detergent (Furuuchi Chemical, Semico Clean 53), distilled water (Wako Pure Chemical, reagent grade), and isopropyl alcohol (Kishida chemical, electronic grade) for 10 min each. After drying with nitrogen blow and UV/O_3 treatment with a Bioforce Nanoscience TC-003 cleaner at room temperature for 20 min. A ZnO layer was prepared on the ITO substrate by a sol–gel method using $Zn(OAc)_2{\cdot}2H_2O$ as a ZnO precursor[45]. The $Zn(OAc)_2{\cdot}2H_2O$ (500 mg), 2-methoxyethanol (5 mL), and ethanolamine (140 μL) were mixed and stirred vigorously for 12 h in air. The ZnO precursor solution was spin-coated at 5000 rpm for 30 s on the ITO substrate. The active layers were annealed 250 °C for 1 h in air. The substrates were transferred into a nitrogen-filled glove box (< 10 ppm O_2 and H_2O) for preparation of active layers. The films were prepared by spin-coating of a DPP solution or a p:n blend solution in $CHCl_3$ at 800 rpm for 30 s, followed by solvent vapor annealing with THF in the glovebox. Finally, LiF (1 nm, 0.01 Å s^{-1}) and Al (70 nm, 0.3 Å s^{-1}) were vapor-deposited at high vacuum (~10^{-4} Pa) through

a shadow mask that defined an active area of 2 × 0.5 mm^2. The general structure of electron-only devices was [ITO/ZnO/active layer/LiF (1 nm)/Al (70 nm)].

Current–voltage (*I–V*) characteristics of the space-charge-limited current (SCLC) devices were measured by using a Keithley 2400 Source Mater. The carrier mobilities were extracted by fitting the *I–V* curves in the linear region according to the modified Mott–Gurney equation.

Fabrication and evaluation of space-charge-limited current hole-only devices

ITO-patterned glass substrates (20 × 20 mm^2, 15 Ω per square) were cleaned by the same procedure as described for the electron-only devices. MoO_3 (15 nm, 0.1 Å s^{-1}) were vapor-deposited at high vacuum (~10^{-4} Pa) on the ITO substrate. The substrates were transferred into a nitrogen-filled glove box (< 10 ppm O_2 and H_2O) for preparation of active layers. The blend films were prepared by spin-coating of a p:n blend solution in $CHCl_3$ at 800 rpm for 30 s, followed by solvent vapor annealing with THF in the glovebox. Finally, MoO_3 (15 nm, 0.1 Å s^{-1}) and Al (70 nm, 0.3 Å s^{-1}) were vapor-deposited at high vacuum (~10^{-4} Pa) through a shadow mask that defined an active area of 2 × 0.5 mm^2. The general structure of hole-only devices was [ITO/MoO_3 (15 nm)/active layer/MoO_3 (15 nm)/Al (70 nm)].

I–V characteristics of the SCLC devices were measured by the same method of SCLC hole-only devices.

Fabrication and evaluation of organic solar cells

ITO-patterned glass substrates (20 × 20 mm^2, 15 Ω per square) were cleaned by the same procedure as described in "Fabrication and evaluation of space-charge-limited current electron-

only devices". PEDOT:PSS (Clevios, AI4083) was spin-coated onto the cleaned ITO surface. After being baked in air at 120 °C for 20 min, the substrates were transferred into a nitrogen-filled glove box (< 10 ppm O_2 and H_2O) for preparation of active layers. Bulk-heterojunction films were prepared by spin-coating of a p:n blend solution in $CHCl_3$ at 1500 rpm for 30 s, followed by solvent vapor annealing with THF in the glovebox. Finally, LiF (1 nm, 0.01 Å s^{-1}) and Al (70 nm, 0.3 Å s^{-1}) were vapor-deposited at high vacuum (~10^{-4} Pa) through a shadow mask that defined an active area of 2 × 2 mm^2. The general device structure was [ITO/PEDOT:PSS (30 nm)/p:n/LiF (1 nm)/Al (70 nm)].

Current density–voltage (*J–V*) curves were measured under simulated AM1.5G illumination at an intensity of 100 mW cm^{-2} using a Bunko Keiki CEP-2000RP solar simulator with a Keithley 2611B source mater unit. The EQE spectra were obtained under illumination of monochromatic light using the same system.

Fabrication and evaluation of organic field-effect transistors

The highly n-doped silicon wafers with a 300 nm-thick thermally grown SiO_2 layer (12 × 12 mm^2) were sequential sonication in detergent (Furuuchi Chemical, Semico Clean 53), distilled water (Wako Pure Chemical, reagent grade), and isopropyl alcohol (Kishida chemical, electronic grade) for 10 min each. After drying with nitrogen blow and UV/O_3 treatment with a Bioforce Nanoscience TC-003 cleaner at room temperature for 20 min. The active layer was prepared by drop-casting with a solution of a DPP derivative in chlorobenzene (0.5 mg mL^{-1}) on the cleaned SiO_2 substrate at 80 °C. Finally, Au as top contact source and drain electrodes were vapor-deposited at high vacuum (~10^{-4} Pa) with a deposition rate of 0.1 Å s^{-1} to a thickness about 50 nm as measured by a quart crystal sensor. OFET characteristics were measured by using Keithley 2400 source maters with or without illumination of

monochromatic light (400, 600, 660 and 800 nm) at intensity of 0.25, 0.50 and 2.5 mW cm^{-2} from a Bunko Keiki CEP-2000RP solar simulator.

Synthesis

Synthesis of compound **13a**

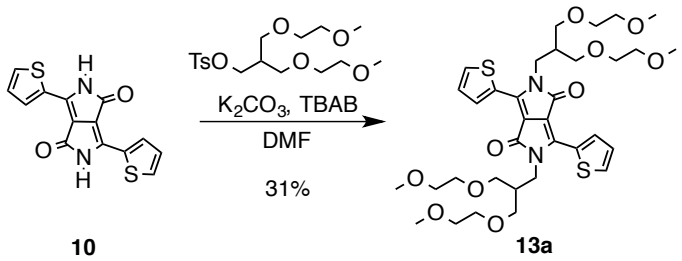

10 **13a**

A mixture of compound **10** (220.0 mg, 735.0 μmol), tetra-*n*-butylammonium bromide (TBAB) (250.0 mg, 775.5 mmol), potassium carbonate (1.000 g, 7.235 mmol) and *N*,*N*-dimethylformamide (15.0 mL) was stirred at 110 °C for 23 h. After cooled to room temperature, the reaction mixture was poured into water and extracted with diethyl ether (30 mL). The organic phase was washed with 1 M HCl (10 mL), water (20 mL × 3) and brine (20 mL), dried over anhydrous Na_2SO_4, filtered, and evaporated. The crude product was purified by gravity silica gel chromatography (ethyl acetate) then the solvent was removed under a reduced pressure to give **13a** as a dark red oil (159.0 mg, 0.224 mmol, 31%). The structure of the product was confirmed ^{1}H NMR (400 MHz, $CDCl_3$): δ 8.81 (dd, *J* = 4.0, 1.1 Hz, 2H), 7.63 (dd, *J* = 5.1, 1.1 Hz, 2H), 7.25 (dd, *J* = 5.1, 4.0 Hz, 2H), 4.23 (d, *J* = 7.3 Hz, 4H), 3.60–3.44 (m, 28H), 2.53–2.44 (m, 2H).[17] q

Synthesis of compound **14a**

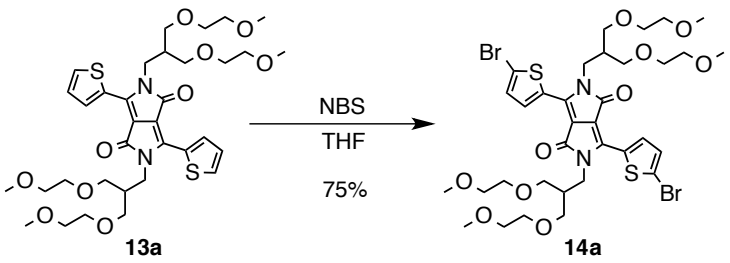

A solution of *N*-bromosuccinimide (NBS) (78.0 mg, 438 μmol, 1.9 equiv) in THF (30 mL) was added to a solution of **13a** (160.0 mg, 226.0 μmol) in THF (30 mL) at 0 °C in the dark. The mixture was stirred at room temperature for 22 h. Then, the reaction mixture was poured into a 30 mL of sodium thiosulfate aqueous solution and extracted with CH_2Cl_2 (50 mL). The organic phase was washed with water (50 mL × 3) and brine (50 mL), dried over anhydrous Na_2SO_4, filtered, and evaporated. The crude product was purified by gravity silica gel chromatography (ethyl acetate) and recrystallization from a $CHCl_3$ solution by adding hexanes to give compound **14a** as a dark red crystalline solid (147.6 mg, 0.170 mmol, 75%). The structure of the product was confirmed ^{1}H NMR (400 MHz, $CDCl_3$): δ 8.56 (d, J = 4.0 Hz, 2H), 7.20 (d, J = 4.0 Hz, 2H), 4.14 (d, J = 7.3 Hz, 4H), 3.58–3.43 (m, 28H), 2.50–2.43 (m, 2H).[17]

Synthesis of **O4-DPP**

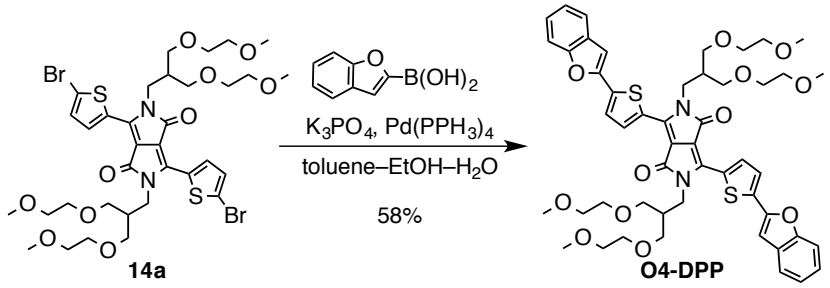

$Pd(PPh_3)_4$ (8.0 mg, 6.9 μmol) was added to a solution of compound **14a** (32.0 mg, 37.0 μmol), K_3PO_4 (153.0 mg, 720.7 mmol), benzofuran-2-boronic acid (13.2 mg, 81.5 μmol) in toluene (2 mL), EtOH (1 mL) and H_2O (1 mL). The mixture was degassed by bubbling argon for 15 min and reflux for 26 h. After being allowed to cool to room temperature, the reaction mixture was extracted with CH_2Cl_2 (50 mL) and the organic phase was washed with water (10 mL × 3) and brine (20 mL), dried over anhydrous Na_2SO_4, filtered, and evaporated. The crude product was purified by gravity silica gel column chromatography (CH_2Cl_2/ethyl acetate, 1:1) and recrystallization from a $CHCl_3$ solution by adding hexanes to give **O4-DPP** as a purple solid (20.2 mg, 21.5 μmol, 58%). ^{1}H NMR (400 MHz, DMSO-d_6): δ 8.75 (d, J = 4.4 Hz, 2H), 7.87 (d, J = 4.4 Hz, 2H), 7.70 (d, J = 7.7 Hz, 2H), 7.64 (d, J = 7.7 Hz, 2H), 7.51 (s, 2H), 7.39 (t, J = 7.7 Hz, 2H), 7.31 (t, J = 7.5 Hz, 2H), 4.18 (d, J = 7.0 Hz, 4H), 3.50–3.40 (m, 24H), 3.19 (br, 12H), 2.37–2.31 (m, 2H); ^{13}C{^{1}H}NMR (125 MHz, $CDCl_3$): δ 161.7, 161.6, 154.9, 150.1, 150.0, 150.0, 139.5, 139.4, 138.1, 137.9, 136.4, 136.3, 136.1, 129.7, 129.4, 128.9, 128.8, 125.5, 125.4, 125.4, 125.3, 123.5, 123.5, 121.2, 111.3, 108.7, 108.6, 103.8, 103.8, 103.7, 71.9, 70.7, 70.3, 59.1, 46.3, 42.0, 40.2, 38.0, 31.9, 31.2, 29.7, 26.3, 22.7, 14.1; IR (ATR): $\bar{\nu}$ [cm^{-1}] 3032 (w, C (sp^2)–H), 2881 (w, C (sp^3)–H), 2821 (w, C (sp^3)–H), 1660 (m, C=O), 1408 (m, C–N), 1112 (w, C–O–C), 1024 (s, C–O–C), 824 (m); HRMS (MALDI–TOF, DCTB) m/z calcd for $C_{50}H_{56}N_2O_{12}S_2^{\bullet+}$ ($M^{\bullet+}$) 940.3269, found 940.3266.

Synthesis of compound **12b**

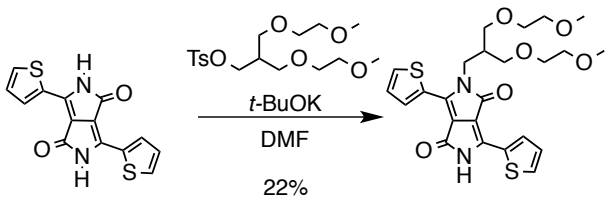

10 **12b**

A mixture of compound **10** (800.0 mg, 2.670 mmol), 3-(2-methoxyethoxy)-2-((2-methoxyethoxy)methyl)propyl 4-methylbenzenesulfonate (1.000 g, 2.666 mmol), potassium *tert*-butoxide (500.0 mg, 4.456 mmol) and *N*,*N*-dimethylformamide (100 mL) was stirred at 110 °C for 20 h. After cooled to room temperature, the reaction mixture was poured into water and extracted with diethyl ether (50 mL). The organic phase was washed with water (20 mL × 3) and brine (20 mL), dried over anhydrous Na_2SO_4, filtered, and evaporated. The crude product was purified by gravity silica gel chromatography (ethyl acetate) to give **12b** as a dark red oil (301.2 mg, 597.5 μmol, 22%). ^{1}H NMR(400 MHz, $CDCl_3$): δ 10.17 (br, 1H), 8.37 (dd, J = 3.7, 1.1 Hz, 1H), 8.00 (dd, J = 3.7, 1.1 Hz, 1H), 7.63 (dd, J = 4.8, 1.1 Hz, 1H), 7.51 (dd, J = 4.8, 1.1 Hz, 1H), 7.14–7.19 (m, 2H), 4.69 (d, J = 5.5 Hz, 2H), 3.72 (d, J = 6.2 Hz, 4H), 3.66–3.64 (m, 4H), 3.57–3.55 (m, 4H), 3.37 (s, 6H), 2.61–2.58 (m, 1H); ^{13}C{^{1}H}NMR (100 MHz, $CDCl_3$): δ 166.0, 162.96, 149.1, 138.9, 138.7, 133.0, 132.3, 131.5, 131.1, 130.3, 130.3, 128.8, 113.6, 112.6, 71.9, 70.2, 69.3, 68.5, 59.0, 39.5; IR (ATR): $\bar{\nu}$ [cm^{-1}] 2081 (w, C (sp^2)–H), 2870 (w, C (sp^3)–H), 1670 (m, C=O) 1599 (m), 1507 (m), 1456 (m, C–N), 1118 (m, C–O–C), 853.3 (m); HRMS (MALDI–TOF, DCTB) m/z calcd for $C_{24}H_{28}N_2O_6S_2^{\bullet+}$ ($M^{\bullet+}$) 504.1383, found 504.1379.

Synthesis of compound **13b**

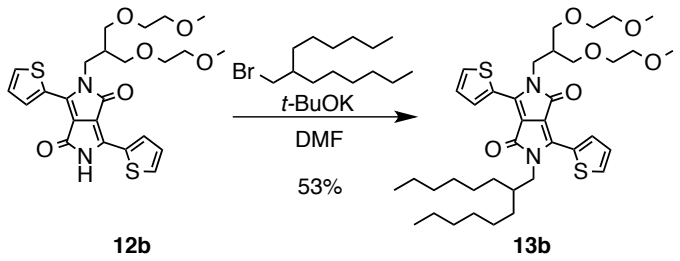

12b **13b**

A mixture of compound **12b** (510.0 mg, 1.015 mmol), 7-(bromomethyl)tridecane (416.0 mg, 1.53 mmol), potassium *tert*-butoxide (290.0 mg, 2.584 mmol) and *N*,*N*-dimethylformamide (20 mL) was stirred at 110 °C for 24 h. After cooled to room temperature, the reaction mixture was poured into water and extracted with diethyl ether (50 mL). The organic phase was washed with water (20 mL × 3) and brine (20 mL), dried over anhydrous Na_2SO_4, filtered, and evaporated. The crude product was purified by gravity silica gel chromatography (CH_2Cl_2/ethyl acetate, 1:1) to give **13b** as a dark red solid (375.2 mg, 0.535 mmol, 53%). ^{1}H NMR (400 MHz, $CDCl_3$): δ 8.84 (dd + dd, J = 3.9, 1.2 Hz, 1H + 1H), 7.64–7.61 (m, 2H), 7.27–7.24 (m, 2H), 4.22 (d, J = 7.7 Hz, 2H), 4.02 (d, J = 7.7 Hz, 2H), 3.60–3.46 (m, 12H), 2.49 (s, 1H), 1.90 (s, 1H), 1.30–1.21 (m, 20H), 0.84 (t, J = 6.8 Hz, 6H); ^{13}C{^{1}H}NMR (100 MHz, $CDCl_3$): δ 161.7, 161.6, 140.3, 140.2, 135.0, 134.9, 130.7, 130.5, 129.8, 129.7, 128.4, 128.32, 107.8, 107.8, 77.3, 77.0, 76.7, 71.8, 70.6, 70.2, 59.0, 46.1, 41.7, 40.1, 37.7, 31.7, 31.0, 29.6, 26.1, 22.6, 14.0; IR (ATR): $\bar{\nu}$ [cm^{-1}] 3103 (w, C (sp^2)–H), 2925 (m, C (sp^3)–H), 2853 (m, C (sp^3)–H), 1671 (s, C=O), 1445 (m, C–N), 1113 (s, C–O–C), 852 (m); HRMS (MALDI–TOF, DCTB) *m*/*z* calcd for $C_{38}H_{56}N_2O_6S_2^{\bullet+}$ ($M^{\bullet+}$) 700.3574, found 700.3571.

Synthesis of compound **14b**

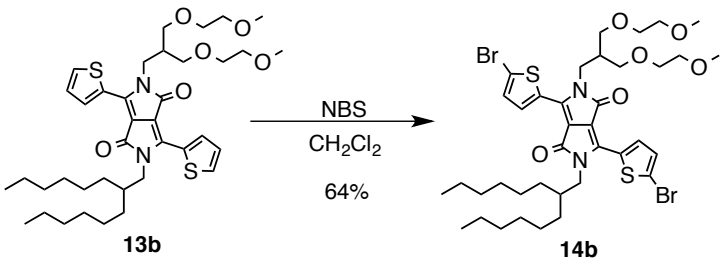

A solution of *N*-bromosuccinimide (29.3 mg, 165 μmol, 1.9 equiv) in THF (30 mL) was added to a solution of **13b** (61.6 mg, 87.3 μmmol) in THF (20 mL) at 0 °C in the dark. The mixture was stirred at room temperature for 15 h. Then, the reaction mixture was poured into 30 mL of a sodium thiosulfate aqueous solution and extracted with CH_2Cl_2 (50 mL). The organic phase was washed with water (30 mL × 3) and brine (30 mL) and dried over anhydrous Na_2SO_4, filtered, and evaporated. The crude product was purified by gravity silica gel chromatography (CH_2Cl_2/ethyl acetate, 1:1) and recrystallization from a $CHCl_3$ solution by adding hexanes to give compound **14b** as a dark red crystalline solid (48.0 mg, 55.9. μmol, 64%). ^{1}H NMR (400 MHz, $CDCl_3$) δ 8.60–8.58 (m, 2H), 7.22 (d, J = 4.0 Hz, 1H), 7.20 (d, J = 4.4 Hz, 1H), 4.14 (d, J = 7.3 Hz, 2H), 3.93 (d, J = 7.7 Hz, 2H), 3.58–3.47 (m, 12H), 2.50–2.47 (m, 1H), 1.8–1.86 (m, 1H), 1.29–1.23 (m, 20H), 0.85 (t, J = 6.6 Hz, 6H); ^{13}C{^{1}H}NMR (100 MHz, $CDCl_3$): δ 161.5, 161.3, 139.3, 139.1, 135.1, 135.0, 131.5, 131.4, 131.4, 131.1, 119.4, 119.0, 107.9, 107.9, 71.8, 70.7, 70.2, 59.1, 46.2, 41.8, 40.2, 37.8, 31.8, 31.0, 29.7, 26.1, 22.6, 14.1; IR (ATR): $\bar{\nu}$ [cm^{-1}] 3087 (w, C (sp^2)–H), 2927 (m, C (sp^3)–H), 1657 (s, C=O), 1411 (w, C–N), 1045 (w, C–O–C), 830 (m); HRMS (MALDI–TOF, DCTB) *m*/*z* calcd for $C_{38}H_{54}N_2O_6S_2{}^{79}Br_2{}^{\bullet+}$ ($M^{\bullet+}$) 858.1785, found 858.1792.

Synthesis of **C14O4-DPP**

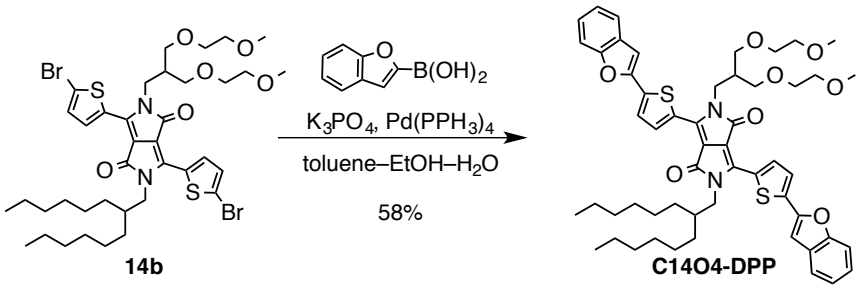

$Pd(PPh_3)_4$ (34.0 mg, 29.4 μmol) was added to a solution of compound **14b** (155.0 mg, 180 μmol), K_3PO_4 (650.0 mg, 3.060 mmol), benzofuran-2-boronic acid (73.0 mg, 450 μmol) in toluene (8 mL), EtOH (4 mL) and H_2O (4 mL). The mixture was degassed by bubbling argon for 15 min and reflux for 7 h. After being allowed to cool to room temperature, the reaction mixture was extracted with CH_2Cl_2 (50 mL) and the organic phase was washed with water (10 mL × 3) and brine (20 mL), dried over anhydrous Na_2SO_4, filtered, and evaporated. The crude product was purified by gravity silica gel column chromatography (CH_2Cl_2/ethyl acetate, 1:1) and recrystallization from a $CHCl_3$ solution by adding hexanes to give **C14O4-DPP** as a purple solid (98.2 mg, 0.105 mmol, 58%). ^{1}H NMR (400 MHz, 1,1,2,2-tetrachloroethane-d_2) δ 8.89 (d, J = 4.0 Hz, 2H), 7.60–7.57 (m, 4H), 7.53 (dd, J = 8.1, 2.9 Hz, 2H), 7.34 (t, J = 7.7 Hz, 2H), 7.26 (t, J = 7.5 Hz, 2H), 7.10 (d, J = 11.0 Hz, 2H), 4.25 (d, J = 7.0 Hz, 2H), 4.05 (d, J = 7.3 Hz, 2H), 3.60–3.47 (m, 12H), 3.30 (s, 6H), 2.53–2.47 (m, 1H), 1.95–1.92 (m, 1H), 1.32–1.22 (m, 18H), 0.81 (t, J = 6.0 Hz, 6H); ^{13}C{^{1}H}NMR (100 MHz, $CDCl_3$): δ 161.7, 161.6, 154.9, 150.1, 150.0, 150.0, 139.5, 139.4, 138.1, 137.9, 136.4, 136.3, 136.1, 129.7, 129.4, 128.9, 128.8, 125.5, 125.4, 125.4, 125.3, 123.5, 123.5, 121.2, 111.3, 108.7, 108.6, 103.8, 103.8, 103.7, 71.9, 70.7, 70.3, 59.1, 46.3, 41.9, 40.2, 38.0, 31.9, 31.2, 29.7, 26.3, 22.6, 14.1; IR (ATR): $\bar{\nu}$ [cm^{-1}] 3032 (w, C (sp^2)–H), 2925 (m, C (sp^3)–H) 1655 (s, C=O), 1542 (s), 1456 (m, C–N), 1106 (w, C–O–C); HRMS (MALDI–TOF, DCTB) m/z calcd for $C_{54}H_{64}N_2O_8S_2^{\bullet+}$ ($M^{\bullet+}$) 932.4099, found 932.4100.

Synthesis of compound **13c**

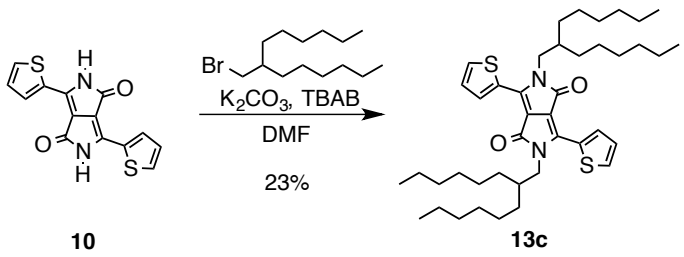

10 **13c**

A mixture of compound **10** (500.0 mg, 1.670 mmol), 7-(bromomethyl)tridecane (1.000 g, 3.606 mmol), tetra-*n*-butylammonium bromide (270.0 mg, 0.838 mmol), potassium carbonate (1.00 g, 7.24 mmol) and *N*,*N*-dimethylformamide (15.0 mL) was stirred at 110 °C for 20 h. After cooled to room temperature, the reaction mixture was poured into water and extracted with diethyl ether (50 mL). The organic phase was washed with water (100 mL × 3) and brine (50 mL), dried over anhydrous Na_2SO_4, filtered, and evaporated. The crude product was purified by gravity silica gel chromatography (CH_2Cl_2/hexanes, 1:1) and recrystallization form a $CHCl_3$ solution by adding hexanes to give **13c** as a dark red solid (263.3 mg, 380.2 μmol, 23%). ^{1}H NMR (400 MHz, 1,1,2,2-tetrachloroethane-d_2) δ 8.79 (dd, J = 4.0, 1.1 Hz, 2H), 7.65 (dd, J = 4.8, 1.1 Hz, 2H), 7.25 (t, J = 4.4 Hz, 2H), 3.97 (d, J = 7.7 Hz, 4H), 1.85 (s, 2H), 1.18–1.25 (m, 40H), 0.81 (t, J = 6.8 Hz, 12H); ^{13}C{^{1}H}NMR (100 MHz, $CDCl_3$): δ 161.74, 140.42, 135.19, 130.47, 129.79, 128.36, 107.90, 46.16, 37.70, 31.74, 31.14, 29.65, 26.13, 22.61, 14.07; IR (ATR): $\bar{\nu}$ [cm^{-1}] 3076 (w, C (sp^2)–H), 2925 (m, C (sp^3)–H), 1733 (s), 1668 (s, C=O), 1405 (m, C–N), 735 (m), 716 (m); HRMS (MALDI–TOF, DCTB) m/z calcd for $C_{42}H_{64}N_2O_2S_2^{\bullet+}$ ($M^{\bullet+}$) 692.4404, found 692.4407.

Synthesis of compound **14c**

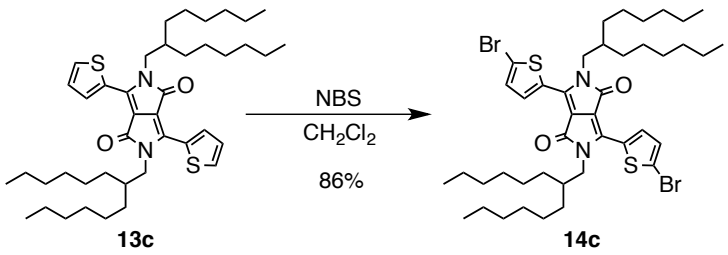

A solution of *N*-bromosuccinimide (51.0 mg, 0.287 mmol, 2.0 equiv) in CH_2Cl_2 (40 mL) was added to a solution of **13c** (100.0 mg, 0.144 mmol) in CH_2Cl_2 (40 mL) at 0 °C in the dark. The mixture was stirred at room temperature for 15 h. Then, the reaction mixture was poured into 30 mL of a sodium thiosulfate aqueous solution. The organic phase was washed with water (30 mL × 3) and brine (30 mL), dried over anhydrous Na_2SO_4, filtered, and evaporated. The crude product was purified by gravity silica gel chromatography (CH_2Cl_2/hexanes, 1:1) and recrystallization from a $CHCl_3$ solution by adding methanol 2 times to give compound **14c** as a dark red crystalline solid (105.0 mg, 123.8 μmol, 86%). ^{1}H NMR (400 MHz, $CDCl_3$): δ 8.62 (d, J = 4.6 Hz, 2H), 7.22 (d, J = 4.6 Hz, 2H), 3.92 (d, J = 7.8 Hz, 4H), 1.87 (m, 2H),1.22–1.29 (m, 40H), 0.85 (t, J = 6.6 Hz, 12H); ^{13}C{^{1}H} NMR (100 MHz, $CDCl_3$): δ161.4, 139.5, 135.4, 131.5, 131.2, 119.1, 108.1, 46.4, 37.9, 31.2, 29.7, 26.2, 22.7, 14.2; IR (ATR): $\bar{\nu}$ [cm^{-1}] 3083 (w, C (sp^2)–H), 2926 (m, C (sp^3)–H), 2855 (m, C (sp^3)–H), 1656 (s, C=O), 1556 (m), 1503 (m), 1447 (m, C–N), 1411 (m), 1398 (m), 1049 (w); HRMS (MALDI–TOF) *m*/*z* calcd for $C_{42}H_{62}{}^{79}Br_2N_2O_2S_2^{\bullet+}$ ($M^{\bullet+}$) 848.2614, found 848.2618.

Synthesis of **C14-DPP**

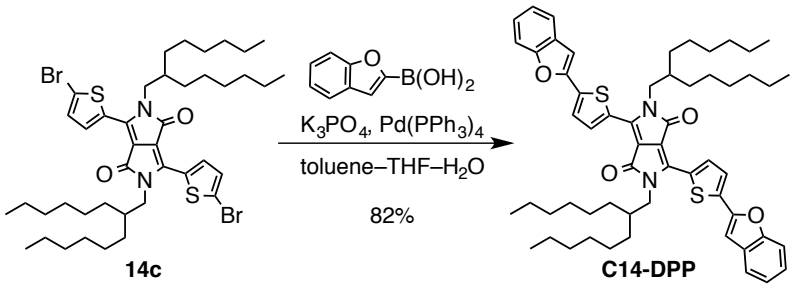

$Pd(PPh_3)_4$ (10.0 mg, 8.66 μmol) was added to a solution of compound **14c** (70.0 mg, 82.4 μmol), K_3PO_4 (300.0 mg, 1.412 mmol), benzofuran-2-boronic acid (34.0 mg, 210 μmol) in toluene (5 mL), THF (10 mL) and H_2O (2 mL). The mixture was degassed by bubbling argon for 15 min and refluxed for 20 h. After being allowed to cool to room temperature, the reaction mixture was extracted with CH_2Cl_2 (50 mL) and the organic phase was washed with water (10 mL × 3) and brine (20 mL), dried over anhydrous Na_2SO_4, filtered, and evaporated. The crude product was purified by gravity silica gel column chromatography (CH_2Cl_2/hexanes, 1:2) and recrystallization from a $CHCl_3$ solution by adding hexanes to give **C14-DPP** as a purple solid (62.7 mg, 67.8 μmol, 83%). ^{1}H NMR (400 MHz, 1,1,2,2-tetrachloroethane-d_2) δ 8.90 (t, J = 4.2 Hz, 2H), 7.59 (t, J = 4.4 Hz, 4H), 7.55–7.52 (m, 2H), 7.37–7.32 (m, 2H), 7.29–7.26 (m, 2H), 7.09 (d, J = 4.4 Hz, 2H), 4.05 (s, 4H), 1.95 (s, 2H), 1.37–1.18 (m, 40H), 0.81 (t, J = 4.8 Hz, 13H); ^{13}C{^{1}H}NMR (100 MHz, $CDCl_3$): δ 161.7, 140.4, 135.3, 135.2, 135.2, 135.1, 130.6, 130.5, 130.4, 129.8, 128.5, 128.4, 128.3, 128.2, 107.9, 46.2, 37.7, 31.7, 31.1, 29.7, 26.1, 22.6, 14.1; IR (ATR): $\bar{\nu}$ [cm^{-1}] 3035 (w, C (sp^2)–H),2963 (m, C (sp^3)–H), 1771 (s), 1659 (s, C=O), 1455 (m, C–N), 820 (m); HRMS (MALDI–TOF, DCTB) m/z calcd for $C_{58}H_{72}N_2O_4S_2^{\bullet+}$ ($M^{\bullet+}$) 924.4928, found 924.4930.

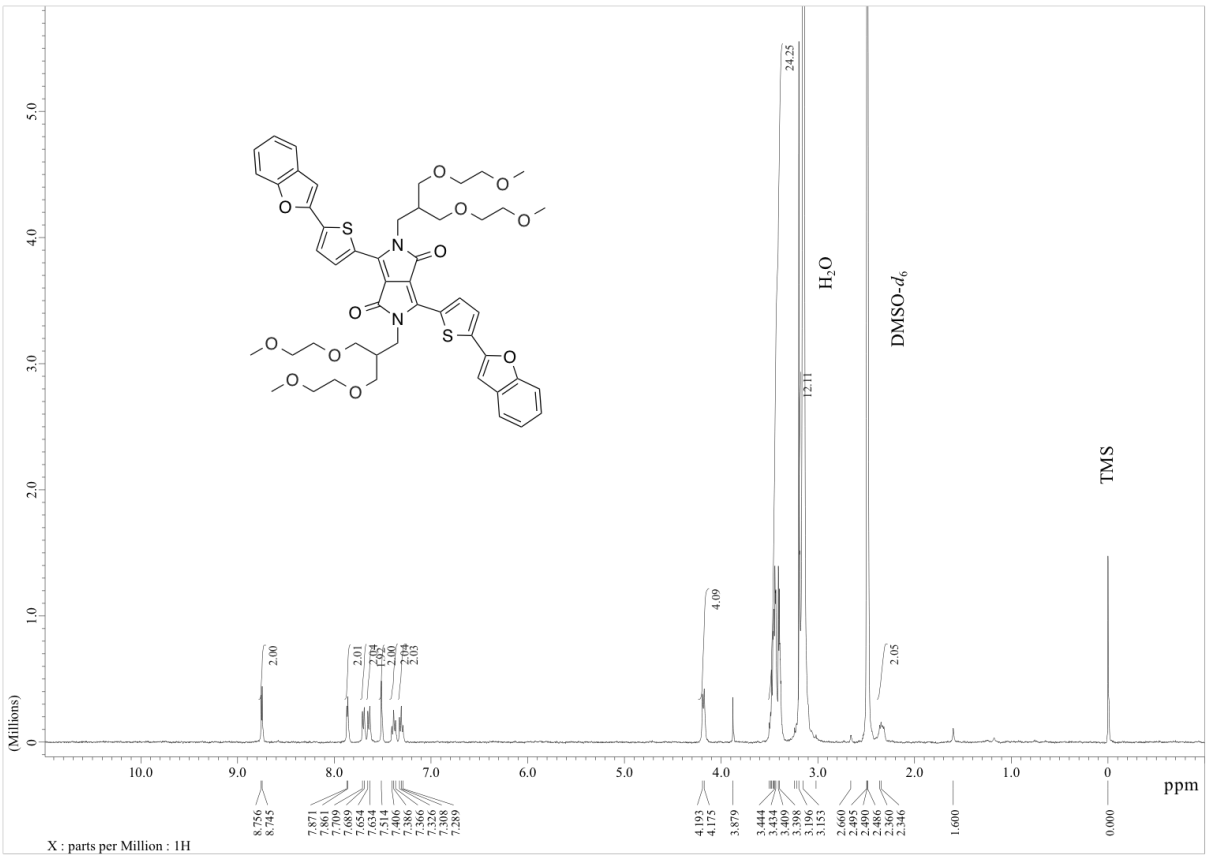

^{1}H NMR spectrum of **O4-DPP** (DMSO-d_6, 400 MHz).

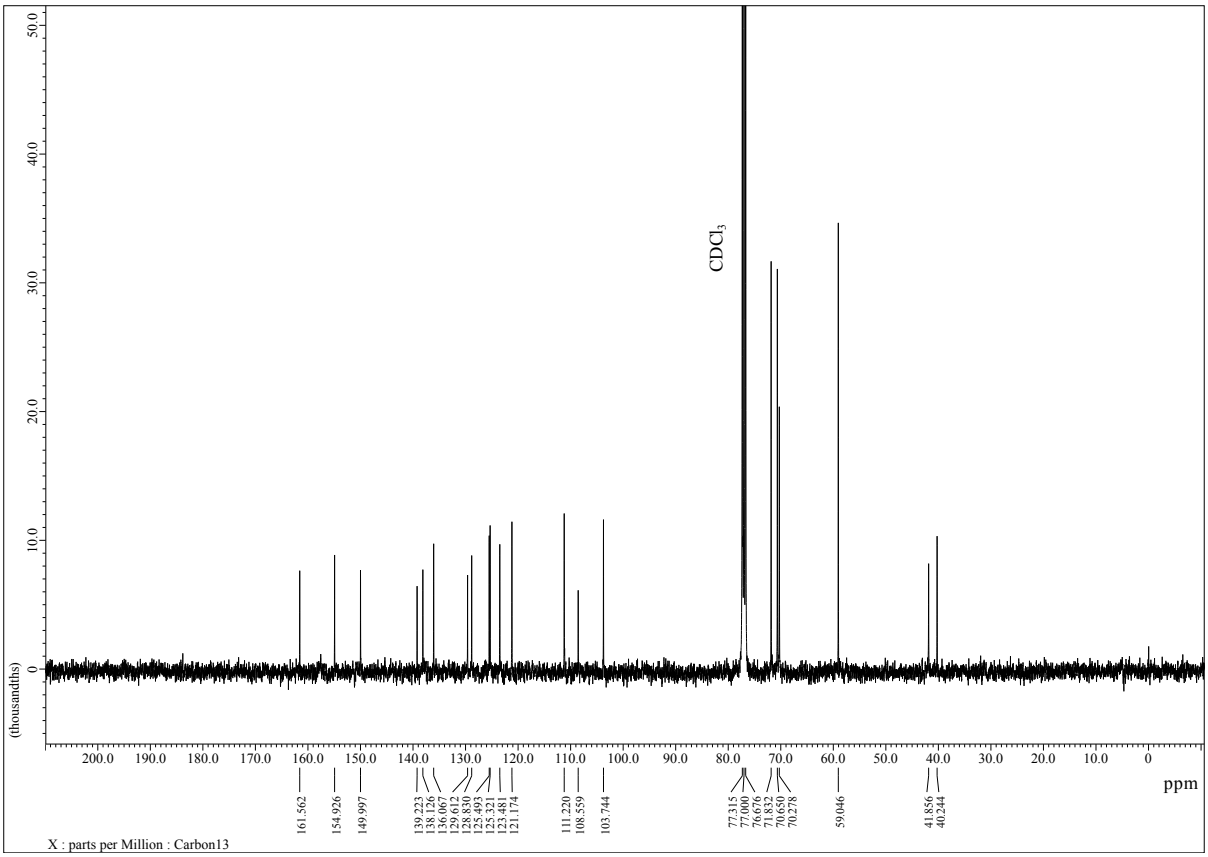

^{13}C{^{1}H} NMR spectrum of **O4-DPP** ($CDCl_3$, 126 MHz).

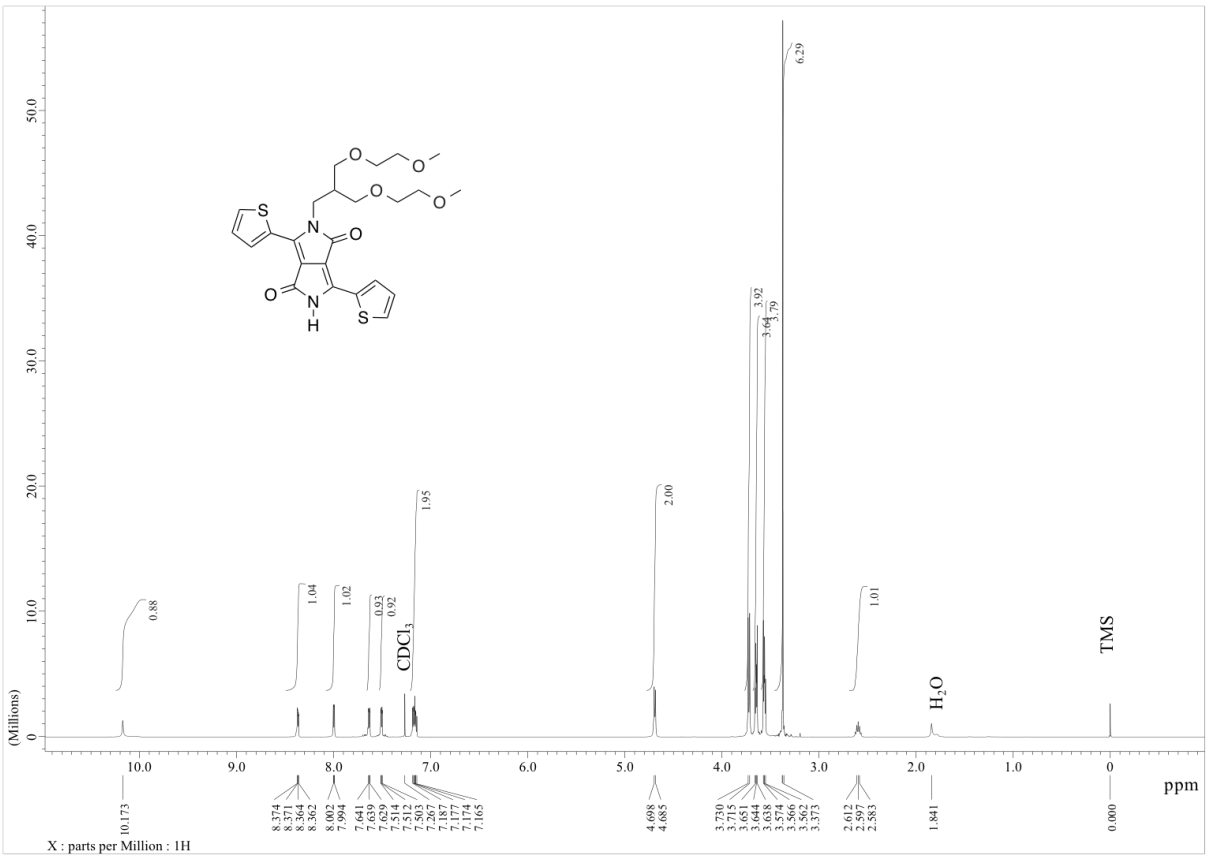

^{1}H NMR spectrum of **12b** ($CDCl_3$, 400 MHz).

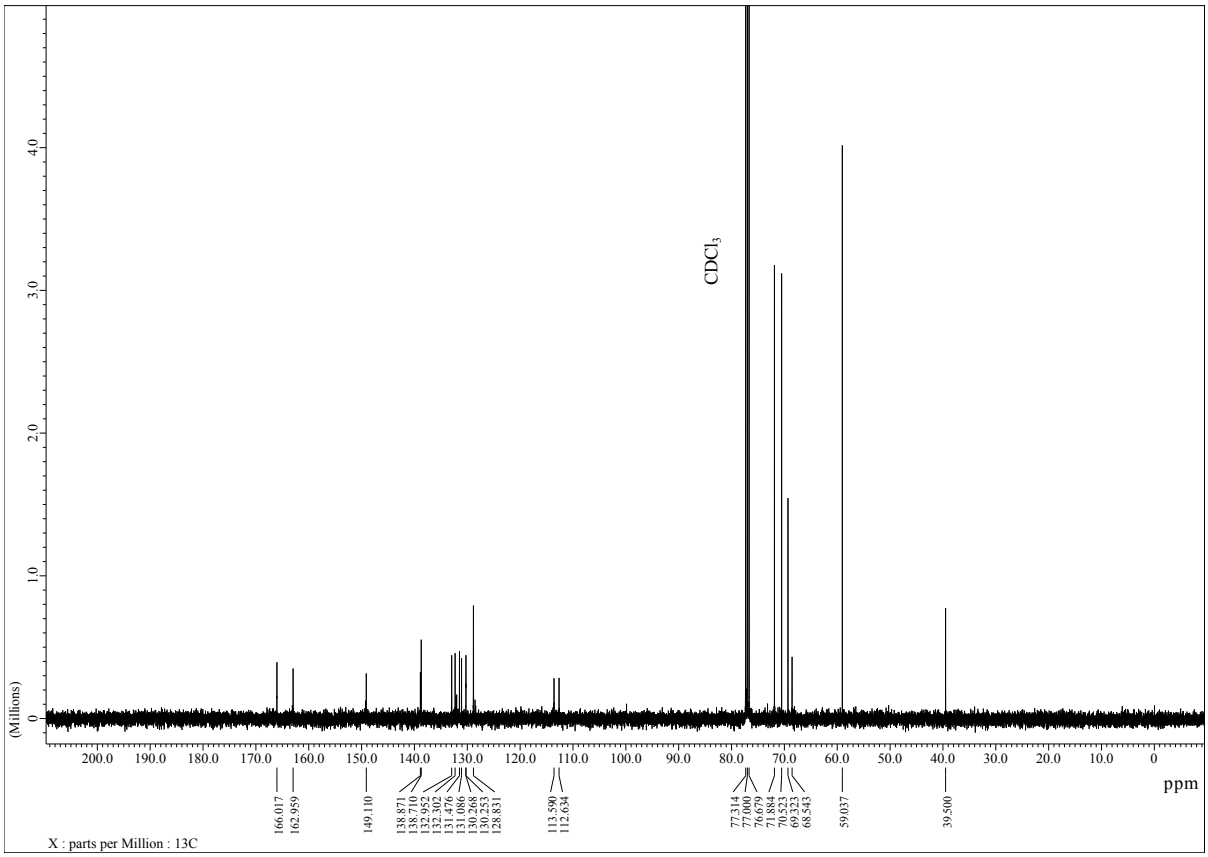

$^{13}C\{^{1}H\}$ NMR spectrum of **12b** ($CDCl_3$, 100 MHz).

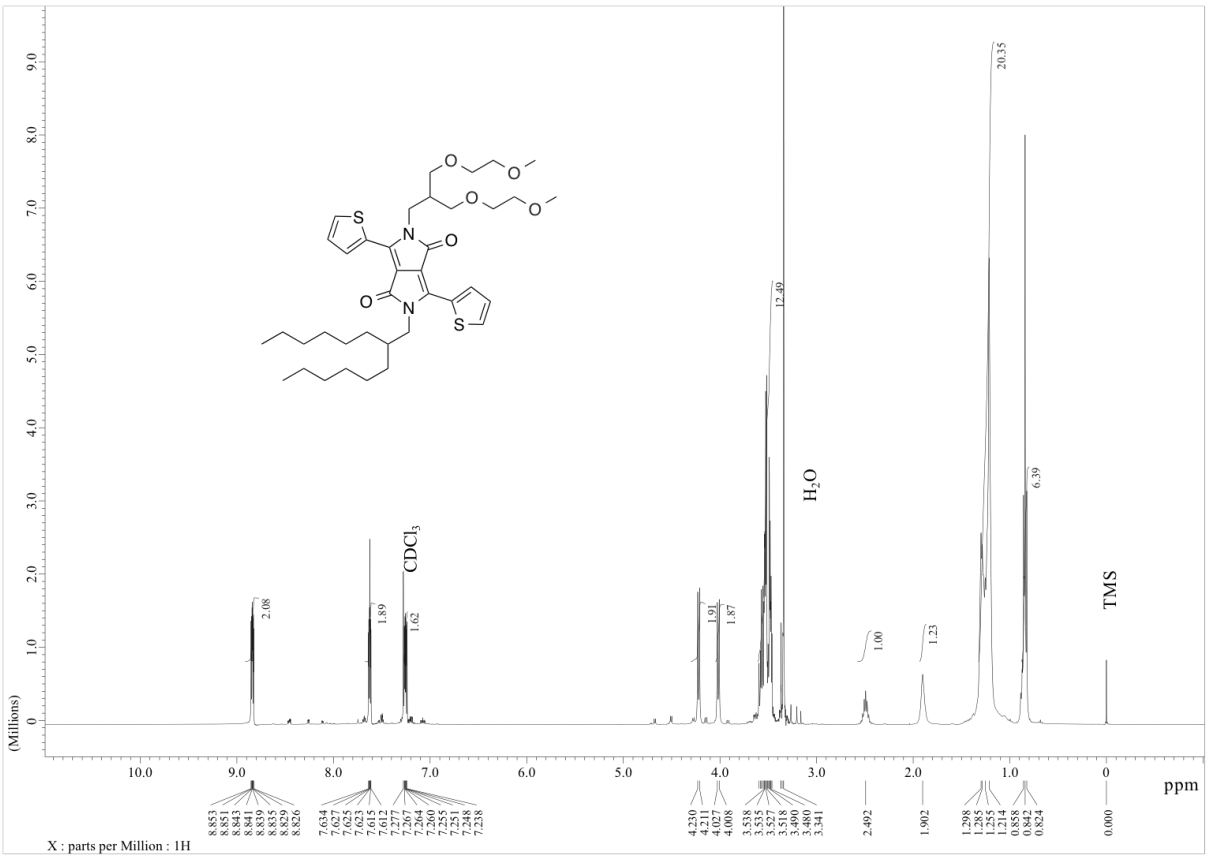

^{1}H NMR spectrum of **13b** ($CDCl_3$, 400 MHz).

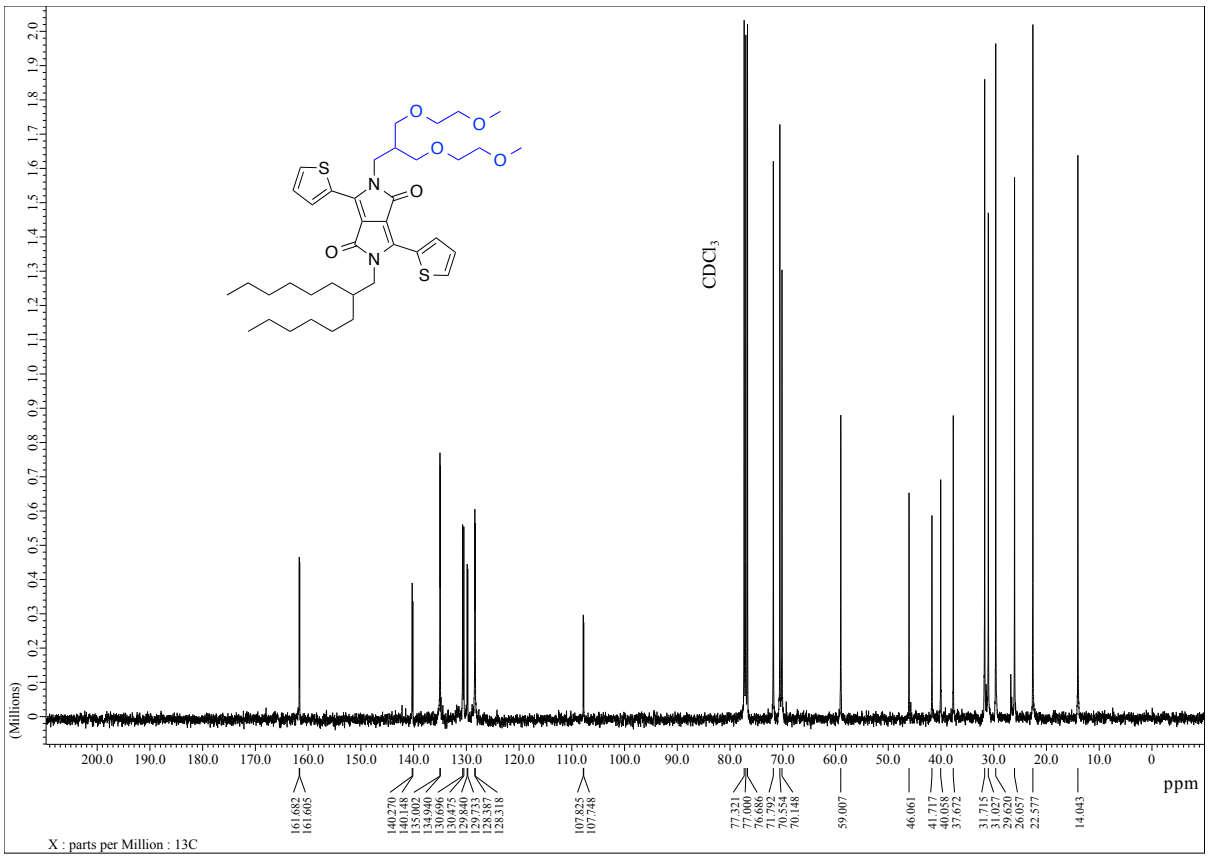

^{13}C{^{1}H} NMR spectrum of **13b** ($CDCl_3$, 100 MHz).

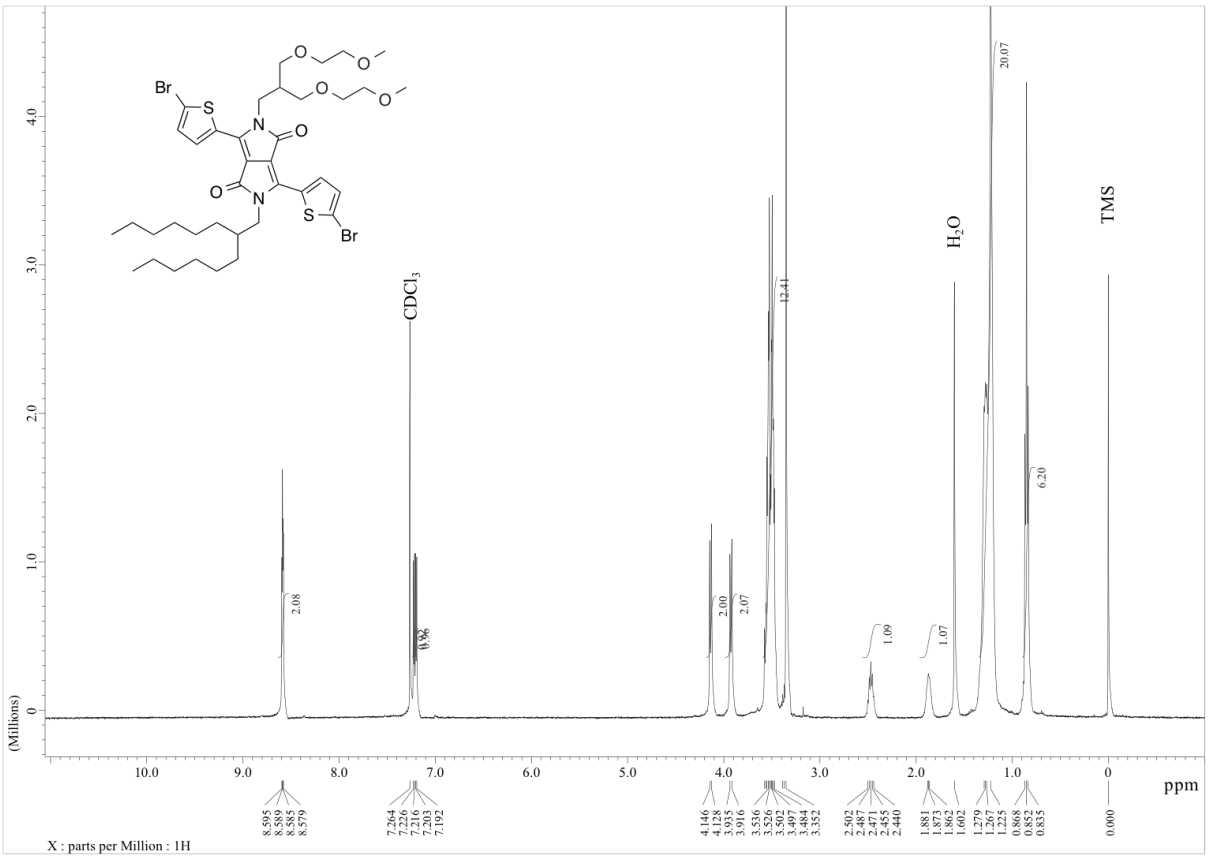

^{1}H NMR spectrum of **14b** ($CDCl_3$, 400 MHz).

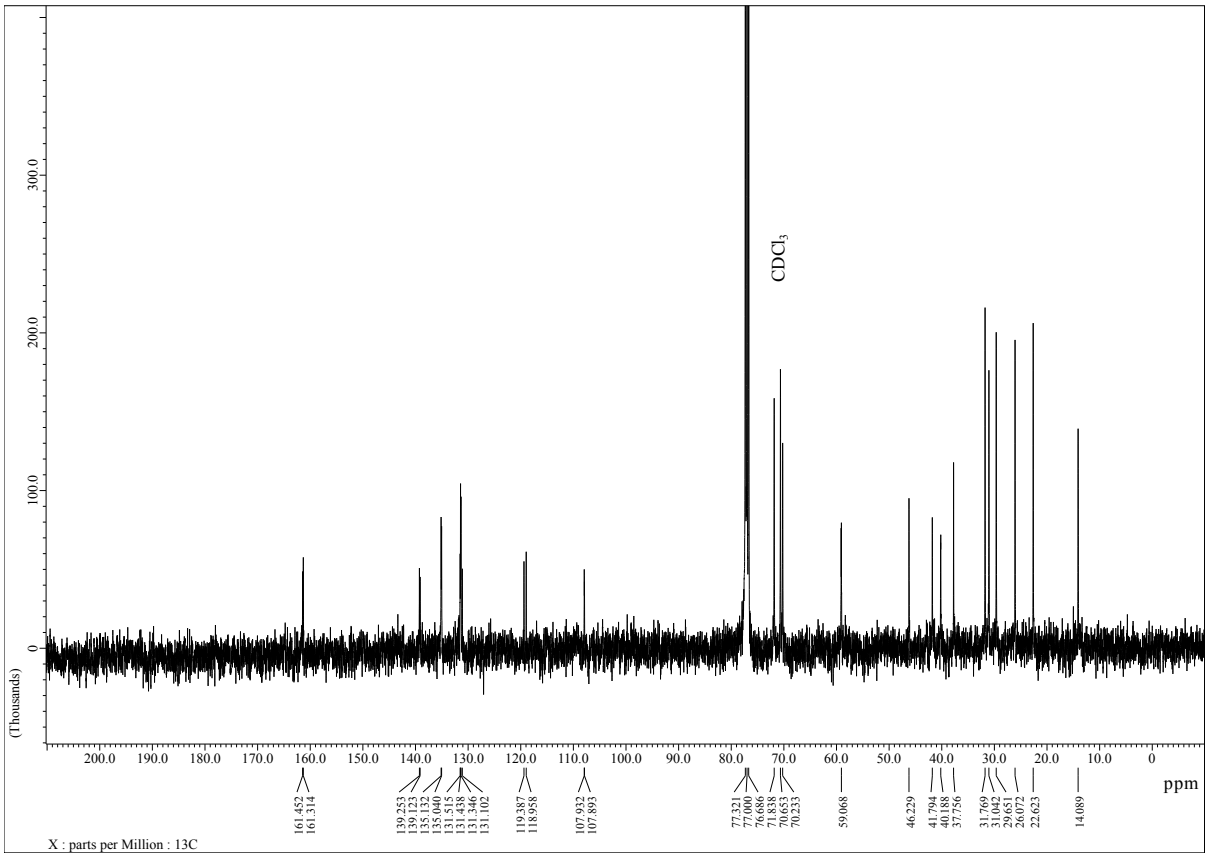

^{13}C{^{1}H} NMR spectrum of **14b** ($CDCl_3$, 100 MHz).

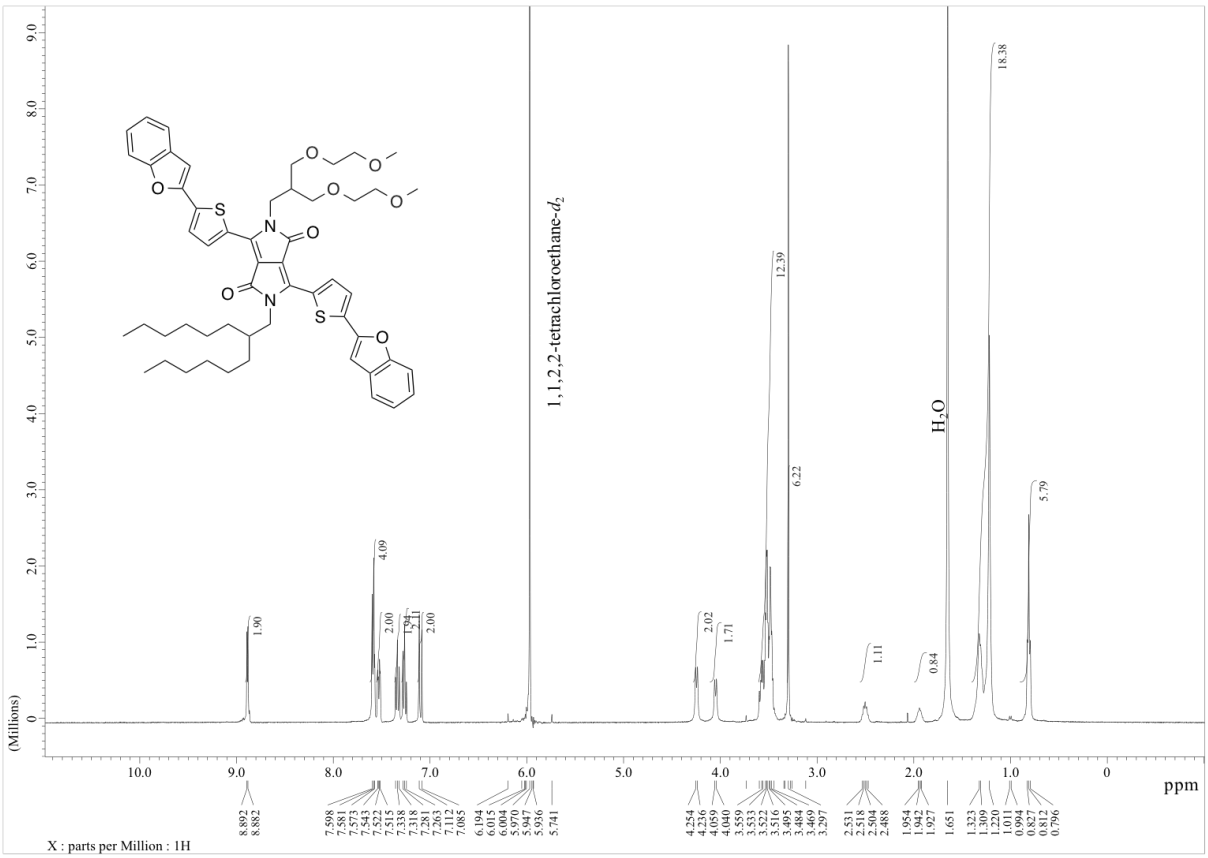

^{1}H NMR spectrum of **C14O4-DPP** (1,1,2,2-tetrachloroethane-d_2, 400 MHz).

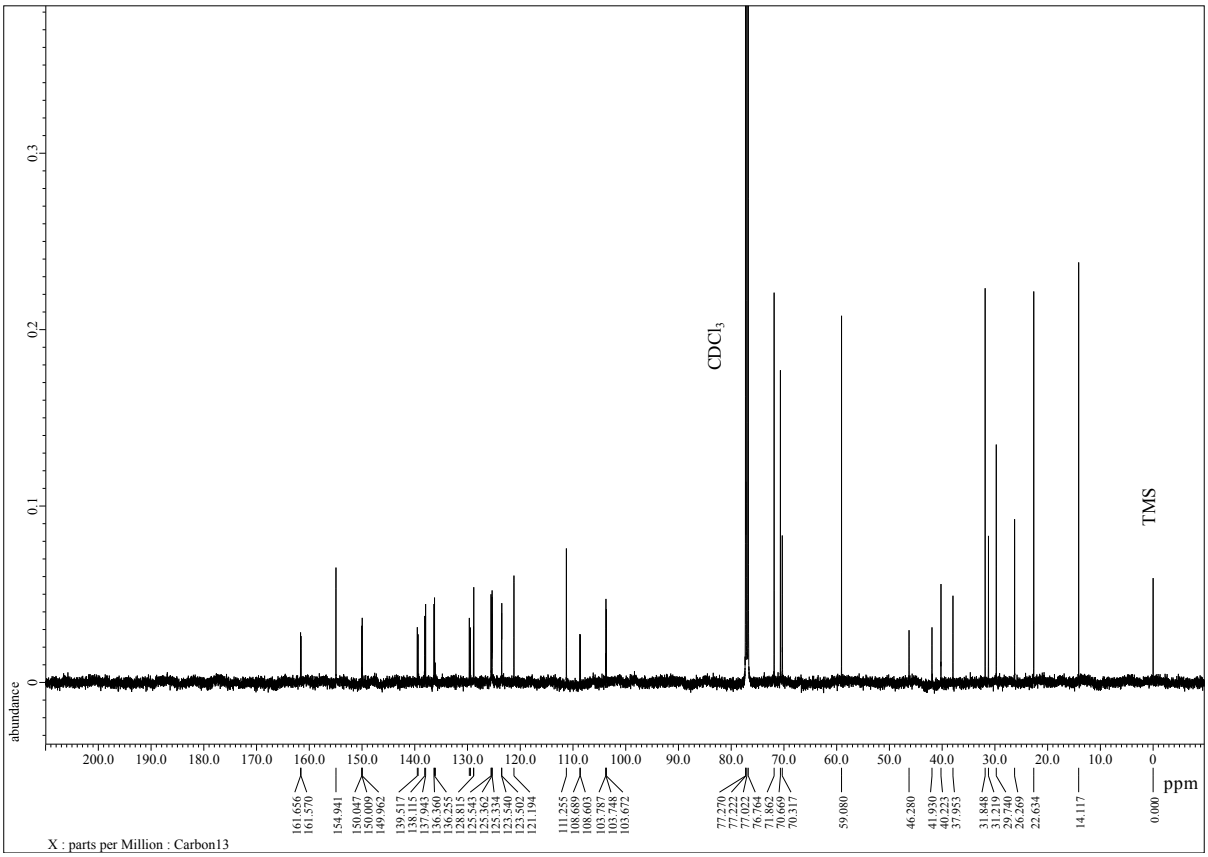

^{13}C{^{1}H} NMR spectrum of **C14O4-DPP** ($CDCl_3$, 100 MHz).

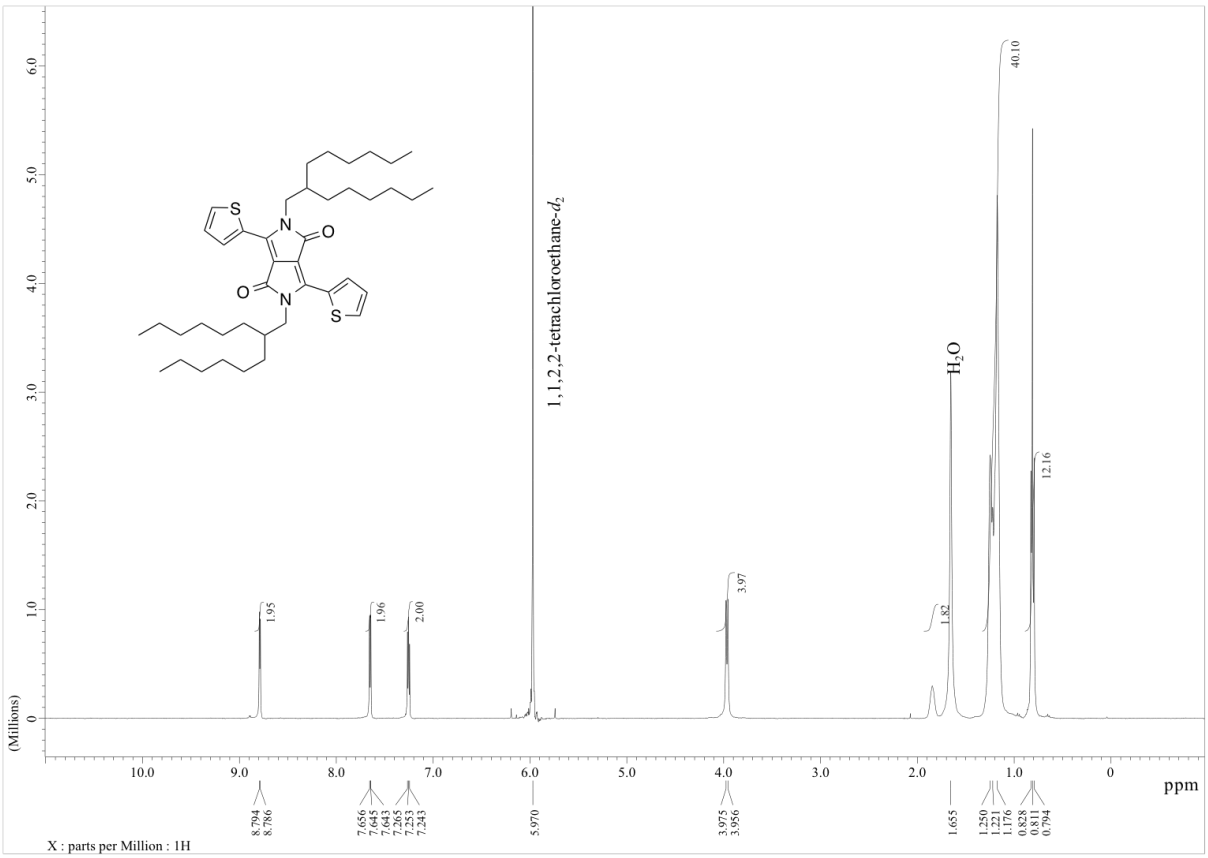

^{1}H NMR spectrum of **13c** (1,1,2,2-tetrachloroethane-d_2, 400 MHz).

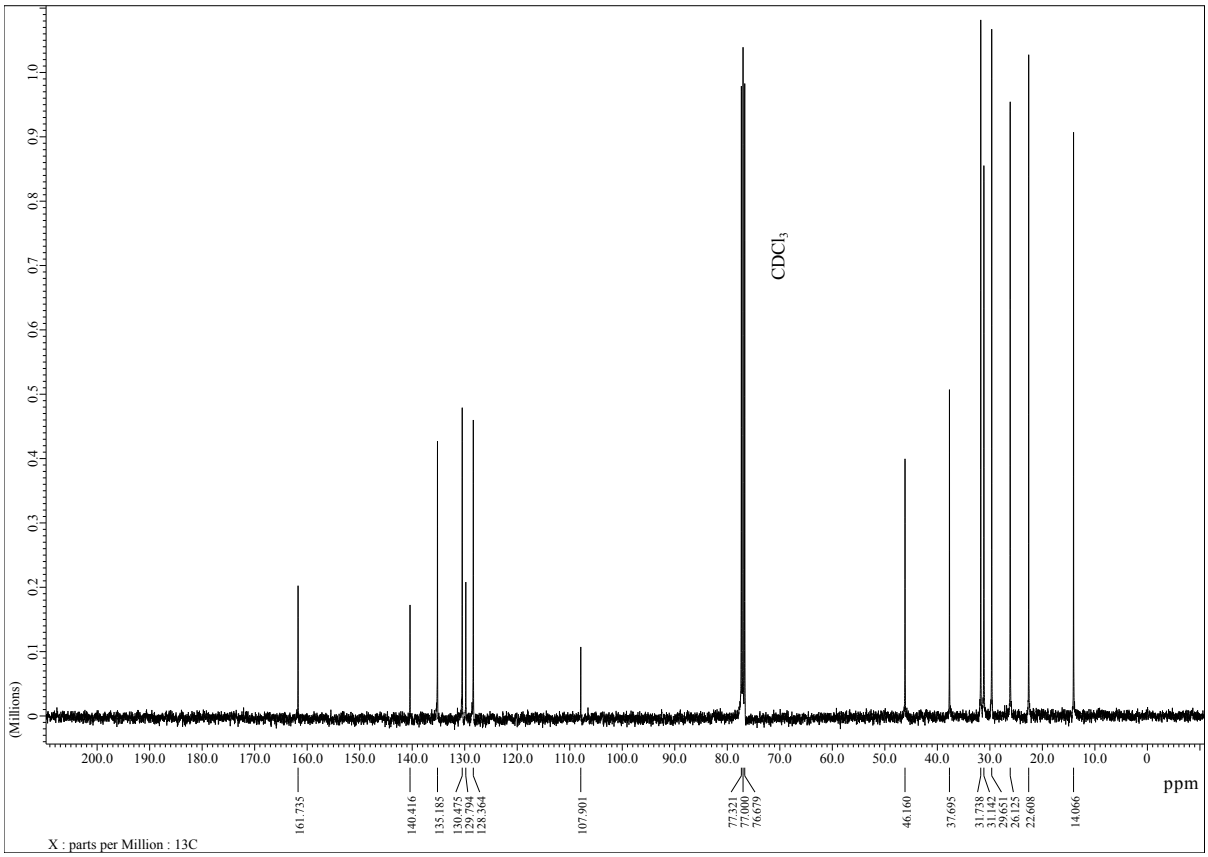

^{13}C{^{1}H} NMR spectrum of **13c** ($CDCl_3$, 100 MHz).

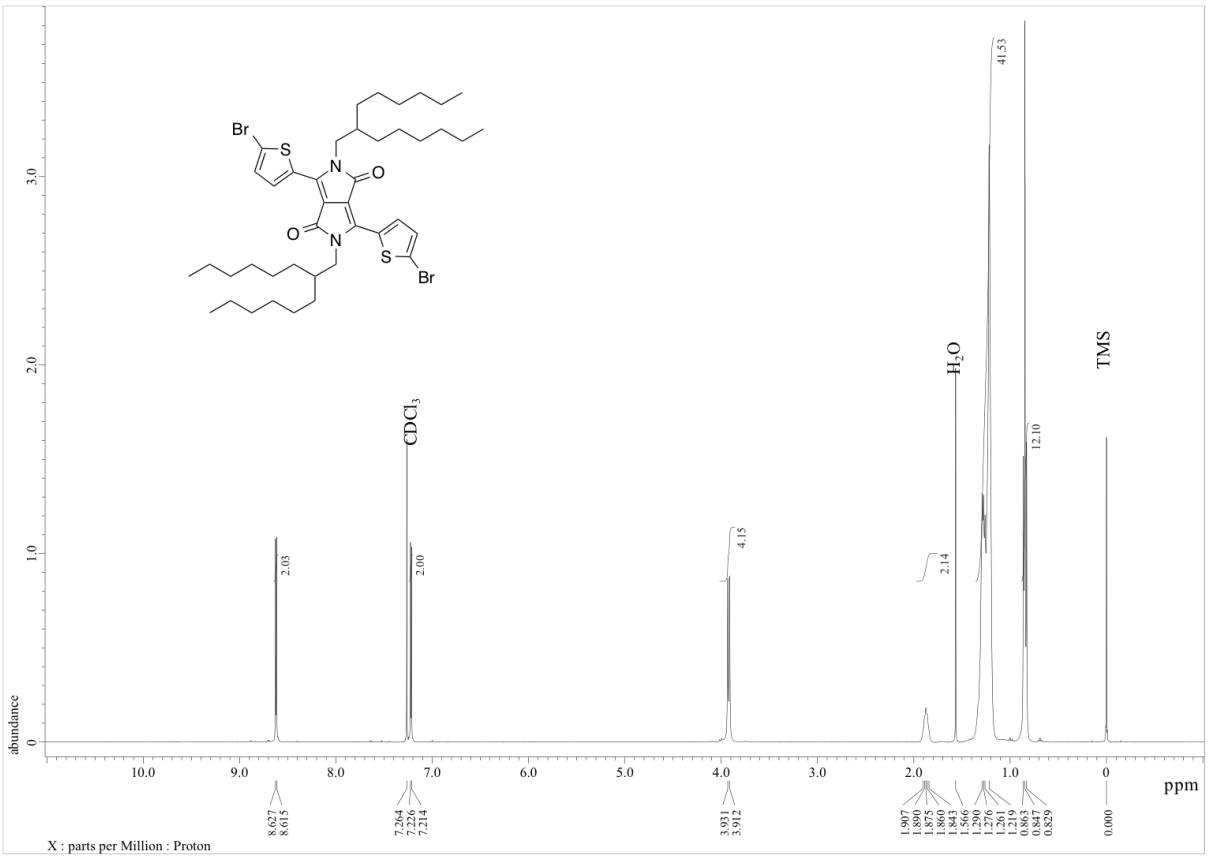

^{1}H NMR spectrum of **14c** ($CDCl_3$, 400 MHz).

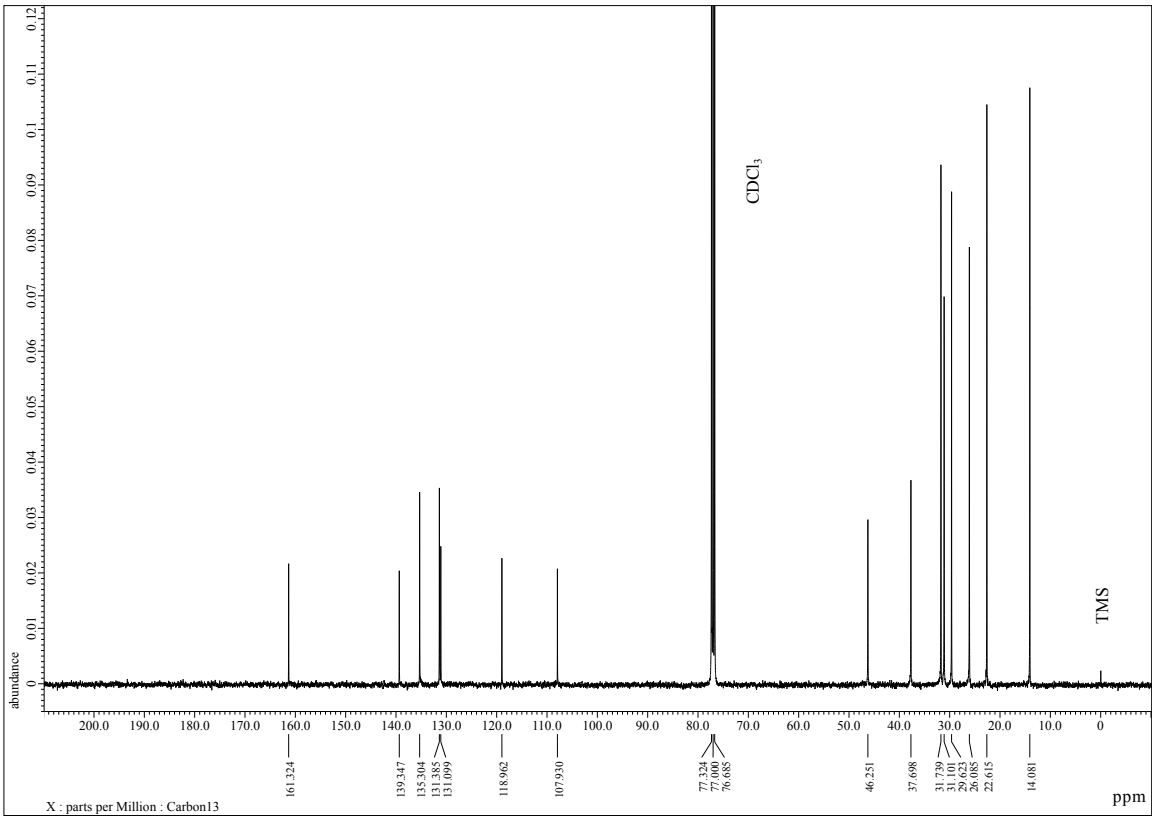

$^{13}C\{^{1}H\}$ NMR spectrum of **14c** ($CDCl_3$, 100 MHz).

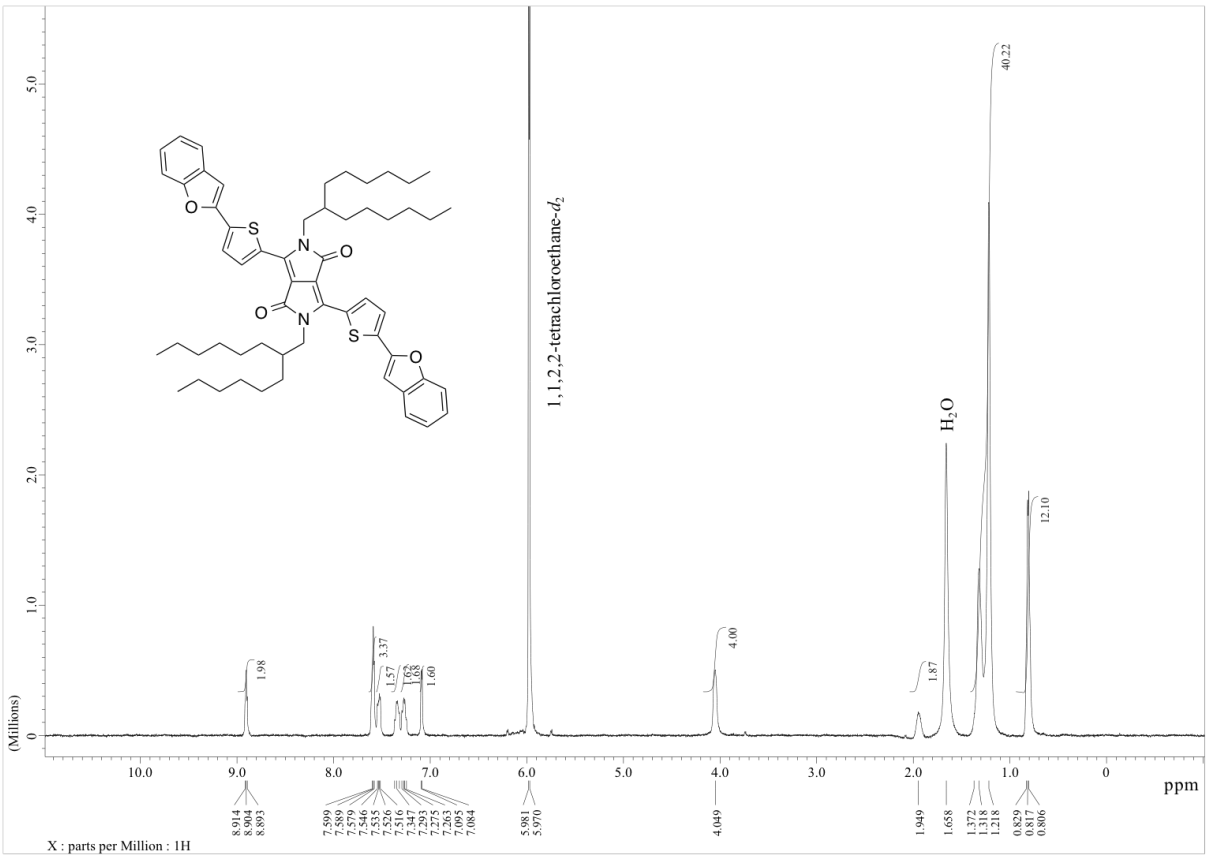

^{1}H NMR spectrum of **C14-DPP** (1,1,2,2-tetrachloroethane-d_2, 400 MHz).

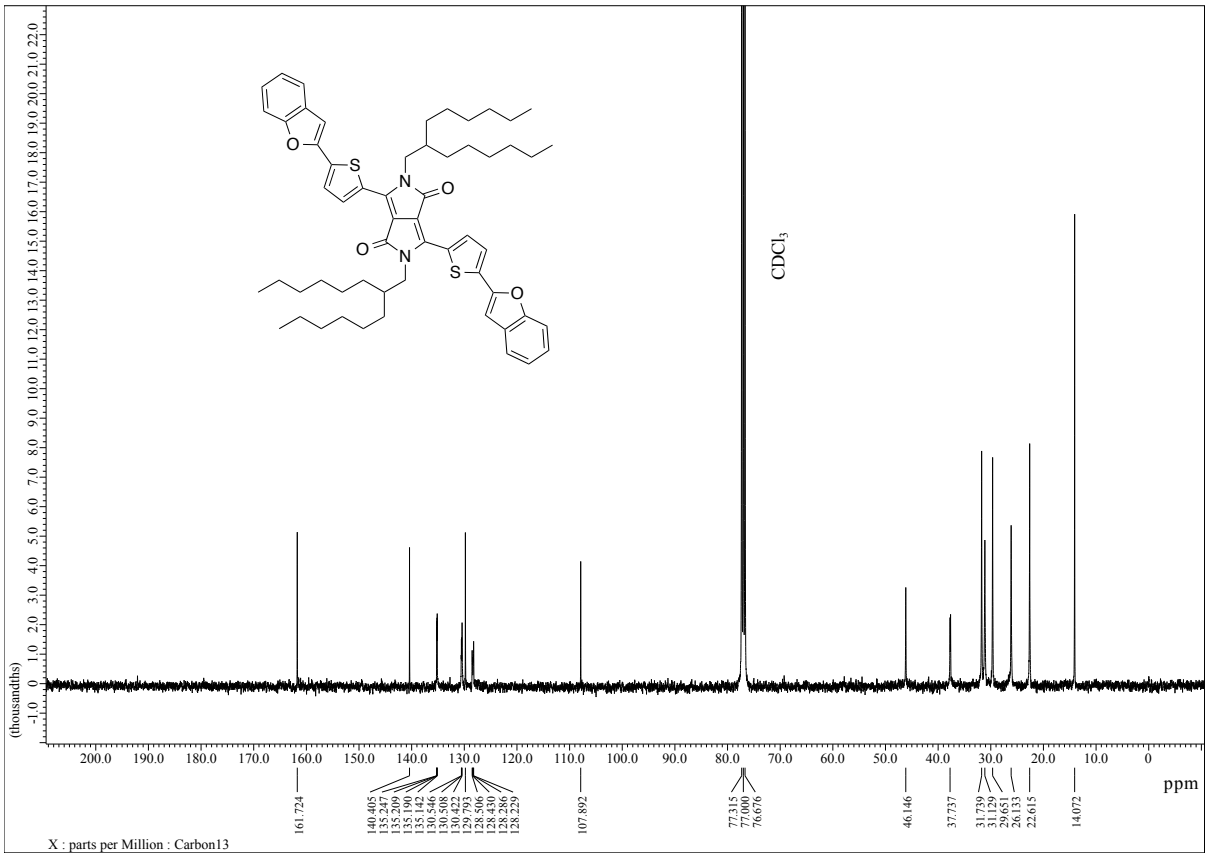

^{13}C{^{1}H} NMR spectrum of **C14-DPP** ($CDCl_3$, 100 MHz).

4-12. References

(1) Mei, J.; Bao, Z. Side Chain Engineering in Solution-Processable Conjugated Polymers. *Chem*. *Mater.* **2014**, *26*, 604–615.

(2) Beaujuge, P. M.; Fréchet, J. M. J. Molecular Design and Ordering Effects in π-Functional Materials for Transistor and Solar Cell Applications. *J. Am. Chem. Soc.* **2011**, *133* (50), 20009–20029.

(3) Mei, J.; Diao, Y.; Appleton, A. L.; Fang, L.; Bao, Z. Integrated Materials Design of Organic Semiconductors for Field-Effect Transistors. *J. Am. Chem. Soc.* **2013**, *135* (18), 6724–6746.

(4) Takahashi, K.; Kumagai, D.; Yamada, N.; Kuzuhara, D.; Yamaguchi, Y.; Aratani, N.; Koganezawa, T.; Koshika, S.; Yoshimoto, N.; Masuo, S.; Suzuki, M.; Nakayama, K.-I.; Yamada, H. Side-Chain Engineering in a Thermal Precursor Approach for Efficient Photocurrent Generation. *J. Mater. Chem. A* **2017**, *5* (27), 14003–14011.

(5) Osaka, I.; Saito, M.; Koganezawa, T.; Takimiya, K. Thiophene-Thiazolothiazole Copolymers: Significant Impact of Side Chain Composition on Backbone Orientation and Solar Cell Performances. *Adv. Mater.* **2013**, *26* (2), 331–338.

(6) Najari, A.; Beaupré, S.; Allard, N.; Ouattara, M.; Pouliot, J.-R.; Charest, P.; Besner, S.; Simoneau, M.; Leclerc, M. Thieno, Furo, and Selenopheno[3,4-c]pyrrole-4,6-dione Copolymers: Air-Processed Polymer Solar Cells with Power Conversion Efficiency Up to 7.1%. *Adv. Energy Mater.* **2015**, *5* (23), 1501213–1501219.

(7) Zhang, G.; Zhang, K.; Yin, Q.; Jiang, X.-F.; Wang, Z.; Xin, J.; Ma, W.; Yan, H.; Huang, F.; Cao, Y. *J. Am. Chem. Soc.* **2017**, *139* (6), 2387.

(8) Deng, D.; Zhang, Y.; Zhang, J.; Wang, Z.; Zhu, L.; Fang, J.; Xia, B.; Wang, Z.; Lu, K.; Ma, W.; Wei, Z. Fluorination-Enabled Optimal Morphology Leads to Over 11% Efficiency for Inverted Small-Molecule Organic Solar Cells. *Nat*. *Commun*. **2016**, *7*, 1–9.

(9) Jung, M.; Yoon, Y.; Park, J. H.; Cha, W.; Kim, A.; Kang, J.; Gautam, S.; Seo, D.; Cho, J. H.; Kim, H.; Choi, J. Y.; Chae, K. H.; Kwak, K.; Son, H. J.; Ko, M. J.; Kim, H.; Lee, D.-K.; Kim, J. Y.; Choi, D. H.; Kim, B. Nanoscopic Management of Molecular Packing and Orientation of Small Molecules by a Combination of Linear and Branched Alkyl Side Chains. *ACS Nano* **2014**, *8* (6), 5988–6003.

(10) Sun, K.; Xiao, Z.; Hanssen, E.; Klein, M. F. G.; Dam, H. H.; Pfaff, M.; Gerthsen, D.; Wong, W. W. H.; Jones, D. J. The Role of Solvent Vapor Annealing in Highly Efficient Air-Processed Small Molecule Solar Cells. *J. Mater. Chem.* **2014**, *2* (24), 9048–9054.

(11) Li, G.; Shrotriya, V.; Huang, J.; Yao, Y.; Moriarty, T.; Emery, K.; Yang, Y. High-Efficiency Solution Processable Polymer Photovoltaic Cells by Self-Organization of Polymer Blends. *Nat. Mater.* **2005**, *4* (11), 864–868.

(12) Proctor, C. M.; Love, J. A.; Nguyen, T.-Q. Mobility Guidelines for High Fill Factor Solution-Processed Small Molecule Solar Cells. *Adv. Mater.* **2014**, *26* (34), 5957.

(13) Henson, Z. B.; Zalar, P.; Chen, X.; Welch, G. C.; Nguyen, T.-Q.; Bazan, G. C. Towards Environmentally Friendly Processing of Molecular Semiconductors. *J. Mater. Chem. A* **2013**, *1* (37), 11117–11120.

(14) Huang, F.; Zhang, Y.; Liu, M. S.; Jen, A. K. Y. Electron-Rich Alcohol-Soluble Neutral Conjugated Polymers as Highly Efficient Electron-Injecting Materials for Polymer Light-Emitting Diodes. *Adv. Funct. Mater.* **2009**, *19* (15), 2457–2466.

(15) Shao, M.; He, Y.; Hong, K.; Rouleau, C. M.; Geohegan, D. B.; Xiao, K. A Water-Soluble Polythiophene for Organic Field-Effect Transistors. *Polym. Chem.* **2013**, *4* (20), 5270.

(16) Meng, B.; Song, H.; Chen, X.; Xie, Z.; Liu, J.; Wang, L. Replacing Alkyl with Oligo(Ethylene Glycol) as Side Chains of Conjugated Polymers for Close π–π Stacking. *Macromolecules* **2015**, *48* (13), 4357–4363.

(17) Chen, X.; Zhang, Z.; Ding, Z.; Liu, J.; Wang, L. Diketopyrrolopyrrole-Based Conjugated Polymers Bearing Branched Oligo(Ethylene Glycol) Side Chains for Photovoltaic Devices. *Angew. Chem. Int. Ed.* **2016**, *55* (35), 10376–10380.

(18) Chang, W.-H.; Gao, J.; Dou, L.; Chen, C.-C.; Liu, Y.; Yang, Y. Side-Chain Tunability via Triple Component Random Copolymerization for Better Photovoltaic Polymers. *Adv. Energy Mater.* **2013**, *4* (4), 1300864–1300867.

(19) Chen, X.; Liu, X.; Burgers, M. A.; Huang, Y.; Bazan, G. C. Green-Solvent-Processed Molecular Solar Cells. *Angew. Chem. Int. Ed.* **2014**, *53* (52), 14378–14381.

(20) Henson, Z. B.; Zalar, P.; Chen, X.; Welch, G. C.; Nguyen, T.-Q.; Bazan, G. C. Towards Environmentally Friendly Processing of Molecular Semiconductors. *J. Mater. Chem. A* **2013**, *1* (37), 11117–11120.

(21) Walker, B.; Tamayo, A. B.; Dang, X.-D.; Zalar, P.; Seo, J. H.; Garcia, A.; Tantiwiwat, M.; Nguyen, T.-Q. Nanoscale Phase Separation and High Photovoltaic Efficiency in Solution-Processed, Small-Molecule Bulk Heterojunction Solar Cells. *Adv. Funct. Mater.* **2009**, *19* (19), 3063–3069.

(22) Walker, B.; Tamayo, A.; Duong, D. T.; Dang, X.-D.; Kim, C.; Granstrom, J.; Nguyen, T.-Q. A Systematic Approach to Solvent Selection Based on Cohesive Energy Densities in a Molecular Bulk Heterojunction System. *Adv. Energy Mater.* **2011**, *1* (2), 221–229.

(23) Ryan, J. W.; Matsuo, Y. Increased Efficiency in Small Molecule Organic Solar Cells Through the Use of a 56-π Electron Acceptor – Methano Indene Fullerene. *Sci*. *Rep*. **2015**, *5*, 591–595.

(24) Liu, J.; Walker, B.; Tamayo, A.; Zhang, Y.; Nguyen, T.-Q. Effects of Heteroatom Substitutions on the Crystal Structure, Film Formation, and Optoelectronic Properties of Diketopyrrolopyrrole-Based Materials. *Adv. Funct. Mater.* **2013**, *23* (1), 47–56.

(25) Sun, K.; Xiao, Z.; Hanssen, E.; Klein, M. F. G.; Dam, H. H.; Pfaff, M.; Gerthsen, D.; Wong, W. W. H.; Jones, D. J. The Role of Solvent Vapor Annealing in Highly Efficient Air-Processed Small Molecule Solar Cells. *J. Mater. Chem. A* **2014**, *2* (24), 9048–9048.

(26) Fernández, D.; Viterisi, A.; Ryan, J. W.; Gispert-Guirado, F.; Vidal, S.; Filippone, S.; Martín, N.; Palomares, E. Small Molecule BHJ Solar Cells Based on DPP(TBFu) 2and Diphenylmethanofullerenes (DPM): Linking Morphology, Transport, Recombination and Crystallinity. *Nanoscale* **2014**, *6* (11), 5871–5878.

(27) Qiao, Y.; Guo, Y.; Yu, C.; Zhang, F.; Xu, W.; Liu, Y.; Zhu, D. Diketopyrrolopyrrole-Containing Quinoidal Small Molecules for High-Performance, Air-Stable, and Solution-Processable N-Channel Organic Field-Effect Transistors. *J. Am. Chem. Soc.* **2012**, *134* (9), 4084–4087.

(28) Wang, C.; Qin, Y.; Sun, Y.; Guan, Y.-S.; Xu, W.; Zhu, D. Thiophene-Diketopyrrolopyrrole-Based Quinoidal Small Molecules as Solution-Processable and Air-Stable Organic Semiconductors: Tuning of the Length and Branching Position of the Alkyl Side Chain Toward a High-Performance N-Channel Organic Field-Effect Transistor. *ACS Appl. Mater. Interfaces* **2015**, *7* (29), 15978–15987.

(29) Lim, B.; Sun, H.; Lee, J.; Noh, Y.-Y. High Performance Solution Processed Organic Field Effect Transistors with Novel Diketopyrrolopyrrole-Containing Small Molecules. *Sci*. *Rep*. **2017**, *7*, 1–8.

(30) Tantiwiwat, M.; Tamayo, A.; Luu, N.; Dang, X.-D.; Nguyen, T.-Q. Oligothiophene Derivatives Functionalized with a Diketopyrrolopyrrolo Core for Solution-Processed Field Effect Transistors: Effect of Alkyl Substituents and Thermal Annealing. *J*. *Phys*. *Chem*. *C* **2008**, *112* (44), 17402–17407.

(31) Lee, M.; Jeong, Y. S.; Cho, B. K.; Oh, N. K.; Zin, W. C. Self-Assembly of Molecular Dumbbells into Organized Bundles with Tunable Size. *Chem*. *Eur*. *J*. **2002**, *8* (4), 876–883.

(32) Pommerehne, J.; Vestweber, H.; Guss, W.; Mahrt, R. F.; Bässler, H.; Porsch, M.; Daub, J. Efficient two layer leds on a polymer blend basis. *Adv*. *Mater*. **1995**, *7* (6), 551–554.

(33) Wu, S. Calculation of Interfacial Tension in Polymer Systems. *J. Polym. Sci.* **1971**, *C34*, 19–30.

(34) Huang, J.-H.; Hsiao, Y.-S.; Richard, E.; Chen, C.-C.; Chen, P.; Li, G.; Chu, C.-W.; Yang, Y. The Investigation of Donor-Acceptor Compatibility in Bulk-Heterojunction Polymer Systems. *Appl. Phys. Lett.* **2013**, *103* (9), 043304.

(35) Scharber, M. C.; Mühlbacher, D.; Koppe, M.; Denk, P.; Waldauf, C.; Heeger, A. J.; Brabec, C. J. Design Rules for Donors in Bulk-Heterojunction Solar Cells—Towards 10 % Energy-Conversion Efficiency. *Adv. Mater.* **2006**, *18* (6), 789–794.

(36) Cho, M. Y.; Kim, S. J.; Han, Y. D.; Park, D. H.; Kim, K. H.; Choi, D. H.; Joo, J. Highly Sensitive, Photocontrolled, Organic Thin-Film Transistors Using Soluble Star-Shaped Conjugated Molecules. *Adv. Funct. Mater.* **2008**, *18* (19), 2905–2912.

(37) Armin, A.; Stoltzfus, D. M.; Donaghey, J. E.; Clulow, A. J.; Nagiri, R. C. R.; Burn, P. L.; Gentle, I. R.; Meredith, P. Engineering Dielectric Constants in Organic Semiconductors. *J. Mater. Chem. C* **2017**, *5* (15) 1–12.

(38) Lu, Z.; Zhang, X.; Zhan, C.; Jiang, B.; Zhang, X.; Chen, L.; Yao, J. Impact of Molecular Solvophobicity vs. Solvophilicity on Device Performances of Dimeric Perylene Diimide Based Solution-Processed Non-Fullerene Organic Solar Cells. *Phys. Chem. Chem. Phys.* **2013**, *15* (27), 11375–11385.

(39) Zhao, G.; Liu, J.; Meng, Q.; Ji, D.; Zhang, X.; Zou, Y.; Zhen, Y.; Dong, H.; Hu, W. High-Performance UV-Sensitive Organic Phototransistors Based on Benzo[1,2-*b*:4,5-*b*′]Dithiophene Dimers Linked with Unsaturated Bonds. *Adv. Electron. Mater.* **2015**, *1* (8), 1500071–1500078.

(40) Spek, A. L. PLATON, A Multipurpose Crystallographic Tool, Utrecht, The Netherlands, 2005.

(41) Particle Size Distribution and X-Ray Diffraction Peak Profiles in Supersaturated Solid Solutions. **1990**, *46* (3), 187–194.

(42) Sheldrick, G. M. A Short History of SHELX. *Acta Cryst* **2007**, *64* (1), 112–122.

(43) Woo, C. H.; Beaujuge, P. M.; Holcombe T. W.; Lee, O. P.; Fréchet, J. M.; Incorporation of Furan into Low Band-Gap Polymers for Efficient Solar Cells. *J. Am. Chem. Soc.* **2010**, *132* (44), 15547–15549.

(44) Sun, Y.; Seo, J. H.; Takacs, C. J.; Seifter, J.; Heeger, A. J. Inverted Polymer Solar Cells Integrated with a Low-Temperature-Annealed Sol-Gel-Derived ZnO Film as an Electron Transport Layer. *Adv. Mater. Weinheim* **2011**, *23* (14), 1679–1683.

(45) Kato, M.; Komoda, K.; Namera, A.; Sarai, Y.; Okada, S.; Yamada, A.; Yokoyama, K.; Migita, E.; Minobe, Y.; Tani, T. Pyrrole Butyric Acid Derivatives as Inhibitors of Steroid 5α-Reductase. *Chem*. *Pharm*. *Bull*. **1997**, *45* (11), 1767–1776.

Chapter 5

General Conclusion

This dissertation focused on providing new knowledge regarding the correlation between the molecular structure and the thin-film properties which affects the performances of the optoelectronic devices.

In Chapter 2, the photovoltaic properties of the porphycene–diketopyrrolopyrole (DPP) conjugates, one dyad and two triads, with extended photoabsorption were described. These dyes served as p-type materials in organic solar cells (OSCs). The comparison of the three conjugates gave the knowledge for the photoabsorption property and inhibition of molecular aggregation in porphycene-based materials.

In Chapter 3, the correlation between 3D molecular architectures of porphycene dimers and their thin-film properties were discussed. Different linkers within porphycene dimers tuned these 3D architectures, and these dimers showed largely different performance in OSC as n-type materials.

In Chapter 4, the effects of hydrophilic oligo(ethylene glycol) (OEG) chains on the photovoltaic and photosensitive properties were described. The OEG chains in DPP-based small molecules induced the increase of HOMO and LUMO energy levels and the decrease of open-circuit voltage (V_{OC}) as compared to the hydrophobic alkyl chains. Another finding was that OEG chains significantly improved a photosensitivity in the organic phototransistor (OPT) devices. This is the first example in which the side-chain effect on the OPT performance was examined.

Although π-conjugated molecular structures of organic semiconductor have been rapidly developed in the last fifteen years, the effect of molecular structure on the thin-film properties and performance of optoelectronic devices is not yet well understood. Thus, future works

should focus on the molecular shape and substituent to bring out potential properties of organic materials.

This dissertation concentrated on OSC and OPT devices which have room for improvement. The revealed effect of molecular structure on thin-film properties will become the guideline for releasing the latent optoelectronic properties of materials. In the active layer of OSC, the optimizations of frontier orbital energy levels and miscibility between materials are key points for improving the photovoltaic performances. The both of those factors can be tuned by changing the molecular shape and substituents.

I found that porphycene is a suitable building block for OSC materials as a photoabsorber unit at the visible–NIR region. However, it has a strong self-aggregation property. To address this issue, the introduction of side chains to a porphycene unit that improves the miscibility between p- and n-type materials can lead to an OSC material with a high performance.

On the other hand, elucidation of the factor that determines the orbital energy levels in the thin-film state can lead high V_{OC} and PCE without changing the π-conjugated structure. For example, the introduction of hydrophilic OEG chains that increase the LUMO levels of small molecular n-type materials in the thin-film state is expected to give a high V_{OC}. In particular, the introduction of hydrophilic OEG chains into the state-of-the-art n-type materials may enable achieving PCEs improve over 15%.

For OPT devices, the correlation between the molecular structure and photosensitivity is still not clear. The knowledge of the switching photosensitivity which depended on the substituents will provide for the molecular designs on the OPT materials.

List of Achievements

List of Publications

(1) Synthesis and Electrochemical Properties of Porphycene–Diketopyrrolopyrrole Conjugates. Takuya Okabe, Daiki Kuzuhara, Mitsuharu Suzuki, Naoki Aratani, and Hiroko Yamada, *Organic Letters* **2014**, *16* (13), 3508–3511.

(2) Synthesis and Electronic Properties of Acetylene- and Butadiyne-Linked 3,3′-Porphycene Dimers. Takuya Okabe, Daiki Kuzuhara, Naoki Aratani, and Hiroko Yamada, *Journal of Porphyrins and Phthalocyanines* **2014**, *18* (10n11), 849−855.

(3) Porphycene Dimer-Based Non-Fullerene Acceptor for Organic Solar Cell. Takuya Okabe, Daiki Kuzuhara, Mitsuharu Suzuki, Naoki Aratani, and Hiroko Yamada, *Journal of Porphyrins and Phthalocyanines* **2016**, *20* (08n11), 1350–1360.

Other Publications

(1) Synthesis, Properties and Crystal Structures of 2,7,12,17-Tetraarylporphycenes. Daiki Kuzuhara, Haruka Nakaoka, Takuya Okabe, Naoki Aratani, and Hiroko Yamada, *HETEROCYCLES* **2015**, *90* (2), 1214–1214.

(2) A novel D–π–A small molecule with N-heteroacene as acceptor moiety for photovoltaic application. Chengyuan Wang, Takuya Okabe, Guankui Long, Daiki Kuzuhara, Yang Zhao, Naoki Aratani, Hiroko Yamada, Qichun Zhang, *Dyes and Pigments*, **2015**, *122*, 231–237.

(3) Synthesis, Characterization and Protonation Behavior of Quinoxaline-Fused Porphycenes. Daiki Kuzuhara, Mika Sakaguchi, Wataru Furukawa, Takuya Okabe, Naoki Aratani, Hiroko Yamada, *Molecules*, **2017**, *22* (6), 908.

Acknowledgements

The studies in this dissertation were accomplished by me and with several research collaborators under the direction of Prof. Hiroko Yamada at Nara Institute of Science and Technology (NAIST).

First of all, I would like to appreciate Prof. Hiroko Yamada, Assoc. Prof. Naoki Aratani, Assist. Prof. Daiki Kuzuhara, Assist. Prof. Mitsuharu Suzuki, and Assist. Prof. Hironobu Hayashi of NAIST for the precious guidance and encouragement throughout my doctoral course. I also thanks Prof. Kiyomi Kakiuchi and Assoc. Prof. Takashi Matsuo at NAIST for insightful advise and encouragements.

I acknowledge Dr. Tomoyuki Koganezawa (Japan Synchrotron Radiation Research Institute) and Dr. Yuji Yamaguchi (Tokyo Chemical Industry Co., Ltd.) for giving the chance to conduct GIWAXD measurement in SPring-8 (Proporsals 2015A1683, 2017A1779 and 2017B1817).

I greatly appreciate to the current and former group members in Prof. Yamada's laboratory for their generous cooperation. In particular, I would like to thank Dr. Hiroyuki Saeki for starting up research environment of organic electronics, I also thanks Dr. Tatsuya Aotake, Dr. Cassandre Quinton, Dr. Kohtaro Takahashi, Dr. Masataka Yamashita, Mr. Keisuke Uchinaga, Mr. Shinpei Yamamoto, Mr. Naoto Nagami, Mr. Kengo Terai, Mr. Yusuke Shimizu, Mr. Akihiro Maeda and Mr. Shuhei Negoro for productive discussion of organic optoelectronics.

My contemporaries students, Dr. Akinobu Matsumoto, Mr. Yuto Tamura and Mr. Akira Tamoto, at Yamada Lab gave me a lot of impetuses for researching.

I would like to thank Mr. Shohei Katao and Ms. Yoshiko Nishikawa in NAIST for measuring and analyzing single-crystal X-ray analysis and high-resolution mass spectrometry, respectively. The author also appreciates all technical staffs in NAIST for giving lectures and continuous maintenance of research facilities.

The financial support from JSPS, Research Fellowship of Japan Society for the Promotion of Science for Young Scientists was indispensable, and my sincerely appreciates.

I would like to thank the Nippon Synthetic Chemical Industry Co., Ltd. for a gift of ethyl isocyanoacetate which was used for the preparation of the starting pyrroles.

Finally, I would like to thank my wife, Mai Okabe, and my parents for their heartfelt encouragement and continuous assist.

Takuya Okabe